Localization of brain oscillatory sources from (S)EEG recordings

Viviana del Rocío Hernández Castañón

To cite this version:

Viviana del Rocío Hernández Castañón. Localization of brain oscillatory sources from (S)EEG recordings. Signal and Image processing. Université de Lorraine, 2023. English. NNT : 2023LORR0010 . tel-04087878

HAL Id: tel-04087878
https://hal.univ-lorraine.fr/tel-04087878

Submitted on 3 May 2023

École doctorale IAEM Lorraine

Localization of brain oscillatory sources from (S)EEG recordings

THÈSE

présentée et soutenue publiquement le 8 février 2023

pour l'obtention du

Doctorat de l'Université de Lorraine

Spécialité Automatique, Traitement du Signal et des Images, Génie Informatique

par

Viviana del Rocío HERNÁNDEZ CASTAÑÓN

Composition du jury

Président :	Theodore Papadopoulo	INRIA Sophia Antipolis Méditerranée
Rapporteurs :	Régine Le Bouquin Jeannes	LTSI, UMR 1099 INSERM, Université de Rennes
	Bertrand Rivet	GIPSA-lab, UMR 5216 CNRS, Grenoble INP
Examinatrice :	Valérie Louis Dorr	CRAN, UMR 7039 CNRS, Université de Lorraine
Encadrants :	Radu Ranta	CRAN, UMR 7039 CNRS, Université de Lorraine
	Steven Le Cam	CRAN, UMR 7039 CNRS, Université de Lorraine

Centre de Recherche en Automatique de Nancy
UMR 7039 - Université de Lorraine, CNRS

Acknowledgments

I take this opportunity to acknowledge those who have been part of this important step in my career.

I would like first to recognize and thank to my supervisors Radu Ranta and Steven Le Cam for this valuable support in the process of this work. Thank you very much for this opportunity. I really appreciate the patience and understanding of the difficulties I faced during this work. For the knowledge shared, the time spent to reach the results of this work, on the supervision of the writing of this manuscript and also all the support you provided me to go through this process that certainly was difficult but worth it as well.

Thanks also to my colleagues from the Central hospital and Ensem, for the partnership, the support, the good times, the meals, the laughs, the talks, for all those things that helped to lighten the weight of this work many times. Thanks also to those who helped me with the paperwork any time, particularly at the beginning when my French skills were quite poor.

Thanks to those I have met in Nancy that also shared with me a really good time. Thanks for the help, the talks, the meals, the laughs.

All my gratitude to my beloved ones in France, Pierre, Berenice, Isabel, Cathy, Jacques, Jeanine and Pierrot. Thanks for being like a family for me. For the support during the pandemic, for all the expressions of affection, for make me feel part of this country and allow me to spend amazing moments as part of the family. Merci d'avoir été comme une famille pour moi. Pour votre soutien pendant la pandémie, pour toutes les expressions de votre affection, pour m'avoir fait sentir faire partie de ce pays et m'avoir permis de passer des moments magnifiques avec vous.

A warm thank you to my family to keep me in your thoughts as I do. For all that love and support. For showing me in different ways that I am present despite the distance. Los amo, Flori, Alba, Yas (thank you for taking care of my health), Eli Daniel, Jorge, Alex, Luis, Angel.

Thank you also to the members of the jury for accepting to be part of this committee and supporting the reviewing of this thesis and to those who provided to me their valuable observations to improve the manuscript.

Finally, many thanks to the Mexican research council, Conacyt, for this 3 years and 9 months of supporting me with a scholarship that allowed me to carry out this research work.

Contents

Résumé en français

Contexte et objectifs

L'activité du cerveau émerge de processus neuronaux complexes qui doivent être analysés à différentes échelles spatiales et temporelles, afin de compendre l'activité déclenchée depuis le niveau cellulaire vers le fonctionnement structurel global. Cette complexité est principalement liée à la constitution du cerveau, possédant environ 120 millards de neurones : 21 à 26 millards de neurones dans le cortex cérébral et autour de 100 millards dans le cervelet [Herculano-Houzel, 2009]. Les structures neuronales sont organisées en réseaux interconnectés et le cerveau peut ainsi être décrit comme un système complexe mettant en œuvre des tâches collaboratives cognitives, réflexives et comportamentales, dont les méchanismes sous-jacents restent largement inconnus. La compréhension de la dynamique temporelle entre les structures impliquées dans un réseau fonctionnel ou phatologique est cruciale pour comprendre le fonctionnement du cerveau et décisive pour résoudre des questions fondamentales en neurosciences.

En particulier, la reconnaissance des visages est une fonction cérébrale importante pour la communication sociale humaine. Cette fonction neuronale peut être étudiée en identifiant les structures neuronales impliquées, leurs rôles spécifiques et leurs dynamique. Si la théorie selon laquelle la reconnaissance des visages implique de multiples zones constituant un réseau est largement acceptée, ce réseau reste encore peu connu. Une analyse pertinente de ces réseaux cérébraux fonctionnels passe par l'identification des noeuds du réseau, à savoir les sources cérébrales impliquées dans le processus de reconnaissance des visages, et par la reconstruction de l'activité de ces noeuds/sources.

Dans le contexte des travaux sur la reconnaissance des visages, la Stimulation Visuelle Périodique Rapide (FPVS) est une technique privilégiée pour étudier ce système cérébral, car elle est bien contrôlée et fournit des réponses hautement reproductibles, avec des rapports signaux à bruit (SNR) élevés. Un exemple est le protocole appelé FACELOC : des images d'objet son présentées à l'observateur à un rythme de six stimuli par seconde, et une image de visage différente est intercalée tous les cinq stimuli. Le protocole induit une réponse générale à la stimulation visuelle à 6 Hz (et harmoniques), et une réponse spécifique visage à 1.2Hz pour certaines structures. Ces activités sont donc à bande très étroite, concentrées sur un ou quelques points de fréquence. Ces signaux électrophysiologiques sont capturés sur les mesures de (S)EEG, offrant une très haute résolution temporelle et fréquentielle, enregistrant ainsi l'activité cérebrale à l'échelle des phénomènes étudiés.

Dans ce travail de thèse, nous nous intéressons particulièrement aux champs électriques enregistrés par l'EEG de surface et les électrodes intra-cérébrales de stéréo-EEG (SEEG), qui sont principalement générés par les activités synchronisées des neurones pyramidaux. Les mesures EEG ont été largement utilisée pour résoudre le problème de la localisation des sources cérébrales, c'est à dire la reconstruction de la position et de l'activité (amplitude et orientation) des générateurs sous-jacents à partir des enregistrements électroencéphalographiques. Cependant en ce qui concerne la localisation des sources cérébrales, une observation beaucoup plus précise de l'activité neuronale peut être obtenue par les électrodes SEEG, car elles sont introduites directement dans le tissu cérébral à proximité des générateurs. Il en résulte un rapport signal/bruit (SNR) beaucoup plus élevé que pour l'EEG. Cependant, les électrodes SEEG ont leurs propres inconvénients. En premier lieu, la géométrie particulière induite par l'implantation des électrodes SEEG conduit à un problème mal conditionné. De plus, la vision locale restrictive de l'activité cérébrale par la SEEG est susceptible de masquer d'autres activités d'intérêt provenant de structures distantes. Dans le cas de l'EEG (mais aussi en partie dans le cas de la SEEG), le SNR peut être très faible en raison de l'atténuation de l'os du crâne, de la peau et des sources d'artefact (c'est-à-dire des sources sans intérêt pour le problème étudié, soit externes, soit provenant du cerveau également). Ainsi, les sources d'intérêt peuvent être masquées par ces composantes d'interférences. C'est pourquoi des étapes de prétraitement sont nécessaires pour augmenter la fiabilité de la localisation, en particulier le re-référencement, des procédures de filtrage, de moyennage, *etc*.

L'objectif principal de cette thèse est d'aborder le problème de la localisation de sources cérébrales dans le contexte de sources périodiques/oscillatoires, répondant au protocole FPVS/FACELOC à partir d'enregistrements EEG/SEEG. Nous formalisons d'abord les spécificités de la localisation de telles sources oscillatoires enregistrées par des capteurs EEG/SEEG et nous identifions les principales difficultés liés à ce problème inverse mal conditionné. Nous présentons le problème d'ambiguïté qui se pose lorsqu'on essaie de distinguer plusieurs sources oscillatoires partageant les mêmes caractéristiques de fréquence, dans le cadre de simulations réalistes. Nous quantifions ensuite dans quelle mesure les algorithmes de localisation peuvent être trompés par l'existence de solutions équivalentes. Sur la base de cette analyse, nous proposons des méthodes reposant sur la parcimonie de la solution comme contrainte de régularisation : il est en effte attendu qu'un nombre réduit de structures répondent aux fréquences de stimulation spécifiques. Des modèles de sources distribuées sont considérés, à orientations fixes connues ou inconnues. Nous introduisons des algorithmes parcimonieux adaptés à ces hypothèses, en nous appuyant sur les algorithmes de régression de la littérature (OLS/SBR), et nous les comparons aux algorithmes dérivés de l'approche MUSIC. Les algorithmes de localisation sont appliqués à la fois dans le domaine temporel et fréquentiel et leurs performances sont évaluées sur des signaux simulés. Enfin, les méthodes sont appliquées à des signaux EEG et SEEG réels enregistrés avec le même protocole FACELOC.

Structure de la thèse, développements et résultats

Chapitre 1 - L'electrophysiologie du cerveau

Le premier chapitre consiste en une introduction générale de l'anatomie du cerveau, décrivant les principales structures cérébrales et l'organisation fonctionelle des regions corticales. Un aperçu de l'électrophysiologie cérébrale est ensuite présenté, en partant de la structure du neurone et de l'activité telle qu'elle est produite par de grandes assemblées de neurones, donnant lieu à l'activité électromagnétique enregistrée par les mesures MEG et EEG/SEEG. Nous décrivons également les principales modalités de neuro-imagerie et électrophysiologiques permettant d'explorer le cerveau, avec une attention particulière sur les signaux EEG (scalp et intracrânien), en soulignant l'intérêt d'aborder les tâches de localisation de sources à partir de ces modalités. Nous nous concentrons enfin sur les donnés (S)EEG enregistrées sous protocoles cognitifs, en particulier lors de stimulations visuelles périodiques rapides (FPVS) appliquées à la reconnaissance cérébrale des visages, qui génèrent des activités oscillantes à la frequence de la stimulation dans des zones cérébrales spécifiques impliquées dans le processus de reconnaissance des images/visages.

Chapitre 2: Problème direct et inverse en localisation de sources cérébrales

La localisation des sources cérébrales implique de calculer un modèle direct. Cette modélisation consiste à calculer le potentiel électrique observé sur un capteur donné lorsque la configuration des sources électriques sous-jacentes (modèle de source) ainsi que les propiétés biophysiques et la géometrie de l'environement de propagation (modèle de tête) sont connues.

Nous définissons d'abord le modèle direct comme un mélange linéaire:

$$\mathbf{X} = \mathbf{K}\mathbf{J} + \varepsilon \tag{1}$$

où $\mathbf{X} \in \mathbb{R}^{M \times T}$ reprsente le potential électrique EEG/SEEG sur M électrodes le long de T échantillons de temps. $\mathbf{K} \in \mathbb{R}^{M \times 3N}$ correspond au champ appelé lead-field représentant l'activité de N sources dipolaires librement orientées (N positions dans le cerveau) sur M électrodes, et $\mathbf{J} \in \mathbb{R}^{3N \times T}$ encode la matrice de densité de courant représentant l'orientation et l'amplitude des N sources à travers T points de temps. ε représente le bruit de mesure et la présence d'artefacts.

Pour simplifier la résolution de ce problème inverse, les informations anatomiques du cerveau peuvent être utilisées pour contraindre l'orientation des sources. Cette contrainte est basée sur l'hypothèse neurophysiologique selon laquelle les principaux générateurs des enregistrements EEG/SEEG sont localement sont orientés perpendiculairement à la surface corticale. Par conséquent, la formalisation des mesures de potentiel électrique devient:

$$\mathbf{X} = \mathbf{A}\mathbf{S} + \varepsilon \tag{2}$$

où le lead-field $\mathbf{A} \in \mathbb{R}^{M \times N}$ encode les gains entre N sources avec des positions donées et des orientations fixes et les M électrodes. Autrement dit, chaque colonne de $\mathbf{A}$ contient les coefficients de propagation entre une position de source d'orientation fixée et les électrodes, et $\mathbf{S} \in \mathbb{R}^{N \times T}$ est une matrice contenant l'amplitude de ces N sources à chaque instant.

Les principales approches pour résoudre le problème de la localisation des sources cérébrales sont ensuite introduites dans ce chapitre. Tout d'abord, les modèles analytiques et numériques de propagation (lead-field) sont décrits. Ensuite, une vue d'ensemble des différentes approaches pour régulariser le problème inverse lié à la localisation des sources cérébrales est présentée, avec une attention particulière sur l'aspect sous-déterminé du problème, où le nombre de dipôles candidats encodés dans la lead-field est beaucoup plus élevé que le nombre de mesures. Etant donné la cible applicative de cette thèse lié à la reconstruction de sources cérébrales impliquées dans la reconnaissance des visage (et en particulier sous protocoles FPVS), nous formulons l'hypothèse raisonnable que peu de région sont impliquées dans le processus de reconnaissance, et nous explorons plus en détail les méthodes basées sur des approches de scanning et matching pursuit renforçant la sparsité des solutions. Nous décrivons égalment les stratégies de prétraitement appliquées aux signaux réels, à savoir le débruitage du signal et la transformation des données dans le domaine fréquentiel.

Chapitre 3: Sur la localisation des sources oscillatoires à partir d'enregistrements (S)EEG

Dans ce chapitre sont analysées les particularités et les difficultés qui doivent être prises en compte lorsque l'on essaie de localiser les activités de sources oscillatoires en utilisant les signaux EEG/SEEG.

3.1 Analyse des signaux EEG/SEEG acquis sous protocole FPVS

Le chapitre commence par une analyse d'un signal réel acquis lors du protocole de stimulation FPVS dénommé FACELOC et décrit précédemment (chapitre1), et met en évidence la présence de pics prédominants dans les spectres d'amplitude de Fourier des signaux EEG (fig.3.1(a)) et SEEG (fig.3.2(a)) à 6Hz et 12Hz (fréquence fondamentale et une harmonique du stimuli visuel). Ces observations indiquent que certaines sources cérébrales (donc structures cérébrales) ont des activités qui se synchronisent à la fréquence du stimuli. Des réponses sont égalment visibles, bien que beaucoup plus faibles à 1.2Hz, 2.4Hz et 3.6Hz (fréquence fondamentale et premières harmoniques des stimuli spécifiques visages), reflétant la presence de zones cérébrale répondant spécifiquement aux images de visage. De la même manière, les données SEEG rélèvent des pics de forte amplitude visibles dans une sélection d'électrodes à la fréquence de base de 6Hz, mais aussi à la frequence impaire de 1.2Hz et aux harmoniques pour un sous-groupe d'entre elles. L'inspection des amplitudes et des phases (tracés polaires) de ces pics proéminents sur les capteurs EEG/SEEG montre que les phases varient dans une large gamme (dans l'example présenté dans la thèse, approximativement de 120° à 240°). De telles variations ne peuvent pas être dues uniquement aux artefacts ou aux activités de bruit, étant donné que les magnitudes de ces activités sont beaucoup plus élevées que celles des autres fréquences. De même, l'inspection des capteurs SEEG, non alignés et présentant donc des phases différentes même pour des contacts voisins (distance inter-contact de 3.5mm), suggère que les capteurs correspondants sont impactés par des sources multiples (une seule source proéminente oscillant à 6Hz aurait donné une seule observation de phase, *i.e.* des points quasi-alignés sur le tracé polaire). On peut alors conclure que ces mesures (y compris les SEEG implantés) ont été générées par un mélange de plusieurs sources de même fréquence mais déphasées entre elles. De plus, la visualisation des données EEG/SEEG dans le domaine fréquentiel, c'est-à-dire la présence de pics élevés et bien résolus synchronisés avec les stimuli périodiques, indique que les sources sous-jacentes ont une orientation stable (des sources d'orientation non fixes auraient donné des pics fréquentiels moins bien résolus). Nous supposons donc un modèle de mélange de sources, chacune à orientation fixe. Une procédure de localisation est nécessaire pour distinguer les différentes sources contribuant aux mesures et pour identifier les structures cérébrales activées.

Les hypothèses qui découle de cette analyse sont: (i) Les sources responsables des activités observées sur les capteurs EEG/SEEG pendant le FPVS/FACELOC ont des amplitudes oscillatoires, ayant soit des fréquences uniques spécifiques, soit quelques harmoniques. (ii) Les capteurs peuvent être impactés par des sources mi-distantes à distantes dont les paramètres d'amplitude et d'orientation sont inconnus. Pour cette raison, les positions de l'espace source sont difficiles à restreindre *a priori* et nous considérons alors le cas général où les sources ne sont pas limitées à des régions cérébrales particulières. (iii) Les sources d'intérêt ont des orientations fixes (quoique inconnues), ce qui est une hypothèse largement adoptée dans la littérature sur l'imagerie des sources cérébrales, mais qui trouve une justification supplémentaire dans la visualisation des données EEG/SEEG dans le domaine fréquentiel. Si dans le cas des capteurs EEG, il est raisonnable de contraindre l'orientation des sources comme orthogonale à la surface du cortex, cette hypothèse est plus difficile à formuler dans le cas de la SEEG et dépend de la précision du modèle de tête segmenté. Dans ce qui suit, la localisation des sources en EEG sera effectuée avec des modèles de sources à orientations fixes soit *connus* soit *inconnus*, alors que pour les données SEEG l'orientation de la source sera considérée comme fixe et *inconnu*.

3.2 Formulation et quantification de l'ambiguïté sur les sources oscillatoires à partir des enregistrements (S)EEG

A partir du modèle linéaire $\mathbf{X} = \mathbf{KJ} + \varepsilon$, et en ne considérant que l'ensemble des N_I sources actives parmi N (avec $N_I \ll N$ sous hypothèse de sparsité), nous pouvons redéfinir le modèle des mesures EEG/SEEG comme une somme des contributions de ces N_I sources actives:

$$\mathbf{X} = \sum_{i \in I} \mathbf{K}_i \mathbf{J}_i + \varepsilon \tag{3}$$

où $\mathbf{K}_i$ (M × 3) est le lead-field 3D, $\mathbf{J}_i$ (3 × T) l'orientation et l'amplitude de chaque position de source i et I l'ensemble des sources actives, de cardinal N_I. $\mathbf{J}_i$ peut être représenté plus explicitement par $\mathbf{o}_i$ (3×1) codant l'orientation fixe et $\mathbf{s}_i$ $(1 \times T)$ l'activité temporelle de chaque source i $(\mathbf{J}_i = \mathbf{o}_i \mathbf{s}_i)$. Nous pouvons alors réécrire le melange en considérant le cas particulier où l'activité des sources est sinusoidale à la fréquence des stimuli:

$$\mathbf{x}(t) = \sum_{i \in I} \mathbf{K}_i \mathbf{o}_i d_i \sin(2\pi f_0 t + \varphi_i) + \varepsilon(t) \tag{4}$$

avec une amplitude en d_i, une phase en φ_i, à la fréquence f_0 (fréquence d'intérêt, *e.g.*, du protocole en FPVS), en ne considérant pour l'instant que la fréquence fondamentale de l'activité périodique.

Si l'on considère que l'orientation de la source dans $\mathbf{o}_i$ est connue, on détermine un modèle où chaque couple de $\mathbf{K}_i$ et $\mathbf{o}_i$ sera représenté par un seul vecteur colonne dans $\mathbf{a}_i$ codant la projection de cette source orientée fixe sur les électrodes M.

$$\mathbf{X} = \sum_{i \in I} \mathbf{a}_i \mathbf{s}_i + \varepsilon \tag{5}$$

A nouveau, l'activité de chaque source est écrite comme sinusoïdale:

$$\mathbf{x}(t) = \sum_{i \in I} \mathbf{a}_i d_i \sin(2\pi f_0 t + \varphi_i) + \varepsilon(t) \tag{6}$$

En toute généralité, cette somme de source oscillantes f_0 avec orientation fixe connue peut être réécrite comme une somme de deux sources oscillantes à la même fréquence, à condition que leurs phases (φ_i) soient différents. L'exemple suivant représente ce développement, avec le cas d'une base orthogonale impliquant des sinus et cosinus à phases nulles, avec des coefficients $\mathbf{c}_s$ et $\mathbf{c}_c$ dépendant des phases, amplitudes et gains de propagation des sources originales:

$$\begin{aligned}
\mathbf{x}(t) &= \sum_{i \in I} \mathbf{a}_i d_i \sin(2\pi f_0 t + \varphi_i) \\
&= \sum_{i \in I} (\mathbf{a}_i d_i \cos(\varphi_i) \sin(2\pi f_0 t) + \mathbf{a}_i d_i \sin(\varphi_i) \cos(2\pi f_0 t)) \\
&= \left(\sum_{i \in I} \mathbf{a}_i d_i \cos(\varphi_i) \right) \sin(2\pi f_0 t) + \left(\sum_{i \in I} \mathbf{a}_i d_i \sin(\varphi_i) \right) \cos(2\pi f_0 t) \\
&= \mathbf{c}_s \sin(2\pi f_0 t) + \mathbf{c}_c \cos(2\pi f_0 t)
\end{aligned} \tag{7}$$

La question qui se pose est de savoir si ces coefficients de propagation alternatifs peuvent être assimilés à ceux encodés dans le modèle de tête utilisé, c'est-à-dire s'il existe deux colonnes de la matrice de lead-field fixe connue dans $\mathbf{A}$ (ou deux blocs de trois colonnes de la matrice librement orientée $\mathbf{K}$ en considérant un modèle de source d'orientation inconnu) s'approchant suffisamment des ces collones alternatives $\mathbf{c}_s$ et $\mathbf{c}_c$ pour pouvoir leurrer les algorithmes de localisation. Cette évaluation est effectuée par régression de $\mathbf{c}_s$ et $\mathbf{c}_c$ sur le lead-field fixe $\mathbf{A}$ (ou sur le lead-field librement orienté $\mathbf{K}$). Dans le premier cas, il s'agit de trouver les deux colonnes de $\mathbf{A}$ les plus corrélées avec chacune des colonnes $\mathbf{c}_s$ et $\mathbf{c}_c$ prises séparément, et dans le second cas de trouver les deux sous-espace 3D $\mathbf{K}_i$ sur lesquels chacune des colonnes $\mathbf{c}_s$ et $\mathbf{c}_c$ se projettent maximalement (on parle de corrélation en sous-espace). Les gains des colonnes (ou des combinaisons linéaires de colonne dans le cas 3D) les plus proches des vecteurs de gain $\mathbf{c}_s$ et $\mathbf{c}_c$ sont alors notés $\hat{\mathbf{c}}_s$ et $\hat{\mathbf{c}}_c$ respectivement.

3.3 Résultats des simulations

Pour quantifier cette ambiguïte, nous avons fait la moyenne de 1000 simulations de signaux EEG et SEEG en considérant différents modèles distribués. Nous avons géneré $M = 64$ signaux EEG (montage standard 10-10) en utilisant deux modèles de tête avec différentes résolutions spatiales et différents modèle direct, soit avec des orientations fixes connues (BEM $\mathbf{A} = 64 \times 6184$ et FEM $\mathbf{A} : 64 \times 509$) ou des orientations fixes mais inconnues (BEM $\mathbf{K} = 64 \times (3 \cdot 6184)$ et FEM $\mathbf{K} : 64 \times (3 \cdot 509)$). Les signaux SEEG ont été calculés en utilisant uniquement le second modèle de tête FEM avec des sources fixes à orientation inconnue et en simulant une implantation intra-cérébrale réaliste de $M = 186$ électrodes ($\mathbf{K} = 186 \times (3 \cdot 509)$). Nous avons simulé $N_I = 3, 4, 5$ sources actives parmi les N possibles, à $f_0 = 6$ Hz, positions, amplitudes et phases aléatoires (orientations également pour les cas d'orientation inconnue fixe). Pour toutes ces simulations, nous pouvons obtenir les gains alternatifs $\hat{\mathbf{c}}_s$ et $\hat{\mathbf{c}}_c$ (voir équation 7) que nous cherchons à expliquer à partir des colonnes $\mathbf{a}_i$ (ou des sous-espaces $\mathbf{K}_i$) des modèles distribués employés.

Les résultats ont été regroupés en trois cas :

- Les deux colonnes alternatives $\hat{\mathbf{c}}_s$ et $\hat{\mathbf{c}}_c$ correspondent à des positions identiques ou proches des deux sources simulées (auquel cas la localisation des sources alternatives est équivalent à la localisation de certaines des sources originales),
- l'une des colonnes alternatives correspond à une position d'une des sources originales, tandis que l'autre est éloignée de toutes les sources originales (ce qui équivaut, en termes de résultats de localisation, à une fausse détection),
- les deux colonnes alternatives correspondent à des fausses détections.

Notez que par positions *proches* nous désignons dans ce travail une position alternative à moins de 1cm de l'une des vraies positions originales (vrai positif).

Pour chacun de ces trois cas, nous avons calculé l'adéquation des données reconstruites par rapport aux mesures simulées (métrique du GOF) des données reconstruites ($\hat{\mathbf{X}}$) à partir dee estimées obtenues $\hat{\mathbf{c}}_s$ et $\hat{\mathbf{c}}_c$, ainsi que les sinus et cosinus respectifs, par rapport aux données simulées $\mathbf{X}$ (résultant d'un mélange de N_I sources actives):

$$\mathrm{GOF} = 1 - \left(\frac{\|\mathbf{X} - \hat{\mathbf{X}}\|}{\|\mathbf{X}\|} \right)^2 \tag{8}$$

Les résultats indiquent que, dans la plupart des cas, les colonnes de lead-field les mieux ajustées avec les colonnes alternatives $\hat{\mathbf{c}}_s$ et $\hat{\mathbf{c}}_c$ ont des positions éloignées ($>$ 1cm) des véritables sources, même si les données alternatives reconstruites $\hat{\mathbf{X}}$ sont très similaires à celles simulées (le GOF reste élevé, supérieur à 0.8 à 0.9 en médiane). En situation réelle, il serait alors difficile de distinguer les erreurs dues au bruit ou aux incertitudes du modèle de celles dues à l'estimation des configurations alternatives. Cela est particulièrement vrai pour l'EEG (voir figure 3.3), notamment lorsque l'orientation est inconnue, donc estimée à l'aide d'un modèle de lead-field 3D (car il implique plus de degrés de liberté). Pour le SEEG (voir figure 3.4), avec un modèle à orientation libre, l'ambiguïté est réduite car le nombre d'électrodes est plus élevé mais aussi plus proche des sources. Lorsque le nombre d'électrodes est réduit sur le SEEG pour être comparable à celui de l'EEG, l'ambiguïté augmente mais reste inférieure à celle observée sur l'EEG (cas librement orienté), très probablement en raison de la proximité des capteurs par rapport aux sources.

Chapitre 4: Localisation des sources oscillantes. Orientation fixe connue

Nous nous proposons dans cette thèse d'appliquer deux algorithmes de Matching Pursuit de la littérature au problème de la localisation de sources dans le cadre d'activités oscillatoires: les algorithmes Orthogonal Least Square (OLS) et Single Best Replacement (SBR). Dans ce chapitre, nous considérons des mesures de type EEG dans le cas de sources à orientations connus (lead-field $\mathbf{A}$), et nous montrons que l'adaptation de ces méthodes à ce problème particulier est immédiat. Ces méthodes sont appliquées et comparées dans les domaines temporels et fréquentiels. Leurs performances sont également comparées à deux approches connues dans le domaine de la localisation de sources cérébrales, à savoir Recursively Applied and Projected (RAP-MUSIC) and Truncated RAP (TRAP-MUSIC).

4.1 Méthodologie

Le prétraitement des données est classique et implique, dans le domaine temporel, un filtrage passe-bande autour des fréquences d'intérêt et le calcul de la moyenne sur la durée de la période de T_0 du protocole (données moyennées notées $\mathbf{X}_{T_0} \in \mathbb{R}^{M \times T_0}$). Dans le domaine fréquentiel, une transformée de Fourier est appliquée aux données, dans laquelle est sélectionné le pic fréquentiel d'intérêt (f_0) ainsi que d'éventuelles harmoniques (on notera N_h le nombre de pics sélectionnés, et $\mathbf{X}_{f_0} \in \mathbb{R}^{M \times 2N_h}$ les données en fréquence). L'avantage en fréquence est que le SNR est plus élevé; en revanche l'écueil est que le nombre de points de données devient très faible ($2N_h$ en considérant les parties réelles et imaginaires de chaque pic), ce qui devient problématique pour le conditionnement du problème de localisation.

La solution OLS (Orthogonal Least Squares) vise à trouver un ensemble de cardinal minimal de sources tout en assurant une reconstruction suffisamment précise des données, c'est-à-dire en obtenant un GOF de la reconstruction supérieur à un paramètre donné du GOF attendu (expGOF) défini par l'utilisateur. Il s'agit d'un algorithme itératif dans lequel, à chaque itération, une nouvelle source est ajoutée, mais toutes les amplitudes des sources déjà sélectionnées dans $\mathbf{s}_i$ sont réestimées. L'erreur de reconstruction diminue à chaque itération (le GOF augmente à chaque itération), d'où le critère d'arrêt pour le problème de minimisation suivant :

$$\{\hat{\mathbf{S}}, \hat{I}\} = \underset{\mathbf{S},I}{\operatorname{argmin}}\,(N_I), \quad u.c. \quad \text{GOF}>\text{expGOF}, \tag{9}$$

Une autre stratégie de sélection appliquant la sparsité est l'approche SBR (Single Best Replacement), où l'ajout d'une source à chaque itération est pénalisé par un facteur noté λ. De plus, dans cette approche, contrairement à la méthode OLS, des sources peuvent être ajoutées ou retirées de l'ensemble des sources déjà sélectionnées à chaque itération, ce qui permet à l'algorithme d'écarter les sources erronées choisies lors des itérations précédentes. Le problème de minimisation s'écrit comme suit :

$$\hat{\mathbf{S}}, \hat{I} = \underset{\mathbf{S},I}{\operatorname{argmin}} \left(\|\mathbf{X} - \mathbf{A}_I \mathbf{S}_I\|_2^2 + \lambda N_I \right), \tag{10}$$

et elle est résolue par régression pas-à-pas comme pour la méthode OLS, où est évalué à chaque itération la fonction de coût lors de l'ajout d'une source, mais aussi du retrait d'une des sources parmi celles déjà sélectionnées.

4.2 Résultats

Pour déterminer les performances des approches en matière de localisation de la source, nous avons calculé la moyenne de 100 simulations de signaux EEG calculés à l'aide de deux lead-field (les mêmes que ceux décrits dans le chapitre précédent) : $\mathbf{A}$ = 64 × 6184 et $\mathbf{A}$ = 64 × 509, à partir d'un modèle de source à orientation fixe connue.

Les méthodes SBR, OLS et RAP/TRAP MUSIC ont été évaluées à la fois dans le domaine temporel et fréquentiel (c'est-à-dire sur $\mathbf{X}_{T_0}$ ou sur $\mathbf{X}_{f_0}$), en faisant varier le nombre de sources ($N_I = 3, 4, 5, 7$) ainsi que le rapport signal-bruit (SNR: 40dB, 20dB, 10dB, 3dB, 0dB, -3dB, -10dB), et en considérant soit des pics de fréquence uniques à $f_0 = 6$Hz, soit plusieurs harmoniques, $N_h = 4 : \{6, 12, 18, 24\}$Hz.

La principale conclusion de ces simulations (basée sur la lead-field avec 6184 positions de sources) est que de meilleurs résultats sont obtenus dans le domaine des fréquences par les méthodes OLS et SBR, car le fait de se concentrer sur les pics de fréquence de l'activité à localiser fournit un meilleur rapport signal-bruit (avec toutefois une meilleure précision pour la méthode SBR que pour OLS, car SBR est capable d'éliminer les sources faussement détectées d'une itération à l'autre). La robustesse au bruit est en effet remarquable puisque les performances restent stables même lorsque le bruit additif est augmenté à un niveau élevé allant jusqu'à $-10db$. Comme attendu, lorsque les harmoniques sont également disponibles pour la localisation, les performances augmentent également, car plus d'informations sont utilisées pour la localisation.

Les conclusions sont différentes en ce qui concerne les méthodes MUSIC. Ces approches nécessitent une estimation du sous-espace du signal à l'initialisation, qui est intrinsèquement limitée à deux dimensions lorsque des sources oscillatoires à fréquence unique sont considérées (dans le cas d'un faible bruit). Logiquement, ces méthodes échouent face à de telles données. Lorsque des harmoniques sont prises en compte, l'utilisation des algorithmes MUSIC devient plus pertinente, en particulier dans le domaine temporel où le nombre de points de données permet de mieux estimer la dimension de l'espace source ainsi que les vecteurs de base de l'espace source. Les performances de RAP et TRAP MUSIC deviennent alors comparable aux méthodes OLS et SBR. Néanmois, pour des configurations peu denses (peu de sources) et avec des niveaux de bruit élevés, la SBR en fréquence surpasse MUSIC (quel que soit le domaine), alors que pour un SBR élevé et des configurations moins denses, les performances sont meilleures pour les versions temporelles de MUSIC que celles des méthodes OLS et SBR (quel que soit le domaine).

Nous avons également évalué les méthodes de localisation de sources avec un lead-field plus clairsemé encodant les projections de 509 sources. Les résultats des deux champs de référence indiquent des performances similaires des méthodes de localisation en fonction du nombre de sources simulées et des SNRs. Les résultats obtenus avec 509 positions de sources et des sources à fréquence unique montrent également que SBR dans le domaine de fréquence est globalement plus performante que les autres méthodes, avec de meilleurs résultats pour la reconstruction des sources cibles et moins de fausses sources. Une fois de plus, une plus grande robustesse est obtenue dans le domaine des fréquences face à l'effet d'un bruit important. Il est intéressant de noter que les performances semblent être légèrement meilleures pour ce lead-field plus clairsemé, pour le même nombre de sources et les mêmes niveaux de bruit.

En utilisant plusieurs harmoniques, les méthodes RAP/TRAP MUSIC s'améliorent considérablement et deviennent plus compétitives, voire même dépasse les méthodes SBR et OLS, bien que de maniére moins évidente que pour le lead-field plus dense (6184 sources). Une fois encore, SBR dans le domaine fréquentiel semble être un bon algorithme candidat pour la localisation de sources parcimonieuses, avec un clair avantage pour les sources à fréquence unique et des performances compétitives pour les sources harmoniques multiples (les résultats sont illustrés dans les figures 4.1, 4.2, 4.3 et 4.4).)

Nous avons également testé les résultats de chaque algorithme de localisation de source sur des données réelles enregistrées pendant le protocole FPVS, en les appliquant à la fois dans les domaines temporel et fréquentiel. Les résultats montrent des disparités assez importantes entre les résultats de chaque algorithme, en particulier lorsque l'on compare les algorithmes OLS et SBR aux les algorithmes RAP/TRAP MUSIC (les résultats sont illustrés dans les figures 4.6, 4.7, 4.8 et 4.9), et ces performances restent à être évaluées et validées sur davantage de données.

Chapitre 5: Localisation des sources oscillantes. Orientation fixe inconnue

Dans ce chapitre, nous présentons de nouvelles méthodes qui étendent les résultats du chapitre précédent aux cas de sources dont l'orientation est fixe mais inconnue. En plus de l'EEG, nous considérons également les mesures SEEG pour lesquels il est difficile de fixer l'orientation des sources au préalable. Les algorithmes MUSIC classiques sont conçus pour estimer à la fois les amplitudes et les orientations des sources. Cependant, lorsque l'orientation fixe mais inconnue doit être estimée pour chaque position de source candidate, les méthodes SBR et OLS de régression itérative doivent être repensées. Nous proposons donc ici une nouvelle version de l'algorithme OLS, dans laquelle une approche parcimonieuse par bloc est introduite, basé sur une contraite de rang 1 par sous espace 3D. Cette procédure a égalment été adoptée pour adapter l'algorithme SBR, dans lequel l'ensemble de sources sélectionnées est réexaminé à chaque itération, soit en supprimant une source, soit en ajoutant une nouvelle source.

5.1 Modèle

L'estimation conjointe de l'orientation $\mathbf{o}_i$ et $\mathbf{s}_i$ est équivalente à l'estimation d'une matrice J_i^1 de rang 1, représentant le moment dipolaire variable dans le temps d'une source á orientation fixe ($\mathbf{o}_i\mathbf{s}_i = \mathbf{J}_i^1$). Le modèle des données s'écrit :

$$\mathbf{X} = \sum_{i \in I} \mathbf{K}_i \mathbf{J}_i^1 + \varepsilon$$

Une autre formulation possible du modèle est l'utilisation d'une matrice diagonale $\mathbf{O}_I$, telle que:

$$\mathbf{X} = \mathbf{K}_I \begin{bmatrix} \mathbf{o}_1 & 0 & \dots & 0 \\ 0 & \mathbf{o}_2 & \dots & 0 \\ \dots & \dots & \dots & \dots \\ 0 & \dots & 0 & \mathbf{o}_{N_I} \end{bmatrix} \begin{bmatrix} \mathbf{s}_1 \\ \mathbf{s}_2 \\ \vdots \\ \mathbf{s}_{N_I} \end{bmatrix} = \mathbf{K}_I \underbrace{\mathbf{O}_I \mathbf{S}_I}_{\mathbf{J}_I^1}$$

Nous reformulons les problèmes de minimisation en OLS et SBR en introduisant la contrainte de rang 1 (ou, de manière équivalente, la matrice diagonale $\mathbf{O}_I$) :

OLS-R1:

$$\min\left(\|\hat{I}\|_0\right) \text{ u.c. } \begin{cases} \|\mathbf{X} - \sum_{i\in\hat{I}} \mathbf{K}_i \hat{\mathbf{J}}_i\|_2 < \varepsilon \\ \text{rank}(\hat{\mathbf{J}}_i) = 1 \end{cases}$$

SBR-R1:

$$\{\hat{I}, \hat{\mathbf{O}}_{\hat{I}}, \hat{\mathbf{S}}_{\hat{I}}\} = \underset{I,\mathbf{O}_I,\mathbf{S}_I}{\text{argmin}}(\|\mathbf{X} - \mathbf{K}_I \mathbf{O}_I \mathbf{S}_I\|_2^2 + \lambda \|I\|_0)$$

Nous nous concentrons sur la description OLS-R1, car l'étape SBR, dans sa forme de base (non pas la formulation informatique de Soussen et al. [2011]) consiste uniquement à réévaluer à chaque itération, la contribution individuelle de chaque source déjà sélectionnée. En effet, l'algorithme OLS ajoute une nouvelle source à chaque itération, il évalue également l'avantage de retirer l'une des sources précédemment sélectionnées.

Une première observation que nous pouvons faire est que le problème d'estimation est séparable.

Ainsi, pour toute matrice d'orientation donnée $\hat{\mathbf{O}}_{\hat{I}}$, la solution optimale de l'amplitude de la source pour $\mathbf{S}_{\hat{I}}$ est : $\hat{\mathbf{S}}_{\hat{I}} = (\mathbf{K}_{\hat{I}} \hat{\mathbf{O}}_{\hat{I}})^{+}\mathbf{X}$, qui peut être trouvée directement par régression (moindres carrés). Le problème clé est donc l'estimation du support $\hat{I}$ et des orientations $\hat{\mathbf{o}}_i \rightarrow \hat{\mathbf{O}}_{\hat{I}}$.

Nous proposons une approche sous-optimale mais toujours monotone, décrite dans les étapes suivantes :

1. Nous calculons à chaque itération une solution classique de OLS (moindres carrés) sans imposer la contrainte de rang 1 des moments dipolaires $\mathbf{J}_i$. Tous les $\mathbf{J}_i$ des sources précédemment sélectionnés sont recalculés à chaque itération et l'erreur de reconstruction diminue avec chaque nouvelle source ajoutée à l'ensemble des solutions (l'erreur $\|\mathbf{X} - \hat{\mathbf{X}}\|$ diminue).

2. Ensuite, nous prenons chaque $\mathbf{J}_i$ sans contrainte et nous calculons sa décomposition SVD : $\tilde{\mathbf{J}}_i = \mathbf{U}_i \Sigma_i \mathbf{W}_i^T$ et son approximation de rang 1 la plus proche $\tilde{\mathbf{J}}_i^1$:

   $$\tilde{\mathbf{J}}_i^1 = \mathbf{u}_{i,1} \sigma_{i,1} \mathbf{w}_{i,1}^T$$

   Si nous utilisons cette approximation de rang 1 pour reconstruire les données, l'erreur augmentera par rapport à celle de l'étape précédente (en utilisant le rang 3 $\tilde{\mathbf{J}}_{\hat{I}}$).

3. Nous pouvons réduire cette augmentation de l'erreur en ne prenant que les vecteurs singuliers de gauche $\mathbf{u}_{i,1}$ ($\hat{\mathbf{o}}_i = \mathbf{u}_{i,1}$) et en les utilisant pour fixer les orientations dans la matrice bloc-diagonale $\hat{\mathbf{O}}_{\hat{I}_p}$:

   $$\hat{\mathbf{O}}_{\hat{I}} = \begin{bmatrix} \mathbf{u}_{1,1} & 0 & \dots & 0 \\ 0 & \mathbf{u}_{2,1} & \dots & 0 \\ \dots & \dots & \dots & \dots \\ 0 & \dots & 0 & \mathbf{u}_{N_I,1} \end{bmatrix}$$

   puis calculer les amplitudes $\mathbf{s}_i$ comme mentionné précédemment par moindres carrés et enfin obtenir une estimation des mesures. A chaque itŕation donc on aura:

$$\hat{\mathbf{S}}_{\hat{I}} = (\mathbf{K}_{\hat{I}}\hat{\mathbf{O}}_{\hat{I}})^{+}\mathbf{X}, \text{ puis } \hat{\mathbf{J}}_{\hat{I}} = \hat{\mathbf{O}}_{\hat{I}}\hat{\mathbf{S}}_{\hat{I}} \text{ et } \hat{\mathbf{X}} = \mathbf{K}_{\hat{I}}\hat{\mathbf{J}}_{\hat{I}}$$

En d'autres termes, à ce stade, nous avons une solution qui respecte notre contrainte de rang 1 et, pour les orientations sélectionnées $\hat{\mathbf{O}}_{\hat{I}}$ (éventuellement sous-optimales), nous avons les amplitudes optimales $\hat{\mathbf{S}}_{\hat{I}}$.

4. Même si l'étape précédente d'estimation de l'amplitude de la source est optimale, l'étape d'approximation SVD (Singular Value Decomposition) conduit à une augmentation possible de l'erreur entre deux itérations. Mais à chaque itération, nous pouvons également choisir la nouvelle source à ajouter sans réestimer l'orientation des sources précédemment sélectionnées. Cette version de l'algorithme est sûrement monotone, car elle ne fait qu'ajouter un nouveau régresseur aux régresseurs sélectionnés précédemment. Nous pouvons alors l'utiliser pour borner supŕieurement l'erreur dans les itérations OLS-R1 décrite ci-dessus et assurer ainsi la monotonie et donc la convergence de l'algorithme.

5.2 Résultats

Pour déterminer les performances des solutions proposées en matière de localisation des sources, nous avons calculé la moyenne de 100 simulations, en utilisant des signaux EEG et SEEG calculés avec le lead-field, FEM $\mathbf{K} : 64 \times (3 \cdot 509)$. Les méthodes OLS-R1, SBR-R1 et RAP/TRAP MUSIC ont été évaluées à la fois dans le domaine temporel et dans le domaine fréquentiel, en faisant varier le nombre de sources ($N_I = 3, 4, 5, 7$), ainsi que le rapport signal-bruit (SNR : 40dB, 20dB, 10dB, 3dB, 0dB, -3dB, -10dB), et en considérant un pic de fréquence unique à $f_0 = 6$Hz, ainsi que des harmoniques $N_h = 4 : \{6, 12, 18, 24\}$Hz.

Globalement, on peut tirer les mêmes conclusions qu'au chapitre 4 en ce qui concerne les méthodes de régression itératives, en considérant les versions de rang un (des sources orientées connues fixes) et bloc (des sources orientées inconnues fixes) des algorithmes OLS et SBR. Par rapport au modèle avec des sources orientées connues fixes, les performances diminuent, car le modèle avec des sources orientées inconnues fixes offre plus de degrés de liberté et renforce le problème d'ambiguïté tel qu'il a été formulé au chapitre 3. D'autre part, les solutions sont plus éparses, ce qui se traduit par une meilleure précision dans la reconstruction des vraies sources. Également, comme indiqué au chapitre 3, l'implantation particulière des électrodes SEEG plus près des sources semble guider le problème et conduire à de meilleurs résultats. Ce n'est cependant pas le cas lorsque les algorithmes MUSIC sont confrontés à des données SEEG, car les méthodes statistiques semblent échouer dans l'estimation de l'espace source adéquat, très probablement parce que cette configuration ne couvre pas bien l'espace des sources et que les sources proches des électrodes ont tendance à masquer les activités de celles qui sont plus éloignées. En ce qui concerne l'enrichissement de la localisation par des harmoniques, les performances sont globalement meilleures pour tous les algorithmes, comme cela a déjà été observé dans le chapitre précédent (les résultats sont illustrés dans les figures 5.1, 5.2, 5.3 et 5.4).

Comme au chapitre 4, quelques exemples de localisation en temps et en fréquence sur des EEG réels sont présentés et, dans ce chapitre, également sur des données SEEG enregistrées pendant le protocole FPVS. Ils ont été inclus principalement à des fins d'illustration. Comme au chapitre 4, ils sont toujours cohérents avec les connaissances neuroscientifiques actuelles sur les régions activées pendant les protocoles de reconnaissance des visages. En conclusion, ces résultats doivent clairement être confirmés sur un plus grand nombre de données permettant d'évaluer une certaine signification statistique.

Introduction

Human face perception is arguably the most important visual function for human social communication. Studying the neural basis of this function is of first importance, starting by identifying the involved neural structures and understanding their specific role. Recent developments have led to quantitative identification of responsive structures to face stimuli in the ventral visual stream. A specific region of the fusiform gyrus, the FFA (fusiform face area), consistently elicits higher response to face stimuli than other regions, making it a central structure for face recognition [Kanwisher et al., 1997; Jonas et al., 2016]. However, it has been demonstrated that the involvement of this area is not sufficient and, depending on the recognition task, the recruitment of other regions in the occipito-temporal cortex is required. While it is now widely accepted that face recognition is characterized by an activation within multiple areas comprising a network [Ishai et al., 2005; Ishai, 2008], this network still remains largely unknown.

In the context of face brain recognition, specific protocols have been developed based on fast periodic visual stimulation (FPVS): the human brain is stimulated at a specific (fast) periodic rate, giving rise to periodic activities within the brain areas involved in the cognitive process targeted by the protocol. These periodic activities may be nearly purely oscillatory, or may involve few significant harmonics beside the fundamental frequency of the stimulation, resulting in narrow band activities concentrated on one or few frequency points. These electrophysiological signals are captured on the EEG and Stereo-EEG (SEEG) measurements, providing temporal resolution of the order of the millisecond, thus recording the brain activity at the temporal scale of the studied phenomena. These modalities hence allow to measure and quantify directly the strength of the brain responses in the frequency domain. Such methodology has led to direct proofs of the involvement of brain areas in the occipito-temporal visual pathways in response to face stimuli, confirming previous studies carried out with fMRI [Rossion et al., 2015; Jonas et al., 2016]. In particular, the key role of the FFA has been confirmed, and activations of previously overlooked regions in the anterior temporal lobe have been revealed.

These studies use SEEG recordings as gold standard. The analysis is carried out based on bipolar montage, *i.e.*, considering the difference between neighbouring measurements on the SEEG sensors, thus providing a local view of the activity. Thus, the position of the neighboring sensors recording the activity of interest is considered as the position of the source of this activity. Following previous studies in the research team [Caune et al., 2014; Le Cam et al., 2017], we argue that (i) on the bipolar montage, by restricting the SEEG to a local view of the brain activity, is likely to miss other activities of interest originating from distant structures, and that (ii) SEEG measurements on common montage are still a mixing of brain source activities, supporting the use of localization algorithm for this setup. SEEG has the advantage to provide high SNR measurements of the brain activity, as the sensors are closer to the source and as the skull and skin propagation barriers are avoided. When it comes to EEG, the use of localization step is required to distinguish between the measurement contributors and to identify the corresponding brain structures. However, the signal has to travel from the brain generators to the sensors through the skin and skull barrier, yielding signals with poor signal to noise ratio, making the reconstruction of the source a particularly challenging task.

The resolution of the brain source inverse problem is known to be severely ill-posed. This thesis work proposes to analyze and evaluate the application of brain source localization methods to solve this inverse problem in this context of periodic/oscillatory sources, using either EEG or SEEG data. We provide evidence that the resolution becomes even more ill-posed when such narrow band activities are to be localized, and we propose several methods relying on the sparsity of the solution (in term of number of reconstructed sources) as a regularization constraint. The rationale for the sparsity underlying hypothesis is that few responsive structures are expected at the specific stimulation frequencies. The localization will be carried out in the time domain after averaging of the signal epochs over the period of the stimulation, thus enhancing the signal to noise ratio. As the stimuli is well localized in the time-frequency plane, we also propose to carry out the localization directly in the frequency domain, requiring to adapt the localization methods and to analyze the behavior of the algorithms when facing with such data. In the following, we provide a brief overview of each of the five chapters composing this manuscript.

Chapter 1 begins by providing a general introduction of the brain anatomy, describing the main brain structures and the functional organization of cortical areas. An overview of the brain electrophysiology is then presented, starting from the structure of the neuron and the activity as produced by large assemblies of neurons, giving rise to the electromagnetic activity recorded by S(EEG) measurements. We also describe the main anatomical and electrophysiological neuroimaging modalities to explore the brain, with a particular insight in electrophysiological recordings (scalp and intracranial EEG), pointing out the interest to address source localization task based on these modalities. We finally focus on (S)EEG data recorded under cognitive protocols, in particular during fast periodic visual stimulation (FPVS) applied to face recognition, who generate oscillating activities at the period of the stimulation in specific brain areas involved in the image / face recognition process.

Chapter 2 presents a state-of-the-art of the main approaches to solve the brain source localization problem. First, analytical and numerical propagation (lead-field) models are described. Then, an overview of different approaches to regularize the inverse problem in brain source localization is given, with a focus on the under-determined problem, where the number of dipole candidates encoded in the lead-field is far higher than the number of measurements. Given the targeted application of this thesis (face recognition/FPVS), we formulate the reasonable hypothesis that few regions are involved in the recognition process, and we explore in more details methods based on scanning and matching pursuit approaches enforcing the sparsity of the solutions. We also describe the preprocessing strategies applied to real signals, involving signal denoising and data transformation in the frequency domain.

Chapter 3 deals with the difficulty to localize multiple sources oscillating at the same frequency. Based on the analysis of FPVS recordings, the oscillatory nature of the recorded signal is illustrated, and the hypothesis of considering fix oriented dipolar sources is justified. We then put forward the fact that a large number of alternative source configurations are likely to explain the measurements, and to mislead the localization methods. This ambiguity is theoretically formalized, and analyzed based on EEG as well as SEEG simulations. The first version of the results presented in this chapter was published in [Hernandez *et al.*, 2022].

Chapter 4 proposes to analyze the problem in the specific context of EEG measurements. In this chapter, the orientation of each dipole is assumed to be fixed and known, *i.e.*, orthogonal to the cortex surface. The methods considered are either based on MUSIC approaches, namely RAP-MUSIC and TRAP-MUSIC, or greedy based Matching Pursuit algorithms as Orthogonal Least Squares (OLS) or its forward-backward extension Single Best Replacement (SBR). The performance of the algorithms is evaluated and compared to the literature using EEG simulated data, reproducing realistic recordings in the context of FPVS. In particular, the advantage of reconstructing sources in the frequency domain against the time domain is quantified in a realistic setup. Finally, the results of the methods are illustrated on real EEG signals recorded under a FPVS protocol (FACELOC). The work presented in this chapter was partly published in [Hernandez *et al.*, 2021].

In **Chapter 5**, we relax the known orientation constrain used in the previous chapter. Unlike the classical OLS/SBR used in the previous chapter, the elements of the dictionary are not vectors anymore, but 3D matrices allowing free oriented dipoles for each location. In order to fulfill the fix oriented dipole constraint, the vectorial regression coefficients representing time varying amplitudes of the source are constrained to unit rank, and a selection procedure to adapt OLS/SBR to this rank one block regression problem is proposed. The convergence properties of these new algorithms are analyzed, and their performance are evaluated on simulated data in the context of EEG as well as of SEEG measurements, both in time and frequency domain. The methods are then applied to the same EEG data set as the one used in the previous chapter, but also to an example of real SEEG data recorded under the same FACELOC protocol.

Finally, in the **conclusion** of this manuscript, we summarize the contributions and findings of this thesis when addressing the problem of oscillatory source localization from scalp and intracranial EEG recordings for specific cognitive tasks, as tested using FPVS protocol. We also suggest in the perspectives future works in this field.

Chapter 1

Electrophysiology of the Human Brain

1.1 Introduction

In this chapter is presented an introduction to the brain anatomy, the generation of the electromagnetic activity and the neuroimaging modalities to explore the brain. In Section 1.2.1, the brain structures are presented, describing the main brain parts, and particularly the functional organization of cortical areas. In Section 1.2.3, an overview of the brain electrophysiology is given, describing the structure of the neuron and then the interconnection between them, giving rise to the electromagnetic field that can be recorded by electrophysiological measurements. We describe in Section 1.3 the main anatomical and functional neuroimaging modalities, emphasizing those modalities having high temporal resolution and providing an important insight in the study of the electrical fields generated by neuronal activity in the brain, such is the case of the electroencephalography. We detail both scalp and intracranial electroencephalography since these modalities have been the subject of this thesis to state and address the source localization problem. Finally, Section 1.4 overviews relevant applications based on surface and intracerebral EEG data analysis and the clinical context of intracranial recordings. We emphasize the importance of cognitive protocols, in particular in the periodic stimulation as observed in the fast periodic visual stimulation (FPVS) protocol, for which we are focused to solve the source localization problem.

1.2 Introduction to the brain

1.2.1 Brain anatomy

The nervous system is divided into two main parts, the central nervous system (CNS) and the peripheral nervous system (PNS). The CNS, made up of the brain and spinal cord, is the processing centre of the body, and the PNS, which encompasses nerves outside the brain and spinal cord, forms the communication network between the CNS and the body parts.

The brain can be divided in three parts: the *cerebellum*, the *brainstem* and the *cerebrum* (see Figure 1.1). The brain lies in the cranial cavity and is protected by the scalp, the skull and the cerebrospinal fluid (CSF).

The *cerebellum* is located underneath the cerebrum in the posterior cranial fossa and lies posterior to the fourth ventricle, pons, and the *medulla oblongata*. It consists of two cerebellar hemispheres joined by a narrow *median vermis*. It receives afferent information concerning voluntary movements from the cerebral cortex and also from muscles, tendons, and joints. Cerebellar output is conducted to the sites that influence motor activity at the segmental spinal level. The cerebellum functions as a coordinator for precise voluntary movement, which requires a continuous balance between output from the cerebral motor cortex and feedback of proprioceptive information from the muscles. This then allows the degree of muscle contraction necessary for a precise voluntary movement to be adjusted.

The *brainstem* lies between the brain and spinal cord and acts as a relay with the spinal cord. It maintains vital body functions such as breathing and heart rate control.

The *cerebrum* is the largest part of the brain. It consists of two cerebral hemispheres, which are connected by a mass of white matter called the *corpus callosum* and are responsible for high level perceptive and cognitive functions. The outer part of the *cerebrum* is the cerebral cortex (2 to 4 mm thick) with multiple folds. Several large fissures separate the lateral surface of the cerebral cortex into four major lobes: frontal lobe, parietal lobe, temporal lobe and occipital lobe. The frontal lobe is separated from the parietal lobe by a space called the *central sulcus*, and from the temporal lobe by the *lateral sulcus*. It is generally where higher executive functions including emotional regulation, planning, reasoning and problem solving occur. The parietal lobe is behind the frontal lobe, separated by the central sulcus. Regions in the parietal lobe are responsible for motor activity, integrating sensory information, including touch, temperature, pressure and pain. The temporal lobe, separated from the frontal lobe by the lateral fissure, contains regions dedicated to processing sensory information, particularly important for hearing, recognising language, and forming memories. The temporal lobe contains the primary auditory cortex, which receives auditory information from the ears and secondary regions, and processes the information, so we understand what we are hearing *e.g.*, words, laughing, a baby crying. Certain regions in the temporal lobe make sense of complex visual information including faces and scenes. The medial (closer to the middle of the brain) temporal lobe contains the hippocampus, a region of the brain important for memory, learning and emotions. The occipital lobe is the major visual processing centre in the brain. The primary visual cortex receives visual information from the eyes, this information is relayed to several secondary visual processing areas, which interpret depth, distance, location and the identity of seen objects.

1.2.2 The cerebral cortex

The cerebral cortex is the outermost layer of the brain that is associated with higher cognitive abilities. It is primarily constructed of gray matter and its most profound tissue consists of nerves fibers, the so-called white matter, which establish connections between distant areas. It is estimated that in the gray matter reside 16.34 ± 2.17 billion of neurons, representing the 19% of all brain neurons [Azevedo et al., 2009], while white matter is mostly composed of the neuron's axons [Kandel et al., 2000]. The over simplified common view is that the gray matter is where most of the brain activity occurs, while the white matter is responsible of the communication between brain areas.

The cerebral cortex has a wrinkled appearance, consisting of bulges, also known as gyri, and deep furrows, known as sulci. The superficial layers mainly consists of glial cells, extensions of apical dendrites of pyramidal neurons and horizontally oriented axons. The simultaneous activations

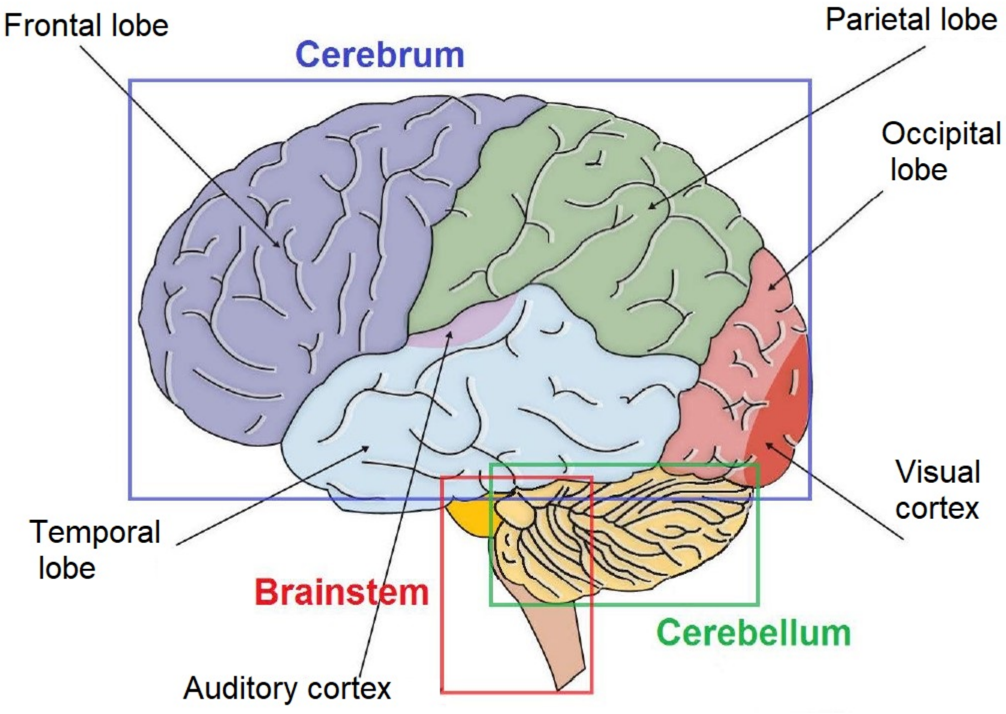

FIGURE 1.1 – Humain brain areas. The three main parts: Cerebrum, cerebellum and brainstem. Four major lobes representing the cerebral cortex in the cerebrum area: frontal, parietal, occipital, temporal [Caune, 2017]

of these pyramidal neurons are at the root of the observable electromagnetic activity.

Interconnections span the whole cortex thickness, yielding connections locally among the layers, forming cortical microcircuits called cortical columns and minicolumns. It has been established that the functional activity of the brain is homogeneous within columns, while abrupt changes are observed in population of close columns [Mountcastle, 1997]. However, the functional organization of the brain is to be observed at a wider scale. Connections between distant cortical and sub-cortical regions are established through the white matter. Indeed, these sub-cortical structures are involved in the processing of specific tasks, often handled collaboratively and their roles can be different from one hemisphere to the other.

Next, the functional organization of the brain is described. Cortical areas related to three subgroups of functions can be distinguished.

- The **sensory** areas are those that receive sensory input from the thalamus, they are the primary visual and auditory cortex and the primary somatosensory cortex which are responsible, respectively, of the vision, the audition and the touch. It has been established that the right hemisphere handles the sensory stimuli of the left side of the body and the left hemisphere of the right side of the body.
- The **motor** areas are responsible for the planning, control and execution of voluntary mo-

vements. These areas are located in both hemispheres withing the frontal lobe. The main structures are the primary motor cortex, the premotor cortex, the supplementary motor area and the basal ganglia.

— The **association** areas are related to our perception of the world, to movement planning, to our ability of memorizing, abstract thinking and language learning. The associated areas are the prefrontal, the inferior temporal and the parietal-temporal-occipital.

1.2.3 Neurons and synapses

1.2.3.1 The neuron

A neuron is a nerve cell. It is estimated that the human brain possesses about 86.06 ± 8.12 billion neurons [Azevedo et al., 2009]. Three main parts characterized a typical neuron.

The cell body, called *soma*, which contains the nucleus, the *axon*, which transmits information to different connected neurons and the *dendrites*, which receive stimuli from thousands of other afferent cells. (see Figure 1.2).

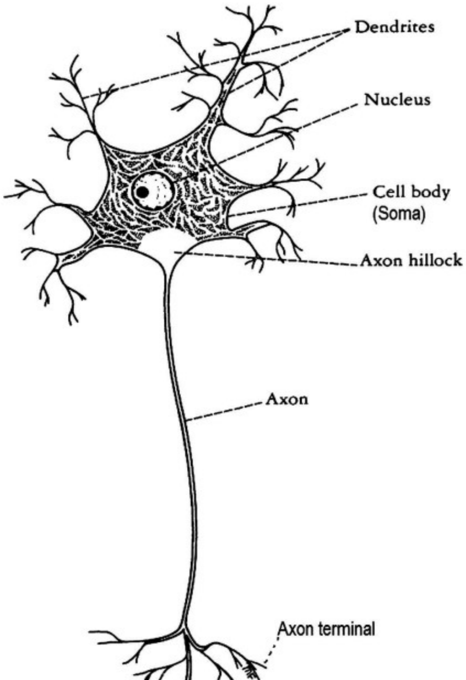

FIGURE 1.2 – Cellular structure of a neuron [Yamada and Meng, 2012].

Neurons are not all the same. It is still complex to determine between types. It is distinguished different types of neurons from the shape of their cell body: star-shaped, fusiform, conical, polyhedral, spherical and pyramidal. These shapes and the number and size of dendrites are related to the specific functions of the neurons. In this thesis, we will focused on the activity of the pyramidal neurons which are responsible of most of the measured electromagnetic activity (see Subsection 1.3.3.1).

The final communication between neurons occurs at specialized anatomical structure called the *synapse*. This communication may occur from axon to dendrite, axon to soma, or axon to axon (see Figure 1.3)

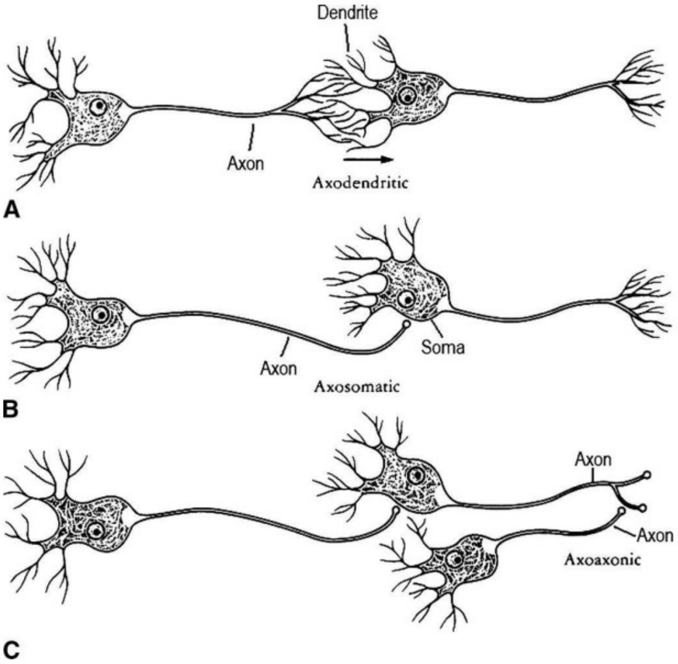

FIGURE 1.3 – Synaptic connections between two neurons. A) Axon to dendrite. B) Axon to soma. C) Axon to axon [Yamada and Meng, 2012].

1.2.3.2 The synapse

The synapse is the anatomical structure where the signals (electric impulse) from one cell is transmitted to another cell; the action potential traveling through the axon reaches the axon terminal as a presynaptic potential. The axon terminal is separated from the surface of the soma or dendrites of another cell (postsynaptic neuron) by a narrow surface (about 2nm) called the synaptic cleft. The electrical signal reaching the presynaptic terminal is transmitted to the postsynaptic neurons as a postsynaptic potential (PSP) by chemical transmission at the synaptic cleft.

The PSP is a graded potential with inhibitory and excitatory changes. An inhibitory PSP (IPSP) is an increase (hyperpolarization) in negative charge on the inside of the neuron which inhibits the neuron from firing an impulse. An excitatory PSP (EPSP) is a decrease (depolarization) in negative charge because if the neuron reaches the critical threshold potential, it can excite the generation of an impulse (action potential). The above is a simplified explanation; in reality much more complex interaction, integration and interfering actions occur among the vast excitatory and inhibitory neurons to generate, at first place, the electric field that gives rise to the formation of dipolar activities which can be recorded by electrophysiological measurement setup (see Section 1.3.3).

1.3 Brain imaging modalities

Currently, different invasive and non-invasive modalities exist to analyse the neuronal activity of the brain. Hemodynamic, anatomofunctional, electrophysiological and even multimodal modalities are used to directly or indirectly image the structures or functions of the brain, offering unprecedented opportunities to study the normal systems, connections and disorders of the human brain. These modalities differ in time and spatial resolution, cost and invasiveness.

1.3.1 Anatomical imaging

Anatomical imaging techniques create post-processed indirect grayscale images such as computed tomography (CT) scan and magnetic resonance (MR), which allow to explore the anatomy of the brain, providing an insight on the possible lesions and malformations in the brain structures (abnormalities or tumors).

1.3.1.1 Computer tomography

Computer tomography (CT) was developed by Hounsfield [Hounsfield, 1973], driven in part by the improvement in computer processing power along with volumetric radiographic imaging. This modality is based on the principle of the acquisition of incremental X-ray scan images from different angles to produce cross-sectional (tomographic) images (virtual "slices") of specific areas of the brain, including the bones, muscles, fat, organs and blood vessels. The distance between two acquired sections is accurate if the object of interest is still, but becomes a problem in the case of brain acquisition which can be affected by the patient motions. The rising and enhancements of Magnetic resonance imaging (MRI) have reduced the use of the CT due to its sensitivity to detect fine lesions [Swartz et al., 1992]. In some circumstances CT is useful, for instance, when an initial evaluation of the pathology is required due to its fast computation. In addition, CT is the only available anatomic imaging modality when the patient has a contraindication to MRI.

1.3.1.2 Magnetic resonance imaging

MRI is based on the science of nuclear magnetic resonance. The magnetic components create detailed images of the brain structures as "slices" or cross-sections when the hydrogen atoms of the brain absorb and emit radio-frequency, and MRI maps these atoms in the brain volume to reconstruct an image. According to the response of the atoms in the brain tissues, gray and white matter can be identified. This modality produces higher resolution images than a CT scan, with a better accuracy for the identification of brain lesions [Swartz et al., 1992].

Multi-modal CT/MRI has emerged as a key tool to track the process of stroke and the impact of therapeutic interventions. CT/MRI provides noninvasive images of brain tissue or parenchyma, angiography or vessels, and perfusion or blood flow in regions of the brain vulnerable to ischemic injury. Research efforts have extended the utility of these tools to identify biomarkers of cerebral ischemia, although clinical trials have yet to simplify the vast resulting imaging data into streamlined protocols [Liebeskind and Alexandrov, 2012].

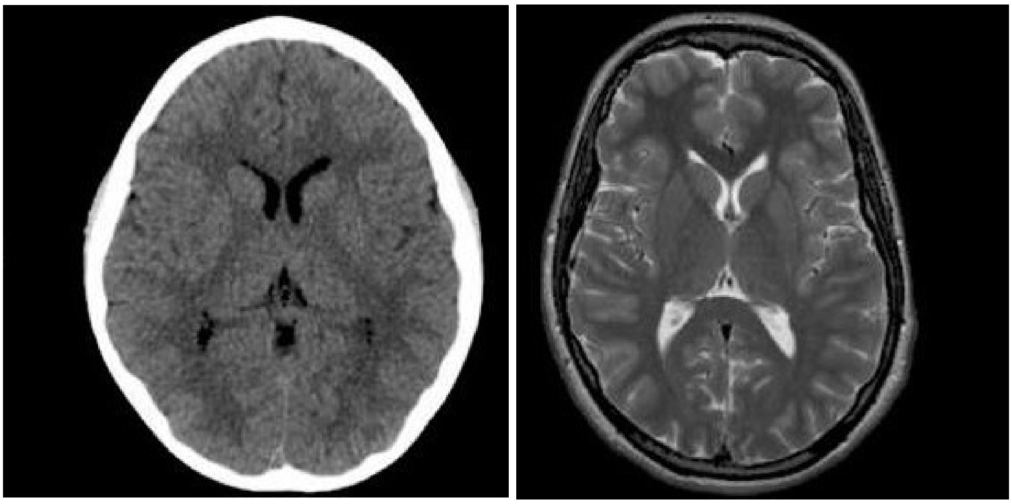

(a) (b)

FIGURE 1.4 – Anatomical imaging. A slice of a CT scan (a) and MRI scan (b).

1.3.2 Functional imaging

Functional imaging techniques attempt to measure simultaneously neuronal activity across the whole brain, providing a functional and structural recording of the brain. These modalities can be used to determine the effects of brain injury or disease on brain systems related to cognition and behavior and to determine how rehabilitation changes brain systems. These techniques include functional magnetic resonance imaging (fMRI), positron emission tomography (PET) and near infrared spectroscopy (NIRS).

1.3.2.1 Functional Magnetic Resonance Imaging

Functional MRI (fMRI) is a type of noninvasive brain scan that uses the MRI technology to measure the changes associated with the blood flow in the brain activity. This modality is based on the fact that blood flow and neuronal activation are both related (hemodynamic response), thus bringing an indirect view of the neuronal activation happening within the cortex and the sub-cortical structures by capturing the Blood Oxygenation Level Dependent (BOLD) signal. fMRI has low temporal resolution, the changes in these activations can be observed in about one second, but relatively high spatial resolution (millimeters), which allows very clear and detailed pictures of the brain structures. Despite of the fact that fMRI has a poor temporal resolution, simultaneous recordings of EEG and fMRI have the potential to localize neuronal activity with both high temporal and spatial resolution [Ritter and Villringer, 2006]. The advantages of fMRI have made it the most commonly used method to explore the functioning of brain structures and, therefore, it is now available in many university and hospital settings.

1.3.2.2 Positron Emission Tomography

Although fMRI is today the dominant form of functional neuroimaging for cognition, positron emission tomography (PET) was a technique used for imaging cognitive systems before fMRI was a wide-spread technology. PET provides a metabolic and functional information unlike CT and MRI anatomic. The creation of this images require the injection of a radioactive, positron-emitting contrast agent into the subject to detect pairs of gamma rays emitted indirectly by the injected tracer. The advantages that PET offers over fMRI is that it is not prone to the loss of signal near air-tissue interfaces as is the case with BOLD contrast fMRI and PET scanning environment suffers from less acoustic noise than the fMRI environment. On the other hand, PET is at disadvantage relative to fMRI both in terms of spatial and temporal resolution, as well as contrast. Moreover, fMRI is noninvasive and does not expose the subject to radiation as PET.

1.3.2.3 Near Infrared Spectroscopy

Optical Imaging or Near Infrared Spectroscopy (NIRS) is a noninvasive modality that measures hemodynamic changes associated to neuronal activity by means of neurovascular coupling. Although visible light is strongly absorbed by various components in body tissue, light in the near infrared frequency range (650-900nm) is less strongly absorbed and thus can penetrate through the skin and skull and a centimeter or two into the typical adult brain which allow the acquisition. NIRS is applied in vivo by placing a light source and a light detector, called channel, adjacent to each other above the region to be measured. A convex banana-shaped tissue region is sampled, corresponding to the light path through the tissue between the source and detector [Saliba et al., 2016]. This modality can also detect the Blood Oxygenation Level Dependent (BOLD) signal from changes in the amount of reflected light. This is an economical alternative to fMRI but is limited to imaging the cortex.

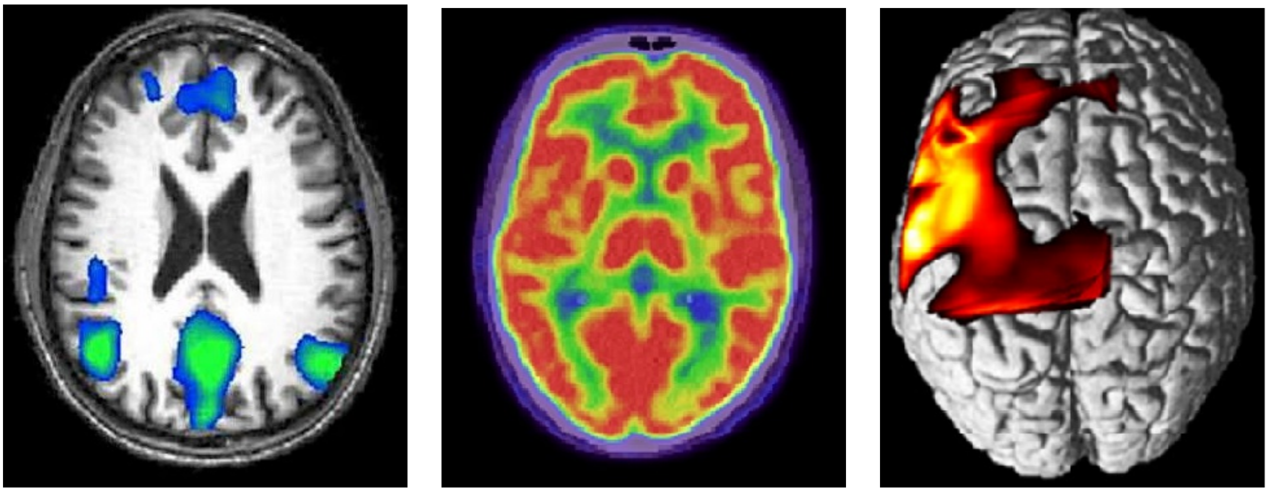

(a) (b) (c)

FIGURE 1.5 – Functional imaging modalities. fMRI (a), PET (b) and fNIRS (c) [Jang et al., 2016].

1.3.3 Electromagnetic measurement

The physiologic activities of the brain generate electrical currents and electromagnetic fields which can be measured by surface and intracranial techniques. In this group, with a superior temporal resolution, among other imaging techniques, is the magnetoencephalography (MEG) which measures changes in magnetic fields associated with changes in electrical activity [Brazdzionis et al., 2022], the scalp electroencephalography (EEG), which measures changes in electrical activity as clusters of neurons become active, and the stereo-EEG, which record invasively the electrical activity nearby the brain generators.

1.3.3.1 Electromagnetic brain signal generation

Brain electromagnetic field are mainly generated by the synchronized activities of pyramidal neuronal cells. These cells are the common neurons found in the cerebral cortex and in sub-cortical structures such as the hippocampus and the amygdala and they are the main electrophysiological generators of the MEG and (S)EEG measurements. Like other type of neurons, the main function of pyramidal neurons is to transform synaptic inputs into an output of action potentials. As illustrated on Figure 1.6(a), this pair of equal and opposite charge poles spanning across the distance between the dendrites and neuron body and making a circular path in neurons and the extracellular conduction medium can be represented by a current dipole.

Each electromagnetic field of a single dipole generated by postsynaptic potential of a single neuron is generally too weak for a sensor on the scalp to detect. However, the sum of activated large pyramidal cortical neurons will produce the electromagnetic fields able to be recorded by magnetoencephalography (MEG) and scalp/intracranial electroencephalography (EEG), because of the coherent distribution of their dendritic trunks locally oriented in parallel and pointing perpendicular

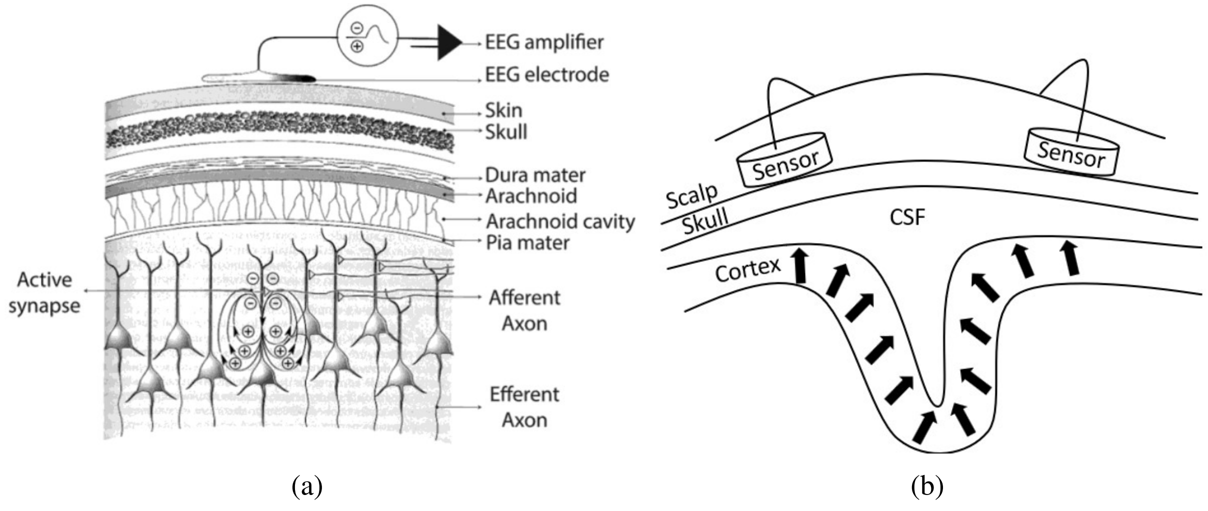

(a) (b)

FIGURE 1.6 – Electric field generated by extracellular currents in a pyramidal neuron [Bastos-Filho, 2020] (a) and measurable signals that are produced by the summation of activated dipoles locally oriented in parallel and pointing perpendicular to the cortical surface (b).

to the cortical surface. Figure 1.6(b) illustrates spatially organized macro-assemblies of pyramidal neurons with their dendrites normally oriented to the local cortical surface. This spatial arrangement and simultaneous activation of a population of neurons contributes to the spatio-temporal superposition of the elemental activity of every neuron, resulting in a current flow that generates signals detectable by MEG/S(EEG) sensors.

1.3.3.2 Magnetoencephalography

Magnetoencephalography (MEG) was discovered by David Cohen in 1963 [Cohen, 1968]. It is based on Biot-Savart law, which states that each elementary stream from the activity of nerve cells produces a perpendicular magnetic field. Sensors on or close to the scalp measure the sum of the fields generated by all the currents. This non-invasive medical modality is used to map the functional brain areas in sensory, motor, language and memory activities, as well as identify location of the source of epileptic seizures. Some advantages of this modality over the scalp EEG (see below) is that the recorded signals are significantly less deformed by the successive layers through which the signal propagates and that it can be recorded without reference. However, its high cost makes it less accessible than EEG and therefore it is commonly used in difficult cases to complement the diagnostic.

1.3.3.3 Electroencephalography

Electroencephalography (EEG) was introduced by the psychiatrist Hans Berger in 1924. Figure 1.7 shows the first EEG recording in human brain reported by Berger.

EEG is the recording of the electric activity, mostly the current that flows during the synaptic excitation of dendrites of many synchronized pyramidal neurons in the cerebral cortex measured on the surface of the scalp with electrodes usually placed at specific positions. Figure 1.8 shows the international 10-20 electrodes montage used on EEG recording. EEG recording consists in a difference of the electric potential between each electrode and a reference electrode or from an artificial reference obtained by subtracting the signal averaged over all sensors from the data of each channel, this strategy is known as a common reference montage [Osselton, 1965].

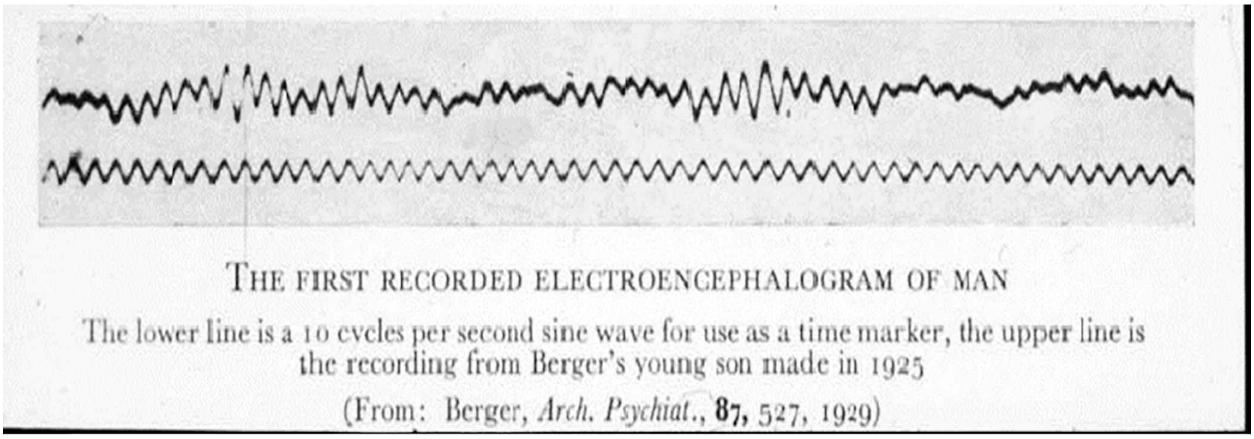

THE FIRST RECORDED ELECTROENCEPHALOGRAM OF MAN

The lower line is a 10 cycles per second sine wave for use as a time marker, the upper line is the recording from Berger's young son made in 1925

(From: Berger, *Arch. Psychiat.*, **87**, 527, 1929)

FIGURE 1.7 – The first EEG recording from the human brain reported by Hans Berger in 1929 [Yamada and Meng, 2012].

The main features that distinguish EEG from other neurodiagnostic studies are: the dynamic nature by which it expresses various physiological and pathological brain functions and the manner in which it instantaneously reflects the level of consciousness. The main features to be examined when recording and evaluating an EEG are [Yamada and Meng, 2012]:

1. *Amplitude*: It may vary over a wide range, from few microvolts to several hundreds microvolts, according to the patient age and the type of activity, either normal or abnormal.
2. *Frequency:* It is the most common way to analyze EEG signals. Activities are conventionally classified as: delta waves <4 Hz, theta waves 4 to 7.5 Hz, alpha waves 8 to 13 Hz, beta waves 14 to 30 Hz, and gamma waves >30 Hz (sometimes separated in low gamma and high gamma waves).
3. *Waveform (morphology) and rhythmicity:* It may be characterized based on their location, amplitude, frequency, morphology and continuity (rhythmic, intermittent or continuous), synchrony, symmetry, and reactivity.
4. *Transients and bursts:* They are paroxymal activities that appear and disappear suddenly and are clearly distinguishable from the ongoing and sustained EEG activities.

Contrary to modalities like CT or (f)MRI, EEG provides, at macroscopic scale, a direct recording of the neuronal activity with millisecond temporal resolution and a large volume of data can

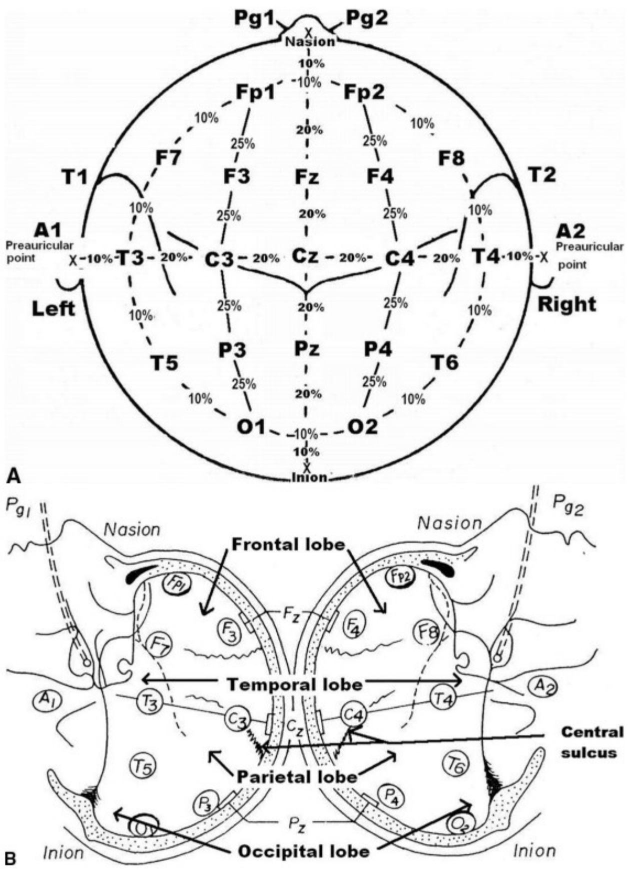

FIGURE 1.8 – A: Top view of the International 10-20 system. B: Lateral view of the international 10-20 system in relation to the surface of the brain [Yamada and Meng, 2012].

be stored more easily. The temporal resolution of these recordings is in a comparable order of magnitude with the dynamic of the physiological or pathological neuronal processes, making the EEG the most popular modality for investigating brain functions.

It is common to think on EEG as a surface measurement, where the sensors are placed on the scalp. Its easy installation, portability and relative low cost make this modality more convenient over other modalities. In particular, it has been extensively used to solve the brain source localization problem. Nonetheless, on the same matter of source localization, much more accurate neuronal activity can be obtained by invasive electrodes placed on the brain surface or introduced within the brain tissue. A first example of implantable electrodes is the electrocorticography (ECoG), developed by Wilder Penfield and Herbert Jasper in the 50s [Palmini, 2006], which consists of a grid of electrodes placed on the surface of the brain, usually organized in patches. A second example, detailed in the next subsection, is the stereo-electroencephalography (SEEG).

1.3.3.4 Stereo-electroencephalography

Stereo-electroencephalography (SEEG) was first performed in France, at the Sainte-Anne Hospital, by Jean Bancaud and Jean Talairach in the late 50s [Talairach et al., 1958]. This technique consists of electrode shafts directly implanted within the brain volume, thus requiring surgical intervention under general anesthesia. During the implantation procedure, the head is maintained by a stereo-taxic frame to prevent any head movement, explaining the name of Stereo-EEG.

Stereo-EEG is a methodology used to confirm or refute hypothesis generated to delineate the epileptogenic zone (EZ) from the sum of non-invasive presurgical work up (anatomical (MRI) and EEG analysis) in patients with pharmaco-resistant focal epilepsy. Because the medical risk involved in the SEEG implantation, the number of implanted contacts is limited to the clinician's area of interest where most of the electrodes are implanted, trying to target the region thought to be responsible for the epileptic events. The number of electrodes required is not fixed, but usually between 6 and 15 are considered. Each electrode contains up to twenty recording contacts. Fewer than 6 electrodes indicates that SEEG may not be necessary, more than 15 indicates possible fishing expedition [Isnard et al., 2018]. The electrodes are mostly implanted within the hemisphere of the suspicious area (the ipsi-lateral hemisphere), whereas only a few of them are implanted in the opposite (contra-lateral) hemisphere.

The main advantage when compared SEEG to scalp EEG is that SEEG "sees" the activity in the vicinity of the generators, having thus a better signal to noise ratio, especially advantageous for signals of weak amplitudes. However, when addressing source localization, SEEG has its own flaws. For instance, the degree of freedom found in the particular geometry induced by the SEEG electrode implantation leading to a poorly conditioned problem [Caune et al., 2014]. We explain in more details in chapter 3 these vulnerability on SEEG recordings, taking the opportunity to emphasize the necessity of performing source localization from this modality.

1.4 Electroencephalography applications

The development of neuroimaging modalities has greatly improved the understanding of the brain activity from research studies of medical applications. In particular, EEG sensors have become a crucial modality for developing applications in the fields of engineering, science and clinic [Soufineyestani et al., 2020]. EEG provides data of human mental health states, thoughts and imagination. These valuable information have been applied in Brain-Computer Interfaces (BCI) to help with mild to severe motor disabilities and those who are not able to communicate with others [Schalk, 2004]. We can also cite more commercial applications such as **Bio-metrics**, where cognitive and emotional brain status has been used to identify people [La Rocca et al., 2012], **Custom Solutions and Neurofeedback (Neurotherapy)** to make a comfortable environment, improve well-being and life quality

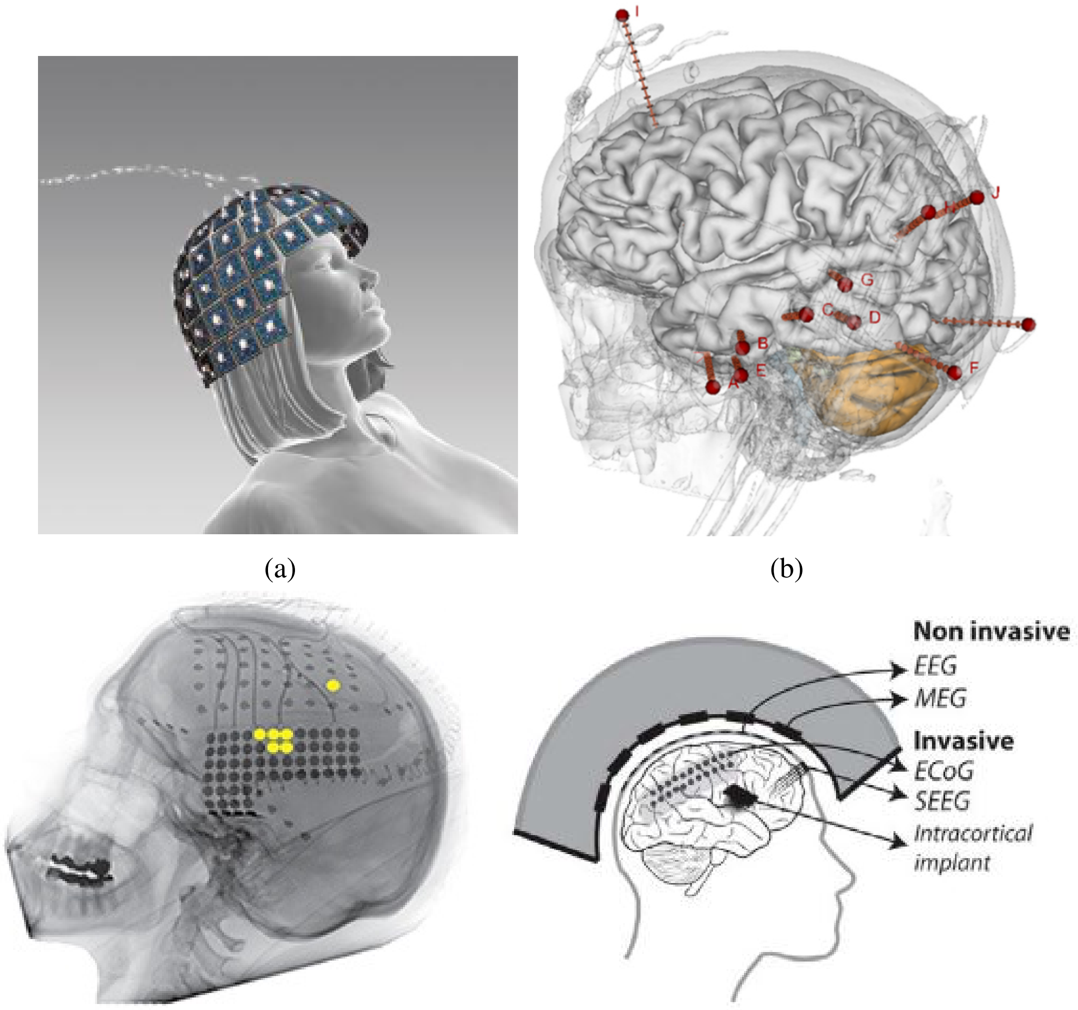

(a) (b)

(c) (d)

FIGURE 1.9 – Sensors of different modalities. MEG (a), SEEG (b), ECoG (c) and illustration of surface and implantable modalities (d) [Astrand et al., 2014].

[Vijayaragavan et al., 2015] and boost the learning process [Mostow et al., 2011], **Neuromarketing** or **Consumer Neuroscience**, where one of the goals is to understand costumer's preferences and expectations regarding a specific product [Soria Morillo et al., 2015].

In **Neuroscience** research, clinical or non-clinical studies have used EEG devices in the cognitive [Cernea et al., 2012] and behavioral [Kalas and Momin, 2016] analysis, to understand how the brain acts when humans experience different emotional states and how the brain works in various mental states.

According to the percentage of studies of EEG data, neuroscience have received the most attention from researchers, i.e. neuroscience 76%, BCI 14%, neurofeedback 6%, neuromarketing 2% and biometrics 2% [Soufineyestani et al., 2020]. A wide range of studies can be found for solving the brain source localization problem based on EEG data, aiming to suit the modeling of the sources and the resolution of the forward model, linking source activities to the potentials measured on the sensors. From the neurological side, brain source localization can bring crucial information on the location of the generators of the studied (normal or abnormal) patterns, helping to provide support to the prior clinician knowledge on the affected structures. We describe next the two most relevant applications, in clinical studies and cognitive neuroscience.

1.4.1 Clinical applications

In presence of a pathology, the brain activity elicits abnormal patterns or suppress and distort normal patterns. The number of abnormalities experimented in the brain is quite large [Sharbrough, 2005] and the use of EEG data in the clinical field has allowed to study many of these brain disorders like epilepsy, Parkinson, Alzheimer, language impairments, seizures, schizophrenia, sleep disorders, anxiety, etc. [Acharya et al., 2013; Klassen et al., 2011; Melissant et al., 2005]. In addition, the use of intracerebral recordings, in particular SEEG, has been an important modality mainly used in the context of severe epileptic pathological case for which the medication is ineffective. Its role is limited to clinical evaluation for confirming the precise location of the epileptic area responsible for the pathology before applying targeted treatments or excision of the identified brain structures. In the following, we present an insight of this pathology, epilepsy, which is relevant for this thesis.

Epilepsy is a pathology that induces important changes in the frequency patterns of the patient electrophysiology, which goes from chaotic signatures to spikes and sharp waves during the period of crisis, which are considered the interictal marker of a patient with epilepsy and are the EEG signature of a seizure focus. Two types of epilepsy can be identified: generalized and partial epilepsy [Caune, 2017]. Generalized epilepsy is a seizure that impairs consciousness and affects the electrical activity of a large portion of the brain, often over both hemispheres. This type of epilepsy sometimes is leading to a violent shaking or vibrating uncontrolled movements of the epileptic subject. Inversely, partial epilepsy occurs in a limited number of cortical brain structures, sometimes spreading to other parts of the brain along the evolution of the crisis.

The mechanism behind focal epilepsy is now widely assumed to be driven by a network of abnormally hyper-connected structures, due to a wrong balance between inhibitory and excitatory neurons within the involved structures [Bromfield et al., 2006]. In the temporal lobe epilepsy, many distinct cortical and sub-cortical structures are recruited during the epileptic seizure [Maillard et al., 2004]. This network reconfigures itself all along the crisis. The identification of its topology and of its dynamics could give a valuable information on the initiating and leading structures, which leads to a better understanding of this pathology and consequently to more accurate and efficient treatments [Achard et al., 2006; Wendling et al., 2010]. The relations between the structures can be deduced from (S)EEG measurements (possibly after source localization and estimation) by computing statistical relationship between the dynamic activity of distinct brain areas [Achard et al., 2006; Wendling et al., 2010]. If such analysis can be done from the EEG data, it is more justified to take into account the volume conduction and signal propagation and mixing. In this case, epileptic source localization and reconstruction of the time-courses is thus the key to perform the analysis of the epileptic event.

1.4.2 Cognitive function analysis

Cognitive functions are brain-based skills we need to carry out for any task from the simplest to the most complex. They are related to the mechanisms of how we learn, remember, problem-solve, pay attention, etc. [Zhang, 2019]. These cognitive functions are mediated by neuronal activity represented by synchronization of brain oscillations and networks.

Brain oscillations have been observed and investigated with various electrophysiological tools. The most widely brain oscillations are based on the frequencies of the brain waves measured in hertz (Hz): delta (δ: 0.5-4 Hz), theta (θ: 4-8 Hz), alpha (α: 8-13 Hz), beta (β: 13-30 Hz), low gamma (γ: 30-60 Hz) and high gamma (γ: 60-200 Hz) [Amo et al., 2017]. These descriptors in frequency, that have been established from the study of the EEG, represent states in the brain such as wakefulness, sleep, resting state or processing state of cognitive or motor tasks [Ismail and Karwowski, 2020]. However, there are oscillatory mechanisms underlying the different cognitive functions that remain unclear.

Event-related potentials (ERPs) constitute an important aspect of EEG recordings that occurs in response to sensory, motor and cognitive events. These potentials arise from the synchronous activity of neuronal populations engaged in information processing. The ERPs are usually obtained by signal averaging *i.e.*, by summation of the time-locked electrocortical responses that occur on each repetition of the event. For example, visual ERP has been measured to investigate the time course of explicit visual/memory processing. The ERP is sensitive to many factors that are important in human cognition, such as hearing your own name, listening to music. EEG reveals brain patterns during sleep and waking, abnormalities during diseases like epilepsy, and even brain areas that respond, for instance, to certain auditory and visual stimulation [Baars and Gage, 2010].

Our interest lies in the analysis of EEG signals, aiming to estimate accurately the neural generators in the brain activity generated from protocols involving visual evoked potentials. In this thesis, we are mainly interested to address the problem of source localization in the context of the fast periodic visual stimulation (FPVS) protocol. FPVS has an important role in cognitive neuroscience research with still many questions to be addressed on the understanding of how this function develops in normal conditions and how it is affected in neurological and neuropsychiatric conditions.

1.4.2.1 Fast periodic visual stimulation

Fast periodic visual stimulation (FPVS) is a privileged technique to study the brain face recognition system, as it is well controlled and provides highly reproducible responses with high SNR. An example of protocol, called FACELOC, consists to present to the observer images of objects at a rate of six stimuli per second, and periodically interleaved with face images, that is, a different face image is presented every five stimuli. The protocol reflects at 6 Hz and its harmonics frequencies (12 Hz, etc.) a general response to visual stimulation, whereas at 1.2 Hz and its specific harmonic frequencies (2.4 Hz, etc.) a face-selective response is observed [Jonas et al., 2016].

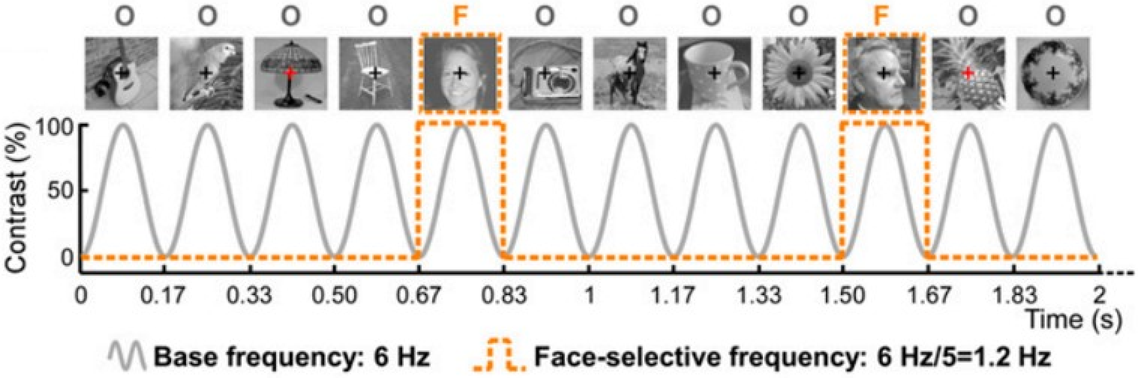

FIGURE 1.10 – Fast periodic visual stimulation (FPVS) protocol corresponding to the FACELOC protocol. [Jonas et al., 2016]

Combined with intracranial electrophysiological measurement (SEEG), these protocols allowed to identify the main areas recruited for face recognition along the ventral occipito-temporal cortex (VOTC) with a right predominance [Jonas et al., 2016]. These areas synchronize their activities with the visual stimuli, both at the base and the oddball frequencies as illustrated in Figure 1.11.

This protocol has been also successfully employed in a number of scalp EEG studies as an efficient way to study multiple levels and types of face categorization [Rossion, 2014], in particular the categorization of natural visual stimuli as faces [Rossion et al., 2015] and more recently combining MEG/EEG recordings [Hauk et al., 2021].

1.5 Conclusion

In this chapter are presented the anatomical aspects of the neural generators which are responsible for producing the measurable potentials recorded using an electrophysiological measurement setup. Among the imagining modalities to explore the structural and functional aspects in the brain, we remark the usefulness of the temporal resolution on EEG recordings from different applications, but in particular when addressing the source reconstruction problem. In addition, from the clini-

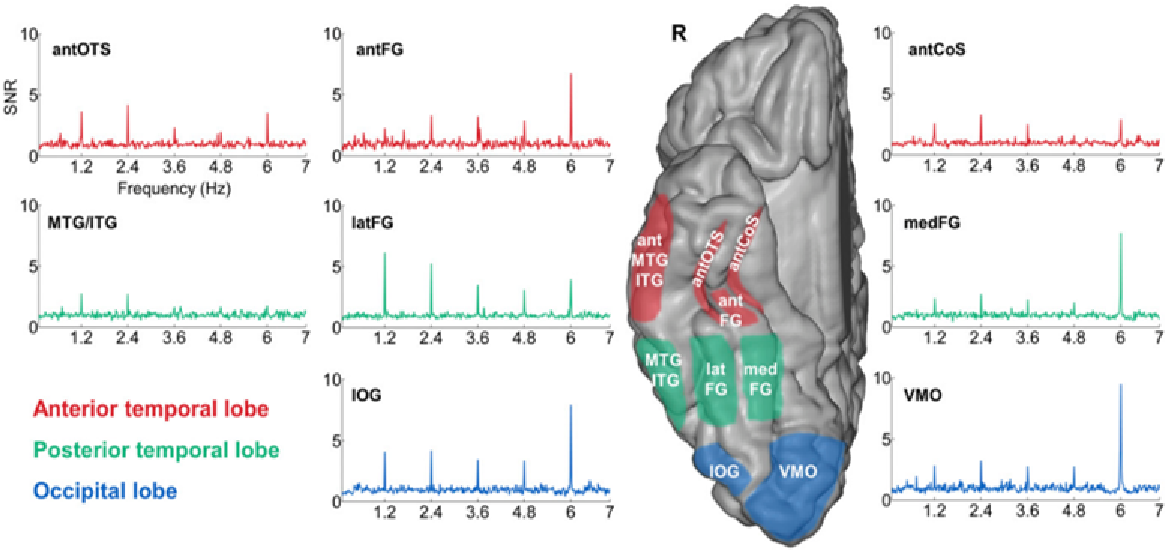

FIGURE 1.11 – Face-selective responses in the ventral occipito-temporal cortex (VOTC), with a right hemispheric dominance. SEEG was recorded in response to FPVS protocol [Jonas et al., 2016].

cal context, we provide an insight of intracranial recordings (SEEG), aiming also to involve this modality in our study of source localization.

The main objective of this work is to address the problem of reconstructing the responsive sources to visual stimulation protocols, and in particular FPVS/FACELOC, from (S)EEG measurements. These responses are well characterized by their oscillatory nature, *i.e.*, the responsive sources of interest are lying in specific frequency bands induced by the frequency of the visual stimulation, and by their rather focal spatial distributions. Relying on these aspects, this thesis aims at proposing methodological procedures and methods for the localization of oscillatory sources, either in time or in the frequency domain based on sparse approximation (greedy) algorithms.

Chapter 2

Forward Modeling and Brain Source Localization

2.1 Introduction

Since the 1950s brain source localization has been an active field of research with interests in both clinical and fundamental neuroscience research. Brain source localization relies on different important steps preceding and following source estimation, all determining the reliability of the final result.

In this chapter, the common practices to solve the source localization problem are presented. In the first section are discussed the different propagation models representing the head medium for the construction of the forward model (lead-field matrix), from simple analytical models to more elaborated numerical models based on a discretized model of the head. We expose their advantages and shortcomings.

Applying localization on real EEG/SEEG data involves data pre-processing steps, including re-referencing and signal denoising. When strong priors are available on the activity of the source to be localized, *e.g.*, in the case of well determined events such as epileptic spikes or responses to cognitive trials, the localization can benefit from temporal averaging of the events for SNR enhancements. Also, when the frequency contents of the source is well established, data filtering in specific frequency bands can be applied, or ultimately single frequency points can be selected if the period of the responses are precisely known, as this is the case with the use of periodic protocols and in particular FPVS.

Then, an overview of different approaches to regularize the inverse problem in source localization is given. First, the solutions based on the distributed source model are presented, where a large number of (fixed-oriented) source candidates are covering the whole source space. We present next some of the most popular approaches to regularize this problem under sparsity priors, such as scanning approaches and dictionary methods based on matching pursuit, which are known to enforce sparsity.

2.2 Forward modeling

In brain source localization, a prerequisite is to compute the forward model. EEG/SEEG forward modeling consists in calculating the electric field potential observed on a given sensor when the configuration of the underlying electrical sources and the biophysical properties and geometry of the propagation environment are known [Hallez et al., 2007]. In the following, we formalize the forward model under the assumption of an instantaneous and linear propagation of the electric field.

2.2.1 Linear mixing model

We use the classic model considering the electrical potential measurements on M electrodes $\mathbf{X} \in \mathbb{R}^{M \times T}$, with T the number of time samples. The linear mixing model can be formalized as:

$$\mathbf{X} = \mathbf{K}\mathbf{J} + \varepsilon \tag{2.1}$$

where the lead-field $\mathbf{K} \in \mathbb{R}^{M \times 3N}$ encodes the propagation coefficients of N freely-oriented dipolar source positions on M electrode contacts, the current density matrix $\mathbf{J} \in \mathbb{R}^{3N \times T}$ encodes the orientation and amplitudes of the N sources through T time points, and ε is the spatio-temporal noise that arises from neural background activity or external artifacts.

The **lead-field matrix K** is a matrix made of $M \times N$ blocks $\mathbf{k}_{mn} = [k_{mn_x},\ k_{mn_y},\ k_{mn_z}] \in \mathbb{R}^{1\times 3}$, each representing the n^{th} source gain on the m^{th} electrode on each Cartesian axis (x,y,z), for fixed source and sensor positions.

$$\mathbf{K} = \begin{bmatrix} \mathbf{k}_{11} & \dots & \mathbf{k}_{1N} \\ \vdots & \ddots & \vdots \\ \mathbf{k}_{M1} & \dots & \mathbf{k}_{MN} \end{bmatrix}$$

Different models to construct the lead-field have been developed, depending on the application and varying in the level of precision. The most common will be described in Section 2.2.2.

The **current density matrix J** describes the widely accepted dipolar model for brain macroscopic sources. A dipole is defined by 6 parameters: 3 for position and 3 for dipolar moments (orientation). In Figure 2.1 is illustrated in Cartesian axis (x,y,z) the vector projection of a dipole with position (X,Y,Z) and projections (J_x,J_y,J_z). This projection represents the orientation and the amplitude of the source, encoded in the dipole current density matrix $\mathbf{J}$, which is composed of columns corresponding to each time instant $t \in 1\dots T$:

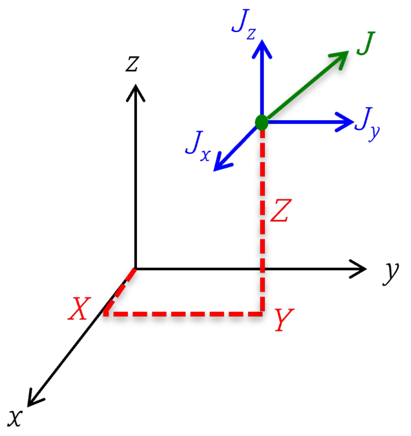

FIGURE 2.1 – Dipole projection in cartesian coordinates (x,y,z), with projections (J_x,J_y,J_z) representing the orientation and amplitude of the source.

$$\mathbf{J} = \begin{bmatrix} \mathbf{j}(1) & \mathbf{j}(2) & \dots & \mathbf{j}(T) \end{bmatrix}$$

and where each $\mathbf{j}(t) \in \mathbb{R}^{3N \times 1}$ vector encodes current densities for all sources $n \in 1 \dots N$ at each time instant.

$$\mathbf{j}(t) = \begin{bmatrix} \mathbf{j}_1(t) \\ \mathbf{j}_2(t) \\ \vdots \\ \mathbf{j}_N(t) \end{bmatrix}$$

$\mathbf{j}_n(t) \in \mathbb{R}^{3 \times 1}$ being the current density vector of n^{th} source at time sample t with its respective vector projection such as:

$$\mathbf{j}_n(t) = \begin{bmatrix} j_{n_x}(t) \\ j_{n_y}(t) \\ j_{n_z}(t) \end{bmatrix}$$

Fixed dipole formalization

To simplify the inversion of source localization problem, anatomical brain information can be used to estimate the orientation of the sources. As described in Section 1.2.3.2, from a neurophysiological point of view, the main generators of the EEG/SEEG recordings are locally oriented in parallel and pointing perpendicularly to the cortical surface. Thus, the number of free parameters is reduced to 4: 3 for position and 1 amplitude component for each source. Therefore, the electrical potential formalization of Equation (2.1) becomes:

$$\mathbf{X} = \mathbf{A}\mathbf{S} + \varepsilon \tag{2.2}$$

where the lead-field $\mathbf{A} \in \mathbb{R}^{M \times N}$ encodes the positions of the M electrodes and the fixed positions and orientations of the N sources. That is, every column of $\mathbf{A}$ contains the propagation coefficients between a specific source position and orientation and the electrodes, and $\mathbf{S} \in \mathbb{R}^{N \times T}$ is a matrix containing the amplitude of these sources at each time instant.

This model can be derived from the more general free oriented model of Equation (4.1). Let $\mathbf{o}_n(t)$ be the normalized moment vector (3×1 vector of unit norm) defining the orientation of this source at time instant t:

$$\mathbf{o}_i(t) = \frac{\mathbf{j}_i(t)}{||\mathbf{j}_i(t)||} \forall t \in [1..T] \tag{2.3}$$

Under fixed dipole assumption, $\mathbf{o}_i(t)$ is a constant vector noted $\mathbf{o}_i$ in the following. Let $\mathbf{O}$ be the

$3N \times N$ block matrix gathering these unit norm orientation vectors for all N sources, such as:

$$\mathbf{O} = \begin{bmatrix} \mathbf{o}_1 & 0 & \cdots & 0 \\ 0 & \mathbf{o}_2 & \cdots & 0 \\ \vdots & \vdots & \ddots & \vdots \\ 0 & 0 & 0 & \mathbf{o}_N \end{bmatrix} \tag{2.4}$$

We then have straightforward relationship between $\mathbf{A}$ and $\mathbf{K}$ as $\mathbf{A} = \mathbf{KO}$.

The $1 \times T$ current amplitude vector $\mathbf{s}_n$ of n^{th} source can be calculated as Frobenius norm of the current density vector $\mathbf{J}_n$ at each time instant t:

$$s_n(t) = \|\mathbf{j}_n(t)\|$$

Note that under fixed source assumption, the dipolar moment matrix $\mathbf{J}_n$ can be written as $\mathbf{J}_n = \mathbf{o}_n \mathbf{s}_n$, meaning that each $3 \times T$ matrix $\mathbf{J}_n$ are of unitary rank. In matrix form, we also have $\mathbf{J} = \mathbf{OS}$.

2.2.2 Propagation models

The main approaches to compute the lead-field model are presented in this section, starting with simple, but easy to compute, analytical models such as Infinite Homogeneous Medium (IHM) model [Sarvas, 1987] or One Sphere Medium (OSM) [Yao, 2000], and then going to the more precise numerical models such as Boundary Element Method model and Finite Element Method model [Hamalainen and Sarvas, 1989], with much higher computational costs.

2.2.2.1 Analytical head models

Analytical models provide direct calculable solutions for the forward model. The main benefit of these models is their rapid computation time, which is advantageous since this calculation might be performed numerous times during *e.g.*, source fitting procedure in the non-discretized propagation medium. Only few parameters are used to compute the lead field from these models, *e.g.*, the conductivity of the propagation medium for Infinite Homogeneous Medium (IHM), or the conductivity, center and radius of the sphere for the One Sphere Medium model (OSM).

Infinite Homogeneous Medium

The Infinite Homogeneous Medium (IHM), is the simplest propagation model, with just a single parameter defined by a constant representing the conductivity of the medium $\sigma \in \mathbb{R}$.

Considering a punctual source with moments $\mathbf{j}$ at position $\mathbf{r}_0$ (see [Sarvas, 1987]), the approximation for the potential at a point $\mathbf{r}$ is:

$$\mathbf{X}(\mathbf{r}) \approx \frac{1}{4\pi\sigma}\frac{(\mathbf{r}-\mathbf{r}_0)\cdot\mathbf{j}}{||\mathbf{r}-\mathbf{r}_0||^3} \tag{2.5}$$

Then, the lead-field matrix elements of the propagation matrix **K** are defined for the IHM model as:

$$\mathbf{k}_{mn} = \frac{1}{4\pi\sigma}\frac{\mathbf{r}_{\mathbf{x}_m}-\mathbf{r}_n}{||\mathbf{r}_{\mathbf{x}_m}-\mathbf{r}_n||^3} \tag{2.6}$$

with $\mathbf{r}_{\mathbf{x}_m} \in \mathbb{R}^{1\times 3}$ as the position of the m-th sensor and $\mathbf{r}_n \in \mathbb{R}^{1\times 3}$ as the position of the n^{th} source. The potential varies with the angle of the source and decreases with the square of the distance to the source.

However, the head conductivity is not spatially uniform. Also, when dealing with EEG recordings, IHM seems too simplistic. Thus, multiple studies have been carried out to calculate the best approximation for the conductivities of the different tissues of the human head [McCann et al., 2019]. Indeed, the electrical field is propagated through of the different inhomogeneous tissues of the head (brain, skull, scalp) and such inhomogeneity in the volume conductor tends to introduce significant errors between the actual electrical potential propagation and the one suggested by the IHM model.

One Sphere Medium model

The One Sphere Medium (OSM) has been proposed to model the shape of the head, taking into account that the head is finite and the air is not conducting. The first solution was provided by [Wilson and Bayley, 1950], and then that initial solution was mathematically simplified by [Frank, 1952] for potential on the surface of the sphere. Other solution was proposed by [Brody et al., 1973], addressing the indeterminations of the previous models, but still only calculating the potential on the surface of the sphere. Later, [Yao, 2000] developed a solution free of indeterminations and able to compute the potential everywhere inside the sphere. For a sphere with the radius r_{sp}, the potentials can be calculated in any point **r** in the sphere [Yao, 2000]:

$$\mathbf{X}(\mathbf{r}) = \frac{1}{4\pi\sigma}\left[\frac{\mathbf{r}-\mathbf{r}_0}{||\mathbf{r}-\mathbf{r}_0||^3} + \frac{(\mathbf{r}-\chi\mathbf{r}_0)}{r_{sp}^3 r_{pi}^3} + \frac{1}{r_{sp}^3 r_{pi}^3}\left(\mathbf{r} + \frac{\mathbf{r}\frac{||\mathbf{r}_0||\,||\mathbf{r}||}{r_{sp}^2}\cos\alpha - \chi\mathbf{r}_0}{r_{pi}+1-\frac{||\mathbf{r}_0||\cdot||\mathbf{r}||}{r_{sp}^2}\cos\alpha}\right)\right]\cdot\mathbf{j} \tag{2.7}$$

where $\chi = \frac{||\mathbf{r}||^2}{r_{sp}^2}$, the center of the sphere being taken from the origin of the coordinates. $r_{pi} = \frac{||\mathbf{r}-\mathbf{r}_0||}{||\mathbf{r}||}$ is the ratio between the source to sensor distance and the sensor distance to the center of the sphere. α represents the angle between vector **r** and $\mathbf{r}_0$. These parameters are illustrated in Figure 2.2 and details are available in [Yao, 2000].

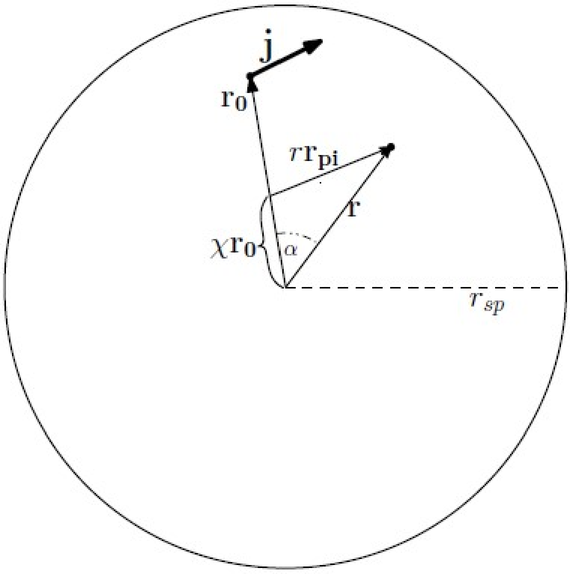

FIGURE 2.2 – Dipole in a homogeneously conducting sphere [Caune et al., 2014].

For EEG recordings, when considering the skull tissue with a conductivity significantly lower than the conductivity of scalp and brain tissues, the volume conductor model of the head was refined and, from the homogeneous OSM, other solutions were introduced. Some of them including Legendre series [De Munck et al., 1993], involving the evaluation of many terms of polynomials and yielding too much expensive calculation costs. Also, other more sophisticated models were derived from OSM to ameliorate the source localization accuracy to a certain degree, such as multiple spheres, with the inner sphere modeling the brain, the intermediate layer modeling the skull ad the outer layer modeling the scalp [Roth et al., 1993]. As well as, eccentric spheres [Cuffin, 1991] and multiple overlapping spheres [Huang et al., 1999]. This development can be considered as a transition from the spherical model to the realistic model, with numerical geometry derived from imaging modalities. We will focus next on the realistic head models. However, it is worth noting that when dealing with SEEG recordings, it might be reasonable to suppose that SEEG are taken inside the brain volume, which is often modeled as homogeneous and isotropic. For this reason, the OSM might be an eligible solution to perform accurate brain source localization from SEEG. Such hypothesis was made in [Chang et al., 2005] and tested in [Cosandier-Rimélé et al., 2007; Caune et al., 2014].

2.2.2.2 Numerical head models

To obtain a more precise geometry of the head, one can take into account medical imaging modalities, such as Computed Tomography (CT) and Magnetic Resonance Imaging (MRI), which have become more accessible and made possible the built of more realistic head models to improve the precision of the forward lead-field. The most common methods include the Boundary Element

Method model (BEM) and the Finite Element Method model (FEM).

Boundary Element Method

The Boundary Element Method (BEM) is a numerical computational method of calculating the surface electrical potentials generated by current sources located in a homogeneous volume conductor. The volume conductor is assumed to consist of multiple piecewise compartments, each with a homogeneous and isotropic conductivity encapsulating a particular tissue of the head. BEM uses a geometric model based on triangulations of the surfaces/interfaces between compartments, which are assumed to have isotropic conductivities (Figure 2.3).

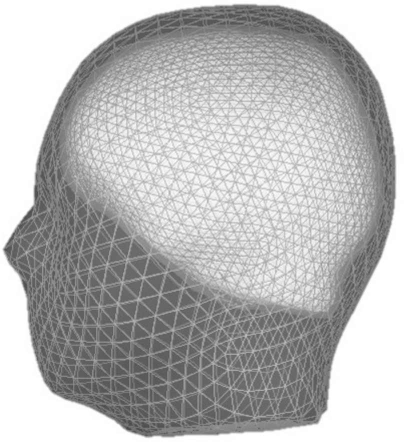

FIGURE 2.3 – Representation of three triangulated surfaces of the head used to compute the BEM forward model : scalp, inner skull and outer skull.

The basis to construct BEM consists of extracting, from an MRI of the subject, surfaces/interfaces describing the anatomy of the head. Such surfaces involve the geometry of the brain, scalp and skull (inner and outer). In Figure 2.4 is shown the kind of geometry that can be segmented from the MRI of a subject's head. From these surfaces, the simplest model consists in assigning a constant conductivity to each region located between two surfaces. Each subregion corresponds to a certain type of head tissue which is supposed to be sufficiently homogeneous to have a constant conductivity. The conductivity of the head are then being approximated as a piecewise constant function [Vallaghé, 2010], constant in each tissue and discontinuous at the interfaces between tissues. So, the head can be considered as a domain Ω made of subregions Ω_k separated by surfaces S_k, each with a constant conductivity σ_k and with $\sigma = 0$ outside Ω.

In [Geselowitz, 1967] was derived a solution of forward problem in integral form for the realistic piecewise conductor model Ω ($\Omega = \bigcup \Omega_k, k = 1, ..., N$) with N interfaces $(S_k, k = 1, ..., N)$:

$$\sigma(\mathbf{r})V(\mathbf{r}) = V_{inf}(\mathbf{r}) + \sum_{k=1}^{N} \frac{\sigma_k - \sigma_{k+1}}{4\pi} \int_{S_k} V_k(\mathbf{r}') \frac{\mathbf{r}' - \mathbf{r}}{||\mathbf{r}' - \mathbf{r}||^3} \cdot \mathbf{n}(\mathbf{r}') dS_k \tag{2.8}$$

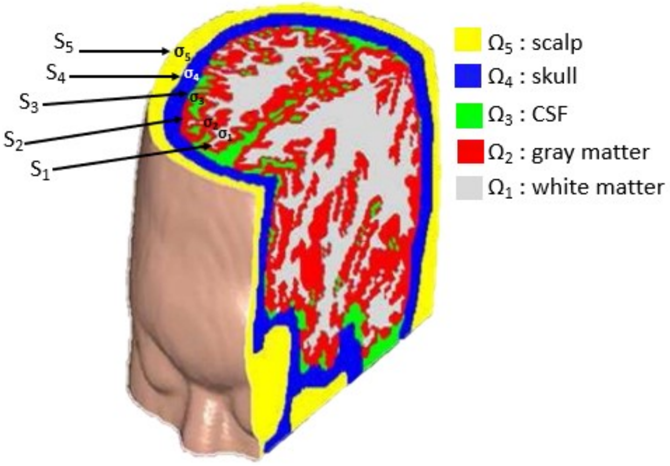

FIGURE 2.4 – Human head model Ω segmented into five tissue compartments Ω_k: scalp, skull, cerebrospinal fluid, gray matter and white matter, each with a constant conductivity σ_k and separated by surfaces S_k. Modified from source [Lee et al., 2012].

where V_{inf} is the potential in an infinite homogeneous medium with $\sigma_{inf} = 1$ and V_k is the potential on k-th surface. Here, $\mathbf{r}$ is every point in Ω but not on any S_k. However, Equation 2.8 cannot be solved because the term on the right implies the integration of the surface potential. But when $\mathbf{r}$ approaches a point on a surface S_k, Equation 2.8 can be modified as [Sarvas, 1987]:

$$\frac{\sigma_k + \sigma_{k+1}}{2} V_k(\mathbf{r}) = V_{inf}(\mathbf{r}) + \sum_{k=1}^{N} \frac{\sigma_k - \sigma_{k+1}}{4\pi} \int_{S_k} V_k(\mathbf{r}') \frac{\mathbf{r}' - \mathbf{r}}{\|\mathbf{r}' - \mathbf{r}\|^3} \cdot \mathbf{n}(\mathbf{r}') dS_k \tag{2.9}$$

where $V_k(\mathbf{r})$ is the potential at $\mathbf{r} \in S_k$. Calculating $V_k(\mathbf{r})$ for each k, Equations 2.8 and 2.9 are combined to get $V(\mathbf{r})$ for $\mathbf{r} \in \Omega$.

It is worth noticing that the quality of the solution can be even more increased by using piecewise quadratic or cubic functions over the simplest space (piecewise constant functions) described above, but the increased complexity of the functions also increases the complexity of the coefficients to be computed for building the linear system.

BEM model is prone to certain numerical errors. One of the reasons is when there are large differences between the conductivities of the different compartments of the head model, which can lead to an amplification of the numerical errors (see the details in [Meijs et al., 1989]). A second reason of numerical error on BEM is when sources are located close in between two tissues, typically at a distance smaller than the size of the triangles used to describe the surfaces, the accuracy of this approximation drops severely. To reduce this effect, a new BEM formulation was proposed in [Kybic et al., 2005] which also allows to consider piecewise constant conductivity models that are not necessarily nested volumes [Kybic et al., 2006].

Finite Element Method

It is know that some of the head tissues do not have a constant conductivity. Nevertheless there are no techniques to get a precise model of the conductivity of the head. For example, the skull has a variable thickness and in the areas of large thickness it is composed of soft bone enclosed between two layers of compact bone, and soft and compact bone have different conductivities. Similarly, the white matter is composed of large bundles of parallel axon fibers which tend to increase the conductivity in the direction parallel to the fibers, so the conductivity is anisotropic with a principal direction which is not constant over space [Vallaghé, 2010]. Therefore, BEM cannot be used with head models where the conductivity is anisotropic or varies even inside the same tissue. In this case, the whole head volume has to be discretized for computing a numerical solution, contrary to BEM where only the interfaces between tissues are discretized. One of the volume discretization methods is the Finite Element Method (FEM).

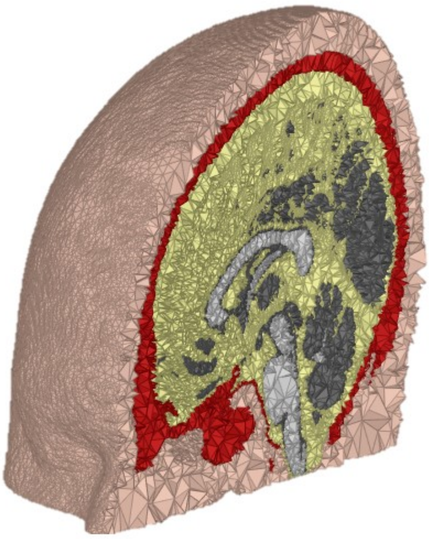

FIGURE 2.5 – FEM head model with 5 different volumes: white matter, gray matter, cerebrospinal fluid (CSL), skull and scalp. This model is provided by ROAST toolbox [Huang et al., 2019].

FEM is one of the realistic head models. It divides the whole head volume Ω in discrete volumetric elements and assigns a conductivity for each of them. FEM is able to handle realistic geometries including inhomogeneous and anisotropic tissue properties [Dannhauer et al., 2011; Güllmar et al., 2010]. Since FEM model can take into account detailed anatomical information and anisotropies of the tissues, such models are difficult to construct and come with a huge computation burden.

Generally, for the design of FEM model, five isotropic compartments are considered, as illustrated in Figure 2.5: white matter, gray matter, cerebrospinal fluid (CSF), skull and scalp. The main drawback of FEM model is the high number of parameters to be computed, such as the number of nodes and the conductivities of each volume. In addition, the segmentation algorithms used to delimit the different head volumes can also greatly influence the outcomes. For detailed explanation of FEM model, please see [Vallaghé, 2010; Hofmanis, 2013].

BEM is considered one of the standard methodologies to compute the forward problem because its lower computational costs compared to FEM. As reported in [Vallaghé, 2010; Hofmanis, 2013; Korats, 2016], the modeling error between both BEM and FEM is small when inner anatomical structures in BEM are approximated with one layer, at least when using current approximations for the FEM parameters (constant scalars conductivities by layer). Similarly, the error becomes negligible when more layers are introduced, while the computational burden is still much more lower for BEM, highlighting its advantage over FEM. However, it is thought that the advantages of FEM can be better exploited in terms of the detailed modeling of brain structures such as CSF, white matter and gray matter and the tissue conductivities, particularly the conductivity values around region boundaries [Neugebauer et al., 2017; Moridera et al., 2021].

2.3 Data pre-processing

Before source localization, data is usually preprocessed to increase the reliability of the localization. This pre-processing implies to cope with the presence of neural background activity or external artifacts that might disturb the localization. There is not a single most optimal manner to deal with artifacts or noise, it depends on the data properties and the applications. In this section, we present briefly some strategies to help in regularizing the solution of the localization.

When the electromagnetic brain activity acquisition takes place in a physical common reference frame, all the potentials are actually measured as a difference against a common extra sensor called a reference sensor. This is the case for both, surface and intracranial electroencephalographic signals, always recorded with respect to some unknown time varying signal called reference. Depending on the measuring setup, the reference electrode can be one among the usual measuring electrodes or a particular one, in principle placed far from the sources of interest. The former situation is typical for surface EEG, while the latter can be a good approximation for SEEG recordings, especially when the depth electrodes implantation sites are far from the (scalp placed) reference electrode. Since the reference adds the same potential to every sensor's measurement (for one time instant), the localization problem becomes more complicated [Koessler et al., 2010b], although, according to [Geselowitz, 1998], it is an additive constant of no physical significance.

In both cases, the algorithms used in source localization need to take into account this problem either by including the reference model in the forward model [Yao, 2001], or by estimating its potential under certain hypothesis [Ranta et al., 2010]. .

For scalp EEG signals, one of the solutions employed is the so-called common average reference, which corresponds to a computational reference that is obtained by subtracting the time signals averaged over all sensors from the data of each channel (REST is a more elaborated technique that uses explicitly the forward model [Yao, 2001]). Unlike for surface signals, in SEEG the common reference cannot be estimated by the average potential of the measurements. This is due to the nature of SEEG acquisition, with sensors not placed quasi-homogeneously around the head. Therefore, a spatial filter based in the subtraction of the average value of the potential of all measurements could not be an eligible option in this case. In order to deal with this problem, a re-referencing method ([Ranta et al., 2010] for more details) has been applied to the SEEG signals under the assumption that the potential on the reference sensor is independent of the SEEG activity.

One must also consider the influence of other physiological sources activated simultaneously with the sources of interest. Indeed, the recorded signals are corrupted by either multiple other physiological or external sources. Consequently, even a very distinct source, clearly seen on one of the electrodes, will be barely visible on distant electrodes, especially when other activities are located closer to these electrodes, this having stronger impact on the measurements. The assumption under this approach is that noise is independent of the source of interest and thus reduced when averaging. Consequently, when dealing with dominant sources localization, averaging data is a suitable strategy to deal with this problem. Classical examples of sources corresponding to this description are interictal spikes. Once a collection of spikes are detected, by any filtering method *e.g.*, high-pass filter, wavelet transform, etc, the potential measurements for every epileptic spike instant, on each electrode separately, are averaged, amplifying thus the effect of the spike activity in question and attenuating the other activities if they are independent from the spiking activity [Koessler et al., 2010a; Akdeniz, 2018].

As mentioned above, it can be expected that a time domain procedure is employed in the case of highly synchronized activity *i.e.*, pronounced peaks in time. Whereas in some cases, the relevant information of the neural activity lies in specific frequency bands, where it is therefore advantageous to proceed in the frequency domain. For instance, when analysing an oscillatory phenomena exposing pronounced peaks in frequency.

To investigate face recognition brain function, FPVS is a privileged technique that elicits a highly reproducible response at specific frequencies underlying the brain activity (see Section 1.4.2.1) and with dominance in some areas of the brain (see also more details in [Jonas et al., 2016]). Since, in this work, our target application is source reconstruction during fast periodic visual stimulation (FPVS) in the brain, the particular oscillatory response allows us to determine priors on predominant frequencies to focus on for the source localization problem on EEG/SEEG data, and we will benefit from high signal to noise ratio at these specific frequencies.

Very few approaches in the literature are addressing explicitly the source localization problem in the frequency domain (dealing with complex values of the FFT)[Lütkenhöner, 1992; Zheng and Wan, 2006]. As enlightened by Lutkenhoner *et. al.* [Lütkenhöner, 1992], FFT is a linear transform of the data and localization in the time and frequency domains are not essentially different. The only difference resides in the fact that frequency domain implies an optimization in the complex domain or jointly on the real and imaginary parts, as both real and imaginary part of the Fourier transform need to be reconstructed together. Existing localization methods can then be adapted in the frequency domain. The objective of this thesis is to provide a deeper analysis of the benefits and drawbacks when dealing with source localization with narrow band representation of the data, in particular when one to few frequency points are selected for localization (*i.e.*, fundamental and harmonics of the periodic activity of interest).

2.4 Brain source localization

Electrophysiological brain source localization consists in estimating the positions and activities (orientations and amplitudes) of neural sources using electrical potential measurements recorded from functional imaging techniques. This is a widely studied topic with applications in cognitive research where the functional mapping of the human brain is investigated, and in clinical applications aiming to improve the understanding and treatments of neurological and neurophysiological disorders such as epilepsy, schizophrenia, depression, and Parkinson's and Alzheimer's diseases.

In the following, we will introduce the principal methods for solving the inverse problem, *i.e.*, estimate **S** from Equation 2.2. We will not consider the equivalent current dipole (ECD) methodology, consisting in an overdetermined problem (more measurements than unknowns) where the dipole parameters (position and orientation) are optimized in the continuous brain source volume, also known as dipole fitting strategies [Scherg et al., 1990; Caune et al., 2014]. We focus in this thesis on methods dealing with distributed source models, *i.e.*, when the brain volume is discretized in a matrix lead-field **K** (or **A** if the orientation is imposed for each position). The size of the solution space N being far higher than the number of measurements M, the problem is known to be severely ill-posed and constraints need to be imposed to reduce the solution space. We will consider in particular methods constraining the sparsity of the solution, *i.e.*, explaining the measurements with a minimum number of sources. In this objective, scanning approaches are presented, and finally dictionary based methods are introduced.

2.4.1 Distributed source approaches

Distributed source approaches are applied when the exact number of sources to be localized is unknown or can not be reduced to a few dipoles. Localization of the source space used for this approach consists of a grid of points, each of these points represents a possible source. The number of these sources becomes of the order of several thousands while the number of measurements are of the order of several dozens to the hundred, making this problem severely underdetermined. Indeed in this case an infinite number of source distributions can produce the same measurements, making necessary to impose constraints to regularize the problem.

One often used constraint is of anatomical order, involving the segmentation of different tissues in the head, using information extracted from magnetic resonance imaging (MRI). Since the primary sources, the main generators of the brain activity, are widely believed to be restricted to the cortex, segmented geometry information is used to compute the forward model and to place the possible sources on the mesh points of the cortex. Also, since the apical dendrites that produce the measured fields are oriented normally to the surface of the cortex, sources can be constrained pointing to the surface of the cortex (see Section 1.2.3.2). Then, the number of elementary sources is reduced and the parameters to be calculated for each source are also reduced: position and direction of each dipole are considered fixed and only the amplitude can change in time. Based on this hypothesis, the forward model can be computed taking the fixed dipole formulation described in Equation 2.2.

Despite the solution space is highly reduced, the number of sources still remains far larger than the measurements space. Therefore, additional strategies can be mathematically formulated based on priors on the temporal and spatial distributions of the source activities.

2.4.1.1 Weighted Minimum norm (MN)

In the absence of noise, a general solution is given by pseudo-inverting the fix-oriented lead-field **A** in Equation 2.2

$$\hat{\mathbf{S}} = \mathbf{A}^{+}\mathbf{X} \tag{2.10}$$

where $\mathbf{A}^{+} = \mathbf{W}^{T}\mathbf{W}\mathbf{A}^{T}(\mathbf{A}\mathbf{W}^{T}\mathbf{W}\mathbf{A}^{T})^{-1}$ is a pseudo-inverse of **A** and **W** is a $N \times N$ matrix introducing a constraint on the solution (*e.g.* source covariance, smoothness, depth weight...). There are an infinity of exact solutions parameterized by the weighting matrix **W**, and source estimation methods with different definition of **W** can be found in the literature. The simplest solution, yet adapted for superficial sources such as the cortical ones, is to simply consider the minimum norm solution obtained by taking **W** as the identity matrix: $\mathbf{A}^{+} = \mathbf{A}^{T}(\mathbf{A}\mathbf{A}^{T})^{-1}$.

Without weighting the lead-field matrix but in presence of noise, Stenroos evaluates in [Stenroos and Hauk, 2013] the performance of the following L2-norm (MN) estimator [Fuchs et al., 1999; Hämäläinen and Ilmoniemi, 1994]:

$$\mathbf{T}_{MNE} = \mathbf{A}^{T}(\mathbf{A}\mathbf{A}^{T} + \lambda\mathbf{C})^{-1} \tag{2.11}$$

where **C** is the covariance matrix of the channel noise ε in Equation 2.2. λ is the regularization parameter that sets the balance between reproduction of measured data and suppression of noise [Gorodnitsky et al., 1992; Grech et al., 2008; Potter and Arun, 1989]. If the covariance is not known, one might simplify the equation by assuming $\mathbf{C}_{N} = \mathbf{I}$.

The Weighted Minimum Norm algorithm takes into account the noise and compensates for the tendency of MNEs to favour weak and surface sources, through the introduction of a particular weighting matrix **W**:

$$\mathbf{T}_{WMN} = \mathbf{W}^T\mathbf{W}\mathbf{A}^T(\mathbf{A}\mathbf{W}^T\mathbf{W}\mathbf{A}^T + \lambda\mathbf{C})^{-1} \tag{2.12}$$

W can take different forms by integrating various *priors*, the simplest one based on the norm of the columns of **A** [Lawson and Hanson, 1995] and others like averaging kernels [Grave de Peralta Menendez et al., 1997]. Also, mathematical solutions were applied by introducing priors on the source [Greenblatt, 1993] or iterative solutions where the weight is changed according to the solutions estimated in the previous step [Gorodnitsky et al., 1995].

2.4.1.2 LORETA

Various methods have been developed that take into account the actual head structure and constraints on radial components when sources approach the surface of the brain [de Peralta-Menendez and Gonzalez-Andino, 1998]. The assumption that the activity of neurons in neighboring patches of cortex is correlated and synchronized has been adopted in the implementation of the algorithm called low resolution brain electromagnetic tomography (LORETA) [Pascual-Marqui et al., 1994]. The estimation matrix is computed as follows:

$$\mathbf{T}_{LORETA} = \mathbf{W}^T\mathbf{L}^T\mathbf{L}\mathbf{W}\mathbf{A}^T(\mathbf{A}\mathbf{W}^T\mathbf{L}^T\mathbf{L}\mathbf{W}\mathbf{A}^T)^{-1} \tag{2.13}$$

The Laplacian operator is implemented in **L** used as a constraint to favor smooth spatial distribution of source amplitudes. Thus the 3D inverse solution corresponds to the "smoothest" current density capable of explaining the measured data. In this manner, this solution is known to provide rather blurred (or "over-smoothed") solutions (see [Michel et al., 2004]). Nevertheless, derivatives from this solution were proposed to exclude bias in the presence of undesirable measurements and structured biological noise, standardized LORETA (sLORETA) and exact LORETA (eLORETA)[Pascual-Marqui, 2007], in principle with better localization performance. sLORETA provides a source estimate that is normalized with respect to the source covariance, which leads to an unbiased solution in the case of a single source [Becker et al., 2014]. eLORETA has reduced the localization error over the previous LORETA family, by formulating a weight matrix in a more adequate way. However, it still suffers of the same spatial resolution like the previous version. Some other constraints based on biological laws have also been introduced to address the localization problem [Menendez et al., 2001].

It has to be noticed that the methods indicated above can all be formulated in a Bayesian framework, using probabilistic modeling [Wipf and Nagarajan, 2009] of the source and noise distribution. Additional constraints and priors can be added under this formulation, providing extensions to the classical weighted minimum norm approaches. The sparse focal nature of the sources, combined spatial and temporal constraints, introduction of anatomical priors from imaging modalities and strategies to penalize ghost sources [Michel et al., 2004] can be introduced.

2.4.1.3 FOCUSS

Much sparser results are provided by FOCal Undeterminded System Solution (FOCUSS), which is a recursive linear estimation procedure, based on a weighted pseudo-inverse solution [Gorodnitsky and Rao, 1997]. The weights at each step are derived from the solution of the previous iterative step. Starting from some initial estimate, the algorithm converges to a source distribution in which the number of parameters required to describe the source currents does not exceed the number of measurements. The algorithm is initialized using a classical weighted MNE pseudo-inverse, using any first initial guess for $\mathbf{W}$ (commonly the identity matrix). $\mathbf{W}$ is then iteratively re-estimated at each step from the covariance matrix if the current estimate $\hat{\mathbf{S}}$, until a given criteria *e.g.*, , a given number of iterations or the convergence of the source amplitude estimation $\hat{\mathbf{S}}$. FOCUSS provides solutions that represent compact but somewhat arbitrarily shaped areas of activation in the head. This approach does indeed produce sparse sources, but can be highly unstable with noisy data.

2.4.2 Scanning approaches

Scanning approaches, also known as spatial filtering, do not try to estimate source activations simultaneously in all possible locations, but they rather scan the solution space and choose the source that explain best the data. As such, the ill-conditioned pseudo-inversion due to a number of measurements much smaller than the number of possible sources is avoided. Moreover, they can even benefit from further reduction of the source space by some preprocessing, as it will be explained.

2.4.2.1 Beamforming

Beamforming performs a spatial filtering on data from a sensor array to discriminate between signals coming from the investigated location and those from other locations [Baillet et al., 2001; Michel et al., 2004; Van Veen and Buckley, 1988]. The principle of beamforming comes from radar and sonar signal processing, and has been applied in a large range of areas, starting from astronomy to biomedical signal processing, mainly in MEG.

For any source position $\mathbf{r}_i$, and assuming the orientation of the dipoles are known [1]. the beamformer estimates the amplitude of this source as:

$$\hat{s}_i = \mathbf{w}_i^T \mathbf{X}$$

---

[1] If the orientation of the dipole is not known, one must construct three spatial filters for each of the Cartesian axis x, y, z

where the spatial filter $\mathbf{w}_i$ is designed to pass with unitary gain the source of interest and to zero sources situated at different locations (and assumed in principle decorrelated with the source of interest) [Baillet et al., 2001]. A popular version of beamformer is the Linearly constrained minimum variance (LCMV), which is achieved by minimizing the output power of the beamformer solution subject to a unity gain constraint at the desired location $\mathbf{r}_i$, thus:

$$\mathbf{w}_i = \underset{\mathbf{w}}{\operatorname{argmin}} \;\; \mathbf{w}^T\mathbf{A}\mathbf{A}^T\mathbf{w} \;\; \text{subject to} \;\; \mathbf{w}^T\mathbf{a}_i = 1 \tag{2.14}$$

where $\mathbf{a}_i$ is the column of the lead-field matrix corresponding to the scanned location. Solving Equation 2.14 using method of Lagrange multipliers yields following solution:

$$\mathbf{w}_i = [\mathbf{a}_i^T\mathbf{R}_{\mathbf{X}}^{-1}\mathbf{a}_i]\mathbf{a}_i^T\mathbf{R}_{\mathbf{X}}^{-1} \tag{2.15}$$

where $\mathbf{R}_{\mathbf{X}}$ is the covariance matrix of the measurements $E[\mathbf{X}\mathbf{X}^T]$.

In the context of brain source imaging, the performance of LCVM is limited due to the synchronized nature of neural generators. Correlations between sources will result in partial signal cancellation.

2.4.2.2 MUSIC approaches

One of the most widely used scanning approaches is called MUltiple SIgnal Classification (MUSIC) [Mosher et al., 1992]. It was initially developed for array signals processing [Schmidt, 1986], and later adapted for the EEG/MEG source localization [Mosher et al., 1992].

The basis of MUSIC is to scan a single dipole through a grid confined to a three-dimensional (3D) head or source volume. At each grid point, the forward model for a putative dipole at this location is projected on a signal subspace estimated from the data. To do so, MUSIC starts with covariance estimate of the data, *i.e.*, the matrix $\mathbf{R}_{\mathbf{X}} = E[\mathbf{X}\mathbf{X}^T]$. The dimension of the source space r is estimated based on statistical criterion, *e.g.*, Minimum Description Length (MDL) [Cichocki and Amari, 2002; Rissanen, 1978; Wax and Kailath, 1985]), and the signal subspace $\mathbf{V}_s$ with size $M \times r$ is extracted, corresponding to the r eigenvectors corresponding to the r highest eigenvalues of $\mathbf{R}_{\mathbf{X}}$. In its original form [Mosher et al., 1992], MUSIC scans each dipole location $i = 1 \ldots N$ and computes the subspace correlation values $\{c_{i_1}, c_{i_2}, c_{i_3}\}$ between the 3D subspace spanned by the $M \times 3$ matrix $\mathbf{K}_i$ with the signal subspace $\mathbf{V}_s$. This procedure results in $3N$ subspace correlation values:

$$\text{subcorr}\{\mathbf{K}, \mathbf{V}_s\} = \{c_{1_1}, c_{1_2}, c_{1_3}, \cdots, c_{N_1}, c_{N_2}, c_{N_3}\} \tag{2.16}$$

The r highest values are finally selected, corresponding to the r source locations explaining best the data, and the orientation for each dipolar source are deduced from matrix rotation computed during subspace correlation procedure (see appendix in [Mosher et al., 1992] for the details)[2]. This brings the identification of r lead-field columns forming the resolution matrix $\mathbf{A}_{1..r}$, and the amplitude of the sources are estimated by pseudo-inversion of $\mathbf{A}_{1..r}$ such as in Equation (2.10). MUSIC is based on the assumptions that the data are the projection of a set of linearly independent dipolar sources corrupted by additive spatially white noise. If two dipoles are synchronized, the initial estimates of the source dimension might be degraded, impacting significantly the results.

A popular extension of MUSIC, RAP-MUSIC algorithm [Mosher and Leahy, 1998], overcomes the synchronized sources problem by recursively building a gain matrix $\mathbf{A}_{1..p}$ formed of the p identified source columns after p iterations. After projecting both the source space and the initial gain matrix into orthogonal complement of $\mathbf{A}_{1..p}$, these two residuals are confronted using the usual MUSIC sub-correlation metric, and the next $(p+1)^{th}$ source is identified [Mosher and Leahy, 1998].

RAP-MUSIC however suffers from the fact that the source information from previous recursion steps are not guaranteed to be canceled out from the source and lead-field subspaces, even after orthogonal projection into the complement of $\mathbf{A}_{\{1..p\}}$. The method may then be mislead in the next iteration and choose a new source in the vicinity of the previously found sources [Mäkelä et al., 2018]. To overcome this problem, the TRAP-MUSIC approach [Mäkelä et al., 2018] proposes to apply a sequential dimension reduction of the estimated remaining signal space at each recursion step, diminishing the dimension of 1 at each step as a new source is added to the solution.

2.4.3 Dictionary based sparse approximation

2.4.3.1 Background

Dictionary based greedy algorithms described in this section, which are closely related to multiple linear regression, are usually applied on vector data. In our application of (S)EEG source localization, this implies addressing the problem separately for each time-instant (similar to moving dipoles ECD methods). We will present here the classical greedy algorithms. The straightforward adaptation to matrix data (which can be seen as fixed or rotating ECD) will be briefly explained in the fourth and fifth chapters. Consider thus a column of the data $\mathbf{X}$, denoted $\mathbf{x}$. Sparse signal decomposition of $\mathbf{x}$ requires finding a limited number of elements from the dictionary $\mathbf{A}$ (*i.e.*, a limited number of columns of the lead-field matrix and thus a limited number of locations) such that their weighted sum best describes the data $\mathbf{x}$. The popularity of sparse approximation algorithms, that will be described next, relies on their ability to provide efficient sparse approximations of a signal for severely underdetermined problems [Soussen et al., 2011].

In spatial domain, sparse signals approximation of some arbitrary chosen data vector(s) $\mathbf{x}$ can

---

[2] 1, 2 or 3 correlation values can be selected for a given source position, in the first case the estimated source dipole is of fixed orientation, in the second case it is a rotating vector in a plan, and in the third case this is a freely rotating vector in 3 dimensions

be formulated as the minimization of the penalized least-square cost function:

$$\min_{\mathbf{s}} \; J(\mathbf{s},\lambda) = \|\mathbf{x}-\mathbf{A}\mathbf{s}\|_2^2 + \lambda \|\mathbf{s}\|_0 \tag{2.17}$$

where the l_0 pseudo-norm of the weight column vector(s) **s**, defined as the number of its non-zero entries, is constrained to remain lower than a given number $p \ll M$. By this equation, a sparse representation of the data is enforced (parametrized by the sparsity *i.e.*, penalty parameter λ), meaning that only a few sources are active. The l_0 norm is a natural measure of sparsity but it leads to NP-complete optimization problem. This means that all the possible combinations of the dictionary elements should be considered and yields computationally expensive exhaustive search algorithms.

Due to the complexity of l_0 optimization, some researchers tend to relax the l_0 constraint in order to solve the optimization problem under l_p norm with $p \leq 1$ as for example showed in [Gramfort et al., 2013]. When minimization of l_1 norm is chosen, least absolute shrinkage and selection operator (LASSO) can be used to minimize the residual sum of squares, subject to the sum of the absolute value of the coefficients being less than a (given) constant. Because of the nature of this constraint, it tends to be stable and produce some coefficients that are exactly 0. Therefore, LASSO give interpretable models like subset selection as shown and explained in [Tibshirani, 1996]. However, a constraint under l_1 does not guarantee the sparsity as it is in l_0 case.

2.4.3.2 Matching Pursuit

Greedy iterative approach such as Matching Pursuit (MP) provide the easiest way to find an approximate solution of the original l_0 pseudo-norm problem by finding a dictionary elements and their corresponding weighting coefficients, *i.e.*, non zero elements of **s** in Equation 2.17. The approximation of the observation **x** found by MP can be written as the following linear expansion [Durka, 2007; Durka and Blinowska, 2001; Mallat and Zhang, 1993]:

$$\mathbf{x} = \sum_{i=1}^{m-1} \langle \mathbf{r}_i, \mathbf{a}_i \rangle \mathbf{a}_i + \mathbf{r}_m \tag{2.18}$$

with $\mathbf{a}_i$ the i-th column of the lead-field matrix **A**. $\mathbf{r}_i$ denotes the i^{th}-order residual of **x**, and $\langle \mathbf{r}_i, \mathbf{a}_i \rangle$ denotes the inner product determining the weight of the i^{th} atom (in our case - column of the lead-field matrix). The MP algorithm is an iterative greedy algorithm that selects at each step the column of **A** which shares the highest correlation with the current residuals $\mathbf{r}_m$. This column is then added into the set of selected columns Q, called support. The principle is summed up in the Algorithm 1.

Matching pursuit suffers from the drawback that a particular atom can be picked multiple times. Although MP provides extremely flexible signal representation since the choice of the dictionary is not limited.

Algorithm 1: Matching Pursuit

```
1: procedure MP($\mathbf{A},\mathbf{x}$)
2:     Initialize the residual $\mathbf{r}_0 = \mathbf{x}$ and initialize the support $Q = \emptyset$. Iteration counter $m = 1$;
3:     Find the most correlated dictionary atom $\mathbf{a}$ with index $q_n$ by maximizing the following expression: $b_n = \max_q |\mathbf{a}_q^T \mathbf{r}_{m-1}|$ with $b_n$ the weight of the most correlated atom. Update support $Q = Q \cup \{q_n\}$;
4:     Update residual $\mathbf{r}_m = \mathbf{r}_{m-1} - b_n \mathbf{a}_{q_n}$. Increase counter $m = m + 1$;
5:     If stopping condition is reached, stop MP. Else, go to line 3.
6: end procedure
```

2.4.3.3 Orthogonal Matching Pursuit

Orthogonal Matching Pursuit (OMP) [Cai and Wang, 2011; Pati et al., 1993; Tropp and Gilbert, 2007] is a popular extension of MP, where at each step all the already extracted weights $b_m = \{b_n\}$ are re-estimated by re-projecting the measurements on the linear subspace spanned by the current support Q. The residual is then updated by extracting this projection to the original data $\mathbf{X}$. Compared with other alternative methods, a major advantage of the OMP is its simplicity and fast implementation. Note that the residuals after each step in the OMP algorithm are orthogonal to all the selected columns of $\mathbf{a}$, so no column is selected twice and the set of selected columns grows at each step. The general structure of the OMP algorithm is given in the Algorithm 2.

Algorithm 2: Orthogonal Matching Pursuit

```
1: procedure OMP($\mathbf{A},\mathbf{X}$)
2:     Initialize the residual $\mathbf{r}_0 = \mathbf{X}$ and initialize the support (set of selected variable) $Q = \emptyset$. Iteration counter $m = 1$;
3:     Find the most correlated dictionary item $\mathbf{a}$ with index $q_n : \max_q |\mathbf{a}_q^T \mathbf{r}_{m-1}|$. Update support $Q = Q \cup \{q_n\}$. Update the current weights $\mathbf{b}_m = \mathbf{A}_Q^+ \mathbf{X}$;
4:     Let $\mathbf{P}_\mathbf{A} = \mathbf{A}_Q (\mathbf{A}_Q^T \mathbf{A}_Q)^{-1} \mathbf{A}_Q^T$ denote the projection onto the linear space spanned by the elements of $\mathbf{A}_Q$. Update residual $\mathbf{r}_m = (I - \mathbf{P}_\mathbf{A})\mathbf{X}$;
5:     If stopping condition is achieved, stop OMP. If not, go to line 3.
6: end procedure
```

This algorithm is a stepwise forward selection algorithm and is easy to implement. A key component of OMP is the stopping rule which depends on the noise structure. In the noiseless case, the natural stopping rule is when signal $\mathbf{X}$ is reconstructed perfectly, thus residual $r_m = 0$ [Cai and Wang, 2011; Tropp et al., 2007; Tropp and Gilbert, 2007]. In other case one might estimate the signals and noise power and stop the OMP when only noise is present in the residual.

2.4.3.4 Orthogonal Least Squares

A more effective and also more computationally expensive method is Orthogonal Least Squares (OLS). In each iteration step, a least squares problem is solved instead of simple product calculation as it is in the standard MP case. Basically, the orthogonal algorithm was developed as an approach to combine parameter estimation and model structure detections. The principal idea of the algorithm is to decouple the candidate terms by introducing an orthogonal transform, so that selected terms will not be affected when a new term is introduced. For most system representations, the orthogonal decomposition approach of the regressor matrix avoids possible ill-conditioning and present more accurate results. The forward OLS algorithm is based on classical Gram-Schmidt method [Wu et al., 2005].

When applied on sparse signal representation, the general structure of OLS is the same as that of OMP. The difference is that at each iteration, OLS solves a large number of least-square problems ($M-k$, where k is the size of the current active set), while OMP only performs the $M-k$ inner products between the current residual and each of the remaining candidate columns $\mathbf{a}_n$. The OLS procedure involves two steps, the first involves finding the most correlated atom from the dictionary, and the second involves a dictionary decorrelation step where the atoms that were not selected are decorrelated from previously chosen atoms [Chen et al., 1989; Soussen et al., 2011]. One of the simplest version of OLS (Algorithm 3) is shown by [Blumensath and Davies, 2007] and [Kaur and Budhiraja, 2014] where at each step the chosen atom is the one minimizing the most the residual norm. Such algorithm is very easy to implement but the computational burden is significantly increased for large dictionaries.

Algorithm 3: Orthogonal Least Squares

```
1: procedure OLS$_1$($\mathbf{A},\mathbf{X}$)
2:     Counter $m = 1$, reconstructed data $\hat{\mathbf{y}}_0 = 0$, dictionary index set $Q_0 = \emptyset$
3:     $q_n = \arg\min_{q, Q_m^q = Q_{m-1} \cup q} \|\mathbf{X} - \mathbf{A}_{Q_m^q}\mathbf{A}^+_{Q_m^q}\mathbf{X}\|$ Index $q$ together with the previous selected index,
   yields the support $Q_m^q$ that optimizes the error
4:     $Q_m = Q_{m-1} \cup q_n$ Update support
5:     $\hat{\mathbf{y}}_m = \mathbf{A}_{Q_i}\mathbf{A}^+_{Q_i}\mathbf{X}$
6:     $\mathbf{r}_m = \mathbf{X} - \hat{\mathbf{y}}_m$
7:     If stopping condition is achieved, stop OLS. If not, go to line 3.
8: end procedure
```

Another version of OLS has been developed by [Gowreesunker and Tewfik, 2009]. As done in the classical MP algorithms, the atom chosen at each step is the one maximizing its inner product with the residual. The current dictionary is then projected in the orthogonal space with respect to this atom, thus its contribution is suppressed. Faster implementation can be reached based on QR factorization [Chen et al., 1989] or modified Gram-Schmidt procedure [Van Loan and Golub, 1996].

Nevertheless, for highly correlated dictionaries OLS together with OMP does not guarantee to find an optimal solution [Soussen et al., 2011].

2.4.3.5 Forward-Backward extensions

An improved way to solve the Equation 2.17 is to use forward-backward greedy algorithms. The advantage of these approaches is their ability to eliminate the errors made in previous iterations. An example of such approach is shown in [Zhang, 2008], where a forward-backward OMP extension is proposed to identify basis functions with non-zero coefficients and reconstruct the target function from noisy observations. However, this approach is efficient only if the basis functions are nearly or completely orthogonal, whereas in our case the data are noisy and dictionary elements may be highly correlated.

In the following, it is explained two other forward-backward optimization schemes, which proved to be very robust and accurate for correlated dictionary elements and noisy measurements.

Sparse approximation using SDMP

A rather specific algorithm was developed for EEG applications. The Source Deflation Matching Pursuit (SDMP) algorithm, as presented in [Wu and Swindlehurst, 2013], is based on the observation that estimating the contribution of a given source is much easier when the contributions of all the other sources have been eliminated by projecting out both from the data and from the lead-field the contributions of all the sources except the one being reevaluated (the projection is done using projection matrix $\mathbf{P}_{\mathbf{A}}^{\perp} = \mathbf{I} - \mathbf{A}[\mathbf{A}^T\mathbf{A}]^{-1}\mathbf{A}^T$, with $\mathbf{A}$ chosen as described below in algorithm 4). The method starts by initializing a set of N_s eligible source positions (indexed in Q_{init}) using a classical MP or OMP algorithm. From this initialization, each of the selected source positions p in Q are iteratively reconsidered, and possible taken out from Q if another within the set of unselected elements yields a higher decrease of the residual. This is done by suppressing from both the data in $\mathbf{X}$ and the lead-field in $\mathbf{A}$ the contributions of the atoms (sources) in Q, at the exception of the current re-evaluated position p. An overview of the SDMP is given as the Algorithm 4.

It was proposed in [Wu and Swindlehurst, 2013] a further refinement of the algorithm by reconsidering the orientation of the dipoles during the optimization procedure. It consists in replacing the selection of the source index (line 4 of the Algorithm 4) by the maximization of a MUSIC algorithm criterion. This version is called the SDMUSIC (Source Deflated MUSIC) algorithm.

Approximation using SBR

A more classical forward-backward scheme was proposed by [Soussen et al., 2011]. The Single Best Replacement (SBR) algorithm is able to deal with correlated dictionary elements and is rather robust to noise. SBR is an Ordinary Least Squares (OLS) forward-backward extension based on

Algorithm 4: Source Deflation Matching Pursuit

```
procedure SDMP($\mathbf{A},\mathbf{X},Q_{init}$)
    Initialize $Q = Q_{init}$. Let $N_s$ be the cardinality of $Q_{init}$. Iteration index $i = 1$
    repeat
        for $p = 1$ to $N_s$ do
            $\mathbf{A}_{Q\backslash p} = [\mathbf{a}_{q_1^i} \dots \mathbf{a}_{q_{p-1}^i} \mathbf{a}_{q_{p+1}^{i-1}} \dots \mathbf{a}_{q_{N_s}^{i-1}}]$;
            $Q_{\backslash p} = \{q_1^i \dots q_{p-1}^i, q_{p+1}^{i-1} \dots q_{N_s}^{i-1}\}$
            for $q \in \{1 \dots N\} \backslash Q_{\backslash p}$ do
                $\mathbf{a}_q^{\backslash p} = \mathbf{P}^{\perp}_{\mathbf{A}_{Q\backslash p}} \mathbf{a}_q$;
                $\mathbf{X}^{\backslash p} = \mathbf{P}^{\perp}_{\mathbf{A}_{Q\backslash p}} \mathbf{X}$;
                $q_{Q\backslash p} = \underset{k}{\text{argmax}}\ \|\mathbf{P}_{\mathbf{a}_k^{\backslash p}} \mathbf{X}^{\backslash p}\|_F^2$
            end
            $Q = \{q_1^i, \dots, q_{p-1}^i, q_{Q\backslash p}, q_{p+1}^{i-1}, \dots, q_{N_s}^{i-1}\}$;
        end
        $i = i + 1$
    until $i \geq N_{i_{max}}$ (max iterations);
end procedure
```

successive updates of the sparse signal support (dictionary element indices) by one element: at each step, the support Q is updated either by inserting a new element or removing an existing element. The forward-backward rule shown in Equation 2.19 ensures that only the best columns of **A** weighted by **S** are chosen.

$$Q \bullet i = \begin{cases} Q \cup \{i\} & \text{if } i \notin Q \\ Q \backslash \{i\} & \text{otherwise} \end{cases} \tag{2.19}$$

This leads to the reconstruction of an active set $\mathbf{A}_Q$, where Q contains the selected columns indices (active source locations). Basically, SBR is designed to solve discrete NP-complete problem and, in fact, is a deterministic descent algorithm that minimizes J from Equation 2.17 with fixed parameter λ. At each step, the support Q is updated (insert "$\cup$" a new element with index i inside the support or remove "\" an existing support element) [Soussen et al., 2011]. The forward-backward rule shown in Equation 2.19 ensures that only the best columns of **A** weighted by **S** are chosen.

$$l \in \underset{i \in \{1,\dots,n\}}{\arg\min} J_{Q\bullet i}(\mathbf{S},\lambda) \tag{2.20}$$

Then, if $J_{Q\bullet l}(\lambda) < J_Q(\lambda)$, the subset Q is updated with the new element $Q = Q \bullet l$. Finally the SBR stops when no replacement decreases the cost function or some predefined stopping condition is met, *e.g.*, the residual is significantly small or the maximum size of subset is reached. If $\lambda > 0$, SBR stops after a finite number of iterations. The summary of SBR in pseudo-code format is provided in Algorithm 5. For more details see [Soussen et al., 2011].

Algorithm 5: Single Best Replacement

```
procedure SBR($\mathbf{A}, \mathbf{X}, Q_{init}$)
    Initialize $Q = Q_{init}$
    STOP = FALSE
    Compute l from Equation 2.20 using Equation 2.19
    while $STOP\ = TRUE$ do
        if $J_{Q \bullet i} < J_Q$ then
            $Q = Q \bullet l$
        else
            STOP = TRUE
        end
    end
end procedure
```

2.5 Conclusions

In this chapter has been described the relevant information concerning brain source localization. The forward modeling has been formalized, same for EEG and SEEG measurements. We have presented the first approximations developed to compute the forward model based on analytical solutions, and those numerical solutions that were developed later to approximate a more elaborated head model. This last solution is adopted in this work. We also have introduced the classical approaches to carry out the inversion for brain source localization.

Since our interest is in approaches enforcing sparsity. We study in Chapter 3 the problem of sparse localization of multiple oscillatory sources, exposing the ambiguity of this problem from the theoretical point of view and then quantifying the frequency of this ambiguity. Afterwards, in Chapter 4 is explored an approach derived from the Single Best Replacement (SBR) method that deals with sparse source localization, where the orientation of the source is constrained and priors of predominant frequencies in the recordings are incorporated in order to regularize the EEG source localization problem. In Chapter 5, the orientation constrain of the source in the previous chapter is relaxed, allowing freely oriented sources and then, from a new source localization approach, we study its convergence properties from this constraint using EEG recordings, but we will also take the opportunity to investigate in this matter from the point of view of SEEG recordings.

Chapter 3

On the localization of oscillatory sources from (S)EEG recordings

3.1 Introduction

We have introduced in the previous chapter the general problem of electrophysiological brain source localization, and we have mentioned the main challenges related to the under-determined aspect of the problem and to the uncertainty of the measured data due to background noise and external artifacts. We are interested in this thesis in the localization of brain sources in response to rhythmic cognitive stimulation protocols, yielding rhythmic activities of the responding brain structures at the same frequency as well as its harmonics. The aim of this chapter is to narrow the analysis of the localization problem to these specific oscillatory signals, and to illustrate the particularities and the difficulties that need to be taken into account when trying to localize these activities. We start by describing examples of real signals recorded in response to a FPVS protocol, both in EEG and SEEG, illustrating the oscillatory nature of these measurements based on their Fourier transforms. Based on these observations, the need for a localization step in the interpretation of these data is again emphasized, especially in the case of the SEEG, which is often considered as a gold standard. We also take advantage of these observations to state the main assumptions on source and propagation models that are used in this thesis.

We then formalize the problem as a sum of (time-shifted) sinusoidal source contributions to the measurements, and explicit the source indetermination issue in this particular case, which adds a supplementary difficulty to the already ill-posed aspect of the localization problem. Indeed, we show that the projection of an arbitrary number of oscillatory sources on the sensors can be equivalently reproduced by the sum of alternative oscillating sources at the same frequency. Provided that appropriate projection patterns of these subsidiary sources can be found in the source space as encoded in the physical forward model (lead-field matrix), these alternative solutions are likely to arise and to mislead the localization procedure. These conclusions are illustrated and partially quantified in the last section of the chapter based on realistic scalp EEG as well as SEEG simulations.

3.2 Analysis of EEG and SEEG signals during FPVS

Fast Visual Periodic Stimulation (FPVS) has been introduced in section 1.4.2.1. These protocols provoke synchronized brain responses at the frequency of the stimulus, *e.g.*, 1.2 Hz and 6 Hz for the Face Localizer protocol (see section 1.4.2.1 for explanation on this specific protocol), yielding prominent peaks for these frequencies and their harmonics on the Fourier magnitude spectra of these signals [Jonas et al., 2016]. Analyzing the signal in the frequency domain then becomes a natural manner to tackle the problem of source localization, by focusing on the information of interest concentrating over deterministic frequency peaks with high signal to noise ratio. Another important aspect is related to the sparsity of the activation maps, since it is known that a reduced number of focal sources are responsive to a given protocol and contributes to the measurements at these specific frequencies.

In this section, we provide illustrations of the spectra of real EEG and SEEG signals recorded during a FPVS (Face Localizer) protocol. Considering first the EEG data of figure 3.1(a), responding activities with predominant peaks at 6Hz and 12Hz are observed in a subgroup of EEG electrodes (32 electrodes selected from a 64 electrode montage), proving that some brain sources (hence brain structures) are responsive indifferently to object or face images. Responses are also visible although much weaker at 1.2Hz, 2.4Hz and 3.6Hz (fundamental frequency and two first harmonics of the oddball, *i.e.* face stimuli), reflecting the presence of brain structures responsive specifically to face images. The measurements related to these two responses can be easily separated in the frequency domain, allowing to analyze separately the responses due to the base frequency and to the oddball.

A first visual analysis of the data at specific frequencies is provided by use of polar plots, which represent the magnitude (radius) versus the phase (angle) of the signal for given frequency values. On figure 3.1(b) is given the polar plot for the 6Hz base frequency for each channel of the EEG data in figure 3.1(a). It can be seen that the most prominent peaks (points with highest radius/magnitudes) have phases varying in a wide range, roughly from 120° to 240°. Such variations cannot be due to the noise or artifact activities solely, considering the magnitude of these activities which are much higher than the magnitude at other frequencies. It can then be concluded that these data have been generated by several sources having the same frequency but shifted in phase, and that the measurements are a mixture of sources oscillating at the base frequency of 6Hz (a single prominent source oscillating at 6Hz would have yielded a single phase observation, *i.e.* quasi-aligned points on the polar plot). Therefore, a localization procedure is necessary to disentangle the different sources contributing to the EEG measurements and to identify the activated brain structures from which they originate.

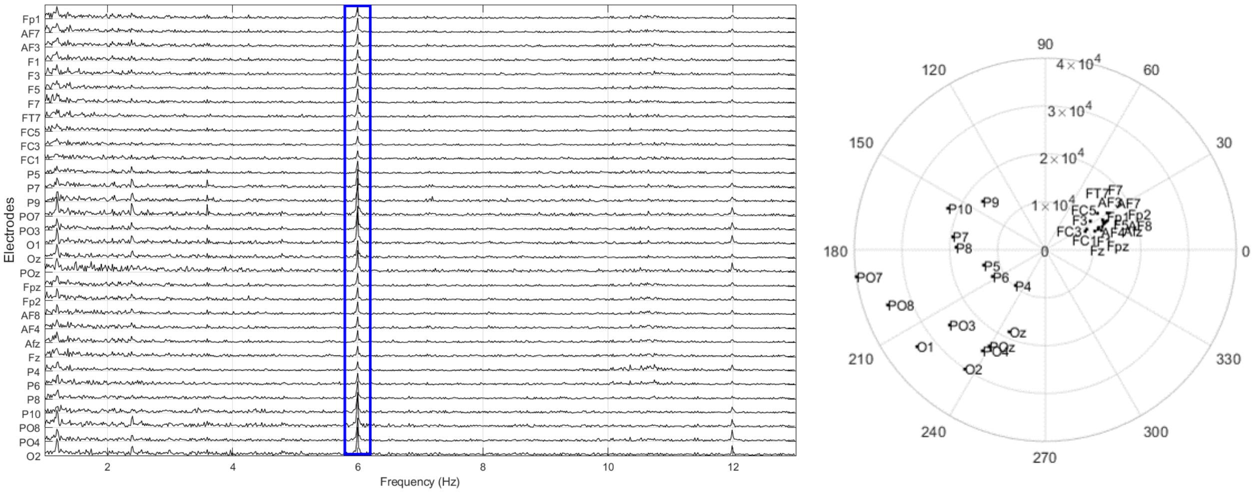

(a) (b)

FIGURE 3.1 – Fast Fourier transform applied to real EEG recorded during the FPVS stimulation. a) Prominent activity at 6 Hz on a group of 32 EEG electrodes and 1.2 and harmonics (*i.e.*, 2.4Hz, 3.6Hz and 12Hz) are observed. b) Representation of the phases and amplitudes of the activity at 6 Hz on the group of the same EEG electrodes.

An example of SEEG data recorded during the same FPVS protocol is also given in Figure 3.2, where a selection of channels most responsive to the base frequency of the protocol (object images response at 6Hz) are displayed (bigger dots in Figure 3.2(c)). In Figure 3.2(a), Fast Fourier Transform magnitudes are given, where high magnitudes are visible at the base frequency of 6Hz on most of the selected channels, but also at the oddball frequency of 1.2Hz and harmonics for a subgroup of them. In contrast to EEG, SEEG signals are strong signals (greater amplitudes), because the advantageous proximity of the SEEG electrodes to the brain sources. SEEG are often considered as gold standard, as they are implanted directly in the brain structures of interest, and they are often

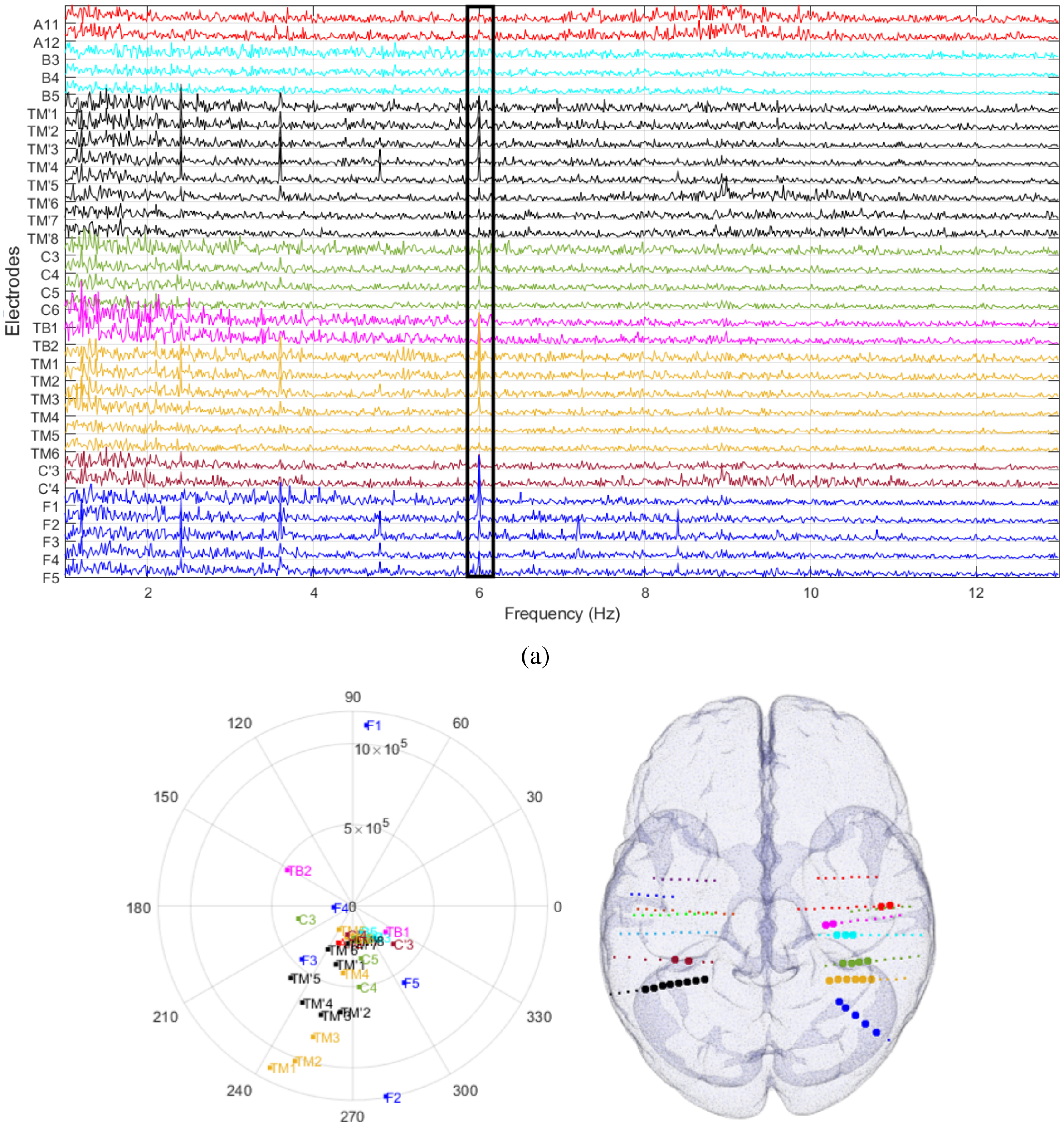

(a)

(b)

(c)

FIGURE 3.2 – Fast Fourier transform applied to real SEEG recorded during the FPVS stimulation. (a) Activity at 6 Hz exhibited on a group of 32 SEEG contacts. (b) Phases and amplitudes of the activity at 6 Hz on the same group of the SEEG contacts (highlighted contacts in (c)).

assumed to record directly and exclusively the activity of the implanted structures. While this might be true when considering bipolar montage (*i.e.* potential difference of neighbouring sensors on a given SEEG shaft), this is no longer the case when dealing with common reference montage, as the SEEG contacts might be impacted by distant sources due to volume conduction (head model).

The inspection of the polar plot of Figure 3.2(b) indeed reveals that multiple phases of 6Hz activities are collected on the SEEG channels. In particular when considering SEEG electrodes TM or TM' with high 6Hz magnitudes, the dots are not radially aligned even for neighboring electrode contacts (3.5mm inter-contact distance), suggesting that the corresponding channels are impacted with several sources responding to the 6Hz base stimuli (at least two, with different weights). Note that similar plots could be obtained for oddball frequencies (1.2Hz and harmonics) as part of the response to the FPVS protocol. These data then keep supporting the idea that SEEG recordings are also a mixture of more or less distant sources and that the SEEG based source localization is a valuable processing step, as it has already been affirmed by previous works of the team [Caune et al., 2014; Caune, 2017].

According to the previous analysis, we can assume that the sources responsible for the activities observed on the sensors (EEG or SEEG) during FPVS protocols have oscillatory amplitudes, having either specific single frequencies or few harmonics. Moreover, the observations of Figure 3.1(a) reveals for example that the 6Hz pattern is widespread all over the scalp EEG electrodes, from right to left hemispheres. This is also the case when considering the SEEG recordings of Figure 3.2(a), where the channels may be impacted by mid-distant to distant sources with unknown magnitudes. For this reason, the positions of the encoded source space in the forward models are difficult to restrain *a priori*, both for surface and intracranial recordings, and we will then consider in the following the general case, that is the sources are not restricted to particular brain regions.

Finally, after making assumptions on the amplitudes and the positions of the sources, the last characteristics to be discussed are the orientations (recall that we consider classical models of dipolar sources). In the following, we will consider that the sources of interest have fixed orientations. Indeed, this is a common and widely accepted assumptions in the brain source imaging literature [Grech et al., 2008]. Moreover, such assumption finds an additional justification through the visualization of (S)EEG data in the frequency domain. Indeed, the presence of high and well resolute peaks synchronized with the periodic stimuli indicate that the underlying sources are with stable orientation (*i.e.* with marginal variations around a mean orientation), as dipolar projections with incoherent orientation variations would considerably weaken or cancel (for completely random orientations) the amplitude of these frequency peaks. A more formal analysis of this point will be given in the next section.

If the source orientations are assumed to be fixed, they are nevertheless not necessarily known *a priori*. In SEEG in particular, the electrodes are implanted in deep brain structures where the gray matter is folded, making it difficult to attribute constraint orientations to the sources, *e.g.* orthogonal to the gray matter surface. The lead-fields considered in this thesis for SEEG source localization will then encode 3D subspaces for each position (*i.e.* three columns per position), leaving the estimation of the orientation to the localization methods. When dealing with EEG electrodes, both unconstrained and constrained orientation models will be tested. The constrained orientation (known and fixed for each position) is supported by the fact that EEG electrodes are assumed to record mainly the radial components of the brain sources, thus roughly imposing source orientations orthogonal to the head surface.

Now that the main hypothesis for source estimation in this thesis are set, we analyze in the next sections of this chapter the particular case of oscillatory sources estimation, and we illustrate the main pitfalls implied when trying to localize such activities, either from EEG or SEEG recordings.

3.3 (S)EEG forward problem for oscillatory sources

3.3.1 Forward modelling

Following the analysis of the real signals presented in the previous section, we define here the forward model corresponding to the recordings of oscillatory sources projected on the sensors. Since we are interested in the localization of rhythmic patterns corresponding to steady-state evoked potential, such activity can be often characterized in the frequency domain as the presence of a fundamental component along with possible harmonics. In this section, we focus on the analysis of purely harmonic activities represented by sinusoidal signals. In other words, all sources of interest share the same frequency, but have potentially different phases and amplitudes. The presence of harmonics can be modeled as the super-imposition on the measurements of such single frequency model at multiple of the fundamentals.

Recall the general model of the forward problem from Equation (2.1).

$$\mathbf{X} = \mathbf{K}\mathbf{J} + \varepsilon \tag{3.1}$$

where the lead-field $\mathbf{K} \in \mathbb{R}^{M\times 3N}$ is the lead-field matrix (M electrodes and N 3D dipolar sources), $\mathbf{J} \in \mathbb{R}^{3N\times T}$ is the current density matrix evolving in time (N sources in 3D and T time points). Dropping the noise and rewriting Equation (3.1) as a sum gives:

$$\mathbf{X} = \sum_{i=1}^{N} \mathbf{K}_i \mathbf{J}_i \tag{3.2}$$

where $\mathbf{K}_i$ are $M \times 3$ matrices encoding the 3-dimensional lead-field for each of the dipolar source position i, and $\mathbf{J}_i$ ($3 \times T$) are the time varying amplitudes (in 3D) of source i.

As the system described above is linear, at least some of the sources (dipolar moments) must oscillate at frequency f_0 in order to observe a peak in f_0 on the sensors. Consider a dipole having an amplitude oscillating at f_0 at position i. Suppose that its orientation is varying in time also (as for rotating dipoles appearing in some of the classical source estimation algorithms such as MUSIC). Under these assumptions, one can write, at time instant t, the dipolar moment $\mathbf{J}_i(t)$ as:

$$\mathbf{J}_i(t) = \mathbf{o}_i(t) s_i(t)$$

with $\mathbf{o}_i(t) = [o_{i_x}(t), o_{i_y}(t), o_{i_z}(t)]^T$ the normalized moment vector for the i^{th} source at each instant t (see Section 2.2.1), and where $s_i(t) = d_i \sin(2\pi f_0 t + \varphi_i)$ is a sinusoidal signal at f_0, with amplitude d_i and phase φ_i. In other words, every row of $\mathbf{J}_i$ (x, y, z components) can be seen as amplitude modulation of the sinusoidal signal s_i. The projection of this dipole on one electrode will itself then be a modulated signal, *i.e.*, $s_i(t)$ multiplied by the weighted sum of $o_{i_x}(t), o_{i_y}(t), o_{i_z}(t)$, with the weights given by the corresponding elements of the lead-field matrix. In other words, we should observe on the sensors the spectra of the time varying orientations $o_{i_x}(t), o_{i_y}(t), o_{i_z}(t)$ shifted around f_0. But, according to the experimental observations (see figures 3.1 and 3.2, the peaks in $f_0 = 6$Hz for example are very precise, very well localized in frequency, which implies in turn that the signals $o_{i,x}(t), o_{i,y}(t)$ and $o_{i,z}(t)$ are constant in time (they have Dirac spectra), *i.e.*, the dipoles of interest (oscillating at f_0) have fixed orientations.

According to this analysis, the forward model that we will consider in the rest of the thesis can be summarized as follows: **the observed signals on the (S)EEG sensors are sums of potentials generated by several dipoles situated at different locations in the brain, having fixed orientations and amplitudes that oscillate at very specific frequencies (and potentially harmonics)**.

In other words, and as already stated in Section 2.2.1, the time varying dipolar moments $\mathbf{J}_i$ ($3 \times T$) appearing in Equation (3.2) can be reduced to rank 1 matrices:

$$\mathbf{J}_i = \begin{bmatrix} o_{i_x} \\ o_{i_y} \\ o_{i_z} \end{bmatrix} [s_i(1) \ \dots \ s_i(T)] = \mathbf{o}_i \mathbf{s}_i \tag{3.3}$$

with $\mathbf{o}_i$ the fixed orientation of the dipole over time (3×1 vector of unit norm) and $\mathbf{s}_i$ a row vector ($1 \times T$) of time instants of the sinusoidal signal $s_i(t)$. Note that (3.3) is valid for the sources of interest in our case, *i.e.*, with a fixed orientation and oscillating amplitude. In the following, we will consider that $p \ll N$ such sources exist. The activity generated by the other brain sources will be assimilated to noise.

At time instant t the forward model will write as:

$$\mathbf{x}(t) = \sum_{i=1}^{p} \mathbf{K}_i \mathbf{o}_i d_i \sin(2\pi f_0 t + \varphi_i) + \varepsilon(t) \tag{3.4}$$

with $\mathbf{K}_i$ ($M \times 3$) and $\mathbf{o}_i$ (3×1) defined as above, d_i and φ_i being the amplitudes and phases of the p sinusoidal sources at f_0 and $\varepsilon(t)$ ($M \times 1$) the other electrical activities superimposed on the sensors.

Note that the previous model (3.4) implicitly considers that the orientations $\mathbf{o}$ are fixed but *unknown*. A somehow simpler model can be written if the orientations are supposed to be known (*e.g.*, orthogonal to the head surface in EEG [Dale and Sereno, 1993], see also Section 2.2.1). In this case, the model writes:

$$\mathbf{x}(t) = \sum_{i=1}^{p} \mathbf{a}_i d_i \sin(2\pi f_0 t + \varphi_i) + \varepsilon(t) \tag{3.5}$$

where $\mathbf{a}_i = \mathbf{K}_i \mathbf{o}_i$ are the p fixed orientation lead-field columns ($M \times 1$) encoding the positions *and* the orientation of the p sources of interest. In matrix form, this writes classically as:

$$\mathbf{X} = \mathbf{A}_{1:p}\mathbf{S} + \varepsilon \tag{3.6}$$

with $\mathbf{X}$ the $M \times T$ measurements, $\mathbf{A}_{1:p}$ ($M \times p$) the collections of the p columns of the fixed-oriented lead-field matrix corresponding to the p sources of interest, $\mathbf{S}$ the $p \times T$ matrix grouping the sources of interest $d_i \sin(2\pi f_0 t + \varphi_i)$ (for $i \in \{1..p\}$) and ε the noise matrix ($M \times T$).

Finally, note that the previous models, while defined for a single frequency, can be easily extended to harmonics by adding, in Equations (3.4) and (3.5), supplementary terms with the harmonics frequencies, phases and amplitudes (but preserving the positions and orientations).

The two previous forward models (3.4) and (3.5) yield two different inverse problems of source estimation. Indeed, solving the source estimation problem from model (3.5) implies estimating the positions, amplitudes and phases of the p sources of interest, while for model (3.4), the (fixed unknown) orientation needs also to be estimated.

3.4 Oscillatory sources localization: the ambiguity problem

Brain source localization is an ill-posed badly conditioned inverse problem in general. One way of tackling these difficulties is to regularize by imposing sparse solutions, which in our case makes sense (recall that we are looking for brain regions responding to specific cognitive protocols such as FPVS), and it was shown by extensive SEEG experiments that the number of responding regions is limited ([Jonas et al., 2016]). Nevertheless, the fact that the sources we are looking for are oscillatory raises supplementary problems, namely the existence of alternative solutions involving a very low number of sources, able to explain measurements that were in fact generated by more regions. This ambiguity problem is formulated below.

3.4.1 Mathematical formulation

Consider for the moment the general model from Equation (3.4). For each of the p sinusoidal sources $s_i(t)$, with amplitudes d_i and phases φ_i, one can collapse the 3D lead-field coefficients and the orientations $\mathbf{o}_i$ into a single column vector $\mathbf{a}_i$ such as $\mathbf{K}_i\mathbf{o}_i = \mathbf{a}_i$ ($M \times 1$). If the orientations $\mathbf{o}_i$ are given (known), the column vectors $\mathbf{a}_i$ will also be known, otherwise they will lay in the subspace spanned by $\mathbf{K}_i$. In both cases, the forward model can be rewritten as:

$$\begin{aligned}
\mathbf{x}(t) &= \sum_{i=1}^{p} \mathbf{a}_i d_i \sin(2\pi f_0 t + \varphi_i) \\
&= \sum_{i=1}^{p} \left(\mathbf{a}_i d_i \cos(\varphi_i) \sin(2\pi f_0 t) + \mathbf{a}_i d_i \sin(\varphi_i) \cos(2\pi f_0 t)\right) \\
&= \left(\sum_{i=1}^{p} \mathbf{a}_i d_i \cos(\varphi_i)\right) \sin(2\pi f_0 t) + \left(\sum_{i=1}^{p} \mathbf{a}_i d_i \sin(\varphi_i)\right) \cos(2\pi f_0 t) \\
&= \mathbf{c}_s \sin(2\pi f_0 t) + \mathbf{c}_c \cos(2\pi f_0 t)
\end{aligned} \tag{3.7}$$

In matrix form (*i.e.*, considering all time instants $t = 1 \ldots T$), (3.7) writes:

$$\mathbf{X} = \begin{bmatrix} \mathbf{c}_s & \mathbf{c}_c \end{bmatrix} \begin{bmatrix} \mathbf{s}_s \\ \mathbf{s}_c \end{bmatrix} \tag{3.8}$$

with $\mathbf{X}$ a rank 2 matrix of dimensions $M \times T$, the row vectors $(1 \times T)$ $\mathbf{s}_s$ and $\mathbf{s}_c$ being the f_0 sine and cosine in time. We dropped the noise here for readability.

This development illustrates that a mixture of p oscillating sources can be reduced to a sum of only two sources, a sine and a cosine, with projection gains $\mathbf{c}_s$ and $\mathbf{c}_c$ $(M \times 1)$ that are obtained as a combination of the original gains, orientations and phases. In other words, these new projection gains $\mathbf{c}_s$ and $\mathbf{c}_c$ are linear combinations of the original gains $\mathbf{K}_i$ of the p sources.

Note that the development of Equation (3.7) is only a particular case, one can always split φ_i in a fixed common phase for all sources φ_0 and a variable part $\delta_{\phi,i}$, in which case the columns $\mathbf{c}_s$ and $\mathbf{c}_c$ will have different values. Indeed, one can easily see that if every φ_i in the first row of (3.7) is replaced by a $\varphi_0 + \delta_{\phi,i}$, this will lead to different alternative columns:

$$\mathbf{c}_{s,\varphi_0} = \sum_{i=1}^{p} \mathbf{a}_i d_i \cos(\delta_{\phi,i}) \qquad \mathbf{c}_{c,\varphi_0} = \sum_{i=1}^{p} \mathbf{a}_i d_i \sin(\delta_{\phi,i}) \tag{3.9}$$

i.e., another linear combination of the original $\mathbf{a}_i$ ($\mathbf{K}_i$) gains. The number of theoretical alternative solutions is then much higher (potentially any linear combination of the lead-field columns of the original p sources). This can be seen by generalizing further the previous arguments: the two “basis” signals $\sin(2\pi f_0 t + \varphi_0)$ and $\cos(2\pi f_0 t + \varphi_0)$ do not actually need to form an orthogonal basis, they just need to be linearly independent in order to span the same space. In other words, for arbitrary but different phases, one can find two columns $\mathbf{c}_{alt,1}$ and $\mathbf{c}_{alt,2}$ that will yield (approximate) alternative solutions as long as the space they span is included into (or close enough in the sense of subspace correlation) the space spanned by the original $\mathbf{a}_i$ ($\mathbf{K}_i$) gains, $i = 1 \ldots p$.

If, on the other hand, these two column vectors $\mathbf{c}_{alt,1}$ and $\mathbf{c}_{alt,2}$ lay into (or are close to) one of the subspaces spanned by any group of 3 columns $\mathbf{K}_i$ of the lead-field matrix, corresponding to some position elsewhere in the brain, source localization algorithms can be mislead: they might converge to these alternative solutions and thus estimate alternative sources at different positions, with different orientations and phases. For simplicity, we will drop the alt, i indices in the following, which is equivalent to considering only the initial alternative model (3.7) with $\mathbf{c}_c$ and $\mathbf{c}_s$.

3.4.2 Physical plausibility of the alternative solutions

The remaining question resides in the existence of some 3-columns lead-field blocks $\mathbf{K}_i$ in the used $\mathbf{K}$ lead-field matrix, such as they can be linearly combined (through some orientation $\mathbf{o}_i$) in order to obtain a vector approximately aligned with (at least one of) these alternative column candidates $\mathbf{c}_s$ and $\mathbf{c}_c$.

This question can be simply addressed by regression: if the vectors $\mathbf{c}_s$ and $\mathbf{c}_c$ lie in the span of any 3-columns lead-field block $\mathbf{K}_i$, that is, if there exists a linear combination (thus an orientation $\mathbf{o}_i$) of the three columns that approximates the alternative gains $\mathbf{c}_s$ and $\mathbf{c}_c$, then a source localization algorithm might converge to those alternative $\hat{\mathbf{c}}_s$ and $\hat{\mathbf{c}}_c$ solutions. Indeed, if the error is small, it will be impossible to distinguish between this kind of alternative solution and the results obtained for noisy signals or for lead-field model errors.

The question arises next is: is this a kind of degenerate case seldom encountered on real localization problems or it is commonly encountered for realistic lead-field models? The following approach aims to bring a quantified answer to this question.

As mentioned above, we restrict the analysis to the identity of equation 3.7 where the sum of p sources break down to the sum of a zero-phase sinus with a zero-phase cosine. For any p sources, the alternative coefficient columns $\mathbf{c}_s$ and $\mathbf{c}_c$ can thus be obtained. Focusing on $\mathbf{c}_s$, we scan the N source positions embedded in the lead-field matrix $\mathbf{K}$ and regress $\mathbf{c}_s$ on the subspace spanned by the columns for each source position, obtaining thus the source amplitude (and orientation) as the regression coefficients. Next, we choose the source position i_s as the one that correspond to the best regression, *i.e.*, to the alternative column $\hat{\mathbf{c}}_s$ that best fits the original $\mathbf{c}_s$. A similar procedure applies for choosing i_c. Formally, this writes:

$$i_s = \underset{i}{\operatorname{argmin}}(\|\mathbf{c}_s - \mathbf{K}_i\mathbf{K}_i^{+}\mathbf{c}_s\|) \quad , \quad \hat{\mathbf{c}}_s = \mathbf{K}_{is}\mathbf{K}_{is}^{+}\mathbf{c}_s \tag{3.10}$$

$$i_c = \underset{i}{\operatorname{argmin}}(\|\mathbf{c}_c - \mathbf{K}_i\mathbf{K}_i^{+}\mathbf{c}_c\|) \quad , \quad \hat{\mathbf{c}}_c = \mathbf{K}_{ic}\mathbf{K}_{ic}^{+}\mathbf{c}_c \tag{3.11}$$

$\mathbf{K}_i^{+}$ represents the pseudo-inverse of the matrix $\mathbf{K}_i$ ($M \times 3$).

Note that, for a fixed known orientation lead-field $\mathbf{A}$ (with columns $\mathbf{a}_i$), as appearing in model 3.5, the best fitting columns $\hat{\mathbf{c}}_s$ and $\hat{\mathbf{c}}_c$ will simply be given by the columns of $\mathbf{A}$, which are the most correlated to the alternative column gains $\mathbf{c}_s$ and $\mathbf{c}_c$. Clearly, ambiguity is less likely because it is more constrained: original sources should have particular amplitudes and phases such as the linear combination of the original $\mathbf{a}_i$ columns yield, or be close to, some other $\mathbf{a}_k$ columns.

In order to quantify the error that such alternative solutions will yield with respect to the original data, one can compute alternative reconstructed measurements using the approximations $\hat{\mathbf{c}}_s$ and $\hat{\mathbf{c}}_c$:

$$\hat{\mathbf{x}}(t) = \hat{\mathbf{c}}_s \sin(2\pi f_0 t) + \hat{\mathbf{c}}_c \cos(2\pi f_0 t) \tag{3.12}$$

Finally, the accuracy between the original signals $\mathbf{X}$ (all time instants) and the ones reconstructed from the alternative sources (Equation 3.12) is computed using the goodness of fit (GOF) metric defined as:

$$GOF = 1 - \left(\frac{\|\mathbf{X} - \hat{\mathbf{X}}\|}{\|\mathbf{X}\|} \right)^2 \tag{3.13}$$

As our aim is to evaluate this ambiguity problem on realistic lead-fields, in the next section a simulation framework is given. At the light of some simulated examples, we then illustrate the pitfalls of localizing sinusoidal source activities having the same frequencies.

3.5 Simulation results

3.5.1 Simulation setup

In this section we describe the realistic setup used to compute the activity of single frequency oscillatory sources recorded by scalp and intracranial EEG electrodes. The forward models used to construct the (S)EEG lead-fields are described. Then, the source configurations to compute both types of recordings are presented.

Scalp EEG simulations

EEG scalp recordings were simulated by using a realistic head model with three compartments (Colin 27) extracted from Brainstorm toolbox ([Baillet et al., 1999]). The cortical layer mesh (inner shell) had 7292 nodes, and the outer skull and the scalp mesh (outer shell) had 1922 nodes. The possible source positions were simulated as a regularly spaced grid (7 mm) constructed inside the inner shell, which yielded N = 6184 source positions. The scalp electrodes (M = 64) were simulated according to the approximate 10-10 system of a Biosemi Cap. Two lead field matrices were constructed, the first using sources with constrained orientations (fixed and known orientations), 64×6184 and the second where the orientations are left unconstrained (in order to simulate fixed but unknown orientations), $64 \times (3 \cdot 6184)$. The EEG scalp potentials were simulated by projecting the sources on the sensors using a boundary element model (BEM) implemented in the Helsinki toolbox [Stenroos et al., 2007], with conductivity ratios of 40:1 between the brain and the skull and 1:1 between brain and scalp.

A second simulation was done using a different lead-field matrix, based on finite element modelling (FEM) (see [Vallaghé, 2010; Hofmanis, 2013; Caune et al., 2014] for a detailed description). We used the non-linear MNI-ICBM152 atlas [Fonov et al., 2011], obtained by averaging the MRI scans of 152 individuals. The head volume is segmented into five meshed compartments: white matter, gray matter, cerebro-spinal fluid (CSF), bone and scalp. Constant isotropic conductivities were assigned for a each tissue, namely $0.33S/m$ for the gray matter, $0.2S/m$ for the white matter, $0.33S/m$ for the scalp and $0.004S/m$ for the skull bones [Geddes and Baker, 1967]). As, for this model, the gray matter mesh is available, we only considered source positions inside the gray matter (on a grid of 1cm). The resulting number of dipole positions was 509. As for the BEM simulation, we used the 10-10 EEG cap electrodes positions, yielding thus lead-field matrices of size 64×1527 for the free oriented models, respectively 64×509 for the fixed (radial) orientation model. The potentials for every electrode were computed using the FEM model implemented in the SciRun software suite developed by the Scientific Computing and Imaging Institute (Utah, USA) [Institute, 2016].

Stereo-EEG (SEEG) simulations

Regarding the SEEG recordings, they were simulated the same FEM model described above (classical BEM models do not evaluate the potentials inside the considered volumes, only on their surfaces). We used the same realistic SEEG implantation as in [Caune, 2017; Le Cam et al., 2017], with 12 electrodes, 9 in the right hemisphere and 3 in the left ($M = 186$ sensors in total). The resulting lead-field matrix $\mathbf{K}$, 186×1527, was used to generate SEEG potentials from the active sources. Unlike in EEG, we did not consider for the SEEG simulation fixed orientation sources: a radial (orthogonal to the head surface) is unjustified for SEEG, while imposing an orientation orthogonal to the gray matter mesh surface remains approximate and highly dependent on the accuracy of the segmentation.

Sources

To compute both scalp and intracranial EEG recordings, different configuration of sources were simulated ($p = 3, 4, 5$). The time courses were in all cases sinusoidal signals at a given common frequency $f_0 = 6Hz$ but having different (random) amplitudes s_i and phases φ_i (amplitudes according to a normal distribution with a mean of 5 (arbitrary units) and a standard deviation of 1, phases drawn from a uniform distribution on $[0, \ \pi]$). The sampling frequency was 2100 Hz and the duration 10s. The positions and orientations of the 3 configuration of sources were selected randomly (orientations according to a normal distribution with 0 mean and positions among the N possible ones). One thousand simulations were computed for each source configuration varying the random parameters above, with no noise.

3.5.2 Results

Ambiguity quantification

In Figures 3.3 and 3.4 are given the results in form of graph bars. The rows correspond to the number of simulated sources, and the columns represent the simulation setup. Figure 3.3 shows the results of the EEG simulations: the first two columns describe results obtained for the BEM based EEG model (6184 sources, 64 electrodes), with either fixed known orientations (first column, model (3.5)) or fixed but unknown orientations (second column, model (3.4)); the next two columns illustrate similar results, but for the FEM based EEG model (509 sources, 64 electrodes), again with known fixed orientations (third column) and with unknown fixed orientations (fourth column). Figure 3.4 shows the results of the SEEG simulations, all the columns using the model with fixed but unknown orientations, but varying the number of sensors (M): the first column illustrates all the SEEG electrodes (9 electrodes, 186 sensors), the second with contacts obtained by down-sampling over the SEEG sensors, the third column using six electrodes (three at each hemisphere) and finally, the fourth column with five electrodes (three in the left and two in the right hemisphere).

The simulation outcomes were grouped in three sets: $2/2$ (in blue), when both i_s and i_c are within a distance of 10 mm from one of the original p positions, $1/2$ (in red) when only one of the two alternative sources is within this distance and $0/2$ (in yellow) when both alternative sources are far from the original ones. For each subfigure, the color bar illustrates the proportion of different outcomes among the 1000 simulations, and the box-plots represent the GOF values (3.13) between the reconstructed signals from the alternative sources (thus using $\hat{\mathbf{c}}_s$ and $\hat{\mathbf{c}}_c$) and the original ones (obtained from the p initial sources with their lead-field gains and orientations). The three box-plots correspond to the three described outcomes ($2/2$, $1/2$, $0/2$).

As observed, undetermined ambiguous situations ($1/2$ or $0/2$ outcomes) are found in all the considered cases, but with various degrees. First, when sources with known (first and third column) and unknown (second and fourth column) orientations projected on EEG electrodes are compared, those with unknown orientations exhibit a higher proportion of alternative sources far from the original ones (in yellow, 0/2), and fewer cases where the alternative sources were close to the original ones (in blue, 2/2). Indeed, model with unknown orientations are far more vulnerable to the ambiguity problem, the degree of freedom offered by the lead-field being higher (*i.e.*, the alternative column vectors only need to approximately lay in the subspace spanned by some of the original lead-field groups of 3 columns, while for the known orientation, they need to be correlated with one of the original lead-field columns). It is also important to note that no significant differences can be seen between the BEM and the FEM simulations, despite the higher density and the much higher number of possible sources in the BEM simulations. Finally, regarding the number of original sources $p = 3, 4, 5$, it is observable the ambiguity becomes more pronounced with the increase of the number of sources. Indeed, recall that the alternative columns $\mathbf{c}_s$ and $\mathbf{c}_c$ are themselves linear combinations of the original lead-field columns of the p simulated sources: the bigger p, the higher the dimension of the spanned subspace, *i.e.*, more degrees of freedom for these alternative gains.

The SEEG simulation yields, on the other hand, different results. When comparing the sources with unconstrained orientations projected on EEG (Figure 3.3, second and fourth column) and SEEG with all the sensors (Figure 3.4, first column), SEEG exhibits a greater number of cases with one alternative source close to the original ones (red, 1/2), following for those cases where the two alternative sources were close to the original ones (blue, 2/2), and with less cases where the two alternative source were far from the original ones (yellow, 0/2). As mentioned previously, for EEG the biggest results correspond to the cases where the alternative sources were far from the original ones (yellow, 0/2), following with the cases where one alternative source was close to the original ones (red, 1/2), and just a minimum of cases where for the two equivalent sources close to the original ones (blue, 2/2). In this EEG/SEEG comparison, we should also consider that SEEG is more dense in terms of number of sensors than EEG. In fact, since there are many and everywhere, a good part of these sources will be seen mainly (*i.e.*, with a big gain) on few electrodes, and it would be easier to find ourselves in the situation without a “real mixture” and therefore less ambiguity. In order to verify this condition, we have tested three more different conditions. In figure 3.4 is illustrated this condition, the second column corresponds to the down-sampling at the electrodes, one contact out of three, resulting in 62 sensors (comparable to the number in EEG), and the second column with three electrodes in each hemisphere, resulting in 95 sensors and the fourth column with five electrodes, the three in the left hemisphere and leaving two electrodes in the right hemisphere, resulting in 65 sensors. The rows again correspond to the number of simulated sources, from top to bottom $p = 3,4,5$. For these three conditions, it is observable the increase of the 0/2 and 1/2 cases, while decreases in 2/2.

In the second column, the results are less far from the results for 185 SEEG sensors, which might indicate that the number of contacts in each electrode keeps a more or less similar condition as the one achieved by 185 SEEG sensors. In the third column, the results expose more notable differences comparing with the previous two conditions, being even worse in the fourth column. We can observe that the number of 2/2 cases is reduced drastically and more 0/2 cases increased over the 1/2 cases, in particular for this last fourth column. Since there are less electrodes distributed in the brain, with most likely small source gains, the possibility of capturing the activity of the sources becomes harder.

Finally and the most important, regardless of the simulation setup (BEM/FEM, EEG/SEEG, known/unknown orientation), the GOFs for the three outcomes ($2/2$, $1/2$, $0/2$) have comparable values, with a median above 0.8 for most of the cases and only few cases where the median nearly reaches this value. In other words, a source localization algorithm, especially in noisy situations, might easily converge to a false solution panel (an alternative one), as it is not possible to distinguish between reconstruction errors due to noise or to wrong (alternative) localization of the sources.

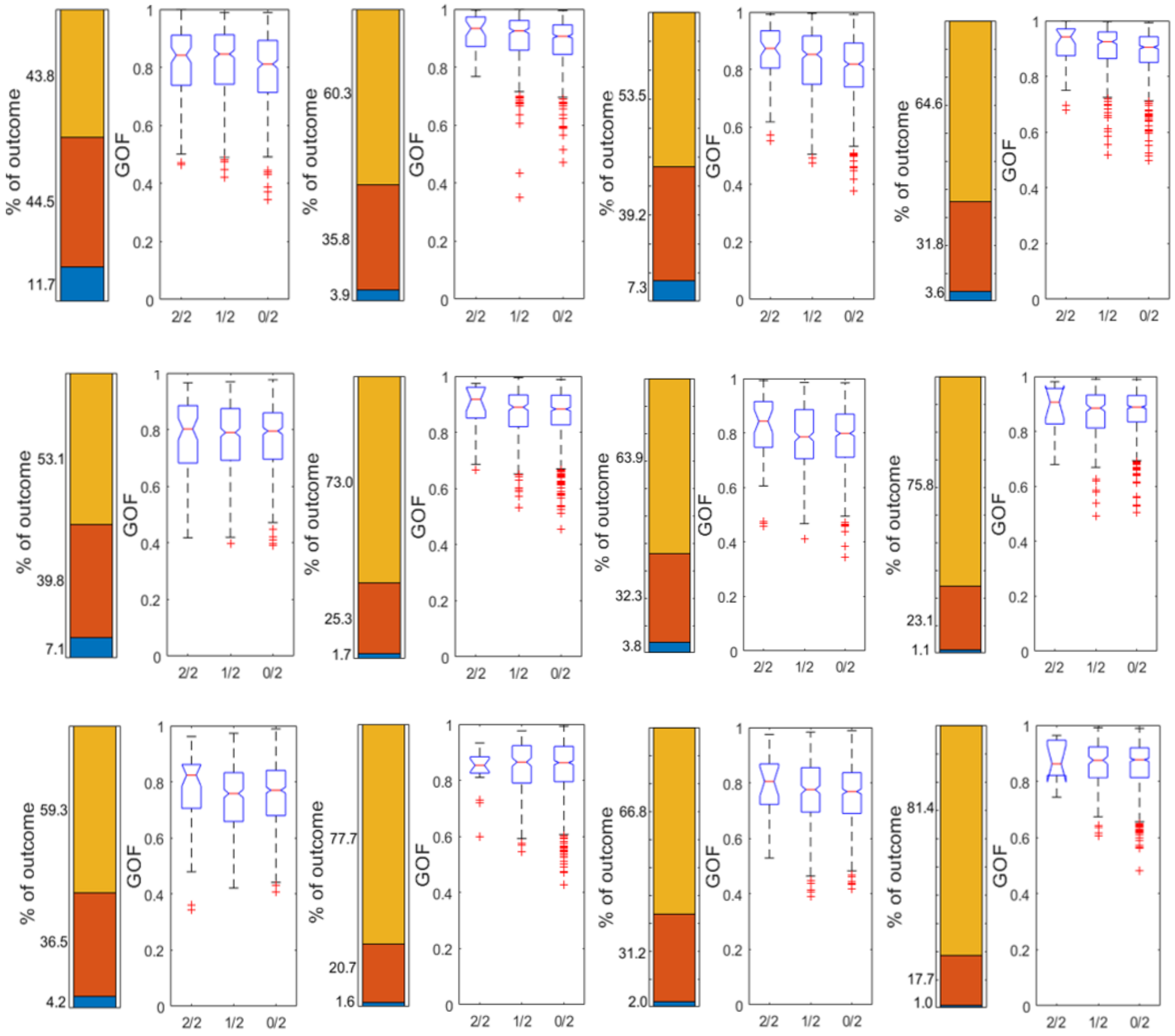

FIGURE 3.3 – Ambiguity quantification results. Each row from top to bottom shows the results depending of number of simulated sources, $p = 3$ (first row), $p = 4$ (second row), and $p = 5$ (third row). Each column from left to right represents the used model on EEG signals : simulated via a BEM model with $N = 6184$ source positions with known fixed orientation (first column) and with unknown fixed orientation (second column), EEG signals simulated via a FEM model restricted to the gray matter, having $N = 509$ source positions with known fixed orientation (third column) and with unknown fixed orientation (fourth column). On each sub-figure, left colored bar shows the proportion of different outcomes. In blue (2/2): both alternative sources were among the corresponding p simulated ones; in red (1/2): one of the sources was far from the simulated ones; in yellow (0/2): both alternative sources were far from the simulated ones. In each subfigure, the right panel presents the GOF of the reconstructed signal $\hat{\mathbf{X}}$ with respect to the original $\mathbf{X}$ for the possible outcomes in the corresponding left panel.

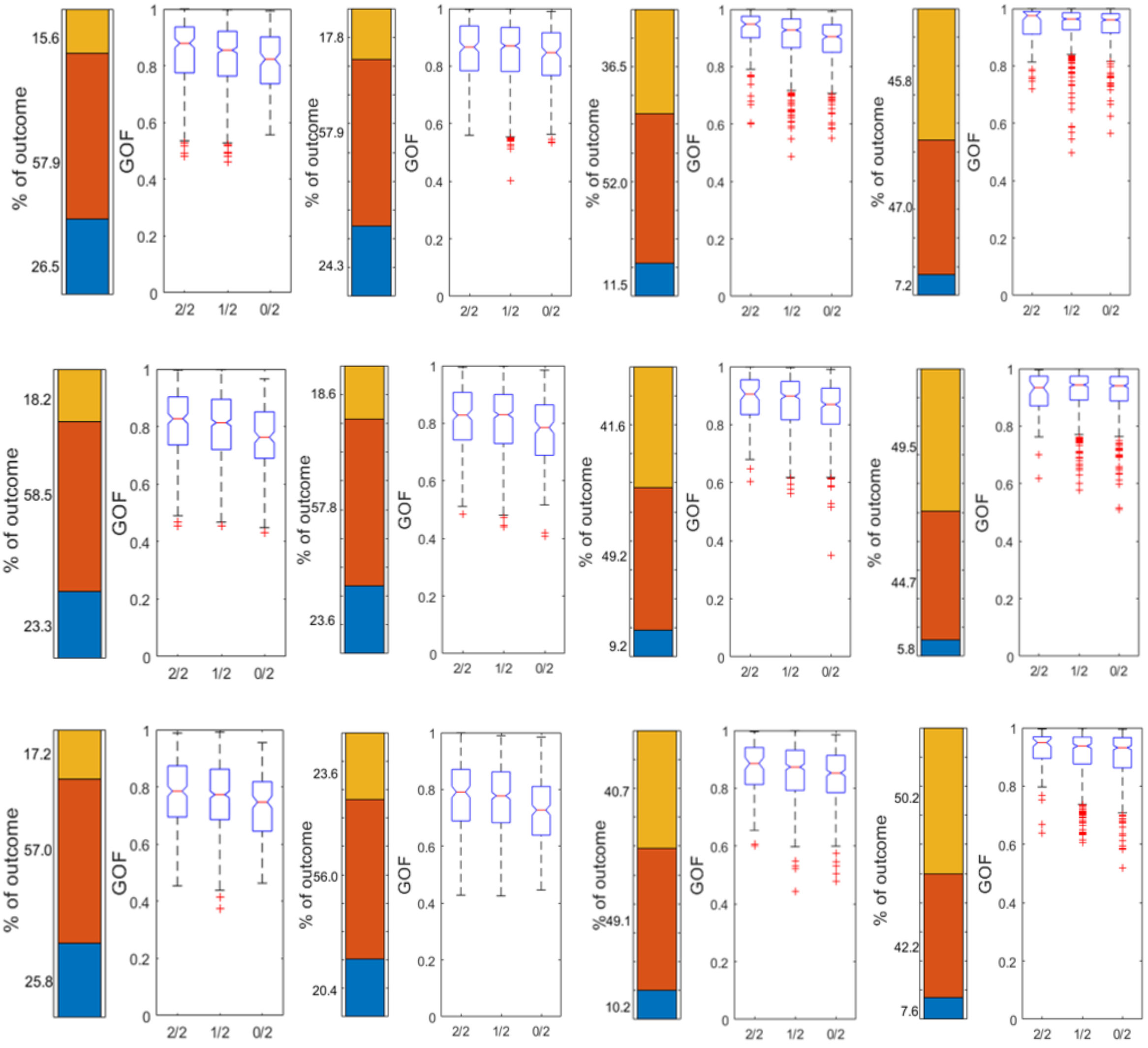

FIGURE 3.4 – Ambiguity quantification results. Each row from top to bottom shows the results depending of number of simulated sources, $p = 3$ (first row), $p = 4$ (second row), and $p = 5$ (third row). Each column represents a setup of sensors in SEEG signals simulated via a FEM model restricted to the gray matter, having $N = 509$ source positions with unknown fixed orientation. The first condition consists in the total SEEG implantation with 186 sensors (first column). The second in taking one contact out of three, resulting in 62 contacts (second column). The third condition consists in taking three electrodes in the right and left hemisphere (from left hemisphere are all ones implanted), resulting in 95 contacts (third column). The fourth condition consists in the three electrodes implanted on the left hemisphere and two electrodes on the right hemisphere, resulting in 65 contacts (fourth column). On each sub-figure, left colored bar shows the proportion of different outcomes. In blue (2/2): both alternative sources were among the corresponding p simulated ones; in red (1/2): one of the sources was far from the simulated ones; in yellow (0/2): both alternative sources were far from the simulated ones. In each subfigure, the right panel presents the GOF of the reconstructed signal $\hat{\mathbf{X}}$ with respect to the original $\mathbf{X}$ for the possible outcomes in the corresponding left panel.

Illustrative examples

We show in this subsection some typical examples of simulated signals. The first aim is simply to validate the signals themselves by comparing them with the real signals analyzed at the beginning of this chapter. The second is to illustrate typical situations in which alternative solutions are most likely to occur (outcome 0/2 in the previous subsection and figure 3.3), as well as when they are unlikely. Finally, the third objective is to illustrate the performances of source localization algorithms for these examples and relate them to the ambiguity problem described above.

We use the oscillating sources setup described in Section 3.5.1 to reproduce frequency domain plots as observed on real FPVS data (such as those presented in Section 3.2), and to analyze how the source localization methods behave facing these particular data. In these examples, both EEG and SEEG signals are simulated based on $p = 3$ oscillating sources projected on the sensors, with different phases. Figures 3.5 and 3.6 illustrate the source configurations for these example cases (top and lateral view, Subfigures (a),(d) and (b),(e) respectively). Two situations are considered, the first one (first row of each figure) being the case when the source are far from each other in the head volume, *i.e.* distant brain regions are activated by the stimuli. The projections of these sources are well separated on the sensors, as illustrated by polar plots on the first row, 3rd column of each figure (Subfigures (c)) where straight aligned points can be seen, thus identifying sub-group of electrodes mainly impacted by a single source. An illustrative example is the source recorded by the sensors in black in the SEEG case in Figure 3.6(c). Big amplitude and phase alignment indicate that the original source is close to those black sensors and also is not disturbed by any other surrounding activity.

Inversely, the second simulated situation involves sources lying in closer brain regions, more precisely projecting onto common electrodes, thus implying that sensors will be impacted significantly by several (two to three sources in these illustrative cases), resulting in a mixture of sources that need to be disentangled by the localization methods. In particular for SEEG electrode projections in Figure 3.6(f), notable variations in the phase values are observed. For instance, those sensors closer to the sources *e.g.*, black, green and purple sensors, clearly show a mixture of phases. The visible not-alignment in phase on these sensors, in addition to their big amplitudes (radius), indicate that they are being disturbed by different surrounding activities.

RAP-MUSIC source localization algorithm, described in Chapter 2, has been applied on these working examples, leading for all of them to the same conclusions: when the sources mainly impact separated sub-groups of electrodes, the localization methods are easily able to retrieve their positions with acceptable precision (set as position errors below $1cm$ in this thesis). This is the case for both first case examples (first row of each figure). For illustration purposes, in Figures 3.5(a) and 3.5(b) and 3.6(a) and 3.6(b) are given the localization results as red arrows when RAP-MUSIC is applied to these data. It is on the other hand noteworthy that only two among the 3 simulated sources were found. This can be explained in two steps. First, as the dimension of the source space is 2 (*i.e.*, the

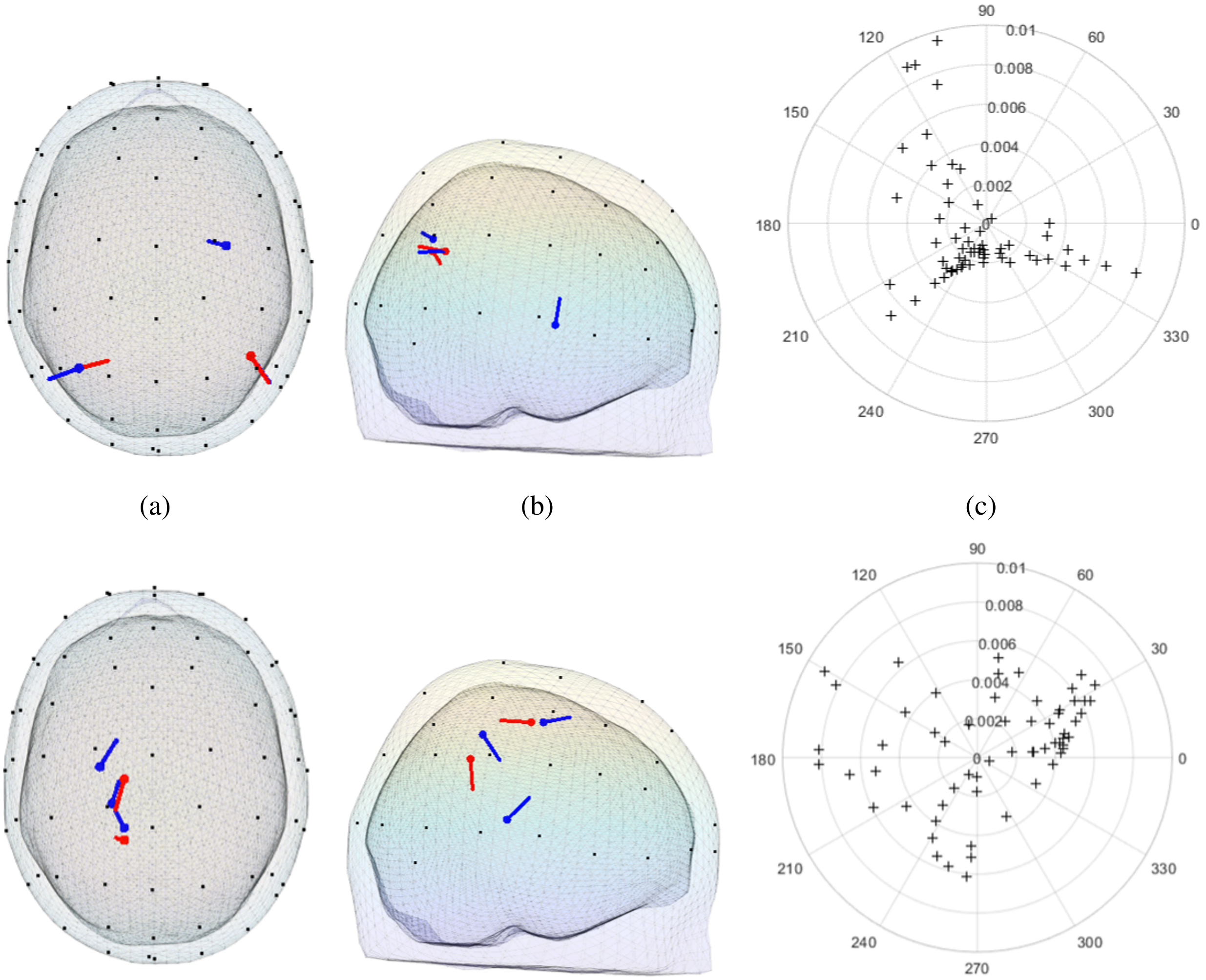

(a) (b) (c)

(d) (e) (f)

FIGURE 3.5 – Examples with $p = 3$ simulated sources on EEG electrodes. Positions and orientations of the sources are represented in blue arrows and EEG electrodes represented in black dots. Top: case representing sources far from each other. Bottom: case representing sources lying in nearby brain regions. First and second columns: top (a),(d) and lateral (b),(e) view of the source locations in the brain. Third column: polar plots (c),(f) representing the magnitudes and phases for the frequency of interest (sources at $6Hz$). In red arrows the reconstructed sources using RAP-MUSIC. For illustrative purposes, source amplitudes are shown 20% larger of their original.

rank of the measurement matrix is 2, as all mixture can be reduced to a sine and a cosine), RAP-MUSIC will only find two sources. Second, when analyzing the mixture models (3.5) and (3.4), the fact that on a subset of electrodes a single source is present translates into the fact that the columns $\mathbf{a}_i$ (corresponding to source i) have negligible values on some electrodes (far from source i). The best source estimates will then be obtained by choosing, among the p ones, the two that generate big amplitudes on the sensors, the third one being simply neglected.

However, and as it could be expected, problems are arising when the main projection of the source activities are visible on the same set of electrodes, hence when the localization methods have to separate these activities and localize them in the source space. On the second example cases with a mixture of sources on the electrodes, none of the algorithms were successful in localizing the sources (results from RAP-MUSIC are again given as examples, red arrows in Figures 3.5(d) and 3.5(e) and 3.6(d) and 3.6(e). More surprisingly at first sight, although the true number of sources was correctly estimated and the electrodes activity well reconstructed (high goodness of fit values), the estimated positions of these sources were still erroneous. This illustrates the existence of an alternative source configuration yielding the same measurements, luring the localization methods. Indeed, taking a closer look at the results, it turned out that the phases and amplitudes of the estimated sources where different compared to those of the simulated ones, pointing out that equivalent purely sinusoidal source configurations can be found in the source space, by combining differently their phases and amplitudes. This illustrates the ambiguity problem formalized previously, explaining why the localization of purely sinusoidal sources turns out to be a particularly challenging task.

3.6 Conclusion

We have analyzed in this chapter the undetermined problem of localizing multiple oscillatory sources with shared frequency rate. We have formalized the ambiguity problem occurring when trying to localize such activities and evaluated under simulation in which extent this problem was likely to occur.

Straightforward mathematical development shows that the sum of an arbitrary number of oscillatory sources at a given frequency can always be decomposed in a sum of two linearly independent sinusoidal activities, up to scaling vector coefficients representing the projection of these alternative sources on the sensors. Focusing on well identified frequency components of the activities to be localized indeed provides higher signal to noise ratio, but at the cost of a worse conditioning of the inverse problem. This inversion is in part regularized by the fact that the scaling (alternative) coefficients need to be aligned with the columns of the used lead-field. However in practice, due to noise and background activities as well as imprecision of the lead field matrix, perfect reconstruction of the data is not feasible, and it becomes difficult to distinguish between errors due to badly localized sources and these due to data and model uncertainties.

This aspect has been illustrated in this chapter on simulated data, under constrained (EEG) or unconstrained (EEG, SEEG) orientation prior. As expected, degrees of freedom are higher when the orientation of the dipoles have to be estimated, resulting in higher indeterminacy of the solution: more alternative source configurations are identified in this case compared to when the orientation of the dipole are determined. However, better regularization on the problem are provided when the sensors cover a wide part of the brain volume, being thus closer to the sources. This is the case in

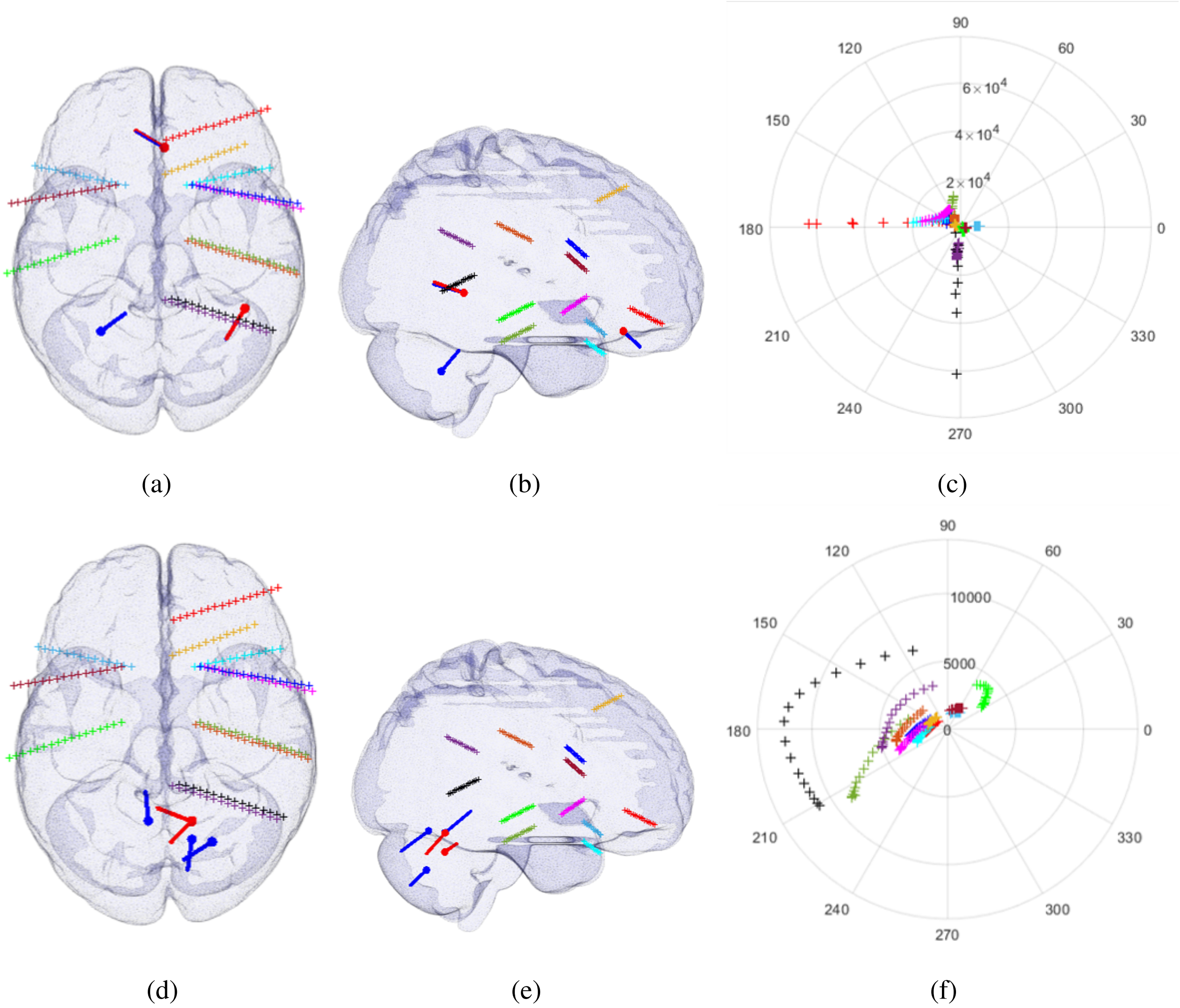

(a) (b) (c)

(d) (e) (f)

FIGURE 3.6 – Examples with $p = 3$ simulated sources on SEEG electrodes. Positions and orientations of the sources are represented in blue arrows and SEEG electrodes represented represented as crosses and each one with a different color. Top: case representing sources far from each other. Bottom: case representing sources lying in nearby brain regions. First and second columns: top (a), (d) and lateral (b), (e) view of the source locations in the brain. Third column: polar plots (c), (f) representing the magnitudes and phases for the frequency of interest (sources at 6Hz). In red arrows the reconstructed sources using RAP-MUSIC.

the SEEG simulations, where a large number of sensors cover the brain volume, and where original columns (positions) of the sources are better recovered.

In the light of these observations, we will propose in the two next chapters different strategies for this specific problem of oscillatory source localization. In Chapter 4, the localization problem with known orientation priors (fix-oriented lead-field $\mathbf{A}$) is addressed, both in time and frequency domain. For the latest, a formalization of the problem is provided and discussed. In Chapter 5 the fixed orientation constraint is relaxed and an original Matching Pursuit type algorithm is developed, where atoms to be selected are rank-1 subspaces of matrices $\mathbf{K}_i$ instead of single columns $\mathbf{a}_i$ (*i.e.*, when both the position and fixed orientation of the sources are to be estimated).

Chapter 4

Oscillatory sources localization. Fixed known orientation case

4.1 Introduction

In this chapter, we evaluate source localization approaches when *a priori* information on predominant frequencies in the activities of the source is available, *i.e.*, when sources of interest are band-limited or even pure oscillations. Since the main hypothesis is that the recorded signals are generated by few active regions, possibly organized in a network, we narrow down our interest to approaches enforcing sparsity principle. Indeed, this solution is applied considering that our target application is source reconstruction during fast periodic visual stimulation (FPVS) (see section

1.4.2.1), for which it was shown (using SEEG recordings) that they are localized in specific brain areas [Jonas et al., 2016]. We focus thus our localization approach on oscillatory sources and spatially sparse approaches. More precisely, we adapt a method derived from the Matching Pursuit principle used for sparse localization in EEG called Single Best Replacement (SBR) [Soussen et al., 2011], already applied on EEG for source localizations enforcing both space and time-frequency sparsity [Korats et al., 2015].

The reconstruction performance is evaluated for SBR and also compared with the another algorithm from the Matching Pursuit/step-wise regression family, *i.e.*, Orthogonal Least Squares (OLS), as well as with two iterative (sparse) versions of MUSIC, *i.e.*, Recursively Applied and Projected (RAP-MUSIC) and Truncated RAP (TRAP-MUSIC). We apply and evaluate these algorithms classically in the time domain, but we also adapt them in the frequency domain, exploiting the available frequency information and the better signal to noise ratio observed in the FPVS protocols we are interested in.

4.2 Methodology/periodic source localization

As described in Section 2.2.1, we consider in this chapter a simplified forward model considering fixed and known source orientations (i.e. for every possible position only one predefined orientation is considered). Although restrictive, this simplified lead-field can be justified by biological considerations: dipolar current sources represent population of pyramidal neurons, which are not freely oriented but mostly orthogonal to the gray matter surface (see Section 1.3.3.1).

4.2.1 Model

Using the notations defined in the previous chapters and the fixed known orientation assumption, a linear forward model projecting N sources to M electrodes expresses scalp recordings $\mathbf{X}$ as a linear combination of source amplitudes $\mathbf{S}$ through the propagation coefficients stored in the lead-field $M \times N$ matrix $\mathbf{A}$, plus noise ε. Every column of $\mathbf{A}$ corresponds to a specific source position (*i.e.*, contains the propagation coefficients between that specific position and the electrodes), while every row of $\mathbf{S}$ represents the time evolution of one source, with a specified position and orientation.

$$\mathbf{X} = \mathbf{A}\mathbf{S} + \varepsilon \tag{4.1}$$

The linear forward model in equation (4.1) is generally expressed in the time domain, meaning that $\mathbf{X}$ and $\mathbf{S}$ are, respectively, measurements and source amplitudes at different time instants (matrices $M \times T$ and $S \times T$, with T the number of time samples). But model (4.1) is valid under any linear transformation of the signals such as the Fourier transform or linear filtering in specific frequency bands. To be more specific, right multiplying (4.1) by the Fourier basis matrix will lead to:

$$\mathbf{X}_f = \mathbf{A}\mathbf{S}_f + \varepsilon_f \tag{4.2}$$

where the index f indicates that the matrices are the complex Fourier transforms.

Moreover, the model is valid for any specific time instant (*i.e.*, for every column of $\mathbf{X}$ and $\mathbf{S}$), when considered in time, as well as for any specific frequency bin (or band after band-pass filtering), when considered in frequency (*i.e.*, for every column of $\mathbf{X}_f$ and $\mathbf{S}_f$) .

The Equation 3.7 illustrating the ambiguity of the forward problem for oscillating sources at f_0 frequency rewrites (taking the Fourier transforms of the sine and the cosine) as:

$$\begin{aligned}
\mathbf{x}(f) &= \frac{1}{2}\mathbf{c}_c\left(\delta(f-f_0)+\delta(f+f_0)\right)+\frac{1}{2j}\mathbf{c}_s\left(\delta(f-f_0)-\delta(f+f_0)\right) \\
&= \frac{1}{2}\mathbf{c}_c\left(\delta(f-f_0)+\delta(f+f_0)\right)-\frac{1}{2}\mathbf{c}_s\left(\delta(f-f_0)-\delta(f+f_0)\right) \\
&= \frac{1}{2}(\mathbf{c}_c-j\mathbf{c}_s)\delta(f-f_0)+\frac{1}{2}(\mathbf{c}_c+j\mathbf{c}_s)\delta(f+f_0)
\end{aligned} \tag{4.3}$$

One can easily see that, for single frequency sources, $\mathbf{x}(f)$ is null for all frequencies except f_0 and $-f_0$ and thus the data matrix $\mathbf{X}_f$ will only have two columns of complex values (first one corresponding to f_0, second one to $-f_0$):

$$\mathbf{X}_f = \frac{1}{2}\begin{bmatrix}\mathbf{c}_c & \mathbf{c}_s\end{bmatrix}\begin{bmatrix}1 & 1\\ -j & j\end{bmatrix} \tag{4.4}$$

Equivalently, instead of taking the complex matrix $\mathbf{X}_f$ for two symmetric frequencies, one can take the real and imaginary parts of one of the two frequencies (f_0 or $-f_0$), which will be equal to $\mathbf{c}_c$ and $(-)\mathbf{c}_s$. In both cases, the data matrix will be rank 2.

It is important to note here that, when considering noise, the time model is not rank deficient (adding independent noise will condition the data matrix $\mathbf{X}$), the price to pay being a lower SNR. On the contrary, in the frequency domain, if only the frequency of interest is selected, the SNR is very high but the problem is badly conditioned.

Finally, note that if several frequencies are selected as being of interest (*e.g.*, fundamental and harmonics), the previous decomposition can be made separately for each one, meaning that the dimension of data space (rank of the data matrix) will be 2 × the number of harmonics (frequencies of interest).

4.2.2 Inverse problem

Since the full lead-field or gain matrix $\mathbf{A}$ $(M \times N, M \ll N)$ has a number of electrodes M much smaller than the number of possible source locations N, the system does not have a unique solution and constraints need to be imposed in order to reduce the solution space. Recall that, as we look for few active regions, our model is given by (3.6), which can be interpreted as a "shift" of the majority of the columns in $\mathbf{A}$ (corresponding to sources not related to the FPVS protocol) into the noise matrix (*i.e.*, only $p \ll N$ columns are selected to form $\mathbf{A}$).

Among the sparsity promoting algorithms, the iterative ones appear to be good candidates, as they will naturally increase the number of sources starting from a single one until a certain Goodness of Fit is obtained (or some other equivalent stopping criterion). We will focus here on two classes of algorithms: the iterative versions of MUSIC (RAP and TRAP, see chapter 2) and the less known, at least in the brain source localization field, regularized $l_2 l_0$ algorithms from the Matching Pursuit family. As we have proposed above, along with the classical time models, a model is proposed for the frequency domain. We will explain the adaptations that are needed for the latter.

MUSIC algorithms. In classical approaches, RAP-MUSIC and TRAP-MUSIC are applied in time domain. They are based on an estimation of the source space using the eigenvalues of the data covariance/scatter matrix $\mathbf{R_X} = E[\mathbf{X}\mathbf{X}^T] = \mathbf{V}\Sigma\mathbf{V}^T$. More precisely, the source space dimension is based on thresholding the eigenvalues (using some model-order estimation methods such as AIC or MDL, which can be seen as keeping only those above the noise values). If r is the number of selected values, a basis for this source space will be constituted by the corresponding r eigenvectors of $\mathbf{R_X}$ (see description in Chapter 2), denoted for convenience $\mathbf{V}_{1..r}$

For oscillatory sources (single frequency) and no-noise models, this dimension will be upper bounded at 2 (or 2 × the number of harmonics), but in noisy situation it needs to be evaluated as mentioned above. Selecting this source space is equivalent to discarding the noise components of the data. Consequently, MUSIC algorithms will only attempt to explain "denoised" data, *i.e.*, the part of the signals belonging to the space spanned by the selected eigenvectors.

In the frequency domain on the other hand, selecting the frequencies of interest (fundamental and possibly harmonics) will directly perform the denoising step very efficiently. The inconvenient of the approach is the conditioning of the new data matrix $\mathbf{X}_f$ and thus of its scatter matrix. Indeed, the rank will be upper bounded by its dimension (the number of columns, which is given by the number of harmonics of interest). This is usually far below the number of sensors, implying that the covariance matrix loses any statistical significance, and so are the model-order selection methods. Classical MUSIC algorithms seem to be inappropriate for this situation.

Still, one can interpret MUSIC geometrically. Performing a singular values decomposition (SVD) of the data matrix will yield singular values equal to the square root of the big eigenvalues and the left singular vectors will span the same source space as the eigenvectors of the covariance matrix $\mathbf{V}_{1..r}$. Looking for the sources that explain this source space is then equivalent to look for lead-field columns $\mathbf{a}_i$ correlated to the space defined by the considered singular vectors, *i.e.*, columns having a minimum angle with the subspace spanned by these r singular vectors $\mathbf{V}_{1..r}$. Successive iterations of (T)RAP-MUSIC will then project out of the data space and of the lead-field matrix the already explained data [Mosher et al., 1999]. To conclude, we can apply iterative MUSIC algorithms in the frequency domain also after selecting the frequencies of interest, knowing just that the source space dimension will be given by the number of selected harmonics and the basis of the source space by the left singular vectors of the data $\mathbf{X}_f$.

Regardless of the domain (time or frequency), if the source space dimension is correctly estimated, it will never be greater than 2×(the number of harmonics). In time domain, it can be overestimated, which might help improving the accuracy of the source estimation (with thus a better GOF but possible false detections). But in the frequency domain, the number of sources will be upper bounded by (twice) the number of harmonics.

Matching Pursuit algorithms. A sparse solution to the source estimation problem can be written as the outcome of the following optimization problem:

$$\min\left(\|\hat{I}\|_0\right) \quad \text{u.c.} \quad \|\mathbf{X} - \sum_{i\in\hat{I}} \mathbf{a}_i \hat{s}_i\|_2 < \varepsilon \tag{4.5}$$

meaning that one looks for the minimum number of dipoles (columns in the lead-field) and their amplitudes (weights in the sum) such as this weighted sum approximates the data with a certain precision. Classical algorithms for solving this problem are those from the MP family. MP algorithms principle is quite similar to the iterative MUSIC ideas: one looks (scans) for the column in the lead-field matrix that best approximates the data with a proper scaling (amplitude). At each iteration, the same operation is done on the residual, *i.e.*, on the part of the data not yet explained by the previous iterations.

As explained in Chapter 2, more elaborated versions of MP are its Orthogonal version (OMP) and mainly the Orthogonal Least Squares algorithm, which is similar to ascending step-wise regression. Indeed, if $\mathbf{X}$ is a single column matrix, minimizing the term $\|\mathbf{X} - \sum_{i\in\hat{I}} \mathbf{a}_i \hat{s}_i\|_2$ boils down to finding the scalar coefficients s_i to multiply the columns $\mathbf{a}_i$ (regressors) in order to approximate the original data.

Alternatively, the estimates of the source amplitudes and of their localization are given by Equation (4.6):

$$\hat{\mathbf{S}}, \hat{I} = \underset{\mathbf{S}, I}{\operatorname{argmin}} \left(\|\mathbf{X} - \mathbf{A}_I \mathbf{S}\|_2^2 + \lambda N_I\right) \tag{4.6}$$

where I contains the indices of the selected columns from the lead-field $\mathbf{A}$, representing source positions, $N_I = \|I\|_0$ represents the number of selected columns (cardinal of I), $\mathbf{S}$ are the magnitudes of the (selected) sources and $\mathbf{A}_I$ is the sub-matrix containing the I indexed columns from $\mathbf{A}$ (hats indicate estimates of the indices I and source amplitudes $\mathbf{S}$; estimating I is equivalent to choosing an estimated sub-matrix $\hat{\mathbf{A}}_I$).

Note that Equation (4.6) writes equivalently in the frequency domain.

In [Soussen et al., 2011], the minimization problem in Equation (4.6) was addressed by a penalized Orthogonal Least Squares (OLS) regression called Single Best Replacement (SBR): the first term decreases with every new added source (index in $\hat{I}$, thus column in $\hat{\mathbf{A}}_I$ and respective magnitude in $\hat{\mathbf{S}}$), while the (second) penalization term increases with a fixed amount defined by the user parameter λ. The algorithm, equivalent to classical OLS for $\lambda = 0$, iterates by adding or removing sources until convergence to a more or less sparse solution depending on the user choice of λ.

As in classical multiple regression, the original SBR is applied on vectors (*i.e.*, $\mathbf{X}$ and $\mathbf{S}$ are column vectors). In our application, $\mathbf{X}$ is an $M \times T$ matrix (in the time domain) or an $M \times 2$ matrix in the frequency domain (for single frequency sources, $M \times 2H$ if H different frequencies are considered).

We need thus to adapt the SBR/OLS to matrices. The adaptation is straightforward: instead of taking the time-instants separately and find distinct sparse source estimates for each of them (with the risk to have different supports from on time sample to the next and thus discontinuous estimates of source amplitudes), we take the full data matrix. This implies, in step 3 of the OLS algorithm 3, to replace the l_2 vector norm with the Frobenius norm (for minimising the residual). The same modification needs to be done of course for the other algorithms from the same family. Note that these adapted algorithm can be applied equally in time or in frequency, *i.e.*, on $\mathbf{X}$ or $\mathbf{X}_f$, with the obvious difference in computational burden.

Applying the matrix version of the SBR will then yield, in time, row vector weights representing time varying amplitudes of the elementary dipoles encoded by the selected columns of the lead-field matrix (these row vectors form together the $\hat{\mathbf{S}}$ matrix). The same N_I selected columns of the lead-field will be selected for all time instants, which will enforce sparsity in space but not in time domain.

In frequency, as only the frequencies of interest are selected, the method can be seen as a localization preceded by non-linear filtering (frequency selection by thresholding). In this sense, the solution will be sparse in space but also in frequency. The weights (rows of $\mathbf{S}_f$) will be the amplitudes of the real and imaginary parts of the complex coefficients that represent the amplitudes of the elementary dipoles in the frequency domain.

In both cases, the final set of selected indices $\hat{I}$ will give the locations of the estimated sources.

Algorithm parameters. The algorithms were implemented in time and frequency domain, with the appropriate parameters. In fact, the parameters of importance are related to the stopping criteria.

More precisely RAP and TRAP-MUSIC stop after reaching the dimension of the source space. This source space dimension, for the time versions of RAP and TRAP, was estimated using the MDL criterion (see Subsection 2.4.2). In the frequency versions, applying MDL has less statistical justification. Nevertheless, its results consistently yielded the dimension of the data (number of columns, *i.e.*, the double of the number of selected frequencies), which was used then to parameterise

MUSIC algorithms[3].

The OLS stopping criterion we used is a target expected Goodness of Fit, *i.e.*, a maximum acceptable error between the reconstructed data and the measured one (see Subsection 2.4.3). In real applications, this is a user parameter and its value cannot be evaluated precisely. In our simulations though, as we know the SNR, we can compute the expected GOF. For a given non logarithmic SNR ($\|\mathbf{X}\|^2/\sigma_\varepsilon^2$, with σ_ε^2 the noise power), the expected GOF can be written as:

$$\text{expGOF} = \frac{SNR}{1+SNR}$$

During the iterations, one can always estimate the current GOF using (3.13) and compare it to the expected value, the iterations being stopped when the current GOF is higher than the target one.

Finally, the SBR will stop when the cost function (4.6) will reach its first minimum. The first term of the function decreases with every new column $\mathbf{a}_i$ (regressor). The second term increases by the fixed amount λ with every new column. The user parameter λ can then be interpreted as the cost of adding a new regressor (thus a new source) for explaining the data $\mathbf{X}$. In all our simulations, we fixed $\lambda = \|\mathbf{X}\|_2^2/100$. In other words, if adding a new source explains less than 1% of the data, the algorithm stops (recall that, at every iteration, SBR also attempts to remove one of the sources/columns of the dictionary in order to decrease the penalty term).

4.3 Results

We present in this section comparative results for oscillating sources localization, both in time and frequency domain, with iterative MUSIC algorithms and greedy regression-like methods. In the first subsection, we focus on simulated data, while in the next one we will present examples of results obtained on real EEG signals recorded during FPVS protocols.

4.3.1 Data simulation

In order to evaluate the source localization performance in the context of multiple oscillating sources at a fixed frequency (or its harmonics), we simulated EEG scalp potentials using the same simulation setup as in Chapter 3 (see Section 3.5.1). We generated two lead-field matrices with 64 electrodes, one based on the dense BEM model Colin27 (lead-field matrix $\mathbf{A}$ = 64 × 6184), the other one based on the sparser MNI FEM model (lead-field matrix $\mathbf{A}$ = 64 × 509). In both cases,

---

[3] We have also evaluated informed time versions of MUSIC and RAP-MUSIC, *i.e.*, we directly specified in the algorithm the correct dimension of the source space. While the informed versions perform better than the MDL based ones, the global ordering of the algorithms doesn't change. For conciseness, we do not report these results here. Besides, in realistic situations the information on the source space dimension is not available so informed version are not applicable.

the orientations were fixed and known (orthogonal to the surface). The source configurations used to create the EEG signals using these two lead-field matrices are described in the following.

Realistic EEG signals during FPVS contain peaks at oddball and base frequencies, *i.e.*, 1.2Hz and 6Hz (and harmonics), being thus a mixture of sources at all these frequencies. While, the actual combination (the respective contributions) of oddball and base frequencies is irrelevant, the important difficulties, as observed in Chapter 3, is coming from the interactions between sources having the same frequency, *e.g.*, 6Hz. Then, we have simulated multiple sources with a single frequency at 6Hz, performing the localization either using the time instants or directly on the peaks at the frequency of interest and also with its harmonics, *e.g.*, 12Hz, 18Hz and 24Hz, after Fourier transform.

We have simulated $p = 3, 4, 5, 7$. The time course of the sources were either cosine waves for the single frequency at $f_0 = 6$Hz or sawtooth waves for $f_0 = 6$Hz (thus with decreasing amplitudes harmonics). These sources having different random amplitudes and phases, where amplitudes were chosen according to a normal distribution with a mean of 5 (arbitrary units) and standard deviation of 1, and phases drawn from a uniform distribution on $[0, \ \pi]$. The sampling frequency was 2100 Hz and the duration 1s. The source positions were selected randomly among the 6184/509 possible ones.

We have simulated increasingly complex signals by combining projections of each number of sources with random parameters described above. For each number of sources, white Gaussian noise was added to the simulated scalp potentials. Seven noise power levels have been used, computed so as to reach SNRs in the set {40dB, 20dB, 10dB, 3dB, 0dB, -3dB, -10dB}. One hundred simulations per number of sources and noise level were performed using the set up described previously for both lead-field matrices.

4.3.2 Performance criteria on simulated EEG data

In order to determine the accuracy and compare the localization methods using simulated data, three criteria are used: the distance of localization error (DLE), the rate of true discovery (TDR) or precision and the rate of true positives (TPR) or sensitivity. For source localization, we will consider as a true positive (TP) an estimated source located within 1cm from a simulated source. All the estimated sources that are farther than 1cm are considered false positive (FP).

The DLE, as proposed in [Becker et al., 2014], gives an estimate of the localization accuracy taking into account the missed simulated sources (false negative, FN), as well as the introduction of spurious sources (false positive, FP):

$$\mathrm{DLE} = \frac{1}{N_{\hat{I}}} \sum_{\hat{i} \in \hat{I}} \min_{i \in I} \|r_{\hat{i}} - r_i\| + \frac{1}{N_I} \sum_{i \in I} \min_{\hat{i} \in \hat{I}} \|r_{\hat{i}} - r_i\| \tag{4.7}$$

$\hat{I}$ is the set of the $N_{\hat{I}}$ reconstructed sources at positions $\{r_{\hat{i}}\}_{\hat{i}\in[1..N_{\hat{I}}]}$, and I is the set of the N_I original simulated sources placed at positions $\{r_i\}_{i\in[1..N_i]}$. The first term of Equation (4.7) penalizes the presence of false positive sources, while the second term penalizes true sources that are not recovered by the source localization method. That is to say, DLE equally penalizes less sparse solutions when introducing spurious sources far from the true sources (first term) and too sparse solutions with missed sources (second term) and this even when the whole set of the true sources is indeed localized.

The rate of true positives (TPR), known also as sensitivity, determines the proportion of true sources that were reconstructed respect to the simulated ones. The number of true positives is divided by the total of simulated sources (true positives and false negatives).

$$\mathrm{TPR} = \frac{\mathrm{TP}}{\mathrm{TP}+\mathrm{FN}} = \frac{\mathrm{TP}}{N_I} \tag{4.8}$$

Finally, the rate of true discovery (TDR), known also as precision, determines the proportion of relevant sources among the reconstructed ones. The number of true positives (TP) is divided by the total of true and false positives.

$$\mathrm{TDR} = \frac{\mathrm{TP}}{\mathrm{TP}+\mathrm{FP}} = \frac{\mathrm{TP}}{N_{\hat{I}}} \tag{4.9}$$

It is noteworthy that, while TDR and TPR can be seen as complementary criteria (high TPR indicates that most of the sources were retrieved, but this usually comes with the price of a higher number of false detections, thus a low TDR), the DLE is a more synthetic way of evaluating the performances of source localization algorithms. Indeed, as TPR and TDR, it includes the indicators of true/false positives/negatives, but it also weights their values with the actual distances between the found and original solutions.

Nevertheless, the source localization methods we used were evaluated considering all three criteria, DLE, TPR and TDR. The values of each criterion were averaged over one hundred simulations for each given number of sources and SNR.

4.3.3 Simulation results

The results of the simulations on scalp EEG recordings, under the assumption of sources with fixed known orientations are exposed in the following figures. The results using the forward model **A** with size 64 × 6184 are exposed in Figure 4.1 (sources at 6 Hz) and in Figure 4.2 (sources at 6 Hz and harmonics at 12 Hz, 18 Hz and 24 Hz). Then, the results using the forward model **A** with size 64 × 509 are presented in Figure 4.3 (sources at 6 Hz) and Figure 4.4 (sources at 6 Hz and harmonics at 12 Hz, 18 Hz and 24 Hz).

These results sum up the performance of source localization from the algorithms SBR, OLS, RAP and TRAP MUSIC (see Sections 2.4 and 4.2.2 for details). We compare these methods in terms of their robustness to the variation of the number of active sources ($p = 3,4,5,7$) and level of noise (SNRs: 40dB, 20dB, 10dB, 3dB, 0dB, -3dB, -10dB), by using the distance of localization error (DLE), the sensitivity or rate of true positives (TPR) and the precision or rate of true discovery (TDR) metrics (see Subsection 4.3.2).

One hundred simulations (varying randomly the source positions, amplitudes and phases) were performed for each combination of p (number of sources) and SNR.

The mean results, averaged over the 100 simulations, are summarized from Figures 4.1 to 4.4.

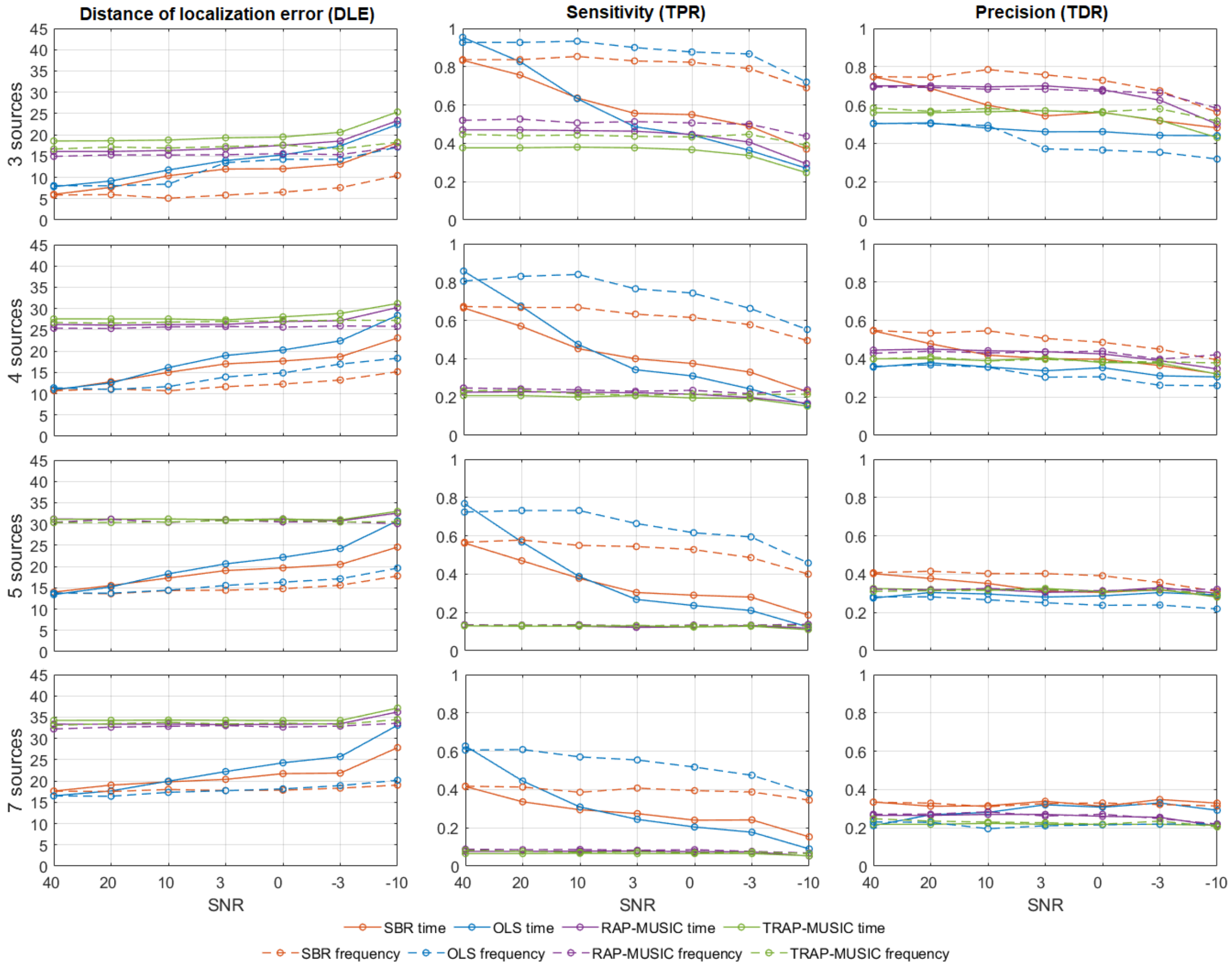

FIGURE 4.1 – Source localization performances of SBR, OLS, RAP and TRAP MUSIC algorithms on multiple oscillating sources at 6Hz, generating scalp EEG recordings using the lead-fied matrix $\mathbf{A}$ of size 64×6184. These algorithms were applied in the frequency (dashed lines) and time (solid lines) domain. By column are shown the results evaluated using DLE (in mm), sensitivity (TPR) that indicates the accuracy of the methods to reconstruct the target sources and precision (TDR) that illustrates the proportion of false reconstructed sources. By rows, the results for each number of simulated sources $p = 3,4,5,7$ are presented. For each subplot, the x-axis shows the SNR (40, 20, 10, 3, 0, -3, -10).

Figure 4.1, compares the performance of the tested algorithms for the dense lead-field (BEM Colin27, size: 64×6184). Analyzing first the performances of the tested algorithms applied in the frequency domain (on $\mathbf{X}_f$) for 3 simulated sources, we can see that SBR shows overall better results than the other tested algorithms. It exhibits DLEs from 0.5cm (40db) to 1cm (-10db), followed by OLS (DLEs from 0.6cm to 1.8cm), and then RAP and TRAP MUSIC (from 1.5cm to 1.8cm). Regarding the sensitivity (TPRs) of these methods, which quantifies the detection success of the true sources with respect to the simulated ones, OLS is the most performant, followed by SBR and then RAP and TRAP MUSIC. However OLS is more vulnerable than the others when evaluating its precision (TDRs): its lower values indicate the presence of more false reconstructed sources. Indeed, this method seems to be the most vulnerable to false detections, while SBR in frequency is the less affected, being overall more efficient in localizing sources. We can also observe that RAP and TRAP MUSIC in frequency have lower sensitivity values (TPRs), being just above of OLS in terms of precision (TDRs).

Comparing the previous values in the frequency domain with those in the time domain, we can notice that the performances of the time versions of the algorithms are worse. SBR overall is the less affected when comparing with the other algorithms. The DLEs along the SNRs for SBR vary from 0.6cm to 1.8cm, OLS from 0.8cm to 2.2cm, RAP MUSIC from 1.6cm to 2.3cm and TRAP MUSIC from 1.9cm to 2.5cm. When observing the sensitivity (TPRs), OLS shows high values but just for $40dB$ and $20dB$ and then rapidly falls. While SBR exposes the same initial high values, but its capability of reconstructing the true sources, slowly fall along the SNRs as seen for OLS. RAP-MUSIC barely reconstructs half of the true sources, even for the best SNR, while TRAP-MUSIC has the lowest sensitivity values. The precision values (TDRs) indicate that RAP-music reconstructs less false sources, SBR is initially precise, *e.g.*, $40dB$ and $20dB$ and then drastically fall its precision, while OLS is the less precise, reconstructing more false sources than in frequency domain.

For 4 simulated sources all the algorithms diminish their performance both in frequency and in time. DLEs in frequency along the SNRs show mean values for SBR from 1.1cm to 1.5cm, OLS from 1.1cm to 1.8cm, RAP MUSIC between 2.5cm and 2.6cm and TRAP MUSIC between 2.6cm and 2.7cm. When comparing with the other algorithms, OLS remains with the highest accuracy (TPRs), with more true reconstructed sources, while its precision is the most affected, exhibiting the lowest values of TDRs as observed already for 3 sources (this seems to be a constant characteristic of this method). SBR is the second more accurate in reconstructing the true sources (TPRs) and more precise with less false reconstructed sources (TDRs). The results for RAP and TRAP MUSIC are the less favorable, with very low sensitivity (TPRs), barely one true source is reconstructed and in addition to that, their precision are also affected (TDRs) because the reconstruction of false sources. The performances of the time versions of the algorithms are more affected as the number of sources increases, but similar patterns are observed as for 3 sources.

We also clearly observe that the increase to 5 and 7 sources compromises more the performances of these methods. Localization in frequency for 5 sources along the SNRs yields DLEs for SBR from 1.4cm to 1.8cm, for OLS from 1.4 to 2cm, for RAP MUSIC remains in 3cm and TRAP MUSIC between 3cm and 3.1cm. For 7 sources, DLEs for SBR are between 1.8cm and 1.9cm, for OLS from 1.7cm to 2.0cm, for RAP MUSIC between 3.2cm and 3.4cm and TRAP MUSIC between 3.3cm and 3.4cm. In time domain, on the other hand, the results still remain less favorable than in frequency. For 5 sources, DLEs for SBR are from 1.4cm to 2.5cm and OLS from 1.3cm to 3.1cm and for 7 sources, SBR from 1.8cm to 2.8cm and OLS from 1.7cm to 3.3cm. While for RAP and TRAP MUSIC, DLEs have no longer considerable variations along the SNRs, remaining on the same results for frequency and time (for 5 sources, both RAP and TRAP, with 3.1cm for $40db$ and 3.3cm for $-10dB$, for 7 sources RAP MUSIC with 3.3cm up to 3.6cm for $-10dB$ and TRAP MUSIC with 3.4cm and only 3.7cm for $-10dB$). When observing the sensitivity (TPRs) and precision (TDRs) results for these 5 and 7 simulated sources. OLS in frequency remains reconstructing more true sources over the other methods, showing higher sensitivity. But its precision (TDRs) is strongly affected due to the reconstruction of false sources, which is larger for 5 and 7 sources. While SBR has tackled better the reconstruction of false sources, with higher precision values (TDRs) over the other methods, but visibly its sensitivity (TPRs) is even more affected because of the presence of more sources, but also due to the effect of the strong noise as observed for $-10dB$ in all the methods. RAP and TRAP MUSIC are the most affected with a scarce reconstruction of true sources (TPRs), which has led them to a poor precision (TDRs) as well.

Comparing these results in frequency with those in time domain, we can conclude that, while both classes are affected when the number of sources increases, the presence of strong noise influences more the time domain methods, for which the only notable results are for $40dB$, with similar values to their counterparts in frequency. For noisy data, the results of the time domain versions drastically diminish as they come close to strong noise cases, *e.g.*, $-3dB$ and $-10dB$. This confirms the denoising effect of the selection of the frequencies of interest and illustrates as well that the loss in conditioning is less important to the localization results than this denoising, especially for the regression-like algorithms.

Regardless of the domain (time or frequency), SBR achieves better results over the other algorithms when considering DLE and TDR, while for TPR the OLS has better results. This can be easily explained by the number of found sources, higher for OLS than for SBR: the price of a higher TPR is a lower TDR. For the family of MUSIC algorithms, as the rank of the data of interest is low, the performances are strongly impacted, while the regression based methods seem less affected.

In summary, the results in Figure 4.1, and especially the synthetic criterion of DLE, allow to conclude that the SBR method outperforms the other source localization methods, *i.e.*, OLS, RAP and TRAP MUSIC, especially when applied in frequency domain on the spectral peaks of interest. The results indicate also that the number of co-ocurring sources and the presence of noise have a considerable impact in the performance of the source localization algorithms. Nevertheless, higher robustness to noise is achieved by addressing source localization in the frequency domain, where the performances decrease to a lesser extent when the noise power increases, compared to the time domain results.

Therefore, the frequency domain becomes relevant to address source localization in the context of multiple sources oscillating at specific frequencies, as for FPVS-type protocols, *e.g.*, for sources with a (single) base frequency of 6Hz like in FACELOC. Frequency domain localization allows to focus on the frequencies of the activity of interest, for which the SNR is far higher (based on the reasonable assumption that the noise is wide band and not concentrated in the same band as the oscillating sources). Besides, this approach also improves the calculation time for the inverse solution, with far less number of components to explain in the data matrix $\mathbf{X}_f$ compared to the time matrix $\mathbf{X}$.

Fast periodic visual stimulation (FPVS) causes rhythmic activities of the responding brain structures at the same frequency as the stimulation, but these periodic activities are in general not purely sinusoidal and harmonics are observed. We may consider relevant, according to the FPVS protocol we are working on (FACELOC), to include also several harmonics of the stimulation frequency in the localization process. To mimic such evoked activities, we have simulated oscillating sources with harmonics (same simulation protocol as for the single frequency ones), aiming to determine if this additional information improved the accuracy when reconstructing the target sources. We proceeded to test the same algorithms in frequency and time, illustrating these results in Figure 4.2.

Comparing these results with the previous ones (single frequency base at 6Hz), at a first glance, one can notice a global improvement in the reconstruction of the simulated sources. Also, unlike for the single frequency simulations, there is no clear advantage for one of the algorithms. In the frequency domain, OLS and mostly SBR have the best values of DLEs for 3 and 4 sources, below 1cm for 3 sources, while for 4 sources DLE is only slightly above of 1cm for SBR at -10dB and for OLS at -3dB and -10dB. For 5 sources, all frequency domain methods have similar DLEs, while for 7 sources TRAP-MUSIC performs better. TPR / TDR balance is also quite similar to the previous simulations, with MUSIC based methods being more sensitive (higher TPR) but less precise (lower TDR), except again for the less sparse configurations with 7 sources.

The results in time show as well an important improvement in the performance of the algorithms when a richer periodic signal with harmonics is to be localized. Unlike in the previous single frequency setups, time domain algorithms perform better, in terms of DLE, than the frequency domain ones up to 5 sources and positive SNR (approximately up to 0dB). This is especially true for time domain MUSIC methods, which outperform both time and frequency domain SBR and OLS, as well as frequency domain MUSIC. Again, when the setups become less sparse, frequency domain MUSIC appear to be more performant.

In terms of sensitivity (TPR), frequency domain methods generally outperform time domain ones, except for very low levels of noise. The counterpart is a lower precision (TDR) in frequency

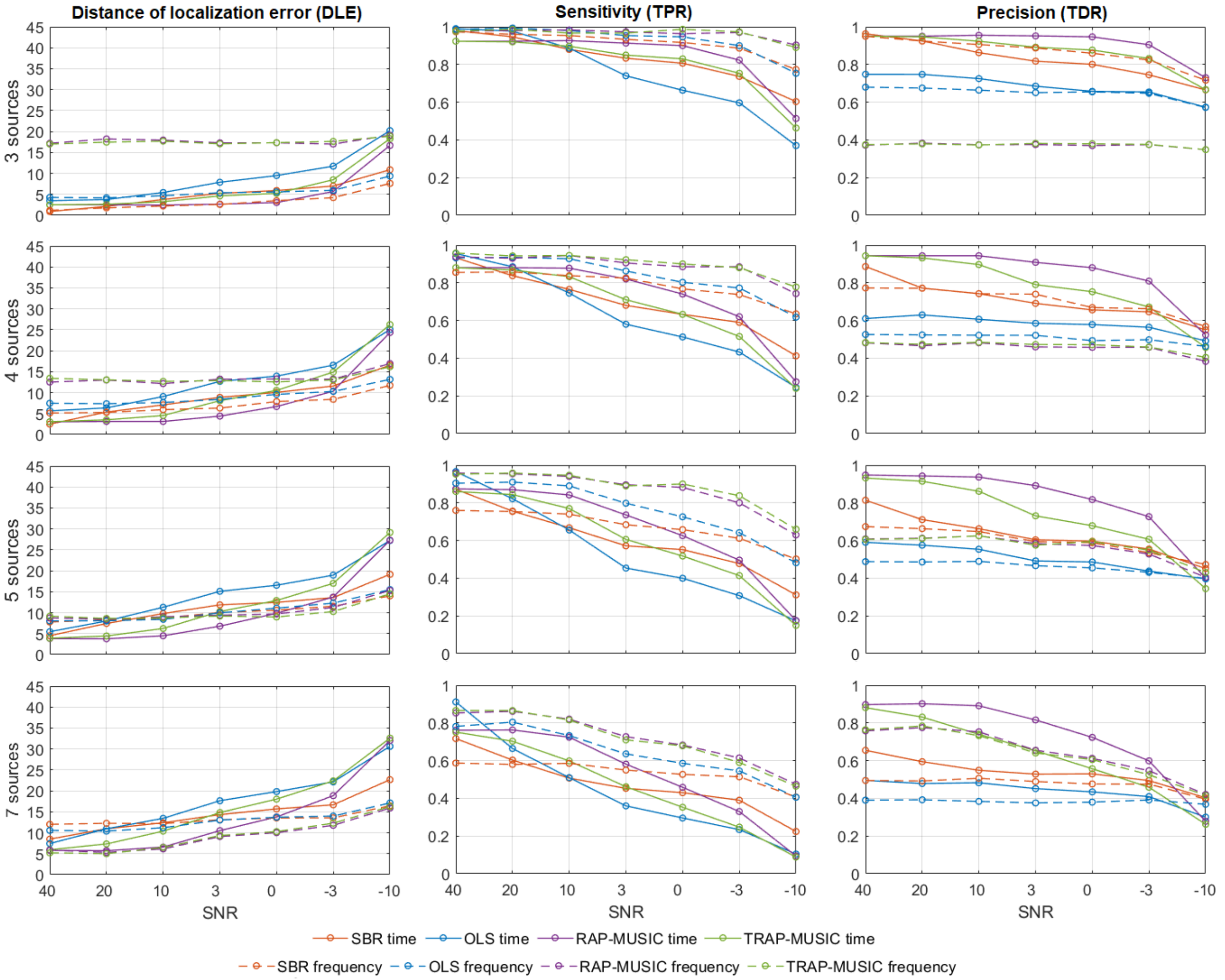

FIGURE 4.2 – Source localization performances of SBR, OLS, RAP and TRAP MUSIC algorithms on multiple oscillating sources at 6Hz and harmonics (12Hz, 18Hz and 24Hz), generating scalp EEG recordings using the dense lead-fied matrix (64×6184). These algorithms were applied in the frequency (dashed lines) and time (solid lines) domain. In columns are shown the results measured using DLE (in mm), sensitivity (TPR) that indicates the accuracy of the methods to reconstruct the target sources and precision (TDR) that determines the effect of the false reconstructed sources. In rows the results for each number of simulated sources $p = 3, 4, 5, 7$. The results are displayed for each SNR (40, 20, 10, 3, 0, -3, -10).

domain. It is noteworthy that RAP and TRAP-MUSIC in time domain have consistently the best precision, while their frequency domain versions have the best sensitivity. Frequency domain regression methods (especially SBR) have balanced performances, with intermediate values of both TPR and TDR.

To conclude, for richer signals (with multiple harmonics), all algorithms perform better. RAP and TRAP-MUSIC, especially in time domain, become very competitive and they achieve better DLE results than the other methods, except for high levels of noise, when their frequency domain versions (for less sparse situations) or frequency domain SBR/OLS (for sparser setups) become more performant. More generally, we can notice that frequency versions are less sensitive to the noise level, as it was the case for the single frequency simulations.

Globally it is observable that the algorithms RAP and TRAP MUSIC seem to take advantage from the diversity induced by the multiple frequencies. Their presence leads to a better estimation of the source space dimension (which is not limited anymore theoretically to 2 - see the ambiguity problem exposed in section 3.4.1). Indeed, this is a sensitive aspect affecting mostly algorithms like RAP-MUSIC and TRAP-MUSIC, which require the estimation of the size of the source space (*i.e.*, roughly the number of linearly independent underlying source components).

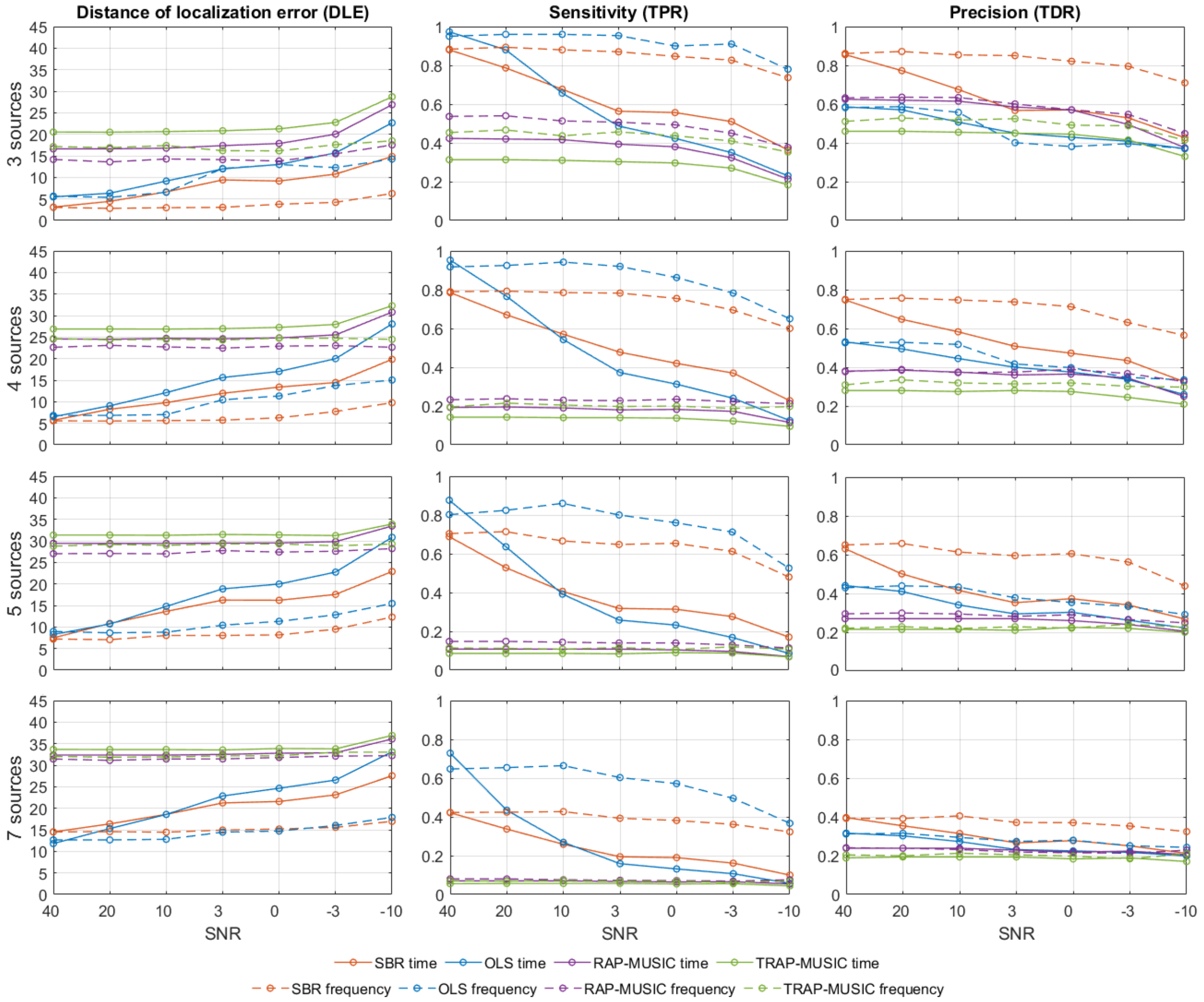

FIGURE 4.3 – Source localization performances of SBR, OLS, RAP and TRAP MUSIC algorithms on multiple oscillating sources at 6Hz, generating scalp EEG recordings using the lead-fied matrix $\mathbf{A} = 64 \times 509$. These algorithms were applied in the frequency (dashed lines) and time (solid lines) domain. In columns are shown the results measured using DLE (in mm), sensitivity (TPR) that indicates the accuracy of the methods to reconstruct the target sources and precision (TDR) that determines the effect of the false reconstructed sources. In rows the results for each number of simulated sources $p = 3, 4, 5, 7$. The results are displayed for each SNR (40, 20, 10, 3, 0, -3, -10).

In the previous chapter, we simulated two families of signals, using both a dense and a sparser fixed-orientation lead-field matrix (dense BEM $\mathbf{A}$ with dimensions 64×6184 and sparser FEM $\mathbf{A}$ with dimensions 64×509). For completeness, we have evaluated the source localization algorithms also on the second lead-field, with less possible source positions. The results are given in Figures 4.3 and 4.4, for single frequency sources in the former and base frequency plus harmonics in the latter. The results of both forward models indicate similar performances of the localization methods according to the number of simulated sources and the SNRs. As discussed above for the forward model with 6184 sources, the results using 509 source positions and single frequency sources show also that SBR applied in frequency domain globally outperforms the other methods, with better results for the reconstruction of the target sources and less false sources. Once again, and as it could be expected, more robustness is achieved in frequency domain when facing the effect of strong noise. Interestingly, the performances seem to be slightly better for this sparser lead-field, with slightly lower DLE for the same levels of noise and number of sources.

For richer sources with several harmonics, results of MUSIC type algorithms improve considerably and they become competitive or overpass SBR and OLS, although in a less evident manner than for the denser lead-field (for example, the frequency domain SBR precision is comparable with time domain RAP-MUSIC for low number of sources). Again then, frequency domain SBR seems to be a good candidate algorithm for sparse source localization, with a clear advantage for single frequency sources and competitive performances for multiple harmonics sources.

4.3.4 Real signal results

We finally applied the previously tested algorithms on real FPVS data. We did not thoroughly evaluated them on an important number of recordings, so the results presented next have no statistical value, they are simply presented as examples. Consequently, it is very difficult to analyze these results and our interpretations must be taken with care.

The data-set consists of a 64-channels real EEG recording (Biosemi Cap [Biosemi, 2022]) at sampling rate of 256Hz. Two sessions of 70 seconds were recorded using the FPVS FACELOC protocol described in Section 1.4.2.1. Average re-referencing was applied to the data. The sessions were synchronized (with respect to the base and oddball stimuli) and then averaged between them. We obtained thus one set of 64 EEG signals, average reference montage. From this raw data, two data matrices were created, one for frequency localization ($\mathbf{X}_f$), the other for time localization ($\mathbf{X}$).

For frequency domain methods, Fourier transform was applied to the raw data, in order to obtain spectra as the ones already presented in Figure 3.1a. The peaks at the base frequency and its first two harmonics (6Hz, 12Hz and 18Hz) were then selected and the $\mathbf{X}_f$ matrix (64×6) was constructed using their real and imaginary parts.

For time domain, the procedure was slightly more involved: in order to avoid confusions bet-

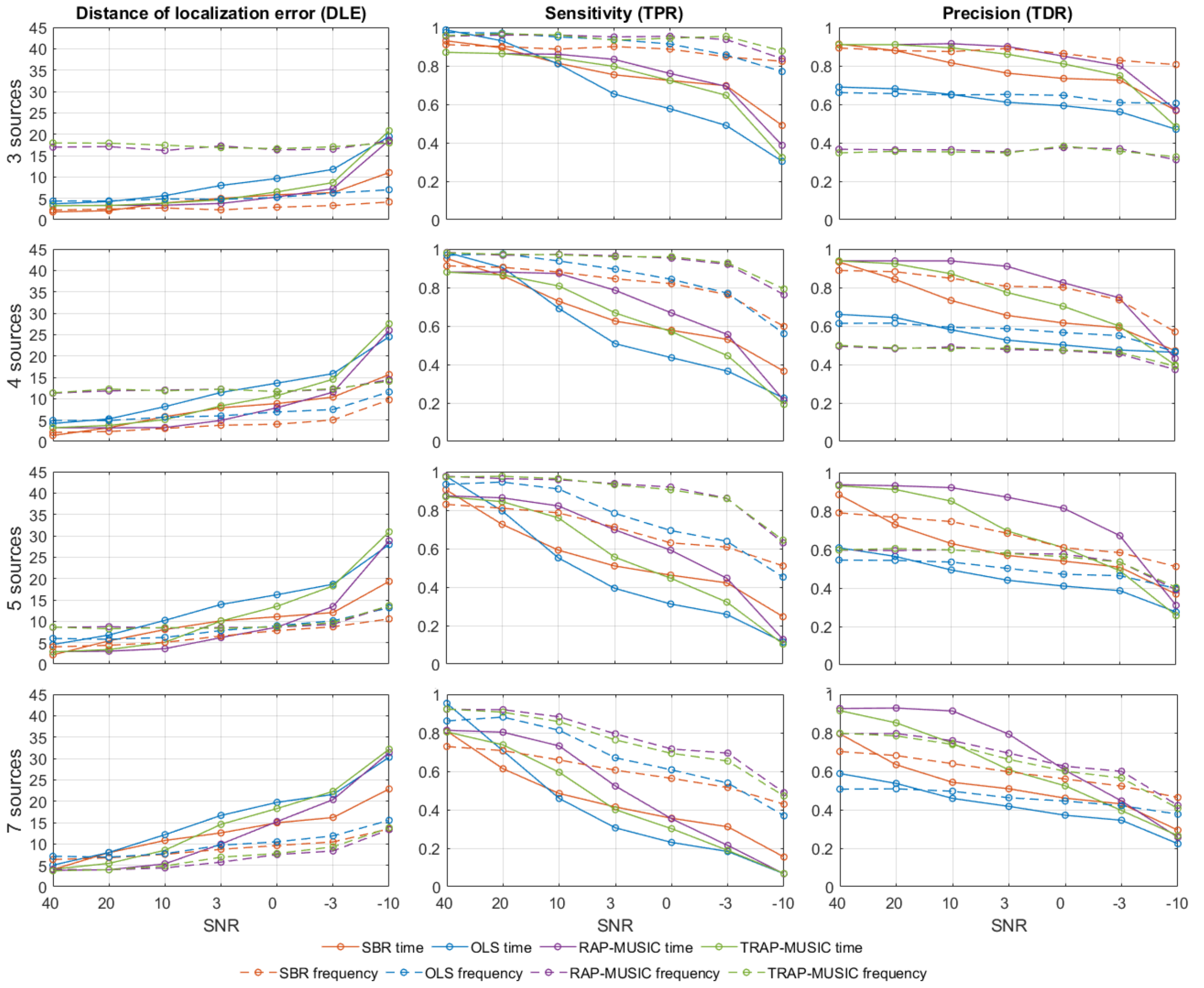

FIGURE 4.4 – Source localization performances of SBR, OLS, RAP and TRAP MUSIC algorithms on multiple oscillating sources at 6Hz and harmonics (12Hz, 18Hz and 24Hz), generating scalp EEG recordings using the low resolute lead-fied matrix (64×509). In columns are shown the results measured using DLE (in mm), sensitivity (TPR) that indicates the accuracy of the methods to reconstruct the target sources and precision (TDR) that determines the effect of the false reconstructed sources. In rows the results for each number of simulated sources $p = 3, 4, 5, 7$. The results are displayed for each SNR (40, 20, 10, 3, 0, -3, -10).

ween activities due to the oddball (1.2Hz and harmonics) and to the base frequencies (6Hz and harmonics), we high-pass filtered the data (4th order Butterworth filter) at 5Hz. Moreover, to reduce the noise, data was segmented in windows of 1/1.2 seconds, synchronized to the oddball stimuli (74 windows for our data). For this segmentation to be precise, we up sampled the data by a factor of 3. We next averaged the 74 windows in order to obtain a single period of the oddball activities (as it is low frequency, a single period contains also the activities at 6Hz and harmonics). We obtained thus a single period, 640 samples and 64 electrodes ($\mathbf{X}$ of size 64×640).

An example on one single electrode (PO8) of the corresponding power spectrum is presented in

Figure 4.5, with representative peaks at the oddball frequency of 1.2Hz and harmonics at 2.4Hz and 3.6Hz (right side). This particular spectrum was recorded on the P08 electrode as observed from the power scalp map at 1.2Hz (left side). Besides, an important peak in the spectrum at the base frequency of 6Hz (right side) is also noticeable (power scalp map in the middle).

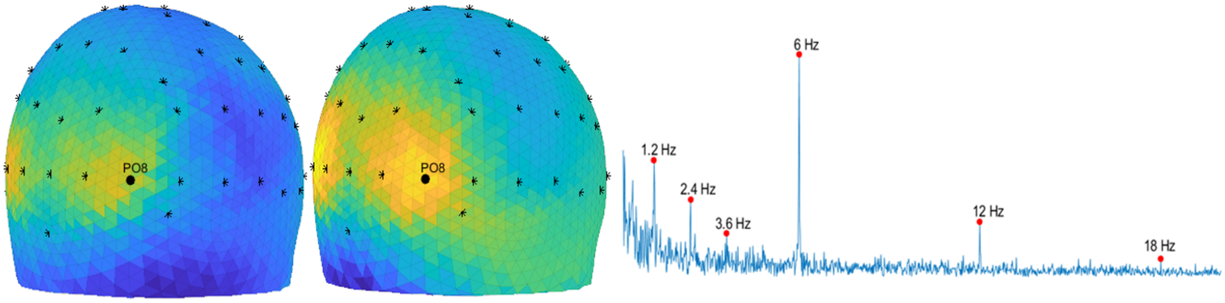

FIGURE 4.5 – Representation of a data vector from the electrode PO8 in the EEG real signals recorded using FPVS protocol. The scalp map at 1.2Hz on the left side, centered on the PO8 electrode, for which the spectrum is displayed nearby and peaks at at the frequencies 1.2 Hz, 2.4 Hz and 3.6 Hz are displayed on the right side from the same PO8 electrode. An important peak at 6 Hz is also noticeable (right side), exposing a strong activity on the posterior brain area (power scalp map in the middle).

For these examples, we used the sparser lead-field matrix ($\mathbf{A}$, size 64×509), for which slightly more precise results were obtained in the simulation. Still, this argument itself must be considered with care: we use here a standardized lead-field computed on an average head model using standard (isotropic) conductivities for every type of tissue. The signals on the the other hand, are obtained on a real patient, for which we have no guarantee that the model is precise. Nevertheless, taking all these precautions, we think it is still useful to present results for the 4 algorithms used above (RAP and TRAP-MUSIC, SBR and OLS), in both frequency and time domains.

For real data, these algorithms need some adaptations. In the frequency domain, RAP and TRAP-MUSIC stopping criterion was the data dimension, *i.e.*, after finding 6 sources (twice the number of harmonics). For SBR, we choose a $\lambda = 0.01$. For OLS, the chosen stopping criterion is an expected Goodness of Fit, that we evaluated in the frequency domain from the ratio between the peaks of the frequencies of interest and the mean of the neighbouring frequency bins:

$$\text{expGOF} = 1 - \left(\frac{\|\varepsilon\|}{\|\mathbf{X}_{f,p}\|} \right)^2 \tag{4.10}$$

with $\mathbf{X}_{f,p}$ the Fourier transform restricted to the peaks of interest and ε the mean magnitude of the FFT in the frequency bins around the frequencies of interest.

In time domain, manually tuned the expected GOF used to stop the OLS iterations to 0.9 and the λ parameter of SBR to 0.1. For MUSIC type algorithms, using classical MDL did not provide good results: the evaluated dimension of the source space was far too high, equal to the number of electrodes. We therefore imposed the dimension of the source space to the number of sources found by SBR. This choice also facilitates the comparison between the algorithms.

The results of source localization (sources at the base frequency, thus responding to any image), are illustrated in Figure 4.6, for frequency domain approaches, and Figure 4.7, for time domain. The same results, for oddball responding sources (1.2Hz and harmonics) are presented in Figure 4.8, for frequency domain approaches and Figure 4.9 for time domain. Two views are displayed in each sub figure, back and top view (left and right panels respectively).

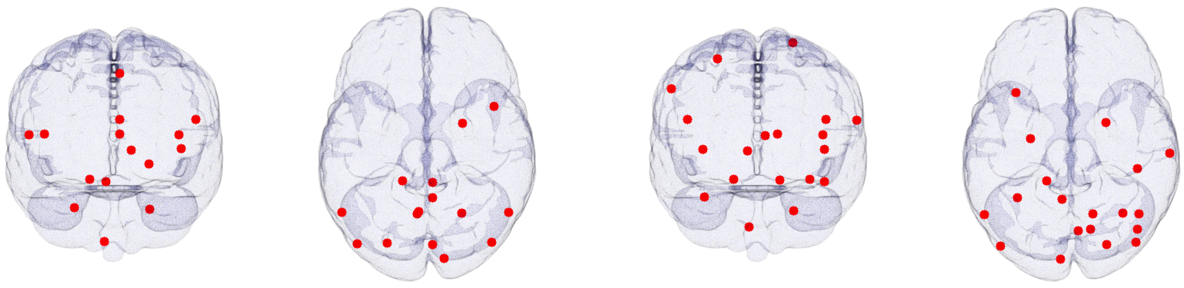

(a) SBR (b) OLS

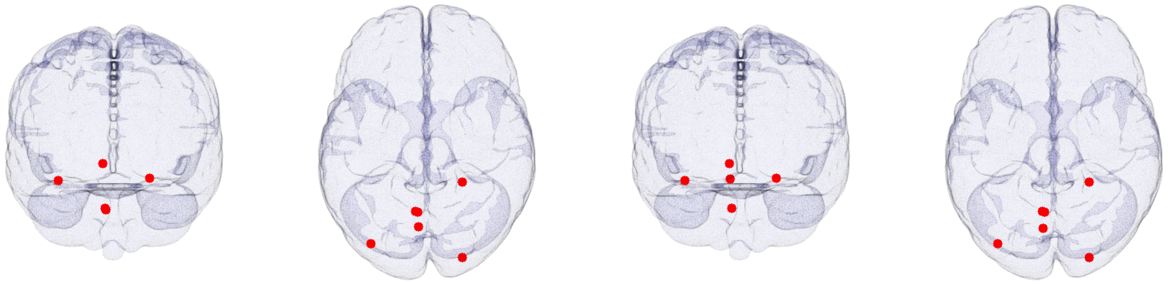

(c) RAP-MUSIC (d) TRAP-MUSIC

FIGURE 4.6 – Real FPVS frequency domain source localization, for sources of oscillating at the base frequency (6Hz and harmonics). The different subfigures show results for SBR, with 15 reconstructed sources and GOF=0.99, OLS with 19 reconstructed sources and GOF=0.98, RAP MUSIC with 6 reconstructed sources and GOF=0.88 and TRAP MUSIC with 6 reconstructed sources and GOF=0.89. Back view (left) and top view (right) are provided for each computed method.

The results obtained by the frequency domain algorithms place sources mostly in the posterior part of both hemispheres, which is expected for visual stimuli. For the oddball frequency (Figure 4.8), SBR is the only algorithm, among the tested ones, that places predominantly the sources in the right hemisphere, which was shown (using depth recordings) to be more responsive to face-like oddball stimuli [Jonas et al., 2016].

For the base frequency (Figure 4.6), the GOF (computed with respect to the data $\mathbf{X}_f$) varies from 0.99 (SBR) to 0.88 (RAP-MUSIC). This is not by itself an indication of quality: SBR reconstructs

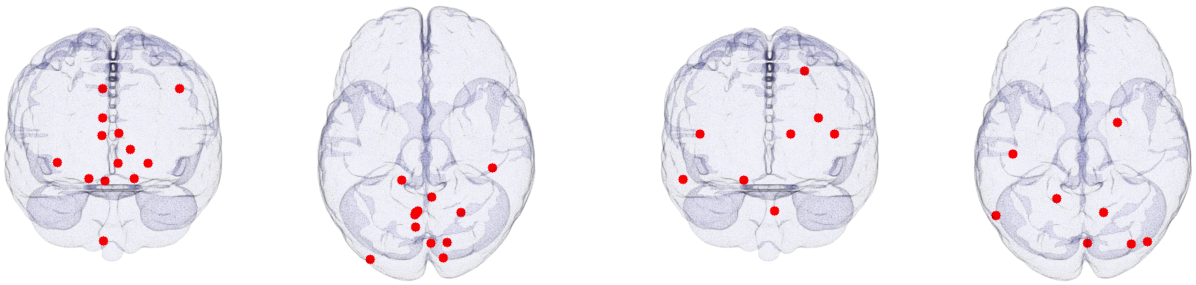

(a) SBR

(b) OLS

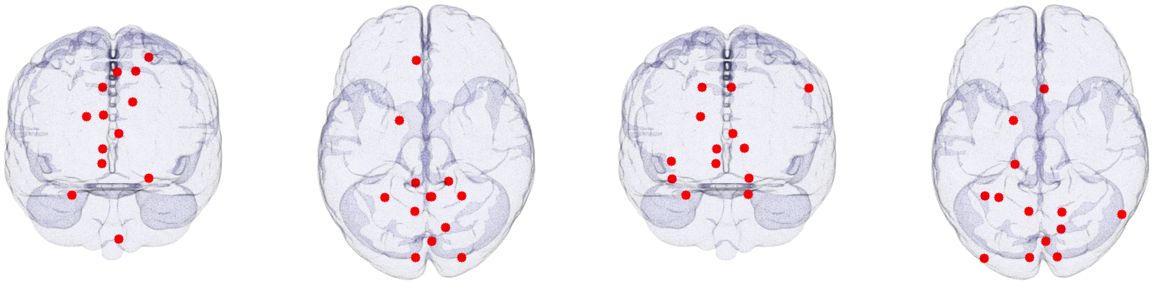

(c) RAP-MUSIC

(d) TRAP-MUSIC

FIGURE 4.7 – Real FPVS time domain source localization, for sources of oscillating at the base frequency (6Hz and harmonics). The different subfigures show results for SBR, with 13 reconstructed sources and GOF=0.97, OLS with 8 reconstructed sources and GOF=0.9, RAP MUSIC with 13 reconstructed sources (see text for explanations) and GOF=0.95 and TRAP MUSIC with 13 reconstructed sources and GOF=0.96. Back view (left) and top view (right) are provided for each computed method.

15 sources, while MUSIC only 6 sources [4].

Between algorithms from the same family one can notice than TRAP has a GOF slightly better than RAP (for the same number of sources), while OLS has a worse GOF for more sources (which highlights the capacity of SBR to discard spurious estimates). The order of the algorithms with respect to the GOF is the same for oddball frequencies, but it is interesting to notice that OLS only finds in this case 2 sources (as mentioned above, the stopping criterion was an expected GOF computed from the amplitudes of the harmonics of interest with respect to the background: in this case, its value was 0.87). One can notice in this particular case that one of the OLS sources is common to the SBR ones (the first found by both); the second OLS source, sufficient to obtain the expected GOF, was dismissed in later iterations by SBR. RAP and TRAP are also quite similar, with a more diverse solution for TRAP (which is expected, as it was specifically designed to avoid neighbouring sources).

When comparing frequency and time domain solutions, we can notice that, for the base fre-

---

[4] In the frequency domain, let recall that the maximum number of reconstructed sources using MUSIC-type algorithms is limited to the double of the number of harmonics, in our case to 6 sources. The GOF for MUSIC-type is consequently lower than this of SBR and OLS.

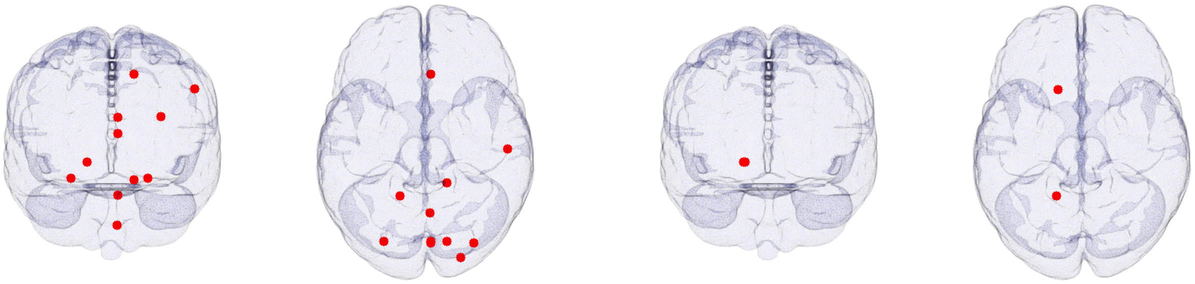

(a) SBR (b) OLS

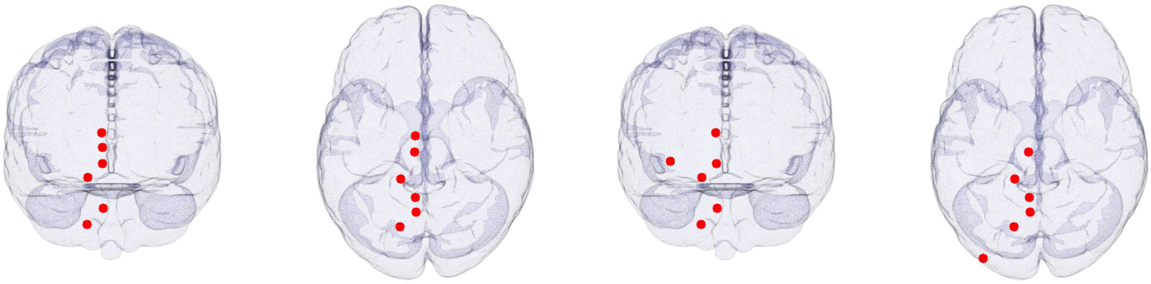

(c) RAP-MUSIC (d) TRAP-MUSIC

FIGURE 4.8 – Real FPVS frequency domain source localization, for sources of oscillating at the oddball frequency (1.2Hz and harmonics). The different subfigures show results for SBR, with 11 reconstructed sources and GOF=0.96, OLS with 2 reconstructed sources and GOF=0.92, RAP MUSIC with 6 reconstructed sources and GOF=0.92 and TRAP MUSIC with 6 reconstructed sources and GOF=0.93. Back view (left) and top view (right) are provided for each computed method.

quency signals, time and frequency domain solutions are relatively similar (between the two domains, Figures 4.6 and 4.7) for SBR and OLS, even if both algorithms yield less sources in time than in frequency (and lower GOFs). This observation remains relatively valid for the oddball sources localization (Figures 4.8 and 4.9), which can be interpreted as stability or robustness. RAP and TRAP-MUSIC provide quite different versions between frequency and time estimates, with more plausible results in time. This observation is to be related to the space source dimension, which is a severely limiting factor for these algorithms in frequency domain (recall also the simulation performances for single frequency sources).

4.4 Conclusion

In this chapter, we have evaluated the performance of several localization algorithms leaning on sparsity in the particular case of oscillatory activities recorded on scalp EEG. These algorithms have been applied both in time and frequency domain with various signal to noise ratio. The chosen methods have been modified and parameterized for this particular application, *i.e.*, Matching Pursuit methods (OLS and SBR) have been adapted to reconstruct matrix data (and not vector data in their

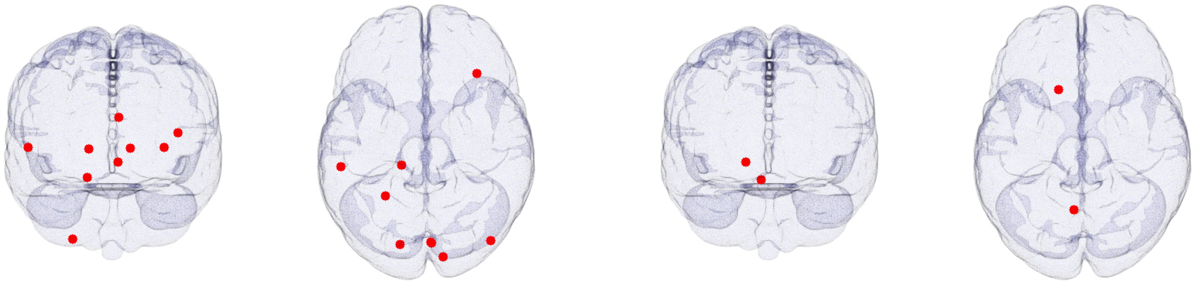

(a) SBR

(b) OLS

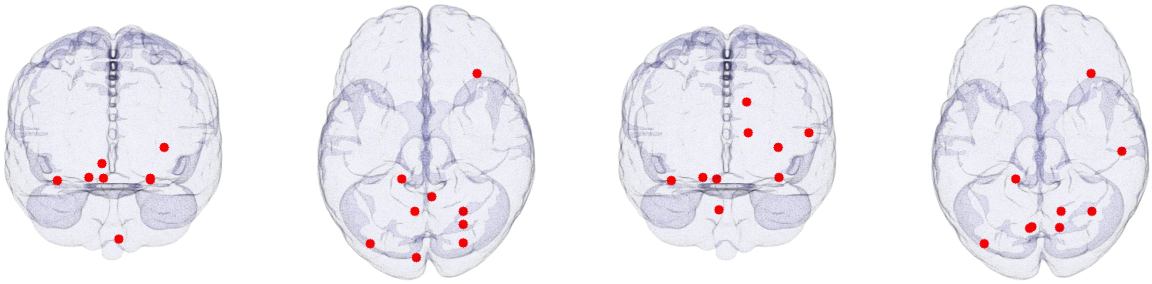

(c) RAP-MUSIC

(d) TRAP-MUSIC

FIGURE 4.9 – Real FPVS time domain source localization, for sources of oscillating at the oddball frequency (1.2Hz and harmonics). The different subfigures show results for SBR, with 9 reconstructed sources and GOF=0.96, OLS with 2 reconstructed sources and GOF=0.91, RAP MUSIC with 9 reconstructed sources (see text for explanations) and GOF=0.94 and TRAP MUSIC with 9 reconstructed sources and GOF=0.94. Back view (left) and top view (right) are provided for each computed method.

original form), and the size of the source space for MUSIC algorithms is limited to twice the number of harmonics considered in the localization process.

The performance of the methods have been evaluated on simulated data, under conditions of multiple co-ocurring sources (from 3 to 7) in the case of single frequency as well as in the case of multiple frequencies (fundamental and harmonics). The scalp EEG data have been simulated using lead-field models encoding the projection of fix-orientation sources, considering either a dense (64×6184) or a sparser (64×509) lead-field.

The results in the single frequency case demonstrate higher robustness when addressing the inversion in the frequency domain, especially for Matching Pursuit type (OLS/SBR) algorithms showing high stability as the noise increases. Focusing on the information of interest (the single frequency peak), the sensitivity to noise is drastically diminished. However, RAP and TRAP MUSIC rather fail in both time and frequency domain, the dimension of the source space being limited to two in this case of single frequency activities.

When the signal gets richer and contains also harmonics, the performance are globally enhanced for all algorithms. In particular, it becomes feasible for MUSIC algorithms to estimate adequately the source space, especially in the time domain. These time versions of MUSIC then provide the best performance when the SNR is above $0db$, being however outperformed by OLS/SBR applied in the frequency domain for lower SNR.

Finally the resolution of the lead-field matrix (number of source positions) has rather low effect on the localization results, as it was already pointed out in Chapter 3. If, on one side, the number of source positions surrounding each of the true sources is indeed increased, potentially enhancing the performance criteria, the ambiguity problem as described in Chapter 3 is, on the other hand, worsen by the increased degrees of freedom induced by a larger lead-field.

We have also illustrated the outcomes of each of the tested source localization algorithms on an example of real data recorded during the FPVS protocol, both applying them in time and frequency domains. The results show rather high disparities between the results produced by each algorithm, especially when comparing MUSIC algorithms with OLS/SBR methods. However the disposition of the sources in posterior brain areas are coherent with previous findings. To further validate the relevance of the methods in reconstructing appropriately the sources, a larger number of cases should be tested and the results confronted to brain atlas to evaluate correspondence of the reconstructed sources with regions known to be activated by such visual stimuli [Jonas et al., 2016].

In the next and last chapter of this thesis, the fixed orientation constraint for the sources will now be relaxed. An adaptation of the OLS and SBR approaches is proposed, where the dictionary atoms on which the data are decomposed are now matrices (3-dimensional atoms $\mathbf{K}_i$) and not vectors as it was the case in this chapter (single lead-field column $\mathbf{a}_i$). The methods will be tested on simulated EEG as well as SEEG data, and an illustrative case on real data will be provided.

Chapter 5

Oscillatory sources localization. Fixed unknown orientation case

5.1 Introduction

The work presented in this chapter pursues the same objectives as the one presented in the previous chapter, *i.e.*, evaluating the performance of localization methods leaning on sparsity for oscillatory brain source localization, at the difference that we aim also to estimate the fixed but unknown orientations of the underlying dipolar sources. While in EEG the dipoles may be constrained to be radial, as this is known to be the main contributors to the EEG measurements, such hypothesis is no longer valid for SEEG data, motivating the work of this chapter. Besides, even in EEG, the orientation is not necessarily radial: the common hypothesis states that dipoles are oriented along the pyramidal neurons situated in the gray matter columns. As the gray matter has a complex folded geometry, one should rather constrain the dipoles to be orthogonal to the gray matter instead of the head surface. But this constraint relies on the accuracy of the head tissues segmentation and numerization and it is thus prone to errors. Having these considerations in mind, we address in this chapter the localization problem jointly with the orientation estimation problem, assuming that the sources of interest have a fixed (unknown) orientation and are persistent all along the recorded data.

In the first section of the chapter, a new greedy algorithm derived from the family of step-wise regressions on a given dictionary (forward model) is proposed. Unlike the version used in Chapter 4, the regressors are not column vectors anymore, but matrices, representing 3D lead-field blocks associated to each possible source position ($M \times 3$, M being the number of electrodes). Moreover, the regression coefficients (vectors varying in time, representing dipolar amplitudes) are constrained to fixed orientations. The next sections formalize this model and explain its usefulness for solving the inverse problem of brain source estimation (Section 5.2), describing the proposed algorithms and analyzing their convergence (Section 5.3) and finally illustrating their performances (Section 5.4) on realistic simulated data and on real signals, both in EEG and SEEG.

5.2 Model

Let recall the (no-noise) forward model at time instant t:

$$
\begin{aligned}
\mathbf{x} &= \begin{bmatrix} k_{11_x} & k_{11_y} & k_{11_z} \\ k_{12_x} & k_{12_y} & k_{12_z} \\ \vdots & \vdots & \vdots \\ k_{1M_x} & k_{1M_y} & k_{1M_z} \end{bmatrix} \begin{bmatrix} j_{1_x} \\ j_{1_y} \\ j_{1_z} \end{bmatrix} + \dots \\
&\dots + \begin{bmatrix} k_{p1_x} & k_{p1_y} & k_{p1_z} \\ k_{p2_x} & k_{p2_y} & k_{p2_z} \\ \vdots & \vdots & \vdots \\ k_{pM_x} & k_{pM_y} & k_{pM_z} \end{bmatrix} \begin{bmatrix} j_{p_x} \\ j_{p_y} \\ j_{p_z} \end{bmatrix} \\
&= \sum_{i=1}^{p} \mathbf{k}_i \mathbf{j}_i = \mathbf{K}_I \mathbf{j}_I, \qquad (5.1)
\end{aligned}
$$

where $\mathbf{x}$ ($M \times 1$) is the vector of measured potentials (electrodes), $\mathbf{k}_i$ ($M \times 3$) represent the propagation coefficients of the unit dipole situated at position i on the M electrodes, and $\mathbf{j}_i$ (3×1) are the 3D projections of the dipolar moments of the dipole at position i (3×1) (k_{ab_c} is the propagation coefficient of the dipole in position $a = 1 \ldots p$ onto the sensor $b = 1 \ldots M$ with direction $c = \{x, y, z\}$). In compact form, the forward mixing model of p sources towards M sensors is written as on the last row of (5.1), with $\mathbf{K}_I$ ($M \times 3p$) the lead-field matrix of the active sources, $\mathbf{j}_I$ the dipolar projections ($3p \times 1$) and I the set of active dipoles. Let recall also that we place ourselves directly in a "sparse" configuration, *i.e.*, when the indices in I do not cover all the columns of the lead-field matrix or, in other words, when I encodes the positions of the active sources. In a fully distributed head-model, as used in minimum norm (MN) type approaches, all positions are taken into account, which yields non-null source estimates distributed in all the head volume (or in some restriction of it, usually the gray matter).

When including several time samples $t = 1 \ldots n$, Equation (5.1) becomes:

$$\begin{aligned}\mathbf{X} &= \sum_{i=1}^{p} \left(\begin{bmatrix} k_{i1_x} & k_{i1_y} & k_{i1_z} \\ k_{i2_x} & k_{i2_y} & k_{i2_z} \\ \vdots & \vdots & \vdots \\ k_{iM_x} & k_{iM_y} & k_{iM_z} \end{bmatrix} \begin{bmatrix} j_{i_x}(1) & \ldots & j_{i_x}(n) \\ j_{i_y}(1) & \ldots & j_{i_y}(n) \\ j_{i_z}(1) & \ldots & j_{i_z}(n) \end{bmatrix} \right) \\ &= \sum_{i=1}^{p} \mathbf{k}_i \mathbf{J}_i = \mathbf{K}_I \mathbf{J}_I \qquad (5.2)\end{aligned}$$

with $\mathbf{X} : m \times n$, $\mathbf{k}_i : m \times 3$ and $\mathbf{J}_i : 3 \times n$ ($\mathbf{J} : 3p \times n$).

According to the model introduced in the previous equations, the matrices $\mathbf{J}_i$ (time courses of the three orthogonal projections of the dipole at position i) are not constrained: for a given dipole i, its projections $[j_{i_x}(t) \;\; j_{i_y}(t) \;\; j_{i_z}(t)]^T$ can vary independently with the time t. In other words, the dipole potentially has a varying orientation in time.

A way of simplifying this general model is to consider that each dipole orientations are fixed and *known*, retrieving the fix dipole model as used in the previous chapter. To do so, one can consider the (normalized) vector of orientations $\mathbf{o}_i$ for each dipole as known and rewrite the model as:

$$\begin{aligned}\mathbf{X} &= \sum_{i=1}^{p} \left(\begin{bmatrix} k_{i1_x} & k_{i1_y} & k_{i1_z} \\ k_{i2_x} & k_{i2_y} & k_{i2_z} \\ \vdots & \vdots & \vdots \\ k_{iM_x} & k_{iM_y} & k_{iM_z} \end{bmatrix} \begin{bmatrix} o_{i_x} \\ o_{i_y} \\ o_{i_z} \end{bmatrix} [s_i(1) \ldots s_i(n)] \right) \\ &= \sum_{i=1}^{p} \mathbf{k}_i \mathbf{o}_i \mathbf{s}_i = \mathbf{A}_I \mathbf{S}_I \qquad (5.3)\end{aligned}$$

with the $M \times p$ fixed orientation lead-field matrix $\mathbf{A}_I = \mathbf{K}_I \mathbf{O}_{B,I}$ (with $\mathbf{O}_{B,I}$ a $3p \times p$ block diagonal matrix having on the diagonal the *known* orientations $\mathbf{o}_i$) and the $p \times n$ amplitudes matrix $\mathbf{S}_I$.

Still, as mentioned in the introduction of this chapter, the fixed known orientation hypothesis is not always justified: the "orthogonal to the head surface" orientation is very restrictive and ignores the folded shape of the cortical surface. Besides, it cannot be used for inverse problems based on intracerebral measurements as in SEEG. On the other hand, the "orthogonal to the cortical head surface" orientation is subject to the imaging quality and to the resolution of the numerical models.

In this chapter, we make a relaxed assumption: the sources are supposed to have fixed but *unknown* orientations. As explained in Chapter 3 from the visualization of real data under a FPVS protocol (Section 3.2), the fact that high and well resolute peaks are visible in the Fourier transform magnitude of the data very likely implies source dipoles with fixed orientation.

To summarize, we assume in this chapter that the measured potentials $\mathbf{X}$ are generated by an unknown number p of dipolar sources situated in unknown positions (corresponding to $M \times 3$ blocks $\mathbf{k}_i$ and indexed in the vector I of cardinal p), having unknown but fixed orientations $\mathbf{o}_i$ (3×1) and time varying amplitudes $\mathbf{s}_i$ ($1 \times n$). Model (5.2) writes then in the same form as (5.3), but with unknown orientations $\mathbf{o}$:

$$\begin{aligned}\mathbf{X} &= \sum_{i=1}^{p} \left(\begin{bmatrix} k_{i1_x} & k_{i1_y} & k_{i1_z} \\ k_{i2_x} & k_{i2_y} & k_{i2_z} \\ \vdots & \vdots & \vdots \\ k_{iM_x} & k_{iM_y} & k_{iM_z} \end{bmatrix} \begin{bmatrix} o_{i_x} \\ o_{i_y} \\ o_{i_z} \end{bmatrix} [s_i(1) \ \dots \ s_i(n)] \right) \\ &= \sum_{i=1}^{p} \mathbf{k}_i \mathbf{o}_i \mathbf{s}_i = \sum_{i=1}^{p} \mathbf{k}_i \mathbf{J}_i^1 = \mathbf{K}_I \mathbf{J}_I^1 \end{aligned} \tag{5.4}$$

In (5.4), grouping the orientations $\mathbf{o}_i$ and the amplitudes $\mathbf{s}_i$ in a single variable yields $\mathbf{J}_i^1 : 3 \times n$ of unit rank. Further, $\mathbf{J}_I^1$ is the $(3p \times n)$ matrix of dipolar sources obtained by stacking the $\mathbf{J}_i^1$ blocks $(i \in I)$.

As model (5.3), model (5.4) can also be written as:

$$\mathbf{X} = \mathbf{K}_I \begin{bmatrix} \mathbf{o}_1 & 0 & \dots & 0 \\ 0 & \mathbf{o}_2 & \dots & 0 \\ \dots & \dots & \dots & \dots \\ 0 & \dots & 0 & \mathbf{o}_p \end{bmatrix} \begin{bmatrix} \mathbf{s}_1 \\ \mathbf{s}_2 \\ \vdots \\ \mathbf{s}_p \end{bmatrix} = \mathbf{K}_I \mathbf{O}_{B,I} \mathbf{S}_I \tag{5.5}$$

where $\mathbf{O}_{B,I}$ is block diagonal *unknown* orientations matrix ($3p \times p$) and $\mathbf{S}_I$ are the stacked time courses of the p dipoles ($p \times n$) (with thus $\mathbf{J}_I = \mathbf{O}_{B,I} \mathbf{S}_I$).

5.3 OLS-R1 and SBR-R1 algorithms

The inverse problem we aim to solve is therefore the following: knowing the measurements $\mathbf{X}$ and the head model $\mathbf{K}$, estimate the positions $i \in I$, the orientations $\mathbf{o}_i$ and the time amplitudes $s_i(t)$, under the assumption of sparseness, *i.e.*, a low cardinal of I. By default, the lead-field matrix $\mathbf{K}$ is "fat", *i.e.*, the total number of potential source positions N is much higher that the number of electrodes M.

5.3.1 MUSIC type algorithms

Although the problem has not been formulated as above, the MUSIC family of algorithms, and especially the recursive versions RAP-MUSIC [Mosher et al., 1999] and TRAP-MUSIC [Mäkelä et al., 2018], provide a possible solution. We recall here briefly their principles (see also the description in Chapter 2). These methods start by finding a "spatial" basis $\mathbf{V}$ of the $\mathbf{X}$ measurements by SVD:

$$\mathbf{X} = \mathbf{V}\mathbf{\Sigma}\mathbf{W}^T$$

In other words, each column of $\mathbf{X}$ (the spatial distribution of measured signals amplitudes at a given time instant) is a weighted sum of the columns of the $\mathbf{V}$ basis. This basis is next truncated by keeping only the r singular vectors corresponding to the largest singular values (assuming thus that the others correspond to noise). These vectors, grouped in the $\mathbf{V}_s$ matrix, constitute a basis for the signal space.

The next step consists in "scanning" the $\mathbf{K}$ matrix and evaluate for each sub-matrix $\mathbf{k}_i$ ($M \times 3$, containing the projection coefficients of the dipole i on the M electrodes) its canonical correlation with $\mathbf{V}_s$ (the truncated basis) [5]. The chosen positions (the set of indices $i \in I$ of the dipoles included in the solution) are those corresponding to the maxima (in absolute value) of the canonical correlation coefficients (in the recursive versions mentioned above, these correlations are computed after a succession of re-projections between the sub-spaces of $\mathbf{V}_s$ and $\mathbf{K}$ and the set of indices I gets larger as the iterations proceed, see for details [Mosher et al., 1999; Mäkelä et al., 2018]).

For every selected position i, the dipolar orientations $\mathbf{o}_i$ (not constrained to be fixed in principle) are in turn provided by the coefficients of the linear combination of the 3 columns of $\mathbf{k}_i$, which generates a vector as close as possible (*i.e.*, with the smallest angle) with the base signal space $\mathbf{V}_s$ (or its residual after reprojection in the iterative versions). For every position, once the orientation is estimated, the 3-columns submatrix $\mathbf{k}_i$ is collapsed into a single column vector by right multiplication with the orientation vector $\mathbf{o}_i$. For the p selected dipoles (positions), this procedure yields the $M \times p$ matrix $\mathbf{K}^1$ (using the notations from Equation (5.5), $\mathbf{K}^1 = \mathbf{K}_I\mathbf{O}_{B,I}$), which is finally pseudo-inverted in order to estimate (as in multiple regression) the dipole amplitudes $\mathbf{s}_i$ (note that in principle, in

---

[5] We speak here of the correlation between the sub-spaces $\mathbf{k}_i$ and $\mathbf{V}_s$ (in other words, the cosine of the principal angle between the two sub-spaces).

MUSIC-like algorithms, it is possible to select a specific position up to 3 times, in which case the dipoles at those specific positions have time varying orientations).

5.3.2 OLS-R1 and SBR-R1 algorithms

We describe next the construction of the new algorithms proposed in this work. They use an alternate optimization technique that aims to re-estimate, at each iteration, the positions, the orientations and the amplitudes of the dipoles indexed in I (note that, in the iterative versions of MUSIC, only the orientation of the current dipole is estimated, while the ones already included in I maintain their previously estimated orientations). To be more specific, we want to estimate a set of sources characterized by their positions $\hat{I}$ and dipolar moments $\hat{\mathbf{J}}_{\hat{I}}$, under the constraint of a fixed orientation. Using the notations from Equation (5.2), we can write the optimization problem as:

$$\min\left(\|\hat{I}\|_0\right) \;\; \text{u.c.} \;\; \begin{cases} \|\mathbf{X}-\sum_{i\in\hat{I}}\mathbf{k}_i\hat{\mathbf{J}}_i\|_2 < \varepsilon \\ \text{rank}(\hat{\mathbf{J}}_i) = 1 \end{cases} \tag{5.6}$$

Alternatively, with the notations from Equation (5.5), we can state the optimization problem as in [Soussen et al., 2011], using a penalization term. More precisely, the goal is to estimate a set $\hat{I}$ of source positions, their fixed orientations $\hat{\mathbf{O}}_{B,\hat{I}}$ and amplitudes $\hat{\mathbf{S}}_{\hat{I}}$, while minimizing the reconstruction error $\|\mathbf{X}-\mathbf{K}_I\mathbf{O}_{B,I}\mathbf{S}_I\|_2$ and the cardinal of I:

$$\{\hat{I},\hat{\mathbf{O}}_{B,\hat{I}},\hat{\mathbf{S}}_{\hat{I}}\} = \underset{I,\mathbf{O}_{B,I},\mathbf{S}_I}{\text{argmin}}(\|\mathbf{X}-\mathbf{K}_I\mathbf{O}_{B,I}\mathbf{S}_I\|_2^2+\lambda\|I\|_0) \tag{5.7}$$

where λ is a user parameter balancing between sparseness and reconstruction error, while $\|I\|_0$ is the cardinal of I.

Before proceeding with the description of the algorithms, we evacuate the problem of estimating the amplitudes $\hat{\mathbf{S}}_{\hat{I}}$. Indeed, for any given estimated positions $\hat{I}$ and orientations $\hat{\mathbf{O}}_{B,\hat{I}}$, the optimal amplitudes can be obtained trivially by regression/least-squares (as also in (T)RAP-MUSIC):

$$\hat{\mathbf{S}}_{\hat{I}} = (\mathbf{K}_{\hat{I}}\hat{\mathbf{O}}_{B,\hat{I}})^{+}\mathbf{X} \tag{5.8}$$

where $^{+}$ is the pseudo-inverse of a reduced dictionary matrix $(\mathbf{K}_{\hat{I}}\hat{\mathbf{O}}_{B,\hat{I}})$ with column elements $(M \times 1)$. In other words, the main difficulty is the estimation of the positions and orientations.

Positions We start by describing an OLS type procedure, adapted to a matrix dictionary $\mathbf{K}$ where, unlike in classical multiple regressions (as for example in Equation (5.8)), every element of the dictionary is a sub-matrix of size $M \times 3$ (the 3-columns "lead-field" matrix for each position). Using this dictionary, a block version of OLS can be written as in Algorithm 6.

Algorithm 6: Block-OLS

```
Initialization $\hat{I} = \emptyset$,  $\hat{\mathbf{X}} = \mathbf{0}$ ;
while $\|\mathbf{X} - \hat{\mathbf{X}}\|_2^2 > \varepsilon \|\mathbf{X}\|_2^2$ do
    /* Scan to chose the new regressor (position)                */
    for $i \notin \hat{I}$ do
        $\hat{I}_t = \hat{I} \cup i$; /* temporary support              */
        $\hat{\mathbf{J}}_{\hat{I}_t} = \mathbf{K}_{\hat{I}_t}^{+}\mathbf{X}$; /* temporary coefficients      */
        $\hat{\mathbf{X}} = \mathbf{K}_{\hat{I}_t}\hat{\mathbf{J}}_{\hat{I}_t}$;
        $\mathrm{err}(i) = \|\mathbf{X} - \hat{\mathbf{X}}\|_2^2$;
    end
    $i_c = \mathrm{argmin}_i(\mathrm{err}(i))$; /* chosen position          */
    $\hat{I} = \hat{I} \cup i_c$; /* update positions vector            */

    /* Update regression coefficients                            */
    $\hat{\mathbf{J}}_{\hat{I}} = \mathbf{K}_{\hat{I}}^{+}\mathbf{X}$;/* orientations and amplitudes  */
    $\hat{\mathbf{X}} = \mathbf{K}_{\hat{I}}\hat{\mathbf{J}}_{\hat{I}}$;
end
```

This algorithm has OLS optimality, the error is obviously monotonically decreasing and thus is convergent (as for any regression, adding more regressors diminishes the error). But it does not fulfill one of the conditions that we imposed, *i.e.*, the orientations are not fixed: $\hat{\mathbf{J}}_{\hat{I}}$ is of dimension $3p \times n$, with *a priori* linearly independent rows.

Orientations Algorithm 6 yields estimations of the time varying orientations and amplitudes embedded in $\hat{\mathbf{J}}_{\hat{I}}$ ($3p \times n$), *a priori* of rank $3p$ (assuming that n is sufficiently high), with p the cardinal of $\hat{I}$. The best approximation of $\hat{\mathbf{J}}_{\hat{I}}$ that fulfills the fixed orientation condition can be constructed by applying an SVD decomposition to each of the stacked p blocks of size $3 \times n$. By SVD, each block can be written as a sum of rank 1 matrices

$$\hat{\mathbf{J}}_{\hat{i}} = \sum_{k=1}^{3} \mathbf{u}_{k,\hat{i}} \sigma_{k,\hat{i}} \mathbf{w}_{k,\hat{i}}^T \tag{5.9}$$

where $\mathbf{u}, \mathbf{w}$ and σ are respectively the left singular vectors, the right singular vectors and the singular values. As the best approximation (in Frobenius norm) of $\mathbf{j}_{\hat{i}}$ is given by the first term of this sum, the best approximation of $\hat{\mathbf{J}}_{\hat{I}}$ is given by:

$$\tilde{\mathbf{J}}_{\hat{I}} = \begin{bmatrix} \mathbf{u}_1 & 0 & \dots & 0 \\ 0 & \mathbf{u}_2 & \dots & 0 \\ \cdots & \cdots & \cdots & \cdots \\ 0 & \dots & 0 & \mathbf{u}_p \end{bmatrix} \begin{bmatrix} \sigma_1 \mathbf{w}_1^T \\ \sigma_2 \mathbf{w}_2^T \\ \vdots \\ \sigma_p \mathbf{w}_p^T \end{bmatrix} \tag{5.10}$$

where, in order to simplify the notations, $\mathbf{u}_i$ is $\mathbf{u}_{1,\hat{i}}$, *i.e.*, the first singular vector of the block $\hat{\mathbf{J}}_{\hat{i}}$ (same for the right vectors and the singular values).

A first approach would be to define

$$\hat{\mathbf{O}}_{B,\hat{I}} = \begin{bmatrix} \mathbf{u}_1 & 0 & \dots & 0 \\ 0 & \mathbf{u}_2 & \dots & 0 \\ \dots & \dots & \dots & \dots \\ 0 & \dots & 0 & \mathbf{u}_p \end{bmatrix} \tag{5.11}$$

and

$$\hat{\mathbf{S}}_{\hat{I}} = \begin{bmatrix} \sigma_1 \mathbf{w}_1^T \\ \sigma_2 \mathbf{w}_p^T \\ \vdots \\ \sigma_p \mathbf{w}_p^T \end{bmatrix} \tag{5.12}$$

The estimated dipoles (with fixed orientations $\hat{\mathbf{O}}_{B,\hat{I}}$ and time courses $\hat{\mathbf{S}}_{\hat{I}}$) are, by construction, the closest approximation of the OLS solution $\hat{\mathbf{J}}_{\hat{I}}$ of algorithm 6. Still, this solution is not optimal in the sense of minimizing the reconstruction error, and moreover, it is not necessarily monotonic not even convergent.

Convergence We propose thus to preserve, from Equation (5.11), only the orientation matrix $\hat{\mathbf{O}}_{B,\hat{I}}$ and to obtain the time courses by Equation (5.8) (and not by Equation (5.12)). As mentioned, for any given positions and orientations, the amplitudes given by Equation (5.8) ensure the smallest reconstruction error, meaning that the best rank 1 reconstruction of the sources $\mathbf{J}$ of Equation (5.12) does not guarantee the best reconstruction of the data $\mathbf{X}$. But, if the amplitudes/coefficients are reconstructed by regression in Equation (5.8), the convergence is ensured, in the sense that the algorithm will converge in at most M iterations (when the cardinal p of I is equal to the number of sensors M, the error $||\mathbf{X} - \hat{\mathbf{X}}||_2$ becomes 0).

A suboptimal but convergent solution respecting the fixed orientation (rank 1) condition can be thus obtained by replacing $\hat{\mathbf{J}}_{\hat{I}}$ in Algorithm 6 by:

$$\hat{\mathbf{J}}^1_{\hat{I}} = \hat{\mathbf{O}}_{B,\hat{I}}(\mathbf{K}_{\hat{I}}\hat{\mathbf{O}}_{B,\hat{I}})^+\mathbf{X} \tag{5.13}$$

which will yield a reconstructed signal $\hat{\mathbf{X}}$:

$$\hat{\mathbf{X}} = \mathbf{K}_{\hat{I}}\hat{\mathbf{O}}_{B,\hat{I}}(\mathbf{K}_{\hat{I}}\hat{\mathbf{O}}_{B,\hat{I}})^+\mathbf{X} = \hat{\mathbf{K}}^1_{\hat{I}}\hat{\mathbf{K}}^{1+}_{\hat{I}}\mathbf{X} \tag{5.14}$$

One can recognize a classical multiple regression, where the dictionary matrix $\hat{\mathbf{K}}^1_{\hat{I}}$ has one-column elements (regressors).

Monotonicity Even if the convergence is ensured by using Equation (5.13), there is no guarantee of sparseness. Indeed, even after this modification, the rank one regression coefficients (and in particular the orientation matrix $\hat{\mathbf{O}}_{B,\hat{I}}$) change at every iteration. Consequently, the dictionary matrix $\hat{\mathbf{K}}^1_{\hat{I}}$ appearing in Equation (5.14) changes at every iteration, which might result in an increase of the reconstruction error $||\mathbf{X}-\hat{\mathbf{X}}||_2$. As a non monotonic algorithm is certainly not optimal in terms of sparseness (as it might choose, because of the change in the dictionary of regressors, elements that increase the error), a way of improving the sparseness is to guarantee that the reconstruction error $||\mathbf{X}-\hat{\mathbf{X}}||_2$ monotonically decreases at every iteration. We propose next an algorithmic modification in order to ensure monotonicity.

Consider the solution after iteration k. At iteration $k+1$, instead of recomputing all the orientations $\hat{\mathbf{O}}_{B,\hat{I}}$ by the SVD based procedure described above (Equations 5.10 and 5.11), the orientations computed at iteration k are preserved and the SVD procedure is applied only to compute the optimal orientation of the currently estimated source at position i_c. This is equivalent to add a new 3×1 block on the diagonal of the matrix $\hat{\mathbf{O}}_{B,\hat{I}}$ (5.11) (which increases in size). Further, this is equivalent to adding a supplementary column to the matrix $\hat{\mathbf{K}}^1_{\hat{I}}$ (5.14), while preserving the previous columns. By construction (adding a new regressor to the dictionary), this will necessarily decrease the reconstruction error, so it ensures monotonicity.

This alternative solution is monotonic but, at a given iteration, it might decreases slower than the solution obtained directly by Equations (5.11) and (5.8). A naturally arising algorithmic solution is the following: at every iteration, compute both solutions (all orientations are re-estimated vs. only the last one is estimated) and choose the solution minimizing the reconstruction error. In this way, the reconstruction error is upper bounded by a monotonically decreasing sequence, thus it is monotonically decreasing itself. Note that a similar argument is proposed for convergence of the K-SVD algorithm [Aharon et al., 2006] (this algorithm, which re-estimates iteratively the regression coefficients but also the regressor dictionary, cannot be applied in the inverse problem that we address here because our dictionary (lead-field) is constrained by the physical properties of the propagation medium).

The final OLS-R1 algorithm will be then obtained by procedure Rank1Constraint, inserted between rows 11 and 12 of the previously introduced Algorithm 6.

Single Best Replacement Finally, one can control sparsity by adding a final step inspired from the SBR procedure proposed in [Soussen et al., 2011]. This implies computing the full objective function from Equation (5.7), *i.e.*, including explicitly the cardinal of the solution $\hat{I}$ through the sparsity parameter λ. SBR, more expensive in computing time, also needs to tune the sparsity parameter λ, or at least to initialize it and let it to adapt automatically as proposed in the CSBR algorithm [Soussen et al., 2015].

We have implemented these different flavors of the step-wise regression, of course including the

```
Procedure Rank1Constraint
/* Standard rank 1 solution */
for $i \in \hat{I}$ do
    Obtain $\hat{\mathbf{O}}_{B,\hat{I}}$ by eq. (5.9) to (5.11);/* re-estimate all orientations */
end
Obtain $\hat{\mathbf{S}}_{\hat{I}}$ by eq. (5.8);/* amplitudes */
Obtain $\hat{\mathbf{X}}$ by eq.(5.14);

/* Alternate rank 1 solution ensuring monotony */
$p = \mathrm{card}(\hat{I})$;/* cardinal of the current solution */
$\hat{I}_{prev} = \hat{I} \setminus \{i_c\}$;/* set of previous positions */
Obtain $\hat{\mathbf{o}}_{i_c}$ by eq. (5.9) ($\hat{\mathbf{o}}_{i_c} = \hat{\mathbf{u}}_{i_c}$);/* estimate current dipole orientation */
Obtain $\hat{\mathbf{O}}_{B,\hat{I},alt} = \begin{bmatrix} \hat{\mathbf{O}}_{\hat{I}_{prev}} & \mathbf{0}_{3(p-1)\times 1} \\ \mathbf{0}_{3\times(p-1)} & \hat{\mathbf{o}}_{i_c} \end{bmatrix}$; /* alternate orientations */
Obtain $\hat{\mathbf{S}}_{\hat{I},alt}$ by eq. (5.8);/* alternate amplitudes */
Obtain $\hat{\mathbf{X}}_{alt}$ by eq.(5.14); /* alternate data reconstruction */

/* Choose optimal monotonic solution */
if $\|\mathbf{X} - \hat{\mathbf{X}}\|_2^2 > \|\mathbf{X} - \hat{\mathbf{X}}_{alt}\|_2^2$ then
    $\hat{\mathbf{J}}_{\hat{I}} = \hat{\mathbf{O}}_{B,\hat{I},alt}\hat{\mathbf{S}}_{\hat{I},alt}$
else
    $\hat{\mathbf{J}}_{\hat{I}} = \hat{\mathbf{O}}_{B,\hat{I}}\hat{\mathbf{S}}_{\hat{I}}$
end
Return $\{\hat{I}, \hat{\mathbf{J}}_{\hat{I}}\}$ /* constrained solution, fixed orientation */
```

fixed orientation constraint. The most significant results are presented in the next section, both in simulation and some real data examples.

5.4 Results

We first present the simulation setup used in this chapter. Then, the results of source localization on multiple oscillating sources are discussed. This task was addressed using recursive versions of MUSIC (RAP and TRAP MUSIC) and greedy regression-like methods (OLS-R1, SBR-R1) described in section 5.3, in time and frequency domain, using different forward model setups for data generation in scalp setup (EEG) and intracranial setup (SEEG). Finally, source estimation examples are presented on real EEG data recorded during the FPVS protocol.

5.4.1 Simulated data

We have simulated electrophysiological EEG and SEEG recordings using realistic forward model setups (BEM and FEM head models). We have used the free-oriented forward models (lead-fields) defined in Chapter 3 (section 3.5.1) to simulate the (S)EEG data. We focus in this chapter only on the sparser FEM model with size $64 \times 3 \cdot 509$, for both EEG and SEEG. As seen in the previous chapter, the results are similar for both lead-fields, while the computation time is far higher for the time domain versions of the localization algorithms when applied on the denser lead-field. The SEEG potentials were simulated with the same FEM model as the scalp EEG potentials, but using intracranial sensors, resulting in a lead-field matrix $\mathbf{K} = 186 \times (3 \cdot 509)$.

The same source configurations as in Chapter 4 (section 4.3.1) were used : $p = 3, 4, 5, 7$, with either single frequency ($f_0 = 6Hz$) alone or along with its harmonics *e.g.*, 12 Hz, 18 Hz, 24 Hz. The same seven noise power levels have been used ({40dB, 20dB, 10dB, 3dB, 0dB, -3dB, -10dB}) and one hundred simulations were performed per each p (randomly taken the source positions, amplitudes and phases) and noise level, using the algorithms SBR-R1, OLS-R1, RAP and TRAP MUSIC in the time domain or directly in the frequency peaks of interest.

5.4.2 Simulation results

The localization results obtained from simulated (S)EEG recordings, assuming a source model with fixed unknown orientation, are exposed. The EEG results using FEM model $\mathbf{K}$ ($64 \times (3 \cdot 509)$) are presented in Figure 5.1, addressing the localization with single frequency at 6 Hz and in Figure 5.2 with 6 Hz and 3 harmonics at 12 Hz, 18 Hz, 24 Hz. The SEEG results using FEM model $\mathbf{K}$ ($186 \times (3 \cdot 509)$), for single 6 Hz frequency are exposed in Figure 5.3, and in Figure 5.4 for 6 Hz plus harmonics.

These results illustrate the source localization on the algorithms SBR-R1, OLS-R1, RAP and TRAP MUSIC (see Section 5.3). We compare the methods in time and frequency domain, when confronting them to the variation of the number of active sources and SNRs (see above) by using the sensitivity (TPR), precision (TDR) and distance of localization error (DLE), this last metric providing a global view on both the sensitivity (TPR) and precision (TDR) of the methods (for details of these metrics refer to the Chapter 4, Subsection 4.3.2).

EEG results

In Figure 5.1 is given the performance of the algorithms in both frequency and time domain for a single frequency source. In frequency, for three sources, SBR-R1 shows better results on the reconstruction of the true sources (TPR), since this method is also less affected by the reconstruction of false sources (TDR), with a DLE varying from 0.7cm to 1.6cm as the SNR diminishes. OLS-R1 shows a slightly better sensitivity than SBR-R1, but its precision is significantly affected by more false reconstructed sources, yielding values of DLE from 1cm to 2.1cm. RAP and TRAP MUSIC show a notable discrepancy with the two previous methods, having values of sensitivity lower than SBR-R1 and OLS-R1 and their precision below the values with SBR-R1. The DLEs for RAP vary from 2.1cm to 2.4cm and for TRAP from 2.3cm to 2.4.

In time, all algorithms expose more abrupt changes along the SNRs. The sensitivity of SBR-R1 and OLS-R1 drastically decrease along the SNRs, which means that the impact is strong as reaching higher noise levels in the signals and the same effect occurs on their precision, with DLEs for SBR-R1 from 0.8cm to 3.2cm and OLS-R1 from 1.1cm to 3.4cm, while for RAP from 2.1cm to 3.1cm and TRAP from 2.4cm to 3.1cm.

When evaluating the results for four sources, the performance of the algorithms logically diminish. Still SBR-R1 in frequency is the one less impacted by the increase of the number of sources, followed by OLS-R1, which achieves a higher sensitivity over SBR-R1, but the counterpart is the reconstruction of more false positives. SBR-R1 gives DLEs from 1.3cm to 2cm and OLS-R1 from 1.4cm to 2.2cm. RAP and TRAP still have lower performance when compared with SBR-R1 and OLS-R1, with very stable DLEs between 3cm and 3.1cm along the SNRs. These methods also show similar results in time domain with DLEs from 3.1cm and up to 3.5cm for $-10dB$.

For five and seven sources, *i.e.*, when the assumption of sparsity is less valid, the performances become weaker. In frequency, values of DLE for both SBR-R1 and OLS-R1 remain very stable with the SNR, for five sources from 2.1cm to 2.6cm and seven sources from 2.4cm to 2.7cm. Their counterparts in time have also similar DLEs, but lower than in frequency, for five sources from 2.1cm to 4cm and for seven sources from 2.4cm to 4.2cm. While for RAP and TRAP their performance are similar, for five sources the DLEs in frequency and time between 3.6cm and 3.7cm, and 4cm for both methods in time for most of the noisy case $-10dB$. While for seven sources, the values are between 4cm and 4.1cm for both domains, and only 4.4cm for both methods in time when the SNR falls to $-10dB$.

Globally for this single frequency case, MUSIC algorithms seem to be ineffective, with DLEs above 1cm in most of the cases. These methods are based on the estimation of the source space at their initialization, which is theoretically limited to two in this case as explained in Chapters 3 and 4 (for time versions, even if the estimated source space is higher, this is mainly due to noise and it does not improve source estimation). The weak performances are also related to the source ambiguity problem as exposed in Chapter 3 (possible presence of alternative source configurations). Compared to the results with fixed and known orientations (Chapters 4), this ambiguity problem is even more likely to appear, because of the higher degree of freedom offered by the free oriented lead-field: the performance are indeed decreased compared to those of the previous chapter, with DLE values about 5mm higher overall.

OLS-R1/SBR-R1 methods provide better performance than MUSIC ones, as they do not rely on a source space estimation at initialization. As it was the case in the previous chapter, high robustness to noise is achieved in the frequency domain by focusing on the frequency points of interest. Performances are similar in the time domain for low noise levels, but quickly decrease with the SNR.

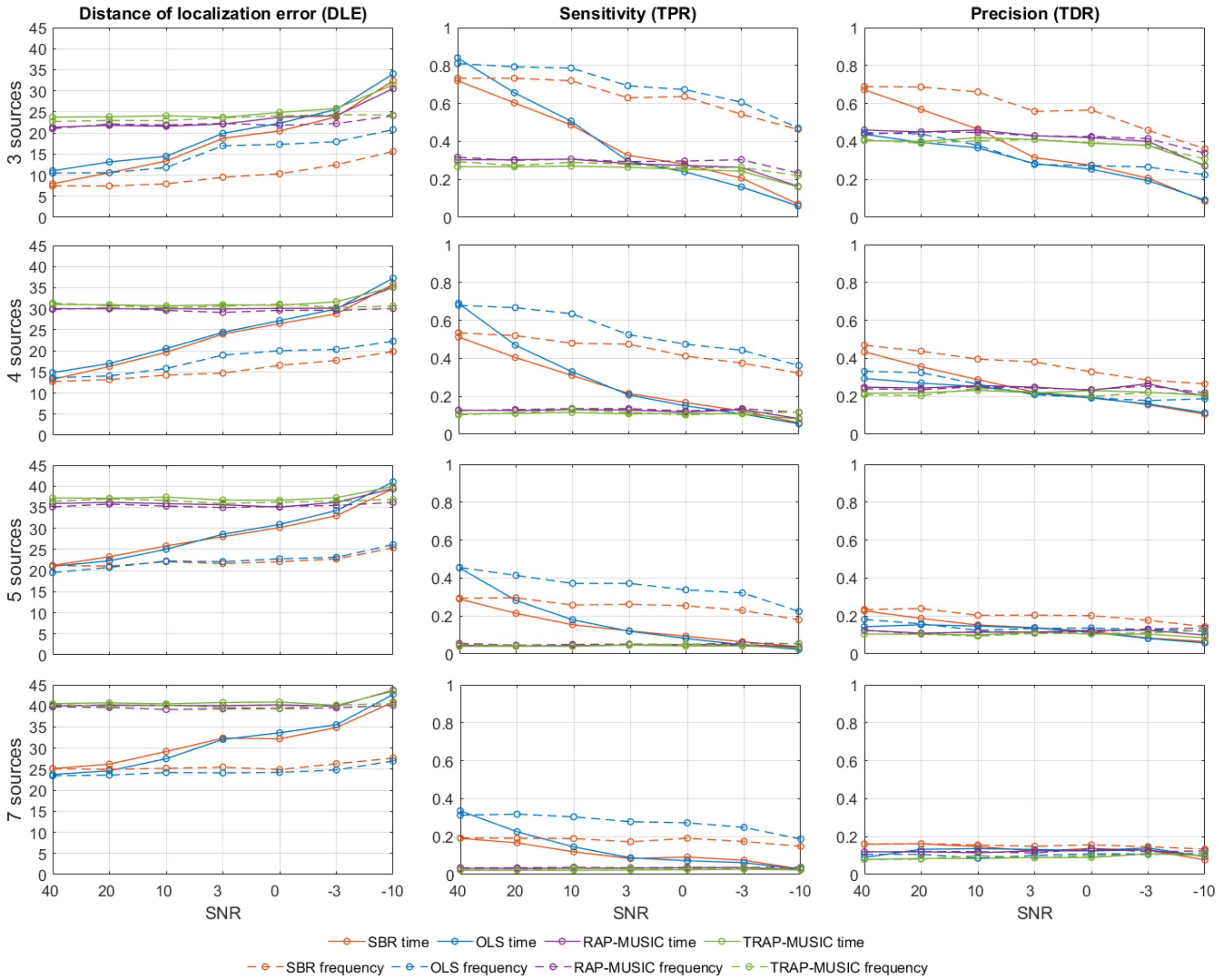

FIGURE 5.1 – SBR-R1, OLS-R1, RAP and TRAP MUSIC localization performance in scalp EEG data simulated using multiple oscillating sources at 6Hz, from the lead-fied matrix $\mathbf{K} : 64 \times (3 \cdot 509)$. These algorithms were applied in frequency (dashed lines) and time (solid lines) domain. By columns, the results of DLE (in mm), sensitivity (TPR) and precision (TDR). By rows, the results for each number of simulated sources $p = 3, 4, 5, 7$. For each subplot, the x-axis shows the SNR (40, 20, 10, 3, 0, -3, -10).

When harmonics are involved, the performance are globally better for all algorithms, as it was already observed in the previous chapter. In frequency, SBR-R1 has improved in sensitivity and precision, and so are the DLEs: for 3 sources, DLE values range from 0.3cm to 1.3cm, while for 7 sources DLEs goes from 1.9cm to 2.4cm. OLS-R1 exposes a good sensitivity, but still fails in precision, with DLEs for 3 sources from 0.6cm to 1.5cm and reaching for 7 sources values from 1.5cm to 2.4cm. As explained in the previous chapter, the dimension of the source space, as estimated by RAP and TRAP MUSIC in the frequency domain, is limited to twice the number of harmonics considered for localization ($2 \times 4 = 8$ for these simulations), this value being often reached by the MDL estimator we use. For low number of sources, this translates in high sensitivity for RAP and TRAP MUSIC with however poor precision values. When the number of sources increases, the methods become weaker in sensitivity but with higher precision, *i.e.*, less true reconstructed sources, but also less false sources. As the DLE is a compromise between precision and sensitivity, the values are rather similar with the number of sources: for 3 sources, DLE values range from 1.5cm to 1.9cm, and from 1.4cm to 2.6cm for 7 sources.

In time, RAP and TRAP improve in sensitivity and precision, as the estimation of the source space is easier (more data points provide higher statistical significance). For 3 sources, these methods show high robustness to noise up to $-3dB$, with drastic decreases of the performance at $-10db$. RAP ranges from 0.3cm to 0.7cm up to $-3db$ and fall to 2.5cm for $-10dB$, and TRAP values vary from 0.5cm to 1.1cm for $4db$ to $-3db$, and drastically 2.7cm for $-10dB$. These methods are more sensitive to noise as the number of sources increases, *e.g.*, for 7 sources RAP ranges from 1.1cm to 3.7cm and TRAP from 1.3cm to 3.9cm. Meanwhile, SBR-R1 and OLS-R1 still provide satisfactory results for higher SNR in time domain, but their performance quickly decreases with the noise. SBR-R1 provides slightly better results than OLS-R1, with DLEs for 3 sources from 0.2cm to 2.9cm (from 0.6cm to 3.4cm for OLS-R1) and from 1.5cm to 3.6cm for 7 sources (from 1.3cm to 4cm for OLS-R1).

It is noteworthy that, when comparing the results for the fixed known and free oriented lead-field (Figures 4.3 and 4.4 in Chapter 4, respectively 5.1 and 5.2 in the present Chapter), the results are better for the fixed known oriented lead-field. This can be explained in several ways: first, the estimation problem is harder as we have more parameters to estimate (orientation); second, the ambiguity problem is more critical when the orientations are free, as one can find more equivalent sources producing the same measurements (see Figure 3.3).

SEEG results

As argued previously, a free oriented lead-field is particularly adapted to SEEG based localization, where imposing some *a priori* information on the sources orientations is less justified. We present thus in this chapter, unlike in the previous one, simulation results for the same (number of sources) - SNR combinations, but using the simulated SEEG setup described in Chapter 3 (and used in [Caune, 2017]).

In Figure 5.3 are given the performance of the four tested algorithms on SEEG data issued from single frequency sources (random positions, amplitudes and phases). In frequency domain, SBR-R1 shows an efficient sensitivity to the reconstruction of the true sources, however below OLS-R1, but it remains more precise with less false reconstructed sources. Overall, when the inversion is applied in frequency, SBR-R1 provides the best results, *e.g.*, for 3 sources very low DLEs from 0.3cm to 0.5cm are obtained. When the number of source increases, the method is robust, with DLEs over

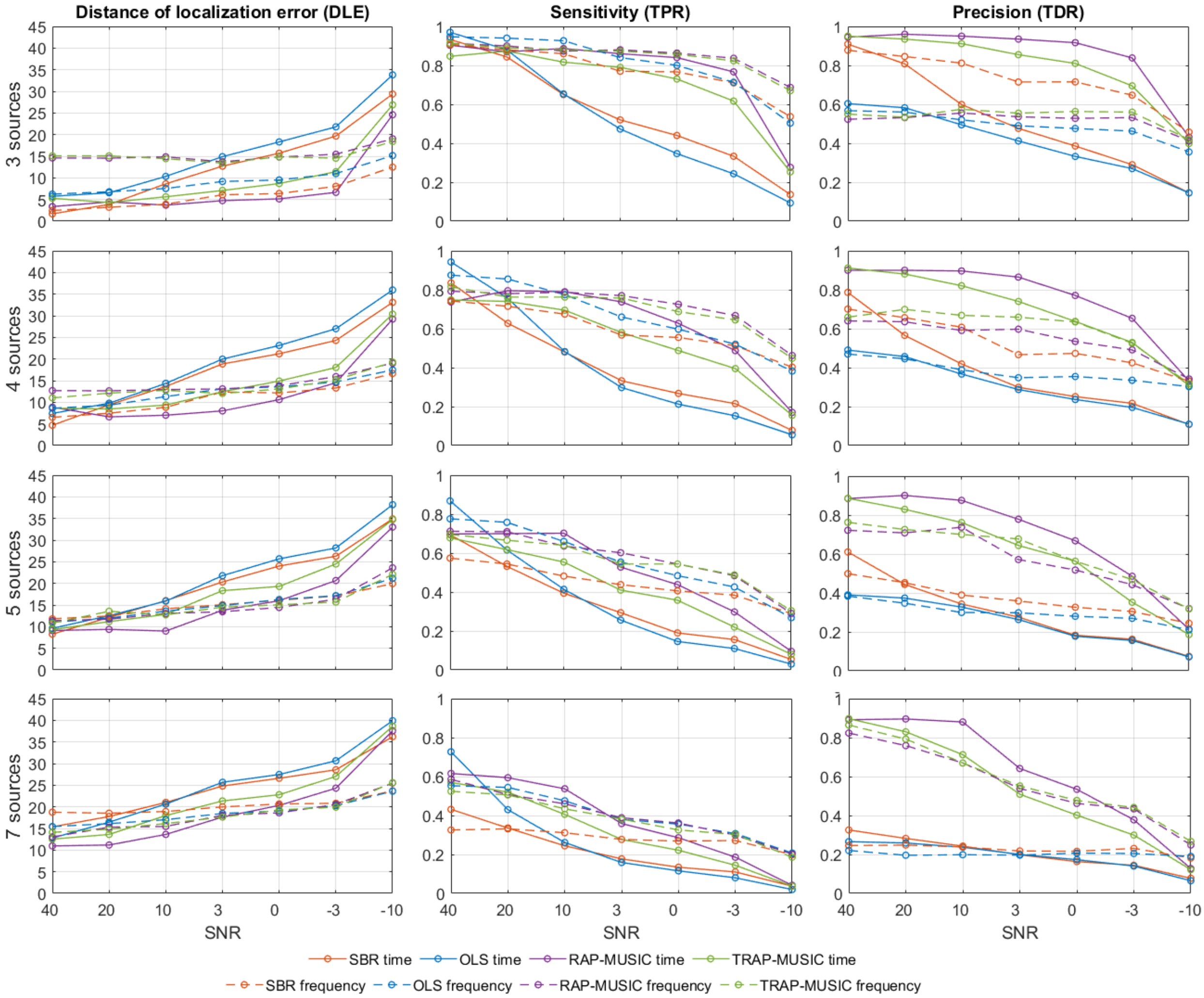

FIGURE 5.2 – SBR-R1, OLS-R1, RAP and TRAP MUSIC localization performance in scalp EEG data simulated using multiple oscillating sources at 6Hz and its harmonics at 12 Hz, 18 Hz and 24 Hz, from the lead-fied matrix $\mathbf{K} = 64 \times (3 \cdot 509)$. These algorithms were applied in frequency (dashed lines) and time (solid lines) domain. By columns, the results of DLE (in mm), sensitivity (TPR) and precision (TDR). By rows, the results for each number of simulated sources $p = 3, 4, 5, 7$. For each subplot, the x-axis shows the SNR (40, 20, 10, 3, 0, -3, -10).

1cm when 7 sources are simulated (1.4cm to 1.6cm). OLS-R1 demonstrates a drop in precision, with more false reconstructed sources, and in particular an abrupt change starting from $3dB$. The DLEs for 3 sources are ranging from 0.3cm up to 2.1cm, and for 7 sources DLEs from 1.3cm to 2cm. Meanwhile RAP and TRAP MUSIC show lower sensitivity, even tough their precision is not strongly affected. RAP has DLEs for 3 sources going from 1.3cm to 1.7cm, and for 7 sources ranging from 2.9cm to 3.1cm. TRAP shows DLEs for 3 sources between 1.7cm and 1.8cm, and up to 3.1cm for 7 sources.

In time domain, OLS-R1 demonstrates better performance to reconstruct more true sources with respect to the other methods, and only followed by SBR-R1 with a small margin, but again with less false reconstructed sources. DLEs for OLS-R1 for 3 sources are ranging from 0.4cm to 2.2cm, and from 1.4cm to 3cm for 7 sources. While for SBR-R1 and 3 sources, the values range from 0.3cm to 2.6cm and from 1.4cm to 3.6cm for 7 sources. As these methods are confronted to more and more noisy signals, their performance decreases fast on the reconstruction of the true sources. RAP and TRAP MUSIC remain with rather poor but stable values with the various SNRs, they only achieve for 3 simulated sources the reconstruction of half of them for the most favorable SNR of 40db, and are more affected than SBR-R1/OLS-R1 by the increase in number of sources. Then, for 3 sources RAP is with DLEs between 1.6cm and 2.5, and TRAP ranges from 1.7cm to 2.6cm. For 7 sources, RAP DLE values are between 3.1cm and 3.2cm and TRAP between 3.1cm and 3.3cm.

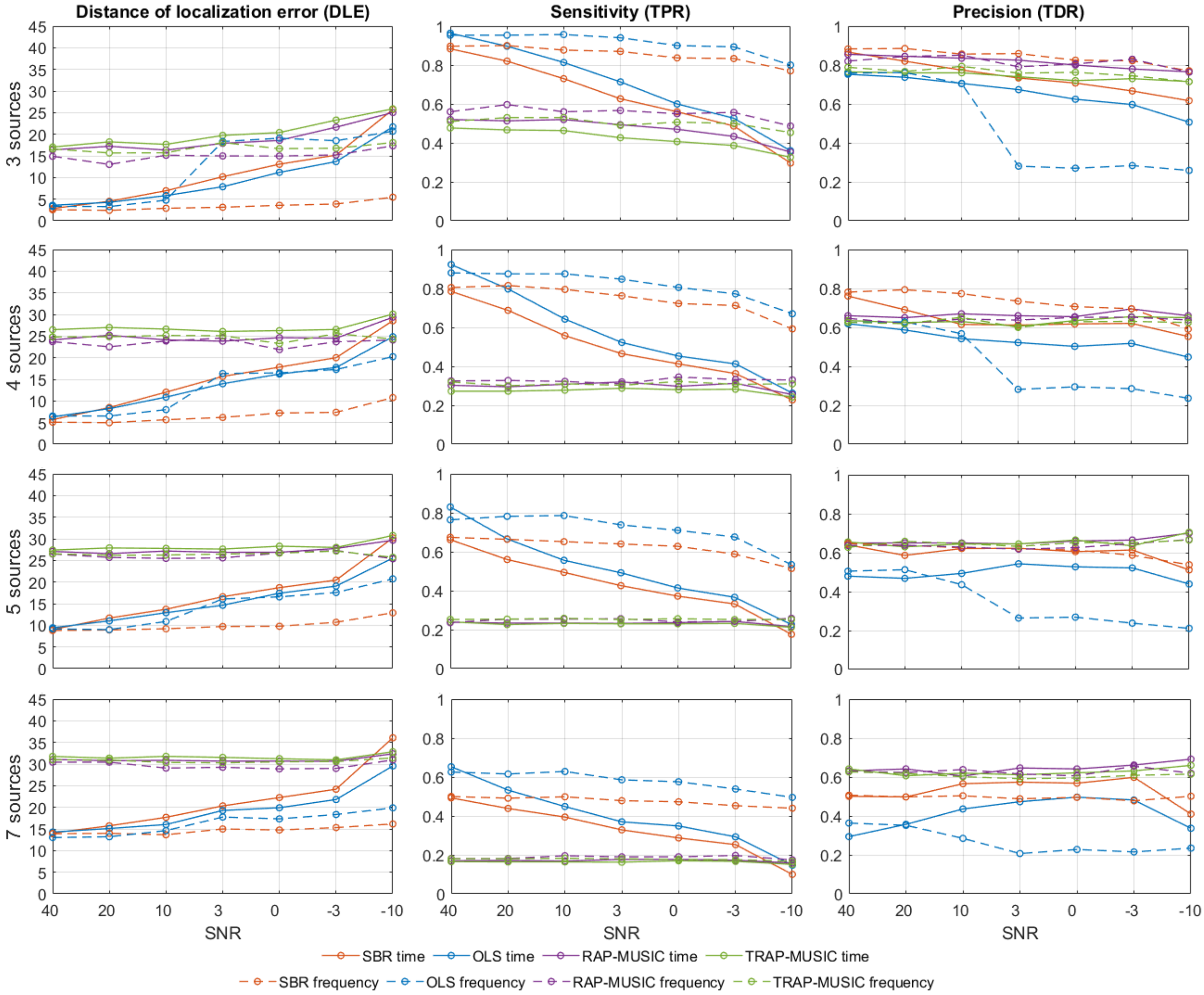

FIGURE 5.3 – SBR-R1, OLS-R1, RAP and TRAP MUSIC localization performance in SEEG data simulated using multiple oscillating sources at 6Hz, from the lead-fied matrix $\mathbf{K} = 186 \times (3 \cdot 509)$. These algorithms were applied in frequency (dashed lines) and time (solid lines) domain. By columns, the results of DLE (in mm), sensitivity (TPR) and precision (TDR). By rows, the results for each number of simulated sources $p = 3, 4, 5, 7$. For each subplot, the x-axis shows the SNR (40, 20, 10, 3, 0, -3, -10).

Next, we compare the previous results in Figure 5.3 with those illustrated in Figure 5.4 using the three first harmonics of the simulated sources at 6Hz (*i.e.*, 12Hz, 18Hz and 24Hz). The results in Figure 5.4, involving the harmonics on the localization task, clearly expose better results on the reconstruction of true sources while is less affected by the reconstruction of false sources. Evaluating the methods in frequency domain, SBR-R1 remains with the best balance between its sensitivity and precision, which overall can be seen along the SNRs, with DLEs for 3 simulated sources going from 0.1cm to 0.5cm and from 0.9cm to 1.4cm for 7 sources. OLS-R1 has achieved outstanding sensitivity with more true sources over the other methods, but inherent to this method, more flaws due to the reconstruction of more false sources. Corresponding DLEs for 3 sources are ranging from 0.2cm to 0.7cm and from 0.8 to 1.4 for 7 sources. RAP and TRAP provide rather close results between each other, with improved sensitivity and precision values when using harmonics, such global results for RAP for 3 sources show DLEs between 1.2cm to 1.4cm and from 1cm to 1.3cm for TRAP, while for 7 sources RAP goes from 1.7cm to 2.1cm and TRAP from 1.9cm to 2.2cm.

In time domain, methods have improved in the reconstruction of true sources, as well with less false reconstructed sources when compared with their equals using only the frequency base at 6 Hz. OLS-R1 provides however higher DLEs, as this method is characterized by its proneness to reconstruct more false sources. Its DLEs for 3 sources are between 0.2cm up to 2cm, and reaching DLE values between 0.6cm up to 2.7cm for 7 sources. SBR-R1 is close to OLS-R1 in performance on the first SNRs, and then is slightly more affected, with DLEs for 3 sources from 0.1cm to 2.4cm and reaching DLEs for 7 sources from 0.7cm to 3.4cm. While for RAP and TRAP, less true sources are reconstructed when compared to OLS-R1/SBR-R1 methods, but higher precision (less false sources) than the two others. Regarding the DLEs for these MUSIC approaches, it is interesting to note that in time domain and for low SNR, the performance are very close to those obtained in frequency domain, and are less stable in comparison when the noise increase. RAP shows DLEs for 3 sources from 0.9cm to 2.1cm and TRAP from 1cm to 2.2cm. For 7 sources, RAP goes from 1.8cm to 2.9cm and TRAP from 2.1cm to 2.9cm. A closer look at the dimension of the source space as estimated by the MDL criterion shows that the size of the dimension is indeed rather underestimated, yielding a high precision but poor sensitivity, hence mitigating the DLEs even for low SNR. The reason of such underestimation need to be explained, and may resides in the particular nature of the used SEEG electrode setup, where the whole head volume is not well covered and sources far from the sensors may be missed. Such behavior was indeed not observed for the EEG setup, where MUSIC algorithms globally provide better results when applied in time domain with several harmonics involved.

Discussion

To sum up all these simulation results (including those of Chapter 3). Overall, and as expected, the localization of activities including fundamental frequency as well as harmonics perform better

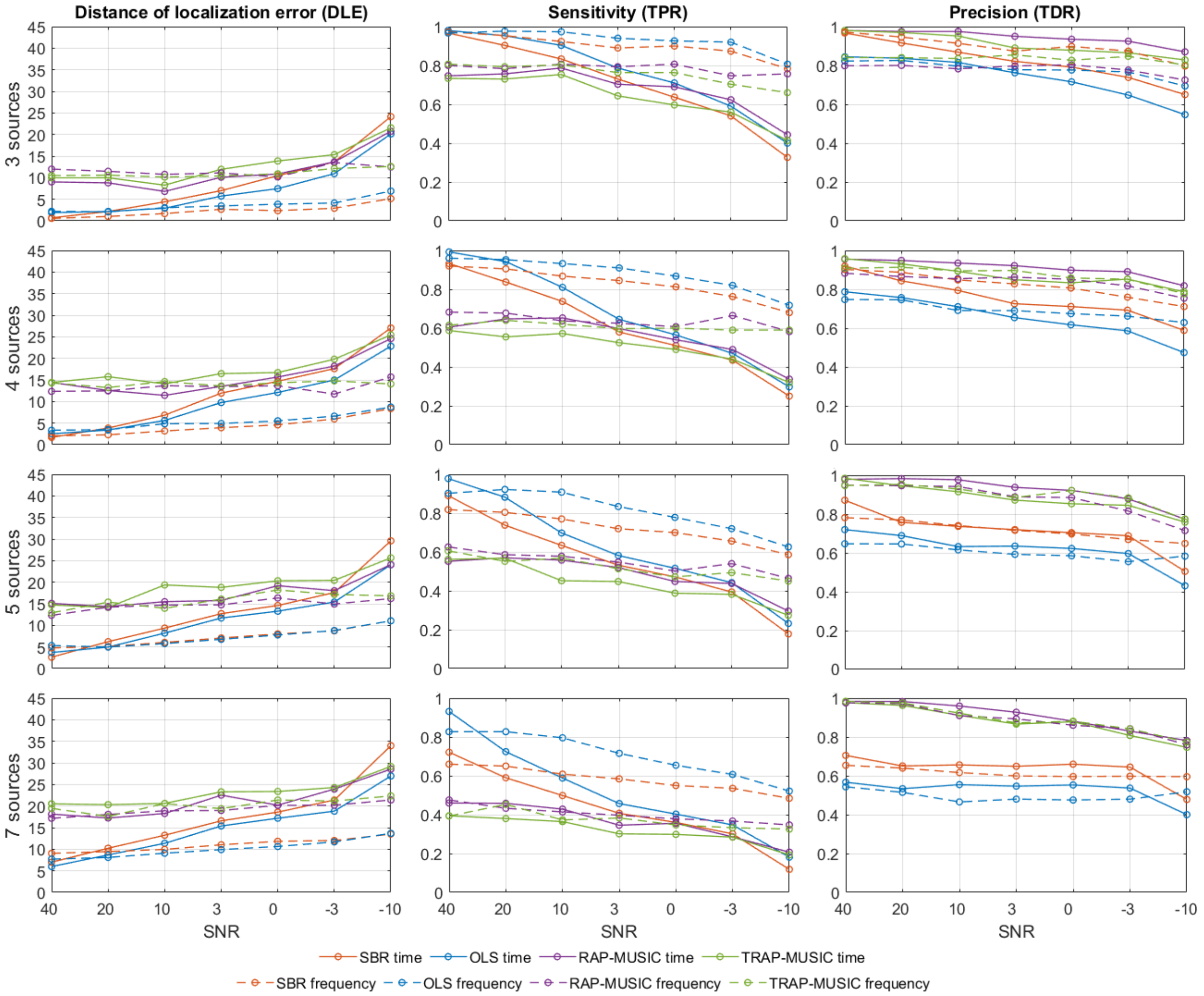

FIGURE 5.4 – SBR-R1, OLS-R1, RAP and TRAP MUSIC localization performance in SEEG data simulated using multiple oscillating sources at 6Hz and its harmonics at 12 Hz, 18 Hz and 24 Hz, from the lead-fied matrix $\mathbf{K} = 186 \times (3 \cdot 509)$. These algorithms were applied in frequency (dashed lines) and time (solid lines) domain. By columns, the results of DLE (in mm), sensitivity (TPR) and precision (TDR). By rows, the results for each number of simulated sources $p = 3, 4, 5, 7$. For each subplot, the x-axis shows the SNR (40, 20, 10, 3, 0, -3, -10).

than when a single frequency is considered, without exception. Considering the localization from EEG or SEEG setup, performance are globally enhanced when intracranial recordings are considered, as the electrodes are closer to the source. This confirmed the observations made in Chapter 3: when a setup with sparser sampling in space is used (*i.e.*, with less sensors and/or poorly distributed in space). This comes however with some exceptions discussed below.

Comparing the methods, we first observe that for both EEG and SEEG data, SBR/SBR-R1 demonstrates to be the most reliable method when applied in the frequency domain, with high robustness to noise. The selection of frequency peaks consist in a pre-processing step where most of the noise is canceled out, then focusing on the activity of interest with enhanced SNR. The difference observed between SBR/SBR-R1 and OLS/OLS-R1 mainly resides in the high number of false positives produced by this last method, proving the efficiency of SBR/SBR-R1 to discard wrongly chosen sources along the iterations. OLS/OLS-R1 shows an important drawback as it tends to overestimate the number of sources, yielding large number of false sources in contrast with the other methods.

As far as MUSIC is concerned, these algorithms turned out to be rather irrelevant in the single frequency case. This is mainly due to the fact that these methods rely on the estimation of the source space at initialization (based on statistical criterion, *e.g.*, MDL in this thesis). In the single frequency case, the size of the source space is limited to two, explaining in most part the poor results. In the presence of harmonics, MUSIC methods still fail in the frequency domain as the estimation of the source space relies on few data points (8 when 4 frequency points are involved), yielding poor identification of the source space vector basis.

When it comes to the time domain, two cases need to be distinguished depending on the sensor setup. For EEG data the results are indeed enhanced as the source space estimates is more reliable (more data available). The results become better than frequency domain SBR/SBR-R1 for SNR over $0db$, then for lower SNR the opposite is observed as frequency domain SBR/SBR-R1 benefit from less noisy data in this domain, achieving again better performance. When it come to SEEG data, the results are a bit different as MUSIC algorithms still struggle in estimating adequately the source space. In this case, frequency domain SBR/SBR-R1 remain the best choice overall for any number of sources and SNR.

5.4.3 Real data examples

5.4.3.1 Surface EEG

We have tested the four algorithms on the same real EEG signals as in Chapter 4 (64 electrodes placed in a 10-10 montage, Biosemi cap, 2 averaged sessions of FPVS protocol FACELOC). As previously, we performed both frequency and time domain localizations for either sources oscillating at the base frequency (6Hz and first two harmonics) or at the oddball frequency (1.2Hz and first two harmonics). In time, we averaged over one period of oddball stimulation and filtered the data either below 5Hz, to keep only oddball harmonics, or above 5Hz, to keep only base frequency harmonics. The results are presented as in the previous chapter, in four figures (frequency/time algorithms, base/oddball sources), from Figures 5.5 to 5.8.

As for the results presented in Chapter 4, it is difficult to asses the validity of these results. All methods place most of the sources in the posterior part of the brain. The GOF values are generally higher for SBR-R1 (with some exceptions, see below), especially in the frequency domain, where they can reach 0.99 for the 6Hz and harmonics activities. This comes with a price, with respect to

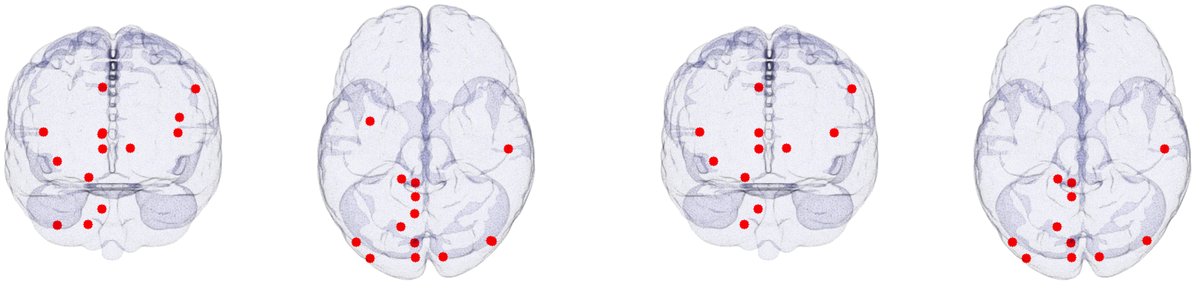

(a) SBR-R1

(b) OLS-R1

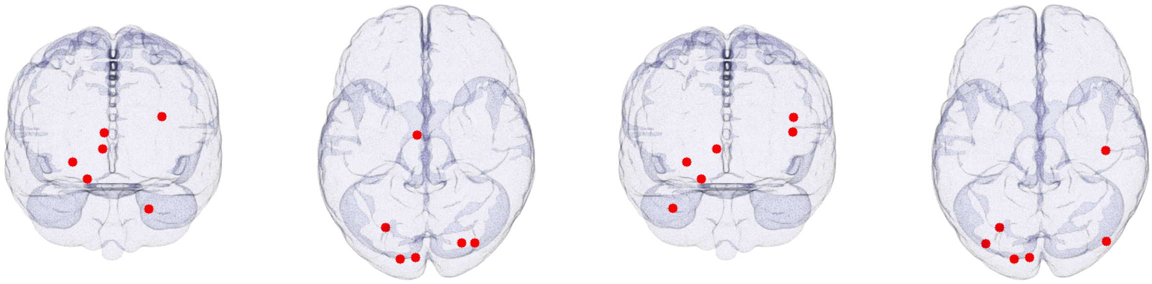

(c) RAP-MUSIC

(d) TRAP-MUSIC

FIGURE 5.5 – Real FPVS frequency domain source localization, for sources of oscillating at the base frequency (6Hz and harmonics). The different subfigures show results for SBR-R1, with 14 reconstructed sources and GOF=0.99, OLS-R1 with 11 reconstructed sources and GOF=0.98, RAP MUSIC with 6 reconstructed sources and GOF=0.91 and TRAP MUSIC with 6 reconstructed sources and GOF=0.93. Back view (left) and top view (right) are provided for each computed method.

OLS-R1, which is sparser. This result is of course dependent on the parameters of the two algorithms - a higher expected GOF would lead to more sources for OLS, while a higher λ parameter would lead to sparser solutions for SBR. Nevertheless, MUSIC algorithms seem to perform worse than the regression ones, both in time and in frequency. In frequency, because of the fact that the number of sources is limited by the dimension of the data; in time, for equal sparsity as SBR, they usually yield lower GOFs (recall the observation made in the previous chapter: MDL like criteria for evaluating the source space dimension fails to estimate a reasonable number and converge to the number of sensors).

One can observe in the last Figure 5.8 an interesting behaviour of SBR-R1 vs OLS-R1, with the former less sparse and with a worse GOF than the latter. Indeed, OLS stops when a target GOF is attained. SBR, on the other hand, continues because the penalty term is not important enough to stop it (*i.e.*, λ is too small). But, during the iterations, increases with every new source and, at some point, it becomes more interesting to limit the number of selected sources by dropping one of them, the one that affects less the error term. This might be one of the first selected sources (among those that OLS also selects). After dropping it, the GOF diminishes but also the penalized

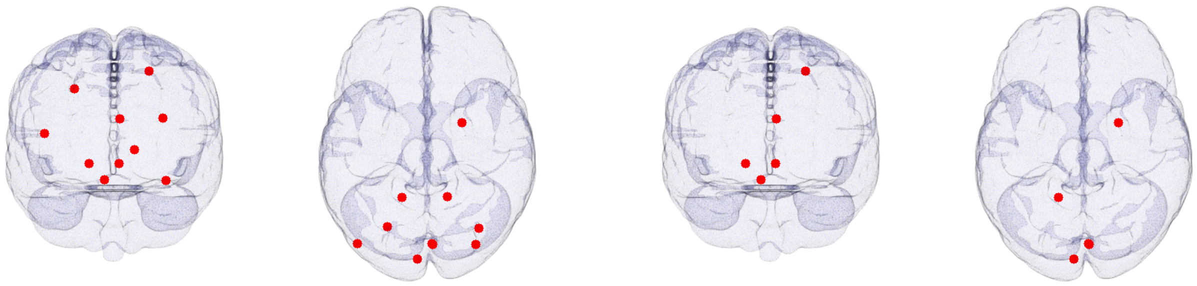

(a) SBR-R1 (b) OLS-R1

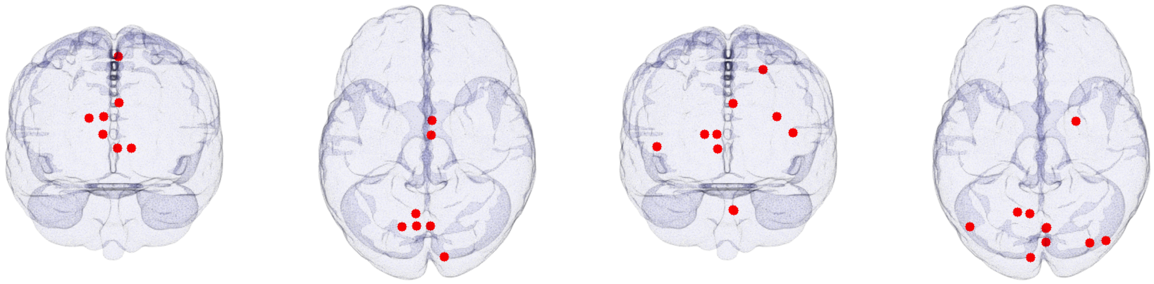

(c) RAP-MUSIC (d) TRAP-MUSIC

FIGURE 5.6 – Real FPVS time domain source localization, for sources of oscillating at the base frequency (6Hz and harmonics). The different subfigures show results for SBR-R1, with 10 reconstructed sources and GOF=0.96, OLS-R1 with 5 reconstructed sources and GOF=0.92, RAP MUSIC with 10 reconstructed sources and GOF=0.88 and TRAP MUSIC with 10 reconstructed sources and GOF=0.96. Back view (left) and top view (right) are provided for each computed method.

criterion in Equation (5.7), which will only start increasing at the next iteration, stopping thus the SBR. Paradoxically, taking a slightly smaller $\lambda = 0.009$ will allow the SBR iterations to continue and, with the price of just two extra sources, the final GOF increases above 0.97.

When comparing the results obtained with a fixed orientation lead-field and a free oriented one (Chapters 4 and 5), one can notice that allowing more degrees of freedom (*i.e.*, not imposing the orientation) yields sparser solutions for the same GOF or same sparsity with a better GOF. There are some exceptions of course, the most flagrant one being the SBR-R1 in time, already discussed in the previous paragraph. Indeed, for the fixed-oriented lead-field setup, SBR converges to 9 sources and a GOF=0.96, while for the free-oriented lead-field it obtains 7 sources but with only a GOF=0.86. Still, as mentioned, a slight decrease of λ yields 9 sources (as in Chapter 4) with a better GOF=0.97.

5.4.3.2 SEEG

We have also evaluated the four algorithms using depth SEEG electrodes. Twelve SEEG shafts were implanted in the brain of an epileptic patient for clinical purposes (pre-surgical evaluation), 7 in the right hemisphere and 5 in the left one. One hundred and forty contacts were recorded at a sampling frequency of 2048Hz. The patient participated in a series of cognitive tests (FPVS

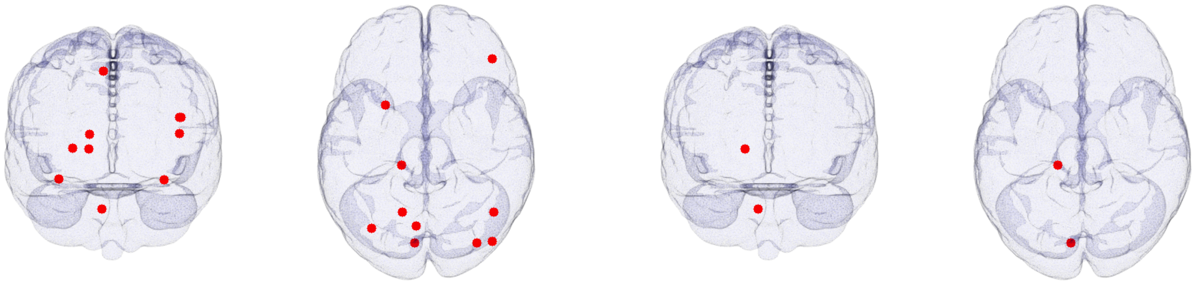

(a) SBR-R1

(b) OLS-R1

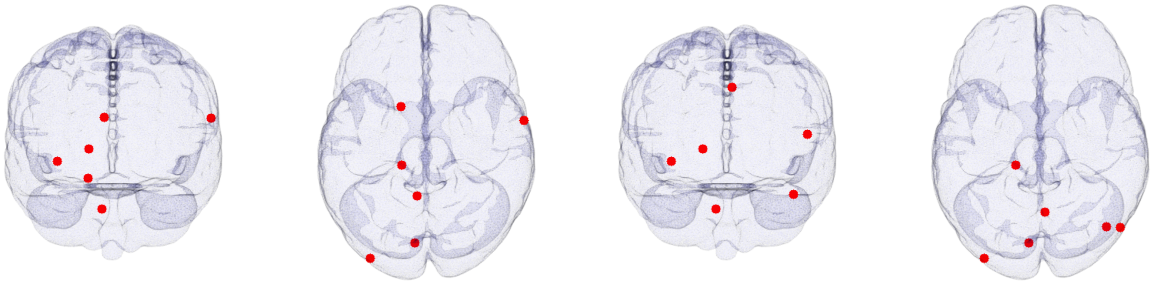

(c) RAP-MUSIC

(d) TRAP-MUSIC

FIGURE 5.7 – Real FPVS frequency domain source localization, for sources of oscillating at the oddball frequency (1.2Hz and harmonics). The different subfigures show results for SBR-R1, with 10 reconstructed sources and GOF=0.96, OLS-R1 with 2 reconstructed sources and GOF=0.87, RAP MUSIC with 6 reconstructed sources and GOF=0.93 and TRAP MUSIC with 6 reconstructed sources and GOF=0.94. Back view (left) and top view (right) are provided for each computed method.

protocols), including FACELOC. The positions of the electrodes in MNI coordinates were detected on the registered MRI/CT images using the procedure described in [Hofmanis, 2013].

We did not compute a precise FEM lead-field from a grid of sources in the gray matter to the 140 electrodes, as our goal here is mainly testing the algorithms. We used instead of the actual head of the patient, the MNI head coordinates we used in simulation [Fonov et al., 2011], in which we placed the electrodes according to their real positions. As it was argued in [Caune et al., 2014; Le Cam et al., 2017], a one sphere analytical model [Yao, 2000] can replace a precise numerical model for SEEG based localizations. This is the procedure that we followed for these recordings - clearly, it is not optimal and the results will certainly be more meaningful using a more precise model, patient dependent, especially knowing that some of the sources of interest can be in the superficial gray matter, close to the brain outer surface and thus to the sphere boundary.

The signals, after Fourier transform, are the same as those presented in 3.2(a), where only a subset of the 140 signals appears with peaks at 6Hz clearly visible. While a few other SEEG contacts exhibit small amplitude peaks at the base frequency. It should be clear that these peaks are not on all of the SEEG signals. Moreover, we couldn’t visually identify any harmonics of the base frequency

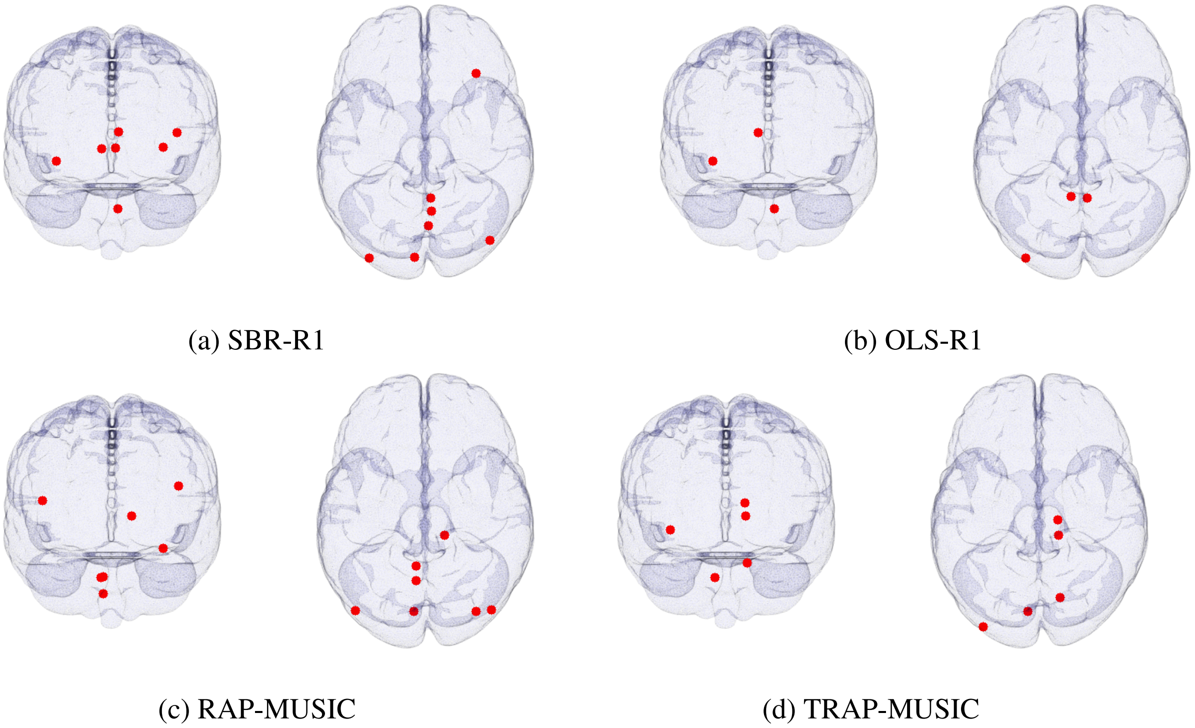
(a) SBR-R1

(b) OLS-R1

(c) RAP-MUSIC

(d) TRAP-MUSIC

FIGURE 5.8 – Real FPVS time domain source localization, for sources of oscillating at the oddball frequency (1.2Hz and harmonics). The different subfigures show results for SBR-R1, with 7 reconstructed sources and GOF=0.86, OLS-R1 with 3 reconstructed sources and GOF=0.91, RAP MUSIC with 7 reconstructed sources and GOF=0.95 and TRAP MUSIC with 7 reconstructed sources and GOF=0.94. Back view (left) and top view (right) are provided for each computed method.

(12Hz, 24Hz, etc), on any of the SEEG contacts. In fact, the peaks at 6Hz indicating sources at the base frequency are above noise level (mean of the neighbouring frequency bins) on 116 SEEG contacts out of 140. The overall expected GOF (computed on all electrodes using the equation (4.10) as mentioned in the previous chapter) equals 0.9 for these activities (note this GOF in frequency does not indicate that oscillations at the base frequency are visible in time - in fact they are covered by noise and they only appear after averaging and filtering).

In the same Figure 3.2(a), one can see peaks on some electrodes at the oddball frequency of 1.2Hz and its first harmonics (2.4, 3.6 and 4.8Hz). While for the oddball the harmonics were clearly present, the number of SEEG contacts on which they could be visually identified is smaller than the ones presenting a peak at 6Hz. For these particular signals, the peaks at 1.2Hz and harmonics (summed) have an amplitude higher than the background noise only for 70 out of 140 SEEG contacts. The signal to noise ratio is very low then for the oddball frequencies, including in the frequency domain, with an expected GOF (4.10) equal to only 0.52.

With all these considerations in mind, we present in the next figures the frequency and time results of SEEG based source localization for the oddball frequencies (1.2, 2.4, 3.6 and 4.8Hz) and for the base frequency (single peak at 6Hz). For the oddball signals, four frequencies are considered, so MUSIC algorithms in frequency will be limited to 8 sources. In time, we have applied the main constraint as for the previous results, *i.e.*, the source space dimension for the MUSIC algorithms was fixed at the number of sources estimated by SBR-R1 (with a fixed $\lambda = 0.01$). The OLS-R1 algorithm stopped when the expected GOF (values given in the previous paragraph) is attained. The results are presented in Figures 5.9 and 5.10 for the oddball and in Figures 5.11 and 5.12 for the base frequency.

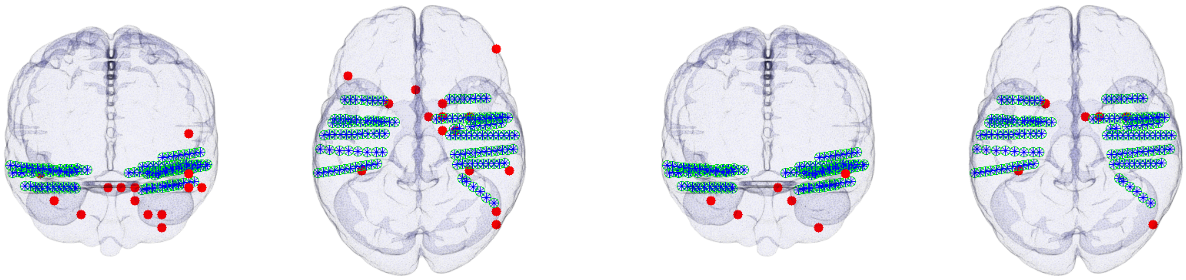

(a) SBR-R1

(b) OLS-R1

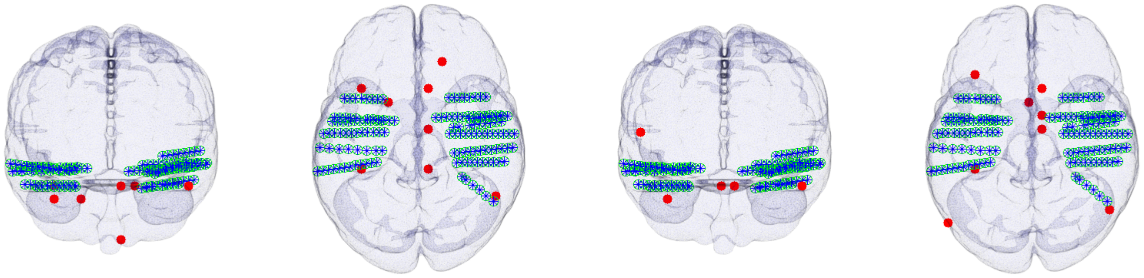

(c) RAP-MUSIC

(d) TRAP-MUSIC

FIGURE 5.9 – Real FPVS frequency domain SEEG source localization, for sources oscillating at the oddball frequency (1.2Hz and harmonics). The different subfigures show results for SBR-R1, with 15 reconstructed sources and GOF=0.7, OLS-R1 with 6 reconstructed sources and GOF=0.54, RAP MUSIC with 8 reconstructed sources and GOF=0.56 and TRAP MUSIC with 8 reconstructed sources and GOF=0.56. Back view (left) and top view (right) are provided for each computed method. Green-blue points represent the SEEG contacts.

Since no ground truth is available, it is difficult to interpret the results. We can still notice that frequency domain GOFs are better than time domain ones for SBR-R1, for both multiple harmonics (oddball) and single peak (base) localizations. They are not very high on the other hand, reaching at most 0.7 for the oddball sources (15 distinct sources were estimated). On the other hand, a too high GOF indicates that (at least) some of the sources are explaining the noise (for the same localization problem, OLS-R1 stops right above the estimated expected GOF at 6 sources). Spatially speaking though, the outcomes of the two regression based algorithms are not very different, with all the regions identified by OLS-R1 also present in the SBR-R1 solution, which yield also some supplementary active areas, difficult to consider as false given the actual state of knowledge [Jonas

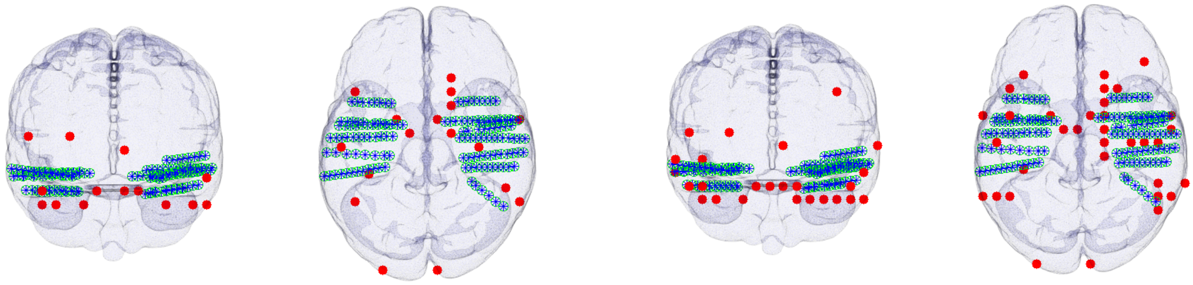

(a) SBR-R1

(b) OLS-R1

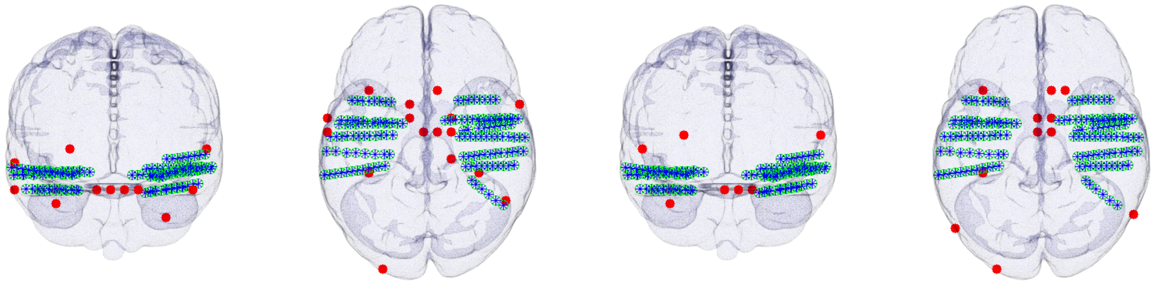

(c) RAP-MUSIC

(d) TRAP-MUSIC

FIGURE 5.10 – Real FPVS time domain SEEG source localization, for sources oscillating at the oddball frequency (1.2Hz and harmonics). The different subfigures show results for SBR-R1, with 17 reconstructed sources and GOF=0.65, OLS-R1 with 34 reconstructed sources and GOF=0.8, RAP MUSIC with 17 reconstructed sources and GOF=0.57 and TRAP MUSIC with 17 reconstructed sources and GOF=0.54. Back view (left) and top view (right) are provided for each computed method. Green-blue points represent the SEEG contacts.

et al., 2016]. RAP and TRAP MUSIC results in frequency domain are difficult to interpret: while for the oddball sources their upper bound in number of sources is equal to 8 (comparable to OLS for example, including in terms of GOF and of spatial locations). For the base frequency they are not reliable as they are limited to 2 sources only.

In time domain, the GOFs are generally slightly below those in frequency and the solutions are less sparse. But, globally, at least some of the identified regions for the oddball sources are common with those identified in frequency and common among the algorithms (*e.g.*, the right hemisphere, with more superficial sources in its posterior part and more profound in its mesial part).

5.5 Conclusion

In this chapter, we have proposed two step-wise regression based algorithms for brain source localization, applied either in time or in frequency domains. They are more general versions of the simplified models SBR and OLS presented in Chapter 4, for which the possible source orientations are assumed to be fixed and known (thus each source position correspond to a single column of the

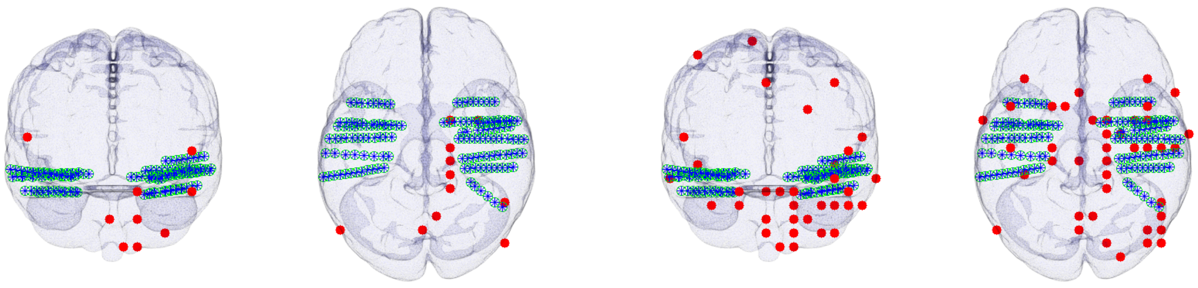

(a) SBR-R1 (b) OLS-R1

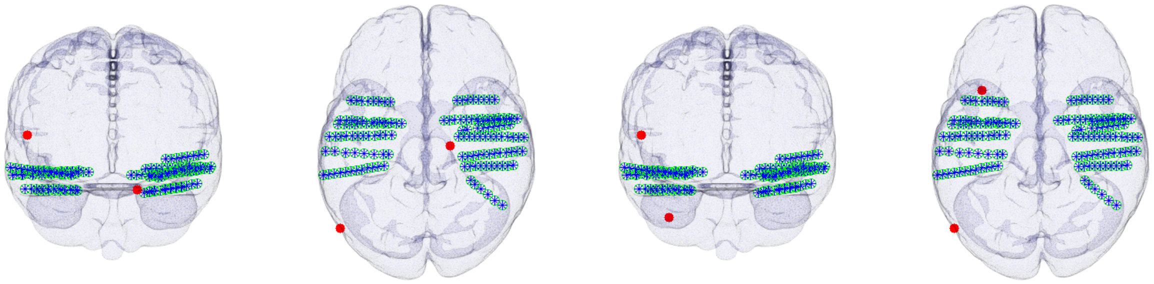

(c) RAP-MUSIC (d) TRAP-MUSIC

FIGURE 5.11 – Real FPVS frequency domain SEEG source localization, for sources oscillating at the base frequency (single peak at 6Hz). The different subfigures show results for SBR-R1, with 11 reconstructed sources and GOF=0.57, OLS-R1 with 44 reconstructed sources and GOF=0.90, RAP MUSIC with 2 reconstructed sources and GOF=0.34 and TRAP MUSIC with 2 reconstructed sources and GOF=0.35. Back view (left) and top view (right) are provided for each computed method. Green-blue points represent the SEEG contacts.

lead-field matrix). The new proposed algorithms were developed in order to ensure block-sparsity of the solutions (*i.e.*, sparse selection of 3-columns blocks of the freely oriented lead-field matrix) and rank 1 (fixed orientation) time varying amplitudes. These two algorithms, OLS-R1 and SBR-R1, were evaluated for source localization problem on scalp and intracranial EEG and SEEG simulated data, generated with multiple oscillatory sources at single 6 Hz frequency or with harmonics. We have compared SBR-R1 and OLS-R1 with iterative RAP and TRAP MUSIC algorithms to determine the robustness to noise and to the co-occurring sources with the same spectra, considering for the inversion the single frequency sources and fundamental plus harmonics. Source localization was addressed both in frequency and time domain, in EEG and SEEG.

We have distinguished globally along the results the efficiency on SBR-R1 for source localization in frequency domain. These results have evidenced that this algorithm outperforms the other methods for this particular inversion problem appearing in steady-state/FPVS cognitive protocols.

As in Chapter 4, we also presented source localization results on real data in EEG, and in this chapter also in SEEG. The results are only illustrative: no ground truth is available for these signals, and we did not confront the algorithms to a bigger database of signals, allowing to asses some sta-

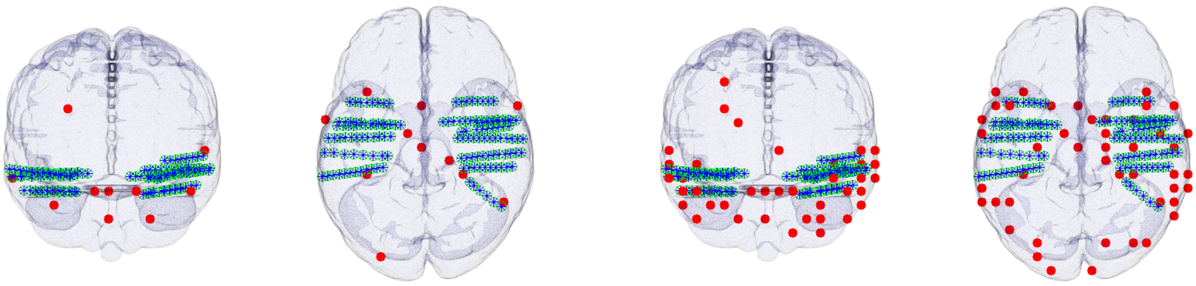

(a) SBR-R1

(b) OLS-R1

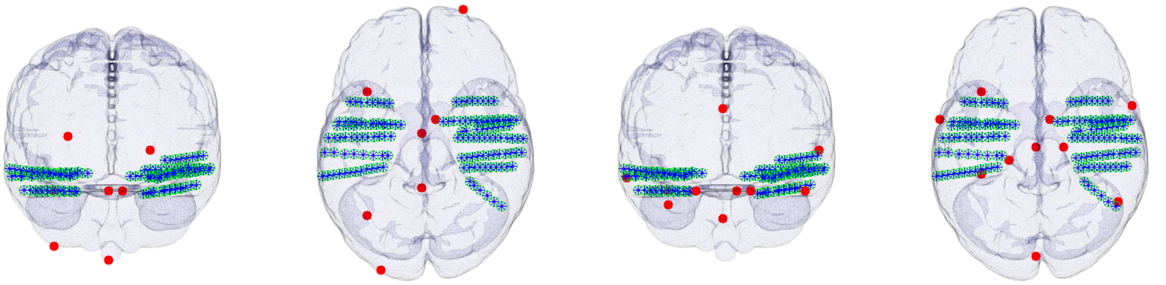

(c) RAP-MUSIC

(d) TRAP-MUSIC

FIGURE 5.12 – Real FPVS time domain SEEG source localization, for sources oscillating at the base frequency (single peak at 6Hz). The different subfigures show results for SBR-R1, with 11 reconstructed sources and GOF=0.44, OLS-R1 with 48 reconstructed sources and GOF=0.8, RAP MUSIC with 11 reconstructed sources and GOF=0.27 and TRAP MUSIC with 11 reconstructed sources and GOF=0.41. Back view (left) and top view (right) are provided for each computed method. Green-blue points represent the SEEG contacts.

tistical significance. Besides, we used standardized head geometries (or even spherical models for the SEEG case) and relatively simple lead-field models (regular grid of sources approximately limited to the gray matter, standardized isotropic conductivities, or even analytical models for SEEG). Still, they are coherent with the actual neuroscientific knowledge in the regions activated during face recognition protocols. To conclude, they clearly need to be confirmed on more data.

Conclusion and perspectives

Conclusion

We have addressed in this thesis the problem of oscillatory source localization both in time and frequency domain, by considering EEG as well as Stereo-EEG (SEEG) electrodes setup. The targeted application is the identification of brain structure responding to specific cognitive protocols, such as human face recognition, as tested using Fast Periodic Visual Stimulation (FPVS). This kind of protocols induce brain source activities responding at the same frequency as the stimulation (with possible harmonics). While these sources have low amplitudes in time and they are usually buried in noise, they appear clearly when transforming the data in the frequency domain. In other words, the sources of interest are highly sparse in frequency, with only a few peaks clearly standing out of the background noise. This characteristic allows to easily select data of interest. Moreover, along with this frequency sparsity, one of the main working hypothesis adopted in this thesis is the spatial sparsity: the reconstructed solution should be sparse in terms of number of estimated sources, as few brain structures are assumed to respond to the stimuli, *i.e.*, are specialized for the specific cognitive task addressed by the protocol. After an Introduction (Chapter 1) and a literature review (Chapter 2), our contributions are presented from Chapters 3 to 5.

In **Chapter 3**, the ambiguity problem arising when trying to distinguish between several oscillatory sources at the same frequency was formalized and analyzed. We put forward that in this case the source space spanned by the activities of these sources is of dimension 2, whatever the true number of underlying sources to be reconstructed. Theoretically, the inverse problem is not identifiable and a large number of alternative solutions (if not infinite) may mislead the localization methods. However, the fact that these alternative solutions need to be aligned with projection patterns encoded in the lead-field may attenuate this ambiguity. This aspect is then evaluated based on simulated data, and we show that a given configuration of alternative solutions (a sum of zero-phase sine and cosine) could be explained by projections of a given lead-field with high GOFs (superior to 0.8 in median over all configurations of number of sources, EEG/SEEG setup, fixed or free oriented lead-field). It might then be difficult to distinguish between the error due to the reconstruction of such alternative source configurations and the error due to the presence of noise or model imprecision. The localization of oscillatory sources then stands as a particularly challenging problem. A first version of the analysis presented in this chapter was published in [Hernandez *et. al.*, 2022].

In the two last **Chapters 4 and 5** of the thesis, we then proposed to evaluate under simulations to which extent this ambiguity problem may mislead the localization methods and to propose algorithms that are more robust to these situation than classical sparse localization methods. Two family of methods have been chosen, both enforcing sparsity. The first one is based on the Multiple SIgnal Classification (MUSIC) principle, a set of methods being well established in the brain source localization literature. MUSIC algorithms are readily applicable for brain source localization, and the two variants chosen on this thesis are RAP-MUSIC and TRAP-MUSIC, which can be seen, because of their iterative nature, as greedy algorithms. The second family of methods is based specifically on greedy (step-wise) regression type algorithms, in particular on the Matching Pursuit type approaches, where the data are explained by successively selecting in a dictionary of atoms the ones that best explains the data / the residual. While these methods (Orthogonal Least Squares - OLS and Single Best Replacement - SBR) are familiar to the signal processing community, they remain rarely used for brain source localization, and need to be adapted to this specific problem.

Chapter 4 is dedicated to the analysis of the performance of these four localization methods, when oscillatory sources are to be estimated from a lead field with *fixed* and *known* orientation for each source position. This particular lead-field modeling is considered as relevant in context of EEG source localization, where the main component of the dipolar source seen by the electrodes are supposed to be orthogonal to the cortex, hence with orientations assumed to be roughly radial. As mentioned above, two version of MUSIC and two versions of greedy regression are evaluated. It is noteworthy that the considered greedy algorithms (OLS and SBR) are easily adaptable to sparse brain source localization when a lead-field with fixed orientation is considered (one possible orientation per source position encoded in the lead-field matrix, whose columns are then the atoms of the dictionary), with only minor modifications.

The methods are evaluated both in time and frequency domain (*i.e.*, directly applied on the frequency peaks of interest), varying the number of sources as well as the Signal to Noise Ratio (SNR), and considering single frequency peak as well as several harmonics of the frequency of interest. The main conclusion arising from these simulations is that better results are achieved in the frequency domain by OLS/SBR methods, as focusing on the frequency peaks of the activity to localize provide enhanced signal to noise ratio (with however better precision for SBR than for OLS, as SBR is able to eliminate falsely detected sources from an iteration to another). Robustness to noise is indeed remarkable as the performance remain stable even when the additive noise is increased to high level up to $-10db$. As expected, when harmonics are also available for localization, the performances are also increased.

The conclusions are different when it comes to MUSIC methods. These approaches require an estimation of the signal subspace at initialization, which are inherently limited to two dimensions when single frequency oscillatory sources are considered. Logically, these methods are failing when facing such data. When harmonics are considered, the use of MUSIC algorithms become more relevant, especially in time domain where the number of data points allow better estimates of the source space dimension as well as source space basis vectors. The performances of RAP and TRAP MUSIC become then comparable wit the OLS/SBR methods: for sparse setups (few sources) and high levels of noise, SBR in frequency outperforms MUSIC (regardless of the domain), while for high SNR and less sparse setups, the performance are better for time versions of MUSIC than those of OLS/SBR methods (regardless of the domain). The main part of these results have been published in an international conference [Hernandez *et. al.*, 2021].

In **Chapter 5**, the problem of estimating both the positions and the orientations of the sources is considered, in a similar manner. In this context, both EEG and SEEG data are considered, as free-oriented lead-field model are more relevant when it comes to intracranial data. The considered MUSIC versions are designed for estimating the orientations as well (by evaluating subspace correlations between residuals of the data and of the lead-field). However, when the fix but unknown orientation need to be estimated for each source position candidate, the greedy regression SBR/OLS methods need to be modified. In this chapter, we then proposed a new version of the OLS algorithm, where a block-sparse approach including a rank one constraint is introduced in order to identify both source positions and orientations from 3D lead-field atoms under fixed orientation constrain for the sources. Such procedure was also adopted to adapt the forward-backward version of OLS, namely SBR, where the current set of selected sources is reconsidered at each iteration by either removing an atom (*i.e.*, a block of 3 columns from the lead-field matrix) or introducing a new one.

Globally, same conclusions can be drawn as in the previous chapter as far as greedy methods are concerned, *i.e.*, considering the rank one/block versions of OLS and SBR in this case. Comparing to fixed-orientation lead-field model, the decrease in performance in terms of DLE is clearly visible, as free-oriented model offers higher degrees of freedom and reinforces the ambiguity problem as formulated in **Chapter 3**. On the other hand, the solutions are sparser, as it can be seen from the better precision (TDR) obtained in the 5th chapter. Also, as already seen and noted in chapter 3, the particular implantation of the SEEG electrodes closer to the sources seems to guide the problem and lead to better results. This is however not the case when MUSIC algorithms are facing SEEG data, as the statistical methods seem to be failing in estimating the adequate source space, very likely because this setup is not covering well the source space, and sources close to the electrodes tend to mask the activities of those more distant ones.

Perspectives

We have only considered two kind of approaches in this thesis, for both of which two variants have been tested. In future works, other methods need to be evaluated, in particular other localization methods based on sparseness. The common rationale for the methods we have evaluated is ascendant regression strategy, where new sources are added to the solution until convergence is reached, either based on a predetermined number of sources to be reconstructed (MUSIC) or on the error of reconstruction of the data (GOF for OLS or penalized GOF for SBR). Methods based on descendent strategy shall be also considered, starting from global solutions involving all source positions in the lead-field (such as a regularized MNE), and pruning out sources from the solution along the iteration by cancelling out to zero their estimated activities. This is the case, *e.g.*, of the FOCUSS approach [Gorodnitsky et al., 1992], but more generally of Bayesian strategies where the weight applied to the minimum norm solution is iteratively learned from the data, and tend (under adequate parametrization [Wipf and Nagarajan, 2009]) to produce solution with low number of active sources. As we are dealing with data recorded under well-controlled and reproducible cognitive protocols (namely FPVS in this thesis), the inclusion of methods confronting trials for a given patient or even for several patients during the localization process [Janati et al., 2020] (instead as in a post-evaluation step as it is usually done [Jonas et al., 2016]) could help could in identifying the most relevant structures that are responding to the tested cognitive task.

Another methodological development that may be addressed is the spatial conditioning and resolution of the sensor setup, further pursuing the work already started in the research team, in particular for the SEEG setup [Caune et al., 2014; Caune, 2017]. Indeed, this particular disposition of the sensors directly implanted in the brain volume asks the question of optimal spatial positioning of the sensors to reach maximal identifiability of the source space. It may result in guidelines at the direction of neurosurgeons for better implantation of the SEEG electrodes. Another direction of investigation is the resolution of the source position encoded in the lead-field matrix. Indeed, a regular sampling of the source space is irrelevant as the reachable localization precision depend on the relative distance of the source to the sensors [Ranta et al., 2019]. Proposing an irregular sampling of the source space adapted to the used sensor disposition is likely to reduce the computational burden of the localization procedure as well as diminishing the indeterminacy of this severely ill-posed problem, which has been demonstrated to be even worse when trying to localize oscillating sources.

The results on real data, as exposed in this thesis, have been mainly included for illustrative purpose, and cannot be considered as a validation of the proposed methodology yet. Extensive results on a real data base need to be carried out. In particular, more careful attention must be given to the used lead-field models. In this thesis, a standard template or even analytical spherical models have been used, putatively resulting in high model uncertainties worsening this already challenging inverse problem. While individual head models are useful for optimal inverse problem solving, it remains true that, in order to compare among patients, the obtained results need to be registered *a posterior* on a brain atlas and averaged over a large number of patients to clarify which are the brain structures that are bearing crucial role for the evaluated cognitive task, as done in [Jonas et al., 2016] based on SEEG measurements of the responses. This first step of source estimation should next open the way for a step of network analysis: the relationships between the identified sources, their potential ordering and thus causal relation constitute also a promising future research direction.

List of Publications

International conferences

[Hernandez *et al.*, 2021] V. del Rocío Hernández-Castañón, S. Le Cam and R. Ranta (2021). Sparse EEG source localization in frequency domain. *In 43rd Annual International Conference of the IEEE Engineering in Medicine & Biology Society (EMBC). Guadalajara, México, 2021*

[Hernandez *et al.*, 2022] V. del Rocío Hernández-Castañón, S. Le Cam and R. Ranta (2022). On the localization of oscillatory sources from (S) EEG recordings. *In 44th Annual International Conference of the IEEE Engineering in Medicine & Biology Society (EMBC). Glasgow, UK, 2022*

Bibliography

Achard, S., Salvador, R., Whitcher, B., Suckling, J., and Bullmore, E. (2006). A resilient, low-frequency, small-world human brain functional network with highly connected association cortical hubs. *Journal of Neuroscience*, 26(1):63–72.

Acharya, U. R., Sree, S. V., Swapna, G., Martis, R. J., and Suri, J. S. (2013). Automated EEG analysis of epilepsy: a review. *Knowledge-Based Systems*, 45:147–165.

Aharon, M., Elad, M., and Bruckstein, A. (2006). K-svd: An algorithm for designing overcomplete dictionaries for sparse representation. *IEEE Transactions on signal processing*, 54(11):4311–4322.

Akdeniz, G. (2018). Verification of dipole fit source localization in patients with epilepsy using postoperative mri. *Neurology Asia*, 23(1).

Amo, C., De Santiago, L., Barea, R., López-Dorado, A., and Boquete, L. (2017). Analysis of gamma-band activity from human EEG using empirical mode decomposition. *Sensors*, 17(5):989.

Astrand, E., Wardak, C., and Ben Hamed, S. (2014). Selective visual attention to drive cognitive brain–machine interfaces: from concepts to neurofeedback and rehabilitation applications. *Frontiers in systems neuroscience*, 8:144.

Azevedo, F. A., Carvalho, L. R., Grinberg, L. T., Farfel, J. M., Ferretti, R. E., Leite, R. E., Filho, W. J., Lent, R., and Herculano-Houzel, S. (2009). Equal numbers of neuronal and nonneuronal cells make the human brain an isometrically scaled-up primate brain. *Journal of Comparative Neurology*, 513(5):532–541.

Baars, B. J. and Gage, N. M. (2010). *Cognition, brain, and consciousness: Introduction to cognitive neuroscience*. Academic Press.

Baillet, S., Mosher, J. C., and Leahy, R. M. (2001). Electromagnetic brain mapping. *IEEE Signal processing magazine*, 18(6):14–30.

Baillet, S., Mosher, J. C., Leahy, R. M., and Shattuck, D. W. (1999). BrainStorm: a Matlab Toolbox for the Processing of MEG and EEG Signals. *NeuroImage*, 9:S246–S246.

Bastos-Filho, T. F. (2020). *Introduction to Non-Invasive EEG-Based Brain-Computer Interfaces for Assistive Technologies*. CRC Press.

Becker, H., Albera, L., Comon, P., Gribonval, R., Wendling, F., and Merlet, I. (2014). A performance study of various brain source imaging approaches. In *2014 IEEE International Conference on Acoustics, Speech and Signal Processing (ICASSP)*, pages 5869–5873. IEEE.

Biosemi (2022). Biosemi : Company that provides products to the scientific community to be used for research applications, Download from: https://www.biosemi.com/.

Blumensath, T. and Davies, M. E. (2007). On the difference between orthogonal matching pursuit and orthogonal least squares. TechReport.

Brazdzionis, J., Wiginton IV, J., Patchana, T., Savla, P., Hung, J., Zhang, Y., and Miulli, D. E. (2022). Measuring the electromagnetic field of the human brain at a distance using a shielded electromagnetic field channel. *Cureus*, 14(3).

Brody, D. A., Terry, F. H., and Ideker, R. E. (1973). Eccentric dipole in a spherical medium: generalized expression for surface potentials. *IEEE Transactions on Biomedical Engineering*, (2):141–143.

Bromfield, E. B., Cavazos, J. E., and Sirven, J. I. (2006). Basic mechanisms underlying seizures and epilepsy. In *An Introduction to Epilepsy [Internet]*. American Epilepsy Society.

Cai, T. T. and Wang, L. (2011). Orthogonal matching pursuit for sparse signal recovery with noise. *IEEE Transactions on Information theory*, 57(7):4680–4688.

Caune, V. (2017). *Brain source localization using SEEG recordings*. PhD thesis, Université de Lorraine.

Caune, V., Ranta, R., Le Cam, S., Hofmanis, J., Maillard, L., Koessler, L., and Louis-Dorr, V. (2014). Evaluating dipolar source localization feasibility from intracerebral SEEG recordings. *NeuroImage*, 98:118–133.

Cernea, D., Olech, P.-S., Ebert, A., and Kerren, A. (2012). Controlling in-vehicle systems with a commercial eeg headset: Performance and cognitive load. In *Visualization of Large and Unstructured Data Sets: Applications in Geospatial Planning, Modeling and Engineering-Proceedings of IRTG 1131 Workshop 2011*. Schloss Dagstuhl-Leibniz-Zentrum für Informatik.

Chang, N., Gulrajani, R., and Gotman, J. (2005). Dipole localization using simulated intracerebral EEG. *Clinical neurophysiology*, 116(11):2707–2716.

Chen, S., Billings, S. A., and Luo, W. (1989). Orthogonal least squares methods and their application to non-linear system identification. *International Journal of control*, 50(5):1873–1896.

Cichocki, A. and Amari, S.-i. (2002). *Adaptive blind signal and image processing: learning algorithms and applications*. John Wiley & Sons.

Cohen, D. (1968). Magnetoencephalography: evidence of magnetic fields produced by alpha-rhythm currents. *Science*, 161(3843):784–786.

Cosandier-Rimélé, D., Badier, J.-M., Chauvel, P., and Wendling, F. (2007). A physiologically plausible spatio-temporal model for EEG signals recorded with intracerebral electrodes in human partial epilepsy. *IEEE Transactions on Biomedical Engineering*, 54(3):380–388.

Cuffin, B. N. (1991). Eccentric spheres models of the head. *IEEE transactions on biomedical engineering*, 38(9):871–878.

Dale, A. M. and Sereno, M. I. (1993). Improved localizadon of cortical activity by combining EEG and MEG with mri cortical surface reconstruction: a linear approach. *Journal of cognitive neuroscience*, 5(2):162–176.

Dannhauer, M., Lanfer, B., Wolters, C. H., and Knösche, T. R. (2011). Modeling of the human skull in EEG source analysis. *Human brain mapping*, 32(9):1383–1399.

De Munck, J., Peters, M. J., et al. (1993). A fast method to compute the potential in the multisphere model. *IEEE Trans. Biomed. Eng*, 40(11):1166–1174.

de Peralta-Menendez, R. G. and Gonzalez-Andino, S. L. (1998). A critical analysis of linear inverse solutions to the neuroelectromagnetic inverse problem. *IEEE Transactions on Biomedical Engineering*, 45(4):440–448.

Durka, P. (2007). *Matching pursuit and unification in EEG analysis*. Artech House.

Durka, P. J. and Blinowska, K. (2001). A unified time-frequency parametrization of eegs. *IEEE Engineering in Medicine and Biology Magazine*, 20(5):47–53.

Fonov, V., Evans, A. C., Botteron, K., Almli, C. R., McKinstry, R. C., Collins, D. L., Group, B. D. C., et al. (2011). Unbiased average age-appropriate atlases for pediatric studies. *Neuroimage*, 54(1):313–327.

Frank, E. (1952). Electric potential produced by two point current sources in a homogeneous conducting sphere. *Journal of applied physics*, 23(11):1225–1228.

Fuchs, M., Wagner, M., Köhler, T., and Wischmann, H.-A. (1999). Linear and nonlinear current density reconstructions. *Journal of clinical Neurophysiology*, 16(3):267–295.

Geddes, L. A. and Baker, L. E. (1967). The specific resistance of biological material - a compendium of data for the biomedical engineer and physiologist. *Medical and biological engineering*, 5(3):271–293.

Geselowitz, D. B. (1967). On bioelectric potentials in an inhomogeneous volume conductor. *Biophysical journal*, 7(1):1–11.

Geselowitz, D. B. (1998). The zero of potential. *IEEE Engineering in Medicine and Biology Magazine*, 17(1):128–136.

Gorodnitsky, I. F., George, J. S., and Rao, B. D. (1995). Neuromagnetic source imaging with focuss: a recursive weighted minimum norm algorithm. *Electroencephalography and clinical Neurophysiology*, 95(4):231–251.

Gorodnitsky, I. F. and Rao, B. D. (1997). Sparse signal reconstruction from limited data using focuss: A re-weighted minimum norm algorithm. *IEEE Transactions on signal processing*, 45(3):600–616.

Gorodnitsky, I. F., Rao, B. D., and George, J. (1992). Source localization in magnetoencephalography using an iterative weighted minimum norm algorithm. In *ASILOMAR CONFERENCE ON SIGNALS SYSTEMS AND COMPUTERS*, pages 167–167. COMPUTER SOCIETY PRESS.

Gowreesunker, B. V. and Tewfik, A. H. (2009). A shift tolerant dictionary training method. In *SPARS'09-Signal Processing with Adaptive Sparse Structured Representations*.

Gramfort, A., Strohmeier, D., Haueisen, J., Hämäläinen, M. S., and Kowalski, M. (2013). Time-frequency mixed-norm estimates: Sparse M/EEG imaging with non-stationary source activations. *NeuroImage*, 70:410–422.

Grave de Peralta Menendez, R., Hauk, O., Gonzalez Andino, S., Vogt, H., and Michel, C. (1997). Linear inverse solutions with optimal resolution kernels applied to electromagnetic tomography. *Human brain mapping*, 5(6):454–467.

Grech, R., Cassar, T., Muscat, J., Camilleri, K. P., Fabri, S. G., Zervakis, M., Xanthopoulos, P., Sakkalis, V., and Vanrumste, B. (2008). Review on solving the inverse problem in EEG source analysis. *Journal of neuroengineering and rehabilitation*, 5(1):1–33.

Greenblatt, R. (1993). Probabilistic reconstruction of multiple sources in the bioelectromagnetic inverse problem. *Inverse problems*, 9(2):271.

Güllmar, D., Haueisen, J., and Reichenbach, J. R. (2010). Influence of anisotropic electrical conductivity in white matter tissue on the EEG/MEG forward and inverse solution. a high-resolution whole head simulation study. *Neuroimage*, 51(1):145–163.

Hallez, H., Vanrumste, B., Grech, R., Muscat, J., De Clercq, W., Vergult, A., D'Asseler, Y., Camilleri, K. P., Fabri, S. G., Van Huffel, S., et al. (2007). Review on solving the forward problem in EEG source analysis. *Journal of neuroengineering and rehabilitation*, 4(1):1–29.

Hämäläinen, M. S. and Ilmoniemi, R. J. (1994). Interpreting magnetic fields of the brain: minimum norm estimates. *Medical & biological engineering & computing*, 32(1):35–42.

Hamalainen, M. S. and Sarvas, J. (1989). Realistic conductivity geometry model of the human head for interpretation of neuromagnetic data. *IEEE transactions on biomedical engineering*, 36(2):165–171.

Hauk, O., Rice, G. E., Volfart, A., Magnabosco, F., Ralph, M. L., and Rossion, B. (2021). Face-selective responses in combined EEG/MEG recordings with fast periodic visual stimulation (fpvs). *NeuroImage*, 242:118460.

Herculano-Houzel, S. (2009). The human brain in numbers: a linearly scaled-up primate brain. *Frontiers in human neuroscience*, page 31.

Hofmanis, J. (2013). *Contribution to the cerebral forward model by depth electric stimulation and SEEG measurements: application in epilepsy*. PhD thesis, Université de Lorraine.

Hounsfield, G. (1973). Computerised transverse axial scanning (tomography). 1. description of the system. *Br. J. Radiol*, 46:1016–1022.

Huang, M., Mosher, J. C., and Leahy, R. (1999). A sensor-weighted overlapping-sphere head model and exhaustive head model comparison for MEG. *Physics in Medicine & Biology*, 44(2):423.

Huang, Y., Datta, A., Bikson, M., and Parra, L. C. (2019). Realistic volumetric-approach to simulate transcranial electric stimulation roast a fully automated open-source pipeline. *Journal of neural engineering*, 16(5):056006.

Institute, S. (2016). SCIRun: A Scientific Computing Problem Solving Environment, Scientific Computing and Imaging Institute (SCI), Download from: http://www.scirun.org.

Ishai, A. (2008). Let's face it: it's a cortical network. *Neuroimage*, 40(2):415–419.

Ishai, A., Schmidt, C. F., and Boesiger, P. (2005). Face perception is mediated by a distributed cortical network. *Brain research bulletin*, 67(1-2):87–93.

Ismail, L. E. and Karwowski, W. (2020). Applications of EEG indices for the quantification of human cognitive performance: A systematic review and bibliometric analysis. *PLoS One*, 15(12):e0242857.

Isnard, J., Taussig, D., Bartolomei, F., Bourdillon, P., Catenoix, H., Chassoux, F., Chipaux, M., Clémenceau, S., Colnat-Coulbois, S., Denuelle, M., et al. (2018). French guidelines on stereoelectroencephalography (SEEG). *Neurophysiologie Clinique*, 48(1):5–13.

Janati, H., Bazeille, T., Thirion, B., Cuturi, M., and Gramfort, A. (2020). Multi-subject MEG/EEG source imaging with sparse multi-task regression. *NeuroImage*, 220:116847.

Jang, S. H., Lee, S. H., Jin, S. H., Seo, J. P., Seo, H. J., Chang, P. H., and Yeo, S. S. (2016). Differences of cortical activation pattern during the use of fork, wooden chopsticks and metallic chopsticks: a functional near infrared spectroscopy study. *Journal of Near Infrared Spectroscopy*, 24(4):399–403.

Jonas, J., Jacques, C., Liu-Shuang, J., Brissart, H., Colnat-Coulbois, S., Maillard, L., and Rossion, B. (2016). A face-selective ventral occipito-temporal map of the human brain with intracerebral potentials. *Proceedings of the National Academy of Sciences*, 113(28):E4088–E4097.

Kalas, M. S. and Momin, B. (2016). Stress detection and reduction using EEG signals. In *2016 International Conference on Electrical, Electronics, and Optimization Techniques (ICEEOT)*, pages 471–475. IEEE.

Kandel, E. R., Schwartz, J. H., Jessell, T. M., Siegelbaum, S., Hudspeth, A. J., Mack, S., et al. (2000). *Principles of neural science*, volume 4. McGraw-hill New York.

Kanwisher, N., McDermott, J., and Chun, M. M. (1997). The fusiform face area: a module in human extrastriate cortex specialized for face perception. *Journal of neuroscience*, 17(11):4302–4311.

Kaur, A. and Budhiraja, S. (2014). Sparse signal reconstruction via orthogonal least squares. In *2014 Fourth International Conference on Advanced Computing & Communication Technologies*, pages 133–137. IEEE.

Klassen, B., Hentz, J., Shill, H., Driver-Dunckley, E., Evidente, V., Sabbagh, M., Adler, C., and Caviness, J. (2011). Quantitative EEG as a predictive biomarker for parkinson disease dementia. *Neurology*, 77(2):118–124.

Koessler, L., Benar, C., Maillard, L., Badier, J.-M., Vignal, J. P., Bartolomei, F., Chauvel, P., and Gavaret, M. (2010a). Source localization of ictal epileptic activity investigated by high resolution EEG and validated by SEEG. *Neuroimage*, 51(2):642–653.

Koessler, L., Salido-Ruiz, R., Ranta, R., Louis-Dorr, V., Gavaret, M., and Maillard, L. (2010b). Influence of source separation and montage on ictal source localization. In *2010 Annual International Conference of the IEEE Engineering in Medicine and Biology*, pages 2898–2901. IEEE.

Korats, G. (2016). *Cortical source imaging: from the laplacian montage to sparse inverse solutions*. PhD thesis, Université de Lorraine.

Korats, G., Le Cam, S., Ranta, R., and Louis-Dorr, V. (2015). A space-time-frequency dictionary for sparse cortical source localization. *IEEE Transactions on Biomedical Engineering*, 63(9):1966–1973.

Kybic, J., Clerc, M., Abboud, T., Faugeras, O., Keriven, R., and Papadopoulo, T. (2005). A common formalism for the integral formulations of the forward EEG problem. *IEEE transactions on medical imaging*, 24(1):12–28.

Kybic, J., Clerc, M., Faugeras, O., Keriven, R., and Papadopoulo, T. (2006). Generalized head models for MEG/EEG: boundary element method beyond nested volumes. *Physics in Medicine & Biology*, 51(5):1333.

La Rocca, D., Campisi, P., and Scarano, G. (2012). EEG biometrics for individual recognition in resting state with closed eyes. In *2012 BIOSIG-Proceedings of the International Conference of Biometrics Special Interest Group (BIOSIG)*, pages 1–12. IEEE.

Lawson, C. L. and Hanson, R. J. (1995). *Solving least squares problems*. SIAM.

Le Cam, S., Ranta, R., Caune, V., Korats, G., Koessler, L., Maillard, L., and Louis-Dorr, V. (2017). SEEG dipole source localization based on an empirical bayesian approach taking into account forward model uncertainties. *NeuroImage*, 153:1–15.

Lee, W. H., Deng, Z.-D., Kim, T.-S., Laine, A. F., Lisanby, S. H., and Peterchev, A. V. (2012). Regional electric field induced by electroconvulsive therapy in a realistic finite element head model: influence of white matter anisotropic conductivity. *Neuroimage*, 59(3):2110–2123.

Liebeskind, D. S. and Alexandrov, A. V. (2012). Advanced multimodal ct/mri approaches to hyperacute stroke diagnosis, treatment, and monitoring. *Annals of the New York Academy of Sciences*, 1268(1):1–7.

Lütkenhöner, B. (1992). Frequency-domain localization of intracerebral dipolar sources. *Electroencephalography and clinical Neurophysiology*, 82(2):112–118.

Maillard, L., Vignal, J.-P., Gavaret, M., Guye, M., Biraben, A., McGonigal, A., Chauvel, P., and Bartolomei, F. (2004). Semiologic and electrophysiologic correlations in temporal lobe seizure subtypes. *Epilepsia*, 45(12):1590–1599.

Mäkelä, N., Stenroos, M., Sarvas, J., and Ilmoniemi, R. J. (2018). Truncated rap-music (trap-music) for meg and eeg source localization. *NeuroImage*, 167:73–83.

Mallat, S. G. and Zhang, Z. (1993). Matching pursuits with time-frequency dictionaries. *IEEE Transactions on signal processing*, 41(12):3397–3415.

McCann, H., Pisano, G., and Beltrachini, L. (2019). Variation in reported human head tissue electrical conductivity values. *Brain topography*, 32(5):825–858.

Meijs, J. W., Weier, O. W., Peters, M. J., and Van Oosterom, A. (1989). On the numerical accuracy of the boundary element method (EEG application). *IEEE transactions on biomedical engineering*, 36(10):1038–1049.

Melissant, C., Ypma, A., Frietman, E. E., and Stam, C. J. (2005). A method for detection of alzheimer's disease using ica-enhanced EEG measurements. *Artificial Intelligence in Medicine*, 33(3):209–222.

Menendez, R. G. d. P., Andino, S. G., Lantz, G., Michel, C. M., and Landis, T. (2001). Noninvasive localization of electromagnetic epileptic activity. i. method descriptions and simulations. *Brain topography*, 14(2):131–137.

Michel, C. M., Murray, M. M., Lantz, G., Gonzalez, S., Spinelli, L., and de Peralta, R. G. (2004). EEG source imaging. *Clinical neurophysiology*, 115(10):2195–2222.

Moridera, T., Rashed, E. A., Mizutani, S., and Hirata, A. (2021). High-resolution EEG source localization in segmentation-free head models based on finite-difference method and matching pursuit algorithm. *Frontiers in Neuroscience*, page 789.

Mosher, J. C., Baillet, S., and Leahy, R. M. (1999). EEG source localization and imaging using multiple signal classification approaches. *Journal of Clinical Neurophysiology*, 16(3):225–238.

Mosher, J. C. and Leahy, R. M. (1998). Recursive music: a framework for EEG and MEG source localization. *IEEE Transactions on Biomedical Engineering*, 45(11):1342–1354.

Mosher, J. C., Lewis, P. S., and Leahy, R. M. (1992). Multiple dipole modeling and localization from spatio-temporal MEG data. *IEEE transactions on biomedical engineering*, 39(6):541–557.

Mostow, J., Chang, K.-m., and Nelson, J. (2011). Toward exploiting EEG input in a reading tutor. In *International conference on artificial intelligence in education*, pages 230–237. Springer.

Mountcastle, V. B. (1997). The columnar organization of the neocortex. *Brain: a journal of neurology*, 120(4):701–722.

Neugebauer, F., Möddel, G., Rampp, S., Burger, M., and Wolters, C. H. (2017). The effect of head model simplification on beamformer source localization. *Frontiers in neuroscience*, 11:625.

Osselton, J. (1965). Acquisition of EEG data by bipolar unipolar and average reference methods: a theoretical comparison. *Electroencephalography and clinical neurophysiology*, 19(5):527–528.

Palmini, A. (2006). The concept of the epileptogenic zone: a modern look at penfield and jasper's views on the role of interictal spikes. *Epileptic disorders*, 8(2):10–15.

Pascual-Marqui, R. D. (2007). Discrete, 3d distributed, linear imaging methods of electric neuronal activity. part 1: exact, zero error localization. *arXiv preprint arXiv:0710.3341*.

Pascual-Marqui, R. D., Michel, C. M., and Lehmann, D. (1994). Low resolution electromagnetic tomography: a new method for localizing electrical activity in the brain. *International Journal of psychophysiology*, 18(1):49–65.

Pati, Y. C., Rezaiifar, R., and Krishnaprasad, P. S. (1993). Orthogonal matching pursuit: Recursive function approximation with applications to wavelet decomposition. In *Proceedings of 27th Asilomar conference on signals, systems and computers*, pages 40–44. IEEE.

Potter, L. C. and Arun, K. (1989). Energy concentration in band-limited extrapolation. *IEEE Transactions on Acoustics, Speech, and Signal Processing*, 37(7):1027–1041.

Ranta, R., Le Cam, S., Bergmanis-Korats, G., Rimbert, S., and Bougrain, L. (2019). On source space resolution in EEG brain imaging for motor imagery. In *2019 9th International IEEE/EMBS Conference on Neural Engineering (NER)*, pages 1025–1029. IEEE.

Ranta, R., Salido-Ruiz, R., and Louis-Dorr, V. (2010). Reference estimation in EEG recordings. In *2010 Annual International Conference of the IEEE Engineering in Medicine and Biology*, pages 5371–5374. IEEE.

Rissanen, J. (1978). Modeling by shortest data description. *Automatica*, 14(5):465–471.

Ritter, P. and Villringer, A. (2006). Simultaneous EEG-fmri. *Neuroscience & Biobehavioral Reviews*, 30(6):823–838.

Rossion, B. (2014). Understanding individual face discrimination by means of fast periodic visual stimulation. *Experimental brain research*, 232(6):1599–1621.

Rossion, B., Torfs, K., Jacques, C., and Liu-Shuang, J. (2015). Fast periodic presentation of natural images reveals a robust face-selective electrophysiological response in the human brain. *Journal of vision*, 15(1):18–18.

Roth, B. J., Balish, M., Gorbach, A., and Sato, S. (1993). How well does a three-sphere model predict positions of dipoles in a realistically shaped head? *Electroencephalography and clinical Neurophysiology*, 87(4):175–184.

Saliba, J., Bortfeld, H., Levitin, D. J., and Oghalai, J. S. (2016). Functional near-infrared spectroscopy for neuroimaging in cochlear implant recipients. *Hearing research*, 338:64–75.

Sarvas, J. (1987). Basic mathematical and electromagnetic concepts of the biomagnetic inverse problem. *Physics in Medicine & Biology*, 32(1):11.

Schalk, G. (2004). A general-purpose brain-computer interface (bci) system. *IEEE Transactions on biomedical engineering*, 51(6):1034–1043.

Scherg, M. et al. (1990). Fundamentals of dipole source potential analysis. *Auditory evoked magnetic fields and electric potentials. Advances in audiology*, 6(40-69):25.

Schmidt, R. (1986). Multiple emitter location and signal parameter estimation. *IEEE transactions on antennas and propagation*, 34(3):276–280.

Sharbrough, F. W. (2005). 12, nonspecific abnormal EEG patterns. *Electroencephalography: basic principles, clinical applications, and related fields. Philadelphia, PA: Lippincott Williams & Wilkins*, page 235.

Soria Morillo, L. M., García, J. A. A., Gonzalez-Abril, L., and Ramirez, J. (2015). Advertising liking recognition technique applied to neuromarketing by using low-cost EEG headset. In *International Conference on Bioinformatics and Biomedical Engineering*, pages 701–709. Springer.

Soufineyestani, M., Dowling, D., and Khan, A. (2020). Electroencephalography (EEG) technology applications and available devices. *Applied Sciences*, 10(21):7453.

Soussen, C., Idier, J., Brie, D., and Duan, J. (2011). From bernoulli–gaussian deconvolution to sparse signal restoration. *IEEE Transactions on Signal Processing*, 59(10):4572–4584.

Soussen, C., Idier, J., Duan, J., and Brie, D. (2015). Homotopy based algorithms for ℓ_0-regularized least-squares. *IEEE Transactions on Signal Processing*, 63(13):3301–3316.

Stenroos, M. and Hauk, O. (2013). Minimum-norm cortical source estimation in layered head models is robust against skull conductivity error. *NeuroImage*, 81:265–272.

Stenroos, M., Mäntynen, V., and Nenonen, J. (2007). A Matlab library for solving quasi-static volume conduction problems using the boundary element method. *Computer methods and programs in biomedicine*, 88(3):256–263.

Swartz, B., Tomiyasu, U., Delgado-Escueta, A., Mandelkern, M., and Khonsari, A. (1992). Neuroimaging in temporal lobe epilepsy: test sensitivity and relationships to pathology and postoperative outcome. *Epilepsia*, 33(4):624–634.

Talairach, J., David, M., and Tournoux, P. (1958). *L'exploration chirurgicale stéréotaxique du lobe temporal dans l'épilepsie temporale: repérage anatomique stéréotaxique et technique chirurgicale*. Masson & Cie, Editeurs.

Tibshirani, R. (1996). Regression shrinkage and selection via the lasso. *Journal of the Royal Statistical Society: Series B (Methodological)*, 58(1):267–288.

Tropp, J., Gilbert, A. C., et al. (2007). Signal recovery from partial information via orthogonal matching pursuit. *IEEE Trans. Inform. Theory*, 53(12):4655–4666.

Tropp, J. A. and Gilbert, A. C. (2007). Signal recovery from random measurements via orthogonal matching pursuit. *IEEE Transactions on information theory*, 53(12):4655–4666.

Vallaghé, S. (2010). *EEG and MEG forward modeling: computation and calibration*. PhD thesis, Citeseer.

Van Loan, C. F. and Golub, G. (1996). Matrix computations. *Johns Hopkins University, Press, Baltimore, MD, USA*, pages 374–426.

Van Veen, B. D. and Buckley, K. M. (1988). Beamforming: A versatile approach to spatial filtering. *IEEE assp magazine*, 5(2):4–24.

Vijayaragavan, G. R., Raghav, R., Phani, K., and Vaidyanathan, V. (2015). EEG monitored mind de-stressing smart phone application using yoga and music therapy. In *2015 International Conference on Green Computing and Internet of Things (ICGCIoT)*, pages 412–415. IEEE.

Wax, M. and Kailath, T. (1985). Detection of signals by information theoretic criteria. *IEEE Transactions on acoustics, speech, and signal processing*, 33(2):387–392.

Wendling, F., Chauvel, P., Biraben, A., and Bartolomei, F. (2010). From intracerebral EEG signals to brain connectivity: identification of epileptogenic networks in partial epilepsy. *Frontiers in systems neuroscience*, 4:154.

Wilson, F. N. and Bayley, R. H. (1950). The electric field of an eccentric dipole in a homogeneous spherical conducting medium. *Circulation*, 1(1):84–92.

Wipf, D. and Nagarajan, S. (2009). A unified bayesian framework for MEG/EEG source imaging. *NeuroImage*, 44(3):947–966.

Wu, S. C. and Swindlehurst, A. L. (2013). Matching pursuit and source deflation for sparse EEG/MEG dipole moment estimation. *IEEE Transactions on Biomedical Engineering*, 60(8):2280–2288.

Wu, X.-F., Lang, Z.-Q., and Billings, S. A. (2005). An orthogonal least squares based approach to fir designs. *International Journal of Automation and Computing*, 2(2):163–170.

Yamada, T. and Meng, E. (2012). *Practical guide for clinical neurophysiologic testing: EEG*. Lippincott Williams & Wilkins.

Yao, D. (2000). Electric potential produced by a dipole in a homogeneous conducting sphere. *IEEE Transactions on Biomedical Engineering*, 47(7):964–966.

Yao, D. (2001). A method to standardize a reference of scalp EEG recordings to a point at infinity. *Physiological Measurement*, 22:693–711.

Zhang, J. (2019). Cognitive functions of the brain: Perception, attention and memory. *arXiv preprint arXiv:1907.02863*.

Zhang, T. (2008). Adaptive forward-backward greedy algorithm for sparse learning with linear models. *Advances in neural information processing systems*, 21.

Zheng, X. and Wan, B. (2006). Study on EEG source localization in frequency domain. In *2005 IEEE Engineering in Medicine and Biology 27th Annual Conference*, pages 5958–5961. IEEE.